Interface Investigations on Titanium Nitride Bilayer Systems

THÈSE N^{O} 5509 (2012)

PRÉSENTÉE LE 21 SEPTEMBRE 2012
À LA FACULTÉ DES SCIENCES DE BASE
LABORATOIRE DE PHYSIQUE DE LA MATIÈRE COMPLEXE
PROGRAMME DOCTORAL EN PHYSIQUE

ÉCOLE POLYTECHNIQUE FÉDÉRALE DE LAUSANNE

POUR L'OBTENTION DU GRADE DE DOCTEUR ÈS SCIENCES

PAR

Dominik Anwar JAEGER

acceptée sur proposition du jury:

Prof. V. Savona, président du jury
Prof. L. Forró, Dr J. Patscheider, directeurs de thèse
Prof. B. Meyer, rapporteur
Prof. P. Muralt, rapporteur
Prof. A. Rossi, rapporteur

ÉCOLE POLYTECHNIQUE
FÉDÉRALE DE LAUSANNE

Suisse
2012

God made the bulk;
surfaces were invented by the devil.
— Wolgang Pauli

I wonder who created the interface?

Dedicated to my office mate and friend Lorenzo Castaldi († 25.03.2012)
and to my parents.

Abstract

Nanocomposite coatings composed of two phases with atomically sharp phase boundaries, show interesting mechanical properties. These properties are often originating from their high interface to volume ratio. Composites of nanocrystalline titanium nitride (TiN) grains surrounded by a one to two monolayer thick interlayer of silicon nitride (Si_3N_4) show an enhanced nanohardness.

The central theme of this thesis is concerned with the interfacial properties of two-dimensional bilayer systems, which are used as model systems to describe the interfaces occurring in nanocomposite coatings. The systems under investigation are TiN interfaces in contact with silicon (Si), silicon nitride (Si_3N_4) and aluminum nitride (AlN). The primary tool used to analyze the interfaces of bilayer systems is X-ray Photoelectron Spectroscopy (XPS) with emphasis put on the shake-up feature of the Ti 2p photoelectron line. Shake-ups in TiN are observed as an additional peak on the lower binding energy side of the energy lines of the Ti 2p orbitals. Shake-ups are strongly influenced by valence electrons and electron density distributions. This makes them a powerful tool to probe the chemical and electronic structure of TiN interfaces. The aim of this study is to utilize the shake-up energy and its intensity to gain insight into interfacial structures and correlate their changes to interfacial polarization and macroscopic mechanical properties.

Single crystalline (sc-) and oxygen-free TiN as well as oxygen-free bilayer systems were deposited by unbalanced magnetron sputtering and analyzed by Angle Resolved (AR-)XPS. Bilayer samples were deposited and their quality was controlled using X-ray diffraction (crystallinity), Rutherford back scattering (elemental composition), and atomic force microscopy (roughness). All XPS samples were fabricated, transfered and analyzed whilst maintaining ultra high vacuum.

A precise and self-consistent XPS data processing method was developed to evaluate Ti 2p spectra. This method accounts for the correct photoelectron line shape, background subtraction and photoelectron peak area intensity. Binding energy, shake-up energy and intensity ratios of shake-ups taken from pristine TiN surfaces are precisely determined, and the influence of oxygen on the information content in peak positions and intensities was investigated. The shake-up energy and intensity of bulk sc-TiN and its origin of the shake-up are discussed.

An analytical description for the XPS signal ratio of bilayer systems is derived to separate the interfacial signals from the bulk information. The results obtained by this analytical description are strongly influenced by the interface thickness that has been found to be proportional to the overlayer thickness. The revealed interface properties show a correlation between the shake-up intensity and the interface morphology, oxygen content, overlayer material and overlayer thickness.

AR-XPS and X-ray Photoelectron Diffraction (XPD) results were used to interpret the crystalline structure of the different TiN/AlN and TiN/Si_3N_4 bilayer systems. AlN shows XPD patterns indicating a crystalline growth of AlN on sc-TiN. The electrically insulating AlN overlayer creates a charge accumulation at the TiN interface, which results in an enhanced shake-up intensity. XPD patterns of Si_3N_4 systems revealed a crystalline growth of Si_3N_4 in the first 0.6 nm. The intensity of the diffraction patterns reduces with increasing Si_3N_4 overlayer thickness due to a change in the growth behavior from crystalline to amorphous structures. Si_3N_4 films show, in comparison to AlN, reduced interface charging and hence a lower shake-up intensity. The crystalline growth of Si_3N_4 in the initial stages is hindered in systems where a bias voltage is applied to the substrate during the deposition process. In contrast to the unbiased systems, which have crystalline interfacial structures, the biased systems no longer show XPD patterns due to a loss of crystallinity. Additionally the shake-up intensity of biased systems is thickness-independent, which is in contrast to unbiased systems. The difference in the shake-up intensity of biased and unbiased Si_3N_4 is explained by a different band gap of the Si_3N_4 structure in the first two monolayers.

This thesis shows that the increase in the shake-up intensity is correlated to intrinsic and extrinsic interface charging. The obtained results, in combination with theoretical structure models from literature, show that in one to two monolayer thick interlayers a build-up of interface polarization is unlikely. The observed nanohardness enhancement in TiN/Si_3N_4 systems is explained with already known hardness effects.

keywords:
Shake-up, titanium nitride, interface polarization, AR-XPS, nanocomposite coatings, hardness enhancement

Zusammenfassung

Mehrphasige dünne nanokomposite Beschichtungen mit atomar scharfen Phasengrenzen besitzen vorteilhafte mechanische Eigenschaften. Verantwortlich für diese aussergewöhnlichen Eigenschaften ist u.a. das hohe Verhältnis von Grenzflächen zu Volumen. Komposite aus nanokristallinen Titannitrid (TiN)- Körnern, umgeben von einer Siliziumnitrid (Si_3N_4)-Zwischenschicht zeigen eine Härteüberhöhung für Si_3N_4 Zwischenschichten mit einer Dicke von ein bis zwei Monolagen.

Das zentrale Thema der vorliegenden Doktorarbeit sind Grenzflächeneigenschaften von zweidimensionalen Doppelschichtsystemen, die als Modellsysteme dienen, um Grenzflächen in Nanokompositen zu beschreiben. Die untersuchten Systeme sind TiN-Grenzflächen im Kontakt mit Silizium (Si), Siliziumnitrid (Si_3N_4) und Aluminiumnitrid (AlN). Primär wurden die Grenzflächen der Doppelschichtsysteme mittels Röntgenphotoelektronenspektroskopie (XPS) analysiert, wobei der Schwerpunkt der Untersuchung auf dem Shake-Up der Ti 2p Photoelektronenlinie liegt. Shake-Ups werden in Titannitrid als zusätzlicher Beitrag auf der niedrigen Bindungsenergieseite des Hauptpeaks der Ti 2p-Linie beobachtet. Shake-Ups sind sehr empfindlich gegenüber Veränderungen in der Valenzelektronenkonfiguration und gegenüber Elektronendichteverteilungen. Daher sind Shake-Ups ein leistungsfähiges Hilfsmittel, um die chemische und elektronische Struktur von TiN-Grenzflächen zu erforschen. Das Ziel dieser Untersuchungen ist es, die Shake-Up-Energie und deren Intensitäten zu nutzen, um Einblicke in die Grenzflächenstruktur zu gewinnen und die Veränderungen des Shake-Ups mit Grenzflächenpolarisation und den makroskopischen Mechanischen Eigenschaften zu verknüpfen.

Einkristallines und sauerstofffreies TiN sowie sauerstofffreie Doppelschichtsysteme wurden mit Unbalanced Magnetron Sputtering abgeschieden und mittels winkelaufgelöster Röntgenphotoelektronenspektroskopie (AR-XPS) analysiert. Doppelschicht-Proben wurden hergestellt und deren Qualität untersucht bezüglich ihrer Kristallinität (Röntgenbeugung, XRD), ihrer Elementzusammensetzung (Rutherford-Rückstreu-Spektrometrie, RBS) und ihrer Rauheit (Rasterkraftmikroskopie, AFM). Alle Proben wurden unter Ultrahochvakuum-Bedingungen hergestellt, transferiert und analysiert. Eine präzise und widerspruchsfreie Methode zur Auswertung von Ti 2p XPS Spektren wurde entwickelt. Diese Methode berücksichtigt die korrekte Form von Photoelektronenlinien, die Hintergrundkorrektur und die Peakintensität. Bindungsenergie, Shake-Up Energie und Shake-Up Intensitätsverhältnisse für reine TiN Oberflächen wurde genau bestimmt, und der Einfluss von Sauerstoff auf den Informationsgehalt der Peakposition und -intensität wurden untersucht. Shake-Up Energie und Intensität von einkristallinem TiN sowie deren Ursprung sind diskutiert. Eine analytische Beschreibung der XPS-Signalverhältnisse von Doppelschichtsystemen ist hergeleitet, um Grenzflächensignale von Tiefeninformationen zu trennen. Die durch diese analytische Beschreibung erhaltenen Ergebnisse sind stark beeinflusst von der Grenzflächendicke, welche proportional zur bedeckenden Schichtdicke ist. Die Untersuchungen der Grenzflächeneigenschaften deckten auf, dass die Shake-Up Intensität mit der Grenzflächenmorphologie, dem Sauerstoffgehalt, dem Grenzflächenmaterial und der bedeckenden Schichtdicke korreliert. Ergebnisse von winkelaufgelöstem XPS und Röntgenphotoelektronendiffraktion (XPD) wurden benutzt, um die kristallinen Strukturen der TiN/AlN und TiN/Si_3N_4 Doppelschichtsysteme zu interpretieren. AlN weist XPD-Muster auf, welche auf ein kristallines Wachstum von AlN auf einkristallinem TiN hinweisen. Die elektrisch isolierende AlN-Schicht verursacht eine Ladungsträgerkonzentration an der TiN-Grenzfläche, die wiederum zu eine Erhöhung der Shake-Up Intensität führen. XPD-Muster von Si_3N_4 deuten auf ein kristallines Wachstum von Si_3N_4 in den ersten 0.6 nm hin. Die Intensität von XPD-Mustern nimmt ab mit zunehmender Si_3N_4 Dicke, verursacht durch einen Wechsel von kristallinem zu amorphem Wachstumsverhalten. Si_3N_4 Schichten zeigen im Vergleich zu AlN eine reduzierte Grenzflächenaufladung und folglich eine niedrigere Shake-Up Intensität. Das kristalline Wachstum von Si_3N_4 in den ersten Lagen wird durch Anlegen einer Bias-Spannung am Substrat während des Abscheideprozesses unterbunden. Diese Systeme zeigen keine XPD-Muster mehr aufgrund des Verlustes der kristallinen Struktur. Ausserdem sind die Shake-Up-Intensitäten in Si_3N_4-Systemen, hergestellt mit Bias, unabhängig von der bedeckenden Schichtdicke, was im Gegensatz zu den Systemen steht, die ohne Bias hergestellt wurden. Der Unterschied in den beiden Si_3N_4 -Systemen wird durch unterschiedliche elektronische Bandlücken in den ersten zwei Monolagen der beiden Si_3N_4 Kristallgitter erklärt. Die Doktorarbeit zeigt, dass die Zunahme der Shake-Up-Intensität mit intrinsischer und extrinsischer Grenzflächenaufladungen korreliert ist. Die gezeigten Ergebnisse belegen, in Kombination mit theoretischen Strukturmodellen aus der Literatur, dass Grenzflächenpolarisation in ein bis zwei Monolagen dicken Zwischenschichten unwahrscheinlich sind. Die beobachtete Erhöhung der Nanohärte wird mit bereits bekannten Effekten zum Härtebeitrag erklärt.

Stichworte:
Shake-up, Titannitrid, Grenzflächenpolarisation, winkelaufgelöster Röntgenphotoelektronenspektroskopie (AR-XPS), nanokomposite Beschichtungen, Härteüberhöhung

Résumé

Les couches minces nanocomposites présentent des propriétés mécaniques remarquables, souvent reliées à un rapport interface/volume élevé. Ainsi les matériaux composites constituées de grains nanocristallins de nitrure de titane (TiN) enrobés dans une intercouche d'une à deux monocouches de nitrure de silicium (Si_3N_4) présentent une nanodureté accrue.

L'objet de ce travail est l'investigation des propriétés d'interface de systèmes bicouche bidimensionnels utilisés comme systèmes modèle pour décrire les interfaces nanocomposites. Sont considérés ici des interfaces de nitrure de titane (TiN) en contact avec du silicium (Si), du nitrure de silicium (Si_3N_4) et du nitrure d'aluminium (AlN). L'outil principal d'analyse des systèmes bicouche étudiés repose ici sur les structures d'excitation " shake-up " observées en spectroscopie de photoélectrons X (XPS). Le phénomène d'excitation shake-up du TiN se manifeste sous la forme d'un pic satellite du côté des plus faibles énergies de liaison du niveau de cœur Ti 2p. Après photoémission d'un électron de cœur Ti 2p deux états finaux peuvent être atteints qui sont responsables de l'apparition d'un pic principal de photoémission et d'un pic shake-up. La différence d'énergie entre le pic principal et le pic shake-up est appelée " énergie de shake-up ". Les pics shake-up sont fortement influencés par les électrons de valence et la distribution de densité d'électrons. Les shake-ups du TiN sont de ce fait un outil puissant pour l'investigation des structures électroniques et chimiques aux interfaces du TiN. Le but de la présente étude est d'utiliser l'énergie de shake-up ainsi que l'intensité du pic shake-up pour obtenir des informations sur les structure d'interface et potentiellement corréler leur évolution à la polarisation d'interface. La polarisation d'interface pourrait en effet expliquer l'augmentation de nanodureté.

Des couches de TiN monocristallin (mc-) exemptes d'oxygène ainsi que des systèmes bicouche sans oxygène ont été fabriqués par pulvérisation cathodique magnétron non-équilibré et analysées par XPS à résolution angulaire (AR-XPS). Différents échantillons d'interface ont été déposés et leur qualité a été contrôlée par diffraction aux rayons X (cristallinité), spectroscopie de rétrodiffusion de Rutherford (composition élémentaire) et microscope à force atomique (rugosité). Tous les échantillons d'XPS ont été déposés, transférés et analysés sous ultra vide.

Une méthode de traitement de données précise et cohérente a été développée. Cette méthode prend en compte la forme exacte du pic photoélectronique, la soustraction de la ligne de base et l'intensité du pic photoélectronique. L'énergie de liaison, l'énergie de shake-up ainsi que les rapport d'intensités des pics shake-up de TiN pure sont déterminés précisément et l'influence de l'oxygène est examinée. L'énergie de shake-up et l'intensité du mc-TiN volumique sont comparés à la littérature et l'origine du pic shake-up est discutée.

Une description analytique des systèmes bicouche est enfin établie qui permet de séparer les signaux provenant de l'interface des informations volumiques. Les résultats ainsi obtenus sont très fortement influencés par l'épaisseur d'interface, elle-même estimée comme étant proportionnelle à l'épaisseur de la surcouche. Les résultats mis en évidence aux interfaces montrent une corrélation entre l'intensité de pic shake-up d'une part, et la morphologie d'interface, la teneur en oxygène, le matériaux constituant de la surcouche ainsi que son épaisseur d'autre part. La structure des différents systèmes bicouche TiN/AlN et TiN/Si_3N_4 a été interprétée à partir des résultats d'AR-XPS et de diffraction de photoélectrons X (XPD). Le spectre XPD de l'AlN indique une croissance cristalline sur mc-TiN. Le caractère électriquement isolant de la surcouche d'AlN est la cause d'une accumulation de charge à l'interface avec le TiN, à son tour responsable d'une augmentation de l'intensité du pic shake-up. Le spectre XPD du Si_3N_4 révèle lui une croissance cristalline sur quelques monocouches seulement. L'intensité des spectres de diffraction diminue par ailleurs avec l'épaisseur croissante de la surcouche de Si_3N_4. Ceci est interprété comme étant la preuve d'un changement de mode de croissance d'une structure cristalline à une structure amorphe. Comparés à l'AlN, les films de Si_3N_4 présentent une accumulation de charge à l'interface moindre, d'oû une intensité de pic shake-up elle-aussi réduite. La croissance cristalline initiale du Si_3N_4 est entravée lorsqu'une polarisation est appliquée au substrat pendant le procédé de dépôt. A l'inverses des système déposés en l'absence de polarisation, qui présentent une structure cristalline à l'interface, les systèmes non-polarisés présentent un spectre XPD plat du à leur perte de cristallinité. La intensité de pic shake-up des systèmes polarisés sont indépendant de la épaisseur des surcouches. Cette différence d'intensité s'explique par une différence de largeur de bande interdite de la structure Si_3N_4 dans les premières deux monocouches.

Dans ce travail de thèse, il est ainsi démontré que l'augmentation d'intensité des pics shake-up est corrélée à une accumulation de charge à l'interface Les résultats obtenus, associés aux modèles de structure théorique de la littérature, montrent qu'aucune polarisation d'interface est improbable développée dans des intercouches de un à deux monocouches d'épaisseur. L'augmentation de nanodureté observée dans le TiN/Si_3N_4 s'explique donc à partir de mécanisme de durcissement déjà connus.

mots-clé :
Shake-up, nitrure de titane, charge à l'interface, spectroscopie de photoélectrons X à résolution angulaire (AR-XPS), couches minces nanocomposites, mécanisme de durcissement

Acknowledgments

First, I want to thank Dr. Jörg Patscheider for giving me the possibility to do my dissertation in his group Thin Films and Coatings, for being my daily advisor, for giving me the freedom to give this thesis my own personal touch and direction, for giving me the opportunity to present my work at international conferences, for very thorough corrections of my oral and written contributions and for being a great supervisor.

I am also very grateful to Prof. Antonella Elsener-Rossi for introducing me to XPS. Her lecture at the ETH Zürich and her further scientific help over the last years formed the scientific basis on XPS of this thesis.

I am also grateful to Prof. Forró László for being my thesis director and for enlightening discussions in Lausanne and in Dubrovnik.

I also would like to thank Prof. Bernd Meyer and Dr. Daniele Passerone for detailed and passionate discussions on the shake-up feature, for their help in understanding quantum mechanics as well as for their pDOS calculations, which will be used in the future.

Thanks also to Prof. Paul Muralt for kindly accepting to be an expert in my thesis jury. I am grateful to Prof. Hans J. Hug for providing leadership in maintaining the infrastructure of the Nanoscale Materials Science laboratory used in this work.

I am grateful to Dr. Max Döbeli for performing and explaining the RBS and ERDA measurements. I want to thank also Prof. Svante Svensson for fruitful discussions on the shake-up. The help of Dr. Pawel Rodziewicz, Prof. Christian Elsässer and the whole team of the DFT2BOP2Exp project is very much appreciated. I want to thank Neal Fairley for enlightening discussions, a great software support and implementing several background types into his software CasaXPS.

The support of the electron microscopy (EM) center at Empa is highly appreciated. I want to thank Prof. Magdalena Parlinska-Wojtan for the tedious sample preparation and her patience in introducing me into TEM. I also would like to thank Dr. Rolf Erni for his support and advices with TEM. Thanks also to Daniel Schreier for the technical support in the (EM) center.

I want to thank also Dr. Oliver Groening and Prof. Roman Fasel for their explanations and discussions on XPD. Thanks also to Prof. Peter Lienemann for his explanations on XRD.

A special thank you to my former and current office mates Chiara Corticelli, Chrysanthi Karageorgaki, Lorenzo Castaldi, Sara Romer and Michael Böttger for an extremely agreeable and entertaining atmosphere, where spontaneous scientific discussions are on the same level as problems of the daily life. Further I want to thank my predecessor Dr. Aude Pélisson for explaining me all the machines used in the group of Nanoscale Materials Science. The help of Dr. Erik Lewin in the lab and also with scientific problems is highly appreciated.

I want to express my gratitude also to Dr. Roland Hauert and Dr. Ulrich Müller for scientific support on the XPS-device. A big thanks goes to Saša Vranjković and Günther Hobi for their technical support in the laboratories. Another big thanks to Dr. Pablo Stickar for helping me with Latex and also for many scientific discussions. I also want to thank the complete Abt. 125 for a very enriching time.
Last, but certainly not least, I want to express my deepest gratitude to my friends and family for all the help and support.

The financial support of the Swiss National Science foundation under
grants nr. 200021-116392 and 200020-130416 is gratefully acknowledged.

Contents

Introduction Part I

1 Motivation and structure

Coatings nowadays are used in a tremendous amount of items. They improve the surface properties, as e.g. corrosion resistivity, wear resistance, hardness, friction or optical properties [1, 2]. Many tools (e.g. drilling bits), medical devices (e.g. hip joints) and consumer products (e.g. solar cells) are covered with a protective, functional and/or decorative coating to enhance their appearance, efficiency and life time. Also intentionally less obvious coatings are used to protect all kind of glasses (e.g. windows and spectacles) and displays (smartphones and tablets); even chocolate is coated to prevent melting in the hand. The global value of the coating market for the year 2017 has been forecasted by Global Industry Analysts, Inc. [3] to be US$ 107 billion. A global market study by Future Markets Inc. [4] estimates, that just the nanocoatings market (including dispersed nanocomposites), in the year 2011 was US$ 1.5 billion and predict a growth up to US$ 7.8 billion by the year 2017. Optimistic estimations for nanoscale and thin film market are up to US$ 13 billion until the year 2016 [5].

1.1 Scientific motivation

Coatings are coverings applied to the surface of an object. In this study thin films (with thickness of less than a few μm) are studied, and more precisely nanocomposite coatings which are thin films built of nanomaterials. The latter are materials containing morphological features in the nanoscale (1 – 100 nm) and show generally special properties stemming from the nanoscale dimensions [6]. Nanocomposites are build up of nanocrystalline (nc-) grains, fibers or crystallites with less than 100 nm diameter (for superhard nanocomposites often grain sizes below 10 nm are present) [1] which are surrounded by an amorphous (a-)[i] matrix. Many different systems, mainly of metal nitrides and carbides, are the subject of current research in literature and reviewed regularly [1, 2, 7–16]. The influence of deposition temperature and pressure on the structure of deposited coatings has been described by Thornton [17]. The structure of the nanocomposite coating has been further correlated to the nano hardness of the film [18–21]. A multitude of publications over the last years [1, 13, 14, 16, 18–46] addressed

---

[i] regarding the following discussion, amorphous (a-) refers in nc-TiN/a-Si_3N_4 to X-ray amorphous

the origin of the hardness in nanocomposites. The mechanical properties of a nanocomposite material are the results of the compounds in the composite, the size, the structure and the amount of mixture. For a certain combination of compounds (given specific interfacial bonding) the mechanical properties are e.g. strongly depending on the thickness of the matrix phase between the crystalline grains [2, 33, 47]. The interface between nanocrystalls and amorphous matrix have been modeled on a TiN and Si_3N_4 system and studied by Hultman et al. [48] using HR-TEM, and by Patscheider et al. [27] using AR-XPS. In the latter a model is proposed to correlate core level peak and satellite intensities of the XPS spectra directly to interface polarizations, which could result in an enhanced interface strength and hence to harder thin films. Some of the photoelectron characteristics of metal nitrides and carbides are still a matter of debate [35, 49, 50], hence a precise evaluation and quantification as well a closer look at the origin of the XPS features are presented in this work.

Nanocomposites possess three-dimensional structures that are in the best case difficult and in most cases impossible to resolve. By reducing the dimensions from a three-dimensional-nanocomposite to a two-dimensional-multilayer systems it is at least partially possible to study the material properties with e.g. AR-XPS or HR-TEM. Multilayers show partially a similar behavior regarding hardness enhancement. The theories of multilayer systems cannot be translated one-to-one to nanocomposite coatings, since additional grain translation, rotation or sliding is possible as well as complex grain geometries, which have to be considered in the case of nanocomposites. In a first step, two dimensional multilayers are used as a model to understand factors influencing hardness, and this insight is transferred and expanded to the case of three-dimensional nanocomposites.

1.2 Structure of the thesis

This thesis is structured in four parts: an introduction (part I), a description of the sample fabrication and characterization methods (part II), an account and discussion of the results (part III) and the conclusions (part IV).

In the first part (part I) the motivation of the presented work is described, including both the commercial (sect. 1) and the scientific motivation (sect. 1.1). In the following section the reader is introduced to the basics of hard coatings (sect. 2) and the relevant hardness enhancement effects (sect. 2.2), state-of-the-art thin film deposition techniques (sect. 2.3) and a summary of layer and film growth behavior (sect. 2.4). Section 3 deals with fundamentals of XPS that are essential for the understanding of the observed features, i.e. the basic photoemission process (sect. 3.2), different energy lines and their line shapes (sect. 3.3-3.6), as well as the background (sect. 3.7), and a method to obtain quantitative elemental concentration from the XPS spectra (sect. 3.8). The third section closes with a brief literature review on XPS spectra of TiN (sect. 3.10).

The second part (part II) deals with the details on the sample fabrication procedures (chapter 4) and the characterization methods (chapter 5): AFM (sect. 5.6), XRD (sect. 5.7), XRR (sect.

5.8), RBS (sect. 5.9), TEM (sect. 5.10) and Profilometry (sect. 5.11). These techniques were used to verify that the samples are oxygen-free, single-crystalline and have atomically sharp interfaces.

Experimental results (sect. III) related to general sample characeristics such as crystallinity (sect. 6.1), overlayer thickness (sect. 6.2), roughness (sect. 6.3) and interface structure (sect. 6.4) are presented in chapter 6. Chapter 7 focuses on XPS spectra of pristine TiN: binding energies (sect. 7.1), different components in the Ti 2p XPS spectra (sect. 7.2), background (sect. 7.3), line shapes (sect. 7.4) and X-ray Photoelectron Diffraction (sect. 7.5) are elucidated. Chapter 8 deals with TiN/Si, TiN/Si_3N_3 and TiN/AlN bilayer systems, where the parameters influencing the shake-up intensity at the systems interface are analyzed. In particular the influence of the oxygen concentration (sect. 8.3), sample charging and interface charging (sect. 8.4), and the interface thickness δ (sect. 8.5) on the shake-up process are revealed. In chapter 9 the expected interface polarization (sect. 9.1) and the effects contributing to a hardness enhancement (sect. 9.2) are discussed.

The conclusions are stated in part IV and are divided in the experimental achievements (sect. 10.1), the data processing (sect. 10.2), the obtained bulk properties of TiN (sect. 10.3), the shake-up process (sect. 10.4), the interface characteristics (sect. 10.5), and the interface polarization in TiN/Si_3N_4 nanocomposites, including hardness effects (sect. 10.6).

2 Hard coatings

There is a variety of hard coatings, ranging from diamond like carbons (with a Vickers hardness of 10 – 30 GPa) [11, 51–54], monolithic TiN (24 GPa) [39, 55], nanocomposites of nc-TiN/a-Si_3N_4 (up to 50 GPa) [28, 32, 34], TiN/VN multilayers (> 50 GPa) [56–58] to BN (≈ 60 GPa)[59–62]. A full literature review on hard coatings is beyond the scope of this work. In this thesis only a few transition metal nitride (TMN) systems have been chosen, namely TiN systems in contact with Si, Si_3N_4 and AlN. Previous studies on the hardness of superhard TiN/Si_3N_4 systems are briefly reviewed in the next section 2.1. Effects underlying hardness enhancement are discussed in section 2.2. The last section 2.3 of this chapter deals with the most common deposition techniques for coatings with the focus on Unbalanced Magnetron Sputtering (UBMS).

2.1 State-of-the-art

Already in 1914 Fleming [63] patented "protective coverings" made out of TiN "for electrodes, resistors, furnace bricks and similar articles". Further patents [64] and studies on chemical and Physical Vapor Deposition (PVD) of TiN as protective coatings followed [65–70]. TiN has found widespread application as a protective coating and as diffusion barrier due to its hardness, corrosion resistance and its high melting point [55, 65, 71]. TiN is also used as a decorative coating [72, 73] since its reflection spectrum is very similar to that of gold. Li Shizhi et al. [74] was the first to report enhanced mechanical properties of nc-TiN and a-Si_3N_4 nanocomposites, that became the "prototype" of a hard nanocomposite [75, 76]. Structure and phase studies on this hard system followed [77] as well as investigations on crack growth resistance [78] and oxidation resistance [79, 80]. Special scientific interest in nc-TiN/a-Si_3N_4 systems arose after it had been claimed by the group of Vepřek that these thin films show ultrahardness of over 100 GPa [81, 82]. The origin of this ultrahardness has been the subject of recent scientific articles [18–34, 83] with the focus on the structure [18–21], the silicon content [31], the grain size [32], the content of impurities [76, 84, 85] or the interface of the nc-TiN grains and the surrounding a-Si_3N_4 matrix [23, 27, 34, 48]. Recently it has been claimed that these values previously reported [81] are overestimated by a factor of ≈ 2 due to deficiencies in the measurement procedure [28]. Nevertheless nc-TiN/a-Si_3N_4 nanocomposites show enhanced hardness under certain conditions and have been used to develop design rules for superhard coatings [2, 86]. Combinations of binary, ternary and quaternary systems, such as Al – Ti – N [87, 88], Zr – Si – N [40, 89], Ti – Al – Si – N [12, 89] and Ti – Al – V – Si – N [89] nanocomposites have been reported to show a similar hardness enhancement upon addition of Si.

2.2 Hardness

The hardness is defined as the resistance of solid matter to plastic deformation. This can be measured in a variety of ways, defining three types of hardness: scratch hardness, indentation hardness and rebound hardness. In this thesis hardness is referred to as indentation hardness. The deposited films are very thin, and hence it is important that the film's, and not the substrate's hardness is measured. In general a nanoindenter is used and certain measurement rules have to be considered [12, 28] to obtain the indentation hardness H:

$$H = \frac{P_{max}}{A} \tag{2.1}$$

where P_{max} is the maximum load and A is the contact area. In crystalline materials any plastic deformation caused by the force of the indenter requires dislocation movement. Dislocations are crystallographic defects or irregularities within a perfect crystal structure. Different kinds exist: edge-, screw- or mixed dislocation which are described by the burgers vector [90]. A dislocation propagates until a barrier or the solid surface is reached. Their movement is impeded by different kinds of stress fields and by other dislocations, inducing a pile-up of dislocations in front of barriers. Hardness is a combination of the intrinsic properties of the film such as ductility, elastic stiffness, plasticity, strain, strength, toughness, viscoelasticity, and viscosity. But also extrinsic effects influence the hardness, such as substrate adhesion, residual stress and the geometry of the indentation tip [91–93].

Coatings can be classified according to a) their hardness: $H > 20$ GPa are called hard, $H \geq 40$ GPa are considered superhard and coatings with $H \geq 80$ GPa are ultrahard or b) can be divided in single- and multiphase coatings. Holleck [91] classified hard coatings according to their bond nature: metallic (transition metal-nitrides, -carbides and -borides), covalent (nitrides, carbides and borides of Al, Si and B, including diamond) and ionic (e.g. oxides of Al, Be, Ti and Zr). A triangle representing the three bond natures and the arising mechanical properties is shown in figure 2.1. Covalent bonds show the highest hardness and the lowest thermal expansion coefficient. Ionic bonds are chemically inert and brittle, while materials with metallic bonds have a high Young's modulus and adhere well to metallic substrates [16]. In the case of e.g. TiN a combination of covalent and metallic bonding predetermine the interplay of adhesive, tough, strong and hard material [95, 96]. The hard materials shown in fig. 2.1 can be compounded to a multiphase coating with improved mechanical properties such as nc-TiN/a-Si_3N_4 composites.

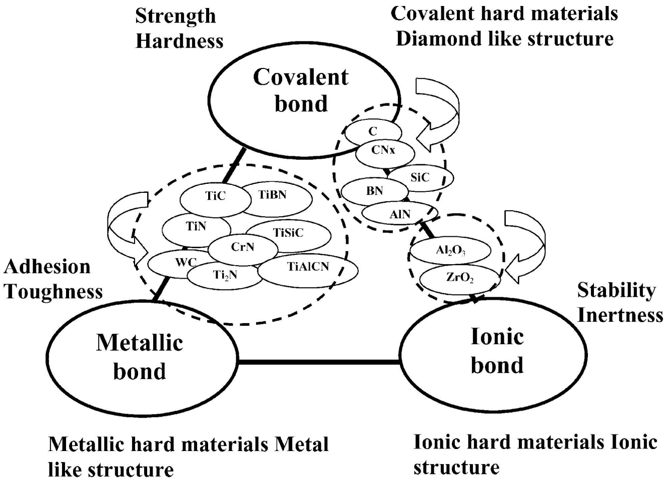

Figure 2.1: The mechanical properties of a material depend on its chemical bonding and can be classified in metallic, covalent and ionic bonds [94].

In this work the processes that cause hardening are grouped in bulk hardening and in thin film hardening. The bulk hardening effects are often used in the metal working industry and imply solid solution strengthening, precipitation hardening, work hardening, martensitic transformation, Hall-Petch strengthening , inverse Hall-Petch softening , and bombardment hardening (sect. 2.2.1). The thin film hardening effects are generated by sputter techniques and encompass hardening effects caused by coherency strains, misfit dislocations, thermal stress, orientation, Koehler stresses, interlayer stabilization, supermodulus effect and polarization strengthening (sect. 2.2.2).

2.2.1 Bulk hardening

Hardening techniques have already been used for more than 5000 years, e.g. cold forming or thermal annealing, as it is used during forging. The bulk hardening effects are mainly used to increase the hardness of bulk material, but can also be partially transfered to nanocomposites. In general hardening is enhanced by hindering or inhibiting dislocation creation or movement. The processes presented in this subsection are commonly used in industry to harden bulk materials (e.g. steel) or their surfaces.

Solid solution strengthening: An alloying element in a crystalline lattice of a base material forms a solid solution. The dissolved element can either replace an atom from its lattice position (substitution) or occupy interstitial sites in between the lattice (interstitial). Dislocations create stress fields within the material and interact with the local stress fields that are formed by the solute atoms. Hence the dislocation movement is impeded and the yield strength and hardness of the material are increased [90, 97, 98].

Precipitation hardening: Precipitation hardening (also called aged hardening) is based on thermal annealing to precipitate fine particles of an impurity phase. Those secondary phase particles cause lattice distortion, resulting in either a tensile (small precipitates) or a compressive stress (large precipitates). The induced stress field interacts with the dislocation stress field and hinders the dislocation movement [90, 97, 98].

Work hardening: Due to plastic deformation the dislocation density increases until a saturation point, where no new dislocations can be formed. A higher dislocation concentration means also enhanced interactions between the dislocations (pile-up), thus the dislocation movement is impeded [99, 100].

Martensitic transformation: The martensitic transformation is a diffusionless phase change. A prominent example is the transformation of body-centered tetragonal (bct) austenite into face-centered cubic (fcc) martensite. The activation energy to transform the bct structure in a fcc is very small. The transformation is induced either by quenching or by applying shear stress; both cases cause an ordered movement of a large number of atoms (displacive transformation). This distortion results in mismatches between neighboring regions and in the formation of crystal defects. The latter hinder the dislocation movement, cause dislocation pile-ups and lead to a harder material.

Hall-Petch strengthening: In the early 1950s E. O. Hall and N. J. Petch discovered independently from each other that the crack length [101] and the brittle fracture [102] in steel are correlated to the grain size d. Strength and hardness (H) increase, for crystallite (grain) size below 1 µm, with decreasing size; this is expressed in the Hall-Petch (HP) formula:

$$H = H_0 + \frac{k_{HP}}{\sqrt{d}} \tag{2.2}$$

where H_0 is the intrinsic hardness, k_{HP} is the material dependent strengthening coefficient and d is the grain size. Dislocations propagate through the material until a grain boundary, where further dislocation movement is impeded, and the dislocations pile up [103]. This phenomenon is prominent for grains sizes of 50 – 100 nm, grain sizes below 10 – 20 nm show a reverse or inverse Hall-Petch (iHP) behavior , i.e. the strength decreases with the grain size [21, 104]. Around this critical value d_c of the grain size the deformation is dominated for $d < d_c$ by intergranular (small scale sliding in the grain boundaries) and for $d > d_c$ by intragranular processes (dislocation nucleation and motion), see fig. 2.2 [105]. This softening of the material is still heavily discussed and can only be completely explained in the limit of a zero grain size, where the material is amorphous [104, 106–110]. Possible explanations are all based on the fact that if the distance between dislocations gets smaller than the grain size, then no more pile-ups can develop. Schiøtz et al. [111] showed by molecular dynamic (MD) simulations that in single phase nc-metals the biggest part of the plastic deformation is mainly caused by small sliding events of atomic planes at the grain boundaries and only a minor part is due to dislocation movement in the grains for $d < 10$ nm [112].

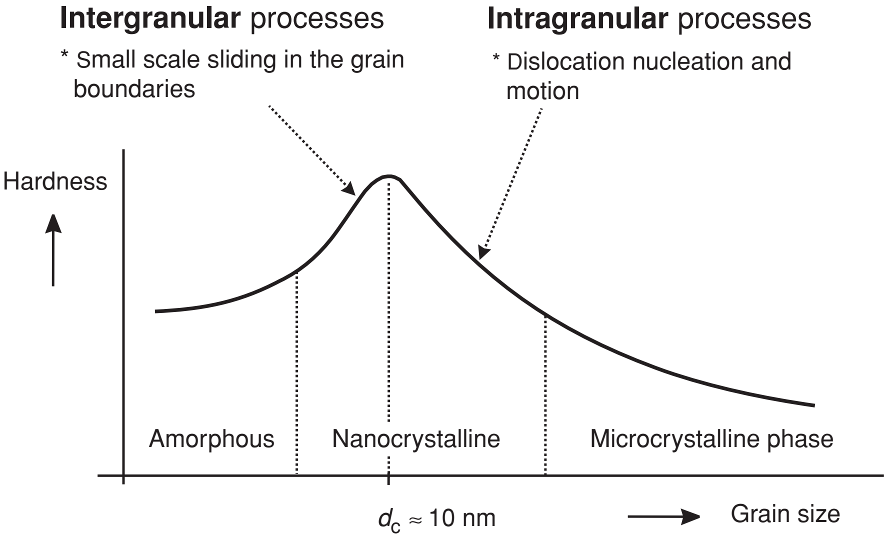

Figure 2.2: Schematic representation of the deformation processes as a function of the grain size. Above the critical grain size d_c HP strengthening occurs and below d_c the iHP behavior is observed. Picture is reprinted with permission from [105].

Texture: The optical, electrical, thermal and mechanical material properties of crystalline materials depend on its crystalline orientation. In 1949 Taylor [113] observed differences in the micro-hardness for different orientations of calcite and quartz. For example, the direction <111> is the strongest in TiN, similar to the weakest bonding direction in diamond [76]. Aligned columns or grains also show a different deformation behavior and hence different hardness [32, 47].

2.2.2 Thin film hardening

Nanocomposite coatings can show hardness enhancement that cannot be explained by bulk hardening processes described above. Solid solution hardening does not contribute to the superhardness in binary systems as e.g. $\mathrm{TiN/Si_3N_4}$ nanocomposites. The fcc-$\mathrm{Ti_{1-x}Si_xN}$ system decomposes into two phases TiN and $\mathrm{Si_3N_4}$ with sufficiently high kinetic energies (e.g. at 500 °C) and in a N-rich deposition process ($p_N \geq 10^{-4}$ mbar) [22, 77, 114]. Hence (Ti, Si)N solutions are only found under low kinetic deposition conditions, and so far no superhardness has been reported in solid solution coatings [115–118]. $\mathrm{Ti_{1-x}Al_xN}$ composites have a demixing energy of about an order lower than Ti – Si – N systems and decompose only at high temperatures into stable fcc-TiN and metastable fcc-AlN [118–120]. Precipitation effects due to annealing cannot explain the hardening of $\mathrm{TiN/Si_3N_4}$, since the two phases TiN and $\mathrm{Si_3N_4}$ are already forming during the deposition process. The samples are not plastically deformed to increase their hardness, hence neither work hardening nor martensitic hardening are affecting the hardness in thin films. In the TiN/Si_3N_4 system the hardness maximum is found for grain sizes between 3 – 5 nm [33, 86, 121]. For grain sizes below $d_c = 10$ nm the iHP behavior should cause a softening, but this is not the case. Similar observations with a hardness enhancement below d_c are made for other nc-TM composites (e.g. TM = V or W) [122].

Therefore bulk hardening effects cannot explain the hardness increase for nanocomposites with grain sizes of ≈ 3 – 5 nm, and new approaches, as explained below, are proposed to explain the hardness enhancement for nanocomposites.

Coherency stress: Epitaxially grown films with a substantial or complete lattice matching generate coherency stresses, also called epitaxial stresses. The stress is induced by elastic coherency strain due to the lattice mismatch. Films with a large misfit show a critical thickness above which the films display in-plane relaxation, resulting in a semi-coherent layer systems [123]. The coherent stress in layer A can be calculated by [124–127]:

$$\tau_{\text{coh,A}} = fE \tag{2.3}$$

where f is the total misfit (see eq. 5.14) and E is the Young's modulus. The induced stress due to coherency strain impedes dislocation movements, resulting in harder materials. The strength of the coherency stress varies strongly depending on the material under investigation. Coherency stresses have been reported from $\tau_{\text{coh}} > 2$ GPa for metal/metal multilayers [127, 128][i] and up to $\tau_{\text{coh}} \approx 34$ GPa in NbN/TaN multilayers [129].

Thermal stress: Thin films are often fabricated at elevated temperatures, therefore after cooling thermal stress is induced. The temperature-dependent stress τ_t of a layer A in contact with layer B can be calculated by [130]:

$$\tau_t = d_B \frac{E_A E_B (\alpha_B - \alpha_A)\Delta T}{(1-\nu_A)E_B d_B + (1-\nu_B)E_A d_A} \tag{2.4}$$

where α_A, α_B are the thermal expansion coefficients of material A and B and ν_A, ν_B are the Poisson ratios of material A and B. Compressive thermal stress in TiN of 0.9 ± 0.1 GPa and tensile stress in Si_3N_4 of 0.16 ± 0.14 GPa are reported [131], and are inducing additional stress fields impeding the dislocation movement.

Koehler stress: Based on the isotropic elastic theory, Koehler [132, 133] predicted in 1970 that a multilayer structure with a periodicity Λ of few nm should result in a harder material. The additional Koehler stress or modulus hardening is induced by a repulsive image force that exists when a dislocation crosses from a material with a lower Young's modulus E to another material with a higher modulus. [21]. The hardness enhancement is proportional to the shear

---

[i] Calculations of τ_{coh} are based on [124–127]

moduli of the two layers. Koehler suggested to choose two high and low modulus materials A and B with an elastic modulus that differs as much as possible and that show a good bonding between each other. In this way the dislocations in B are hindered to cross the interface B/A and very large stress is required to move the dislocation through the interface [132]. Also the formation of new dislocations by the Frank-Read source (FRS) mechanism is impeded, when the FRS loop does not fit in the layer. The maximum stress τ_k to move a dislocation through multilayer systems can be calculated in a first approximation as a bilayer system by equation (2.5) [134] that is based on the Peierls dislocation model as laid out in Pacheco and Mura [135][ii]. The maximum stress τ_k to move a dislocation through an interface is given by:

$$\tau_k = (G_B - G_A)\frac{\sin\Theta_s}{\pi^2} \tag{2.5}$$

where G_A, G_B is the shear modulus of material A and B respectively with $G_A < G_B$ and Θ_s is the angle between interface and slip plane. The Koehler stress τ_K, being the maximum shear stress required to move a dislocation within and through material A, is the sum of:

$$\tau_K = \tau_k + \tau_A \tag{2.6}$$

where τ_A is the shear stress applied within material A. Koehler's predictions were verified first in Al/Cu and Al/Ag systems by Lehoczky et al. [136, 138], later in epitaxial heterostructures of TiN/VN [56] and TiN/NbN [139, 140] and in polycrystalline multilayers of Ti/TiN, W/WN$_x$ and Hf/HfN [141]. Calculations using the embedded atom method [142] verified that the Koehler strengthening is significant, especially when the lamellae are very thin. According to Vepřek and Reiprich [86] those studies [56, 139–141] verify Koehler's prediction, but are not sufficient to explain the hardness maximum for layers between 5 – 8 nm. Also for VN/NbN superlattices this is not a reasonable explanation for the observed hardness enhancement, since NbN and VN have nearly identical elastic properties [143]. A deficit of the Koehler formalism is that it does not take into account the different thicknesses of the different layers, but only the predominant wavelength Λ of alternating layers.

Supermodulus effect: The supermodulus effect describes the change of the elastic modulus (biaxial, flexural, shear and Young's) as a function of the wavelength Λ of composition modulations of various transition metal-nobel metal superlattices. The reported elastic moduli for 1 nm < Λ < 3 nm are 2-4.5 times higher than expected from the bulk values of the two combined materials [144–146]. The existence [146, 147] as well as the origin [144, 145, 148] of the supermodulus effect are still controversial [89, 149–152]. Such elastic anomalies may result in hardness enhancement due to the line tension of a dislocation [153].

[ii] Some authors [129, 136] used the formalism of Head [137] to calculate the Koehler stress in thin multilayers: $\tau_k = \frac{G_B - G_A}{G_B + G_A} G_B \frac{\sin\Theta_s}{8\pi}$. Please note that this equation holds only true for dislocations far away from the interface, which is not the case in multilayers if the individual layers are very thin.

Interlayer stabilization: Some multilayers e.g. TiN/AlN [154] or TiN/Si_3N_4 [131] show a stabilization of an epitaxial cubic crystal structure. In both cases, AlN and Si_3N_4, the preferred crystal structure is a hexagonal phase at ambient pressures, but also cubic synthetic structures are possible. The hexagonal structure of $\beta - Si_3N_4$ (19 GPa [155]) is much softer than the cubic γ-structure (47 GPa [156]). A stabilized structure with a higher strength results in a higher film hardness. This is considered by using the stabilized interface hardness in the calculations of the Koehler stress (eq. 2.6).

Polarization strengthening: Patscheider et al. [27] proposed an additional electrostatic field effect that results in hardening. A conducting and an insulating material in contact align their Fermi levels (E_F) . Since no singularity is allowed, those bands bend to adjust their E_F level difference. According to Patscheider et al. [27] no significant bending of the bands at the interface is present, and electrons accumulate at the phase boundary. This causes an electrostatic polarization at the TiN/Si_3N_4 interface, see fig. 2.3. The polarization effect is bigger for materials with a wide band gap, hence the interface strength increases from Ti, Si to Si_3N_4 in contact with TiN. The deformed volume of nanoindented thin films contain a few hundreds of grains along the deformation directions. Each grain in the nanocomposite has several interfaces where the polarization effects occur, and hence the strength of the film is enhanced tremendously. The polarization effect is discussed further in section 9.1.

Bombardment hardening: The kinetic energy of bombarding ions plays an important role and can result in a hardness enhancement. During the sputter deposition ions are bombarding the growing film continuously; by applying a positive or negative bias the ion energy can be reduced or increased. The bombardment can densify and/or modify the film morphology [157, 158] (sect. 6.1) and cause various defects: creation of interstitials and vacancies (reminiscent of solid solution), dislocations (similar to work hardening), Argon implementation (interstitial solid solution hardening), and grain boundaries (compare to Hall-Petch hardening) [33]. Thermal annealing of the films can reduce the defects and decrease the hardness [159, 160]. Hence bombardment hardening is not a single effect describing the hardness enhancement, it is rather a mix of the defect sources described above [33].

Vaz et al. [18] showed that applying a negative bias of −50 V results in a hardness increase in $Ti_{1-x}Si_xN_y$ systems of up to 8 GPa. An applied bias also changes the composition [15] and the morphology of the sample [158, 161], and it remains unclear whether the ion bombardment or the decreasing grain size causes the hardening. Since morphology and composition have a strong influence on the hardness, the ion bombardment must have a minor influence and is neglected in this work as an hardening effect.

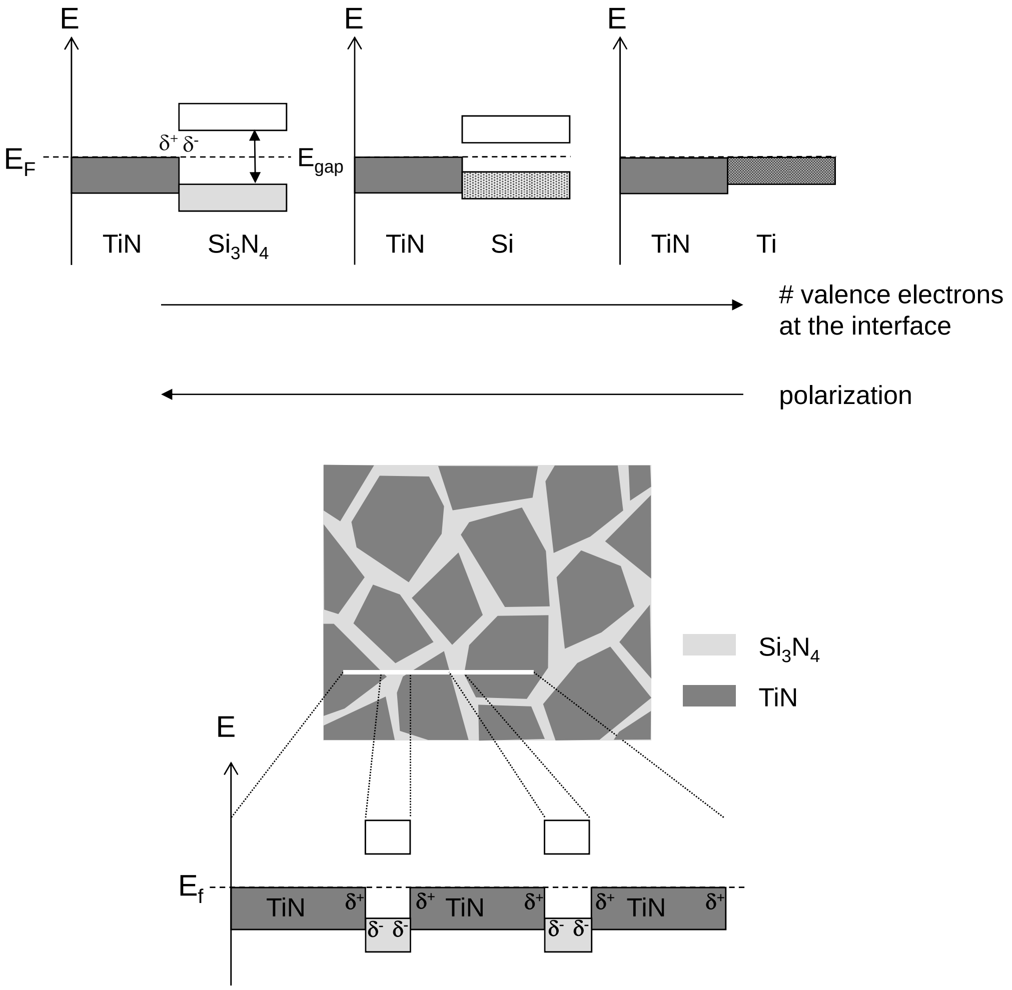

Figure 2.3: (top) Sketch of the valence bands of TiN in contact with Si_3N_4, Si and Ti as in [27]; (bottom) schematic illustration of a single crystalline (sc-)TiN/a-Si_3N_4 nanocomposite showing the polarization at the grain boundaries.

2.2.3 Modeling hardness

The diversity of the proposed theories illustrates how difficult it is to explain the origin of hardness. This is mainly due to difficulties in obtaining precise experimental data or images of the deformation process of nc-grains. A way of gaining insight into the deformation processes on the nanoscale are MD simulations [111, 162–165], numerical simulations [166–169], and theoretical modeling [170–179]. Numerical simulations based on finite element method (FEM) can imitate the deformation process of materials. FEM calculations of metals performed by Fu et al. [166] show that in a uni-phase nanocrystalline (nc-) material four factors contribute to grain boundary strengthening: multi slip activation in the grain-boundary region, elastic anisotropy effects resulting in additional stresses in grain-boundary surrounding, grain boundaries acting as barriers to plastic flow and as dislocation sources. FEM simulations by Wei and Anand [168] decoupled the deformation in two parts: cohesive grain boundaries deformation and a crystal plasticity model. As those FEM results have been adjusted to the experimental values, it is difficult to separate the two phases. Warner et al. [169] used a multiscale model (FEM and atomistics) on nc-Cu with no secondary phase between the grains. Their model contains only bulk properties of Cu and interfacial properties of the grain boundary. The grain boundary structures were simulated independently from the atomistic simulations. It is shown that Hall-Petch (HP) strengthening fits intragranular deformation when partial dislocation is considered active. The primary challenge in FEM is to derive an equation describing the mechanical deformation processes. Hence a precise *a priori* knowledge of the hardening processes, as described above, needs to be at least partially implemented .

A more fundamental approach is the MD simulation, here atomistic potentials describe the interaction of molecule clusters. Recent MD simulations [180] use polycrystalline Cu nano grains in a cube of 30 nm with up to $7 \cdot 10^6$ atoms. Tucker et al. [180] modeled different grain sizes and demonstrated that for nc-Cu the deformation mechanisms is related to the grain size. For large grained structures the lattice strain and dislocation slip are more dominant while for grain sizes below 15 nm grain boundary mediated deformation (as e.g. grain boundary migration, sliding, and atomic shuffling) play a significant role. This is in good agreement with what has been reported previously by Schiøtz et al. [111, 164, 169]. So far no MD modeling has been performed on metall nitride (MeN)/$\mathrm{Si_3N_4}$ nanocomposite, but increasing computer power and a tremendous interest in those systems make it only a matter of time until those will be performed.

The simplest model to describe the hardness H_n of a two-phase nanocomposite is given by the rule of mixture [181]:

$$H_n > \frac{H_1 V_1 + H_2 V_2}{V_n} \tag{2.7}$$

where H_1, H_2 and V_1, V_2 are the hardness and volume of first and second phase. A maximum value $H_{n,max}$ can be more than twice greater than that of the hardest component [105]. The rule-of-mixture can be applied e.g. to $\mathrm{TiN_{1-x}C_x}$ systems that form a solid solution [182].

The rule of mixture gives a lower limit of the hardness, since effects such as cohesive forces between atoms, dislocation-dominated plastic deformation (sect. 2.2.1) and nanostructure of the material (sect. 2.2.2) are not included in this approach.

Chu and Barnett [183] derived a model to describe the superlattice strength/hardness of miscible systems with the same slip system. Their calculations include dislocation movement across layers and within individual layers. Their model is based on two mechanisms: dislocation movement through the layers and within the individual layers. The formalism accounts for the interface topography and the fact that in thin layers the dislocation generation is impeded [132]. A maximum hardness is experienced in the multilayer system, if the layer thickness inhibits dislocation motion across the boundaries without having dislocation movement within the layer. The described model of Chu and Barnett [183] agrees with the experimental observations and shows a maximum hardness at bilayer thicknesses of 5 – 10 nm. Recently Fu et al. [166, 184] proposed a mathematical model based on FEM simulations. The model uses an affected zone (7 lattice parameters) to describe the plastic deformation. This affected zone model is questioned [169] since TEM images [185] show that the nano grains are crystalline up to the grain boundary. Farrokh and Khan [179] developed a new phenomenological model with eight constants, that can only explain the hardness by adjusting the model parameters to the experimental data.

The mathematical models describing the hardness of a two phase nanocomposite are still limited, and the transition from multilayers with a periodicity of Λ to a nanocomposite containing randomly oriented grains with different grain sizes is not trivial. In section 9.2 an approximation is used to describe the expected hardness for the nc-TiN/SiN_x nanocomposite.

2.2.4 Interface studies

A major part of the volume in nanocomposites is the grain-matrix interface. As it has been shown in MD simulations [164, 169, 180] the interface or grain boundary mediated deformation is the dominating mechanism during plastic deformation. Almost all hardening effects are based on interface interactions and hence interfaces play an important role in the strengthening [21]. Interfaces have been studied by means of Transmission Electron Microscopy (TEM), X-Ray Diffraction (XRD), X-Ray Reflectometry (XRR), Elastic Recoil Detection Analysis (ERDA) and computer simulation. In the case of TiN/SiN_x many groups [22, 23, 48, 76, 117, 131, 186–191] investigated the interface. It is generally agreed that the structure of one monolayer[iii] (ML) SiN_x between TiN (001) slabs is somehow crystalline. For thicker interlayers the structure transforms into an amorphous SiN_x structure [25, 188]. Such an epitaxial stabilization of a non-equilibrium phase is called pseudomorphic growth. No consent is found yet on the structure, stoichiometry or on what critical thickness this transition from crystalline to amorphous occurs [194, 195]. Also for AlN a stabilized rocksalt structure in the superlattice AlN/TiN(001)

[iii] The thickness is sometimes given in the unit ML MonoLayer. There have been some controversial reports [192] that make it difficult to compare the data. Depending on the structure whether $\beta-$ Si_3N_4, c- Si_3N_4 or SiN is assumed the unit ML may vary from ≈ 0.2 nm [48, 188] to ≈ 0.3 nm [12, 193].

has been observed by Madan et al. [154] using XRD, TEM and energy analysis.

TEM studies are a powerful tool for studying the structure on an atomistic length scale (sect. 5.10). First TEM investigations on TiN/Si_3N_4 (brazed) interfaces were performed by Iwamoto and Tanaka [186]. The interface was 'wavy' and the TiN nanoparticles aligned in [110] direction parallel to the [0001] direction of Si_3N_4 with $(1\bar{1}1)$ TiN planes parallel to $(10\bar{1}0)$ Si_3N_4 . It is argued that this relationship is caused by polar-plane matching to minimize the electrostatic potential at the interface [186]. Söderberg et al. [131] observed that a cubic (c-) SiN_x structure forms in TiN/Si_3N_4/TiN multilayer systems. XRD, XRR and High Resolution TEM (HR-TEM) studies on interlayers of SiN_x with a thickness of ≥ 0.8 nm show a random structure, while for ≤ 0.3 nm an epitaxial cubic crystalline structure is observed. In a subsequent paper cubic SiN_x formations were reported by the same group [188] up to ≈ 0.55 nm and a metastable rocksalt structure is suggested for the SiN_x interlayer. The cubic interlayer minimizes the interfacial energy by lowering the strain energy during the growth, with increasing thickness the elastic energy and a molar enthalpy increase until the preferred structure is a-SiN_x [188]. These results are confirmed by HR-TEM, Scanning Tunneling Microscopy (STM) and Low-Energy Electron Diffraction (LEED) [48].

Similar studies were performed on TiN/AlN interfaces [196–199], in which a transformation of pseudomorpic grown c-AlN to a wurtzite (w-) structure is observed. The critical thickness at which c-AlN undergoes this change is much higher compared to c-SiN_x [154, 200, 201]. HR-TEM studies and first-principle based calculations by Chen et al. [202] revealed that the critical thickness for c-AlN between TiN (001) slabs is ≈ 1.95 nm.

As an exact resolution of the interface structure lies beyond the reach of current experimental techniques, it was expected that first-principle calculations could give a definite answer. Comprehensive Density Functional Theory (DFT) calculation on α, β, γ structures with 55 configurations between TiN and Si_3N_4 were performed by Hao et al. [187]. The DFT results show two structures between TiN (111) slabs being most stable: either a thin β- like (1×3) Si_2N_3 or a (1×1) Ti-Si structure depending whether the structure is formed in a N-rich or N-poor environment, respectively [76]. Zhang et al. [203] focused on the Gibbs free energy obtained by DFT simulations and found that the fcc-$Ti_{1-x}Si_xN$ undergoes spinodal decomposition into fcc-TiN and fcc-SiN under ideal thermodynamic (N-rich) and kinetic (high deposition temperature) conditions. Later calculation [22, 189] show also that up to two ML of SiN_x are strengthened by valence charge transfer from the metallic TiN . Due to limited computing power the calculations of Zhang et al. [189] were performed only on the TiN (111) structures. *Ab initio* calculations by Hultman et al. [48] show the formation of c-SiN (see fig. 2.4) for interface thicknesses below two to three ML, while thicker layers also contain an amorphous phase. Alling et al. [190] examined the previously considered metastable rocksalt (B1) and zinc-blende (B3) SiN structures and found that both are dynamically unstable. Two new pseudo-B3 Si_3N_4 phases are suggested where the Si_3N_4 phases are derived from a cubic $L1_2 - B3$- or a tetragonal $D0_{22}$-type distribution of Si vacancies and are considered dynamically stable.

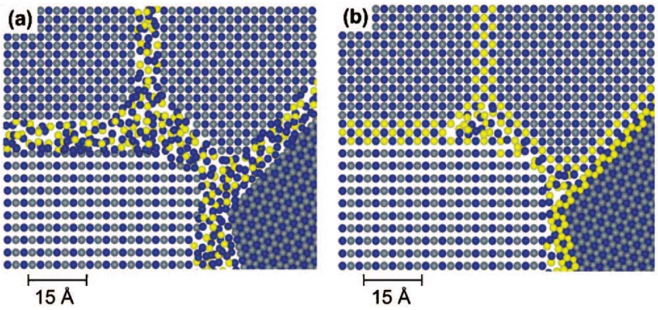

Figure 2.4: Schematic illustration of a cross section of a TiN/SiN$_x$ nanocomposite (Ti: gray; N: blue; Si: yellow) as obtained from ab-initio calculations in [48]: (a) two phase model with an a-Si$_3$N$_4$ tissue phase (b) three phase model with either epitaxial c-SiN (thicknesses below two or three ML) or bilayers of c-SiN and a-Si$_3$N$_4$ (thicker than three ML)

DFT simulations by Marten et al. [23] demonstrate that the interface formation is independent of the environmental conditions (N-rich or N-poor) during the deposition process. Marten et al. [23] put a clear question mark behind previously reported Si$_1$N$_1$ and suggest different stoichiometries with SiN$_x$ ($x > 1$). Shortly after the same group [194] found a B3-like geometry for one ML SiN$_x$ between a B1-TiN sandwich, indicating that the Si is tetrahedrally coordinated by N. The thin one ML structure is stable with respect to Si vacancies and to lattice vibrations. For thicker layers (more than three ML) a tetragonal D0$_{22}$-like order of Si vacancies stabilizes the B3 interface lattice. It is noted that the one ML thick interface is metallic and has a nonzero electronic density of states (DOS) at and above the Fermi level with a distinct pseudo gap below the Fermi level [194]. All those described structures were calculated allowing vibrational relaxations but being at 0 K. Ivashchenko et al. [195] extended the previous models by first-principle quantum molecular dynamics (QMD) calculations at 300 K with an annealing process at 1400 K. After cooling down to 300 K the interfacial structure between TiN(001) slabs shows a strongly distorted Si$_3$N$_4$-like structure, while between TiN(111) the B1-SiN, Si$_3$N$_4$-like SiN and Si$_3$N$_4$-like Si$_2$N$_3$ are stable over the whole temperature range. For non-perfect conditions oxygen impurities can stabilize most likely the $\alpha-$ Si$_3$N$_4$ [195]. Unfortunatelly no projected DOS (pDOS) are presented in the publication of Ivashchenko et al. [195]. Earlier studies of Hao et al. [187] on similar system show for the Si$_3$N$_4$-like Si$_2$N$_3$ structure in between TiN (111) stacks that the Si 3p-N 2p hybrid states are metallic at the Fermi level. This is due to the hybridization of the N 2p orbitals with the Ti 3d and hence result in a metallic behavior of the Si$_3$N$_4$-like Si$_2$N$_3$ interlayer [187].

Real three-dimensional nanocomposites are more complex than the experimental multilayer model restrictions or *ab initio* constraints; many crystallographic orientations at the grain faces, enclaves between grains (see fig. 2.4), non-sharp interfaces, and impurities are to be expected, making the real world anything else but ideal.

2.3 Thin film deposition

Thin films (in the range of a few tens nm up to several μm) can be fabricated by various deposition techniques, the most commonly used are divided in two groups:

- chemical techniques:
    - wet processes: e.g. plating, spray pyrolysis [204]
    - vacuum environment: Atomic Layer Deposition (ALD) [205], Chemical Vapor Deposition (CVD) [206, 207]
    - plasma environment: Plasma Enhanced CVD (PECVD) [208]
- physical techniques, PVD [205, 209, 210]:
    - vacuum environment: Molecular Beam Epitaxy (MBE)
    - plasma environment: Pulsed Laser Deposition (PLD), magnetron sputtering [211, 212], High Power Impulse Magnetron Sputtering (HIPIMS) [213], Ion Beam Assisted Deposition (IBAD) [214]

The technique chosen in this work for the sample fabrication is Unbalanced Magnetron Sputtering (UBMS) that belongs to the group of magnetron sputtering processes. The latter is explained in more details below, for all other techniques the reader is referred to the review articles given above or to standard textbooks on thin film deposition [210, 215–220].

Unbalanced Magnetron Sputtering (UBMS) In sputter deposition processes ions are accelerated towards a solid source (target) and eject atoms from the target material. Those atoms are then collected on the substrate and form a thin film.

Sputter processes are usually performed in vacuum chambers, where a plasma is ignited (see figure 2.5). The plasma contains high energetic ions of a non-reactive process gas (e.g. Ar) and/or a reactive gas (e.g. N_2). To prevent cross contamination, a so called chimney is placed around the target. The target forms the negative biased cathode. The walls of the chimney and the chamber inside are grounded and form the anode. Electrons are emitted from the cathode and are accelerated towards the anode. On their way the electrons ionize the gas atoms and form a plasma. The positively charged ions (e.g. Ar^+) are accelerated in the electric field towards the cathode. They impact on the target and if the impulse of the ions is high enough, then atoms of the target material and electrons are ejected. Those atoms then fly to the substrate where they condense. Reactive gases allow a reaction of the target material (forming e.g. TiN on the substrate and on the target (poisoning)). The reactivity of the gases is enhanced by the presence of the plasma.

Deposition rates are increased by increasing either the kinetic energy of the impinging ions (50 – 2000 eV) or their amount per unit time. The kinetic energy can simply be adjusted by applying a higher voltage to the target, but is limited by the maximum voltage/power of the supply. The number of ions bombarding the target can be increased by either controlling the diode discharge, the gas pressure or the magnetic field. The diode discharge is also restricted to the properties of the power supply. The gas pressure allows, on the one hand a higher

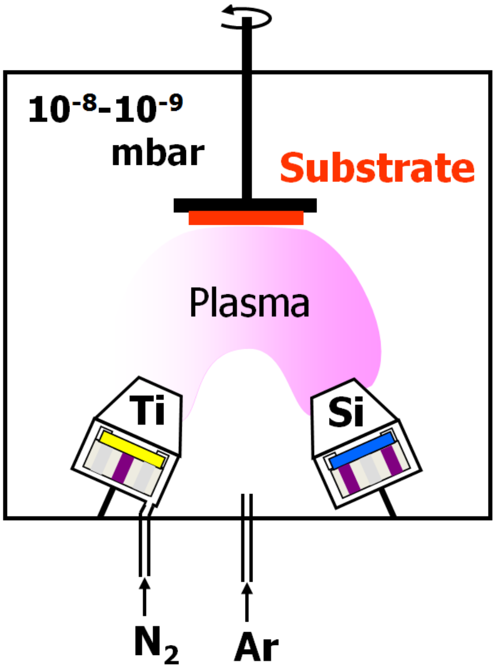

Figure 2.5: Sketch of the used deposition system. The background pressure is in general between 10^{-8} mbar and 10^{-9} mbar, Ar and N_2 are used as process gases, the substrate is heated to 800 °C if not mentioned explicitly. Sketch is adopted from [12].

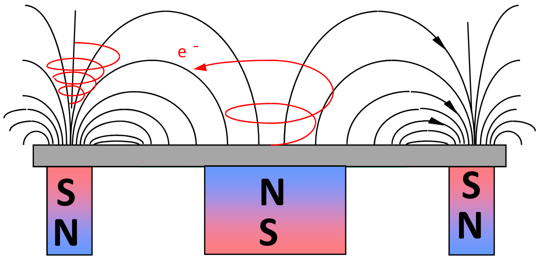

Figure 2.6: Sketch of a magnetron as it is used in UBMS. Magnets (red-blue) are positioned underneath a target (grey) and electron trajectories are disturbed due to the magnetic field.

plasma density, but on the other hand a shorter path length of the emitted target atoms is obtained and therefore no significant increase in the deposition rate is attained. Applying a permanent magnetic field to the plasma is an efficient way of increasing the plasma density. The trajectories of electrons in a magnetic field are disturbed, and they spiral around the magnetic field (see fig. 2.6). Hence their pathway, the probability to ionize the gas atoms and the plasma density are increased, resulting in a higher deposition rate. In most UBMS devices the center of the target has a certain magnetic pole orientation in one direction (e.g. north) and along the edges of the target the magnetic field points in the other direction. In this way the electrons are trapped between the magnetic force lines. Their overall movement is along the trace between the two magnetic poles and hence the substrate is eroded faster along those race tracks. As mentioned before the target acts as a cathode, any changes of the topography will change the electric field that further results in a change of the ion trajectory and consequential influences the deposition rate.

A limiting factor of PVD systems is the target cooling, especially with materials that are either brittle (as Si) or have a low melting temperature (Sb). The plasma heats up the target and if the cooling flux is not sufficient, then the quickly rising heat gradient causes a breaking of the target. High temperatures might even cause melting of the target. For those reasons the target is mounted on a water cooled Cu block (Cu is selected due to its high thermal conductivity) and hence damages are prevented.

A bias with a certain voltage can be applied to the substrate, and in the case of insulating samples a radio frequency (RF) bias can be used. A negative bias at the substrate automatically increases the ion bombardment by increasing the ion-to-atom ratio and provides a higher surface energy. The additional ion impact causes denser materials and/or defects.

Due to the vacuum environment the vaporized particles undergo few collisions and hence their trajectory is more or less linear. This causes shadowing at the edges of the sample, i.e. the part of an edge that is pointing away from the target is not sufficiently covered with arriving atoms. This effect can be reduced by rotating the sample during the deposition process.

2.4 Layer growth

In UBMS the thin film builds up with deposition rates typically less than a few tens of Å/s. The film growth structure is divided into a first stage (atomistic regime) where only a few monolayers are deposited and a second stage (microstructure) when thicker films of a few tens of nanometers are formed [221]. In the early stage the film growth is dominated by nucleation. During the deposition process single atoms approach the surface and are able to migrate along the surface. Depending on the substrate and deposited material different growth behaviors are observed. The growth types of the first few nanometers are distinguished in:

- Frank-van-der Merwe [222–224]: planar layer-by-layer growth
- Stranski-Krastanov [225]: layer-plus-island growth
- Volmer-Weber [226]: three-dimensional island growth

What type of growth pattern arises depends on the adatom mobility, the lattice mismatch, surface contaminations and the surface and interfacial energies of the substrate and the film [227]. If the atomic mobility is high enough then the adatoms move on the surface until they are subject to the attractive potential of another already adsorbed atom, hence favoring planar growth (Frank-van-der Merwe growth). High interfacial energy on the other side enhances three-dimensional growth (Volmer-Weber growth). The Stranski-Krastanov growth is favored for systems where the interfacial energy between adsorbates and substrate is low, but a high surface energy of the epilayer and a high mobility of the adatoms is present. Thus the first layer formed is homogeneous and planar, while the next layers form islands. All three growth

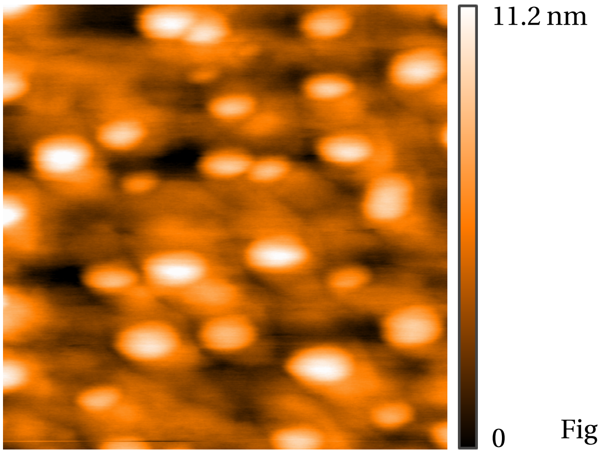

Figure 2.7: AFM images of Ag on TiN.

types are influenced by the lattice mismatch, if it is small then two-dimensional growth is preferred [227].

These three growth types are only applicable for the first layers of the film growth, for a microstructure description the empirical Sputter Zone Model (SZM) of Movchan [228], Thornton model [229, 230] or modifications [158, 230] are useful. The Thornton model describes the film structure depending on the pressure during the deposition process and the temperature ratio T/T_m, where T is the temperature during the deposition process and T_m is the melting temperature of the film. The temperature ratio is directly correlated to the atomic mobility. The influence of the substrate [231–236], the N_2 flow [221, 232, 237–240], the film thickness [241–246], the substrate temperature [240, 247, 248], ion-to-atom ratio [249, 250] and the ion energy [243, 251–255] on the TiN growth have been thoroughly studied. An overview how those parameters are influencing the microstructure is found in [256].

For specific elements and certain conditions dewetting is part of the film development, resulting in an agglomeration and a formation of beads, e.g. Au on Si [257, 258] or Ag on TiN (see fig. 2.7 or [259]). The theory is based on the capillary instability that has been reported as early as the late 19th century by Plateau [260], Rayleigh [261]. The driving force in dewetting is the reduction of the surface energy, hence dewetting is enhanced for materials with a high surface energy. Very thin films have a high surface to volume ratio and the release of surface energy can result in cluster agglomeration far below their melting temperature. The agglomeration size can be controlled e.g. by adjusting the substrate temperature [257]. This controlled nano cluster formation is e.g. used for ordered nano arrays [262]. The growth behavior of coatings predetermines the macroscopic properties as e.g. roughness [42], optical properties [232, 233] and hardness [39].

3 X-ray Photoelectron Spectroscopy (XPS)

Photoelectron Spectroscopy (PES) is based on the photoelectric effect [263–266] in which electrons are emitted through electromagnetic radiation. In X-ray Photoelectron Spectroscopy (XPS), as the name states, X-rays are are causing the emission of photoelectrons (PE) (see figure 3.1 left side). Compared to Ultraviolet Photoelectron Spectroscopy (UPS) where the energy of the radiation is only a few tens of eV, the energy of X-rays is in the order of a few thousand eV. Therefore UPS is only able to excite electrons from the outer valence band, while XPS excites electrons from the outer and inner core shells of the molecule. XPS and UPS are both surface sensitive non-destructive methods to probe the first layers. The information depth of XPS is roughly in the order of up to 10 nm (depending on the material), but is most sensitive in the first 4 nm [267].

Auger lines are also recorded during XPS measurements. Auger electrons are emitted by a three electron process (see fig. 3.1 right side). First a core hole is created (e.g. in the K-shell) and this hole is filled by a second electron from an outer shell (e.g. L_1). During this relaxation process energy is released which can be used to emit an electron (e.g. $L_{2,3}$) with a lower $\mathrm{E_B}$ than the second electron. Unfortunately the N KLL and Ti LMM Auger lines overlap and an evaluation is very difficult. Also XPS provides a better quantification of the peak areas than AES. An introduction to XPS and AES can be found in [268]. In this document the terminology defined by the American Society for Testing and Materials (ASTM) [269] is used.

3.1 Brief history of XPS

More than a hundred years ago, in 1907, Innes recorded the velocity of electrons emitted from different metal surfaces exposed to X-rays [270]. From his observations he noted an atomic disintegration, that might result from free 'corpuscles'. Innes' experimental setup already contained all the necessary parts that are still used today, see fig. 3.2. Nowadays technical achievements like turbomolecular pumps replace the Töpler pump so that ultra high vacuum (UHV), $p < 10^{-9}$ mbar can be reached, reducing the measuring times tremendously. Also hemispherical analyzers are used instead of horse shoe electromagnets with a photographic

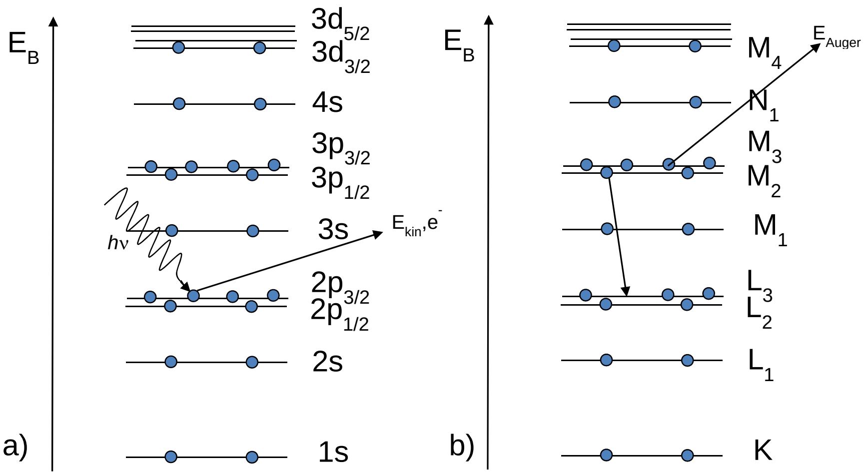

Figure 3.1: Schematics of a) XPS and b) AES.

plate (fig. 3.3). Latest developments have returned to atmospheric XPS, where the sample is either observed through graphene membranes [271] or through differential pumping of the analyzer [272] to study e.g. liquid solution samples at low vacuum (1 mbar). The Rutherford experiment followed in 1911 [273] and Bohr's atom model was described in 1913 [274]. In the same year [275, 276] the observed photoelectric effect on X-ray spectra was used to confirm the Broek's hypothesis that the central charge and number of electrons in an atom is equal to its position in the periodic table.

Fifty years later technical improvement in the setup have been implemented mainly by Siegbahn et al. [277]. Siegbahns group also noted that the XPS spectra can be used for chemical analysis, therefore XPS is sometimes also called Electron Spectroscopy for Chemical Analysis (ESCA), for which he received the Nobel Price in 1981. The interested reader is referred to the review article on the history of the XPS by Jenkin et al. [278].

3.2 The photoemission process

In XPS the photoelectric effect is used to investigate the binding energy ($\mathrm{E_B}$) of the electrons in the sample. The molecules of a sample are exposed to X-rays with a defined energy, $h\nu$. If the energy is high enough, electrons can be emitted from the sample (see figure 3.1). Not only are the number of emitted electrons detected, but also their kinetic energy E_{kin}. $\mathrm{E_B}$ can be calculated in a first approximation as the difference between the photon energy $h\nu, E$ and ϕ:

$$E_B = h\nu - E_{kin} - \Phi \tag{3.1}$$

where Φ is the work function, i.e. a potential including surface potential of the sample and a correction factor to the actual referencing point for $\mathrm{E_B}$ [267]. The latter is not only characteristic for each element but also for its electronic surrounding. Therefore this method can be used to

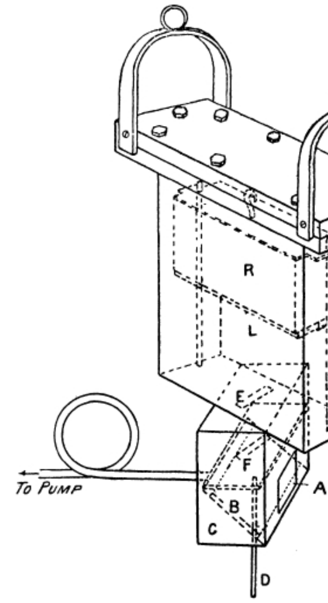

Figure 3.2: Original Setup of [270] A: inlet, B: metallic sample, R: Box with photographic plate, a horse shoe electromagnet is used (not shown)

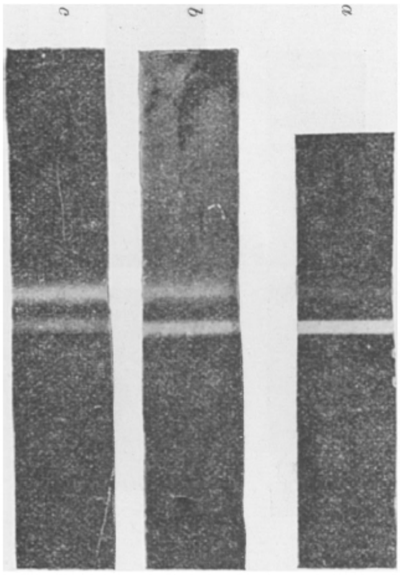

Figure 3.3: First XP-Spectra of gold recorded by [270] , a-c: different photographic plates with different exposure times and different X-ray energies are used

investigate quantitatively the elemental composition and its chemical environment. While it is easy to detect *qualitatively* even traces of elements below 1 ‰, it is quite difficult to determine a *quantitative* concentration rates within the order of ±1%. Calibration measurements done with Rutherford Back-Scattering (RBS, (sect. 5.9)) have to be performed to receive such high accuracy.

The XPS device, used in this work, consists of a UHV chamber that contains an x-ray source, e.g. an aluminum K_α X-ray source (1489.6 eV), an electron analyzer and a sample holder (for more details on the system see sect. 5.1). In the case of AR-XPS the latter is pivot mounted and can tilt the sample in front of the detector. By tilting the sample in front of the detector, the information depth can be varied (see sect. 5.3). A good, general overview on XPS is given in textbooks [50, 267] or in the overview article of Turner and Schreifels [279].

3.3 Line Types

In general the kinetic energy of the photoelectron (PE) is recorded and the position and line shape contains important information on their origin. Besides the main electron line, many other line types can occur (see fig. 7.1).

Below are all photoelectron lines listed and briefly described [50, 267, 280]:

- Main lines are caused by photoelectrons that are emitted either from any core level or the valence band, provided that the energy of the radiation is higher than that of the electrons in a given level.

- Auger lines [281–283] are caused by a three electron process, first an electron is emitted due to the photoelectric effect, secondly an electron from outer shells fills the created hole via photo emission and can transmit the gained energy to a third electron which is emitted from the atom. The kinetic energy of Auger electrons is therefore much lower than the one of photoelectrons, for TiN their kinetic energy is below 500 eV.
- *X-ray* satellites refer here to peaks due to non-monochromatic radiation of an ideally pure X-ray anode (note: it is referred to as X-ray satellites not peak satellites) [267, 280].
- X-ray ghost lines are caused by impurities in the X-ray anode material resulting again in non-monochromatic radiation [267, 280].
- Spin-orbital splitting is based on an initial state effect due to coupling of the electron spin momentum with its orbital angular momentum, this results in a splitting of the electron energy levels [284].
- Multiplet or exchange splitting requires unpaired electrons in the initial state of the atom. After photoemission an unpaired electron remains in the core shell. This unpaired core electron can couple with the outer shells (spin-spin-coupling) and causes a multiplet splitting. A famous examples is the N 1s- level multiplet splitting in nitrogenoxide [285]. Multiplet splitting is a final state process and spin-orbit splitting an initial state process [280, 286, 287].
- Plasmon peaks (sect. 3.4) caused by the excitation of electrons of the conduction band. The oscillations are quantized and therefore the plasmon peaks repeat in constant energy distances with decreasing intensity [267].
- Shake-ups are defined as: Any photoelectron peak on the lower binding energy side of the main line that is caused by *discrete intrinsic* electron electron interaction is called shake-up. See also section 3.5.
- Shake-offs are similar to shake-ups, shake-ups are caused by exciting electrons at the Fermi level into unoccupied discrete orbitals. Shake-offs excite not into discrete states but into the continuum and add up to the background [267].
- Shake-downs are caused by an photoelectron- valence electron process, where the valence electron is relaxed into a lower unoccupied state.

Please note: Satellite peaks are any peaks accompanying the main energy line, while shake-ups are a specific kind of satellite. In this thesis the term satellite will not be used for shake-ups in order to not confuse shake-ups with any other satellite as e.g. the X-ray satellites. Also the shake-up is (independent from its higher intensity) defined as the peak on the higher binding energy side of the main peak.

Please also note: In the early days of XPS [288, 289] every shake-process is called shake-off, presently [267, 290] the notation shake-off refers to emitted electrons that excite electrons at the valence band into the continuum. The "shaked-off" electrons yield to a continuous energy loss added to the background. Sometimes in XPS the shake-up is called main peak and the undisturbed (since it has a lower intensity) is called shake-off. Sometimes shake-offs are defined as the main peak belonging to a shake-up[i], in this work all shake lines are defined as above.

3.4 Plasmons

The excitence of plasmons was first suggested by Bohm and Pine in 1952/53 [292] and was experimentally detected in aluminum such as by Baer and Busch [293], Powell and Swan [294]. Highly mobile electrons can be excited into collective oscillations, called plasmons, which have certain characteristic frequencies ω_p. Every time emitted electrons interact with the plasmons, they lose the energy $E_p = \hbar\omega_p$. Plasmon-photoelectron interactions can occur several times, each time causing the same energy loss E_p. Therefore higher-order plasmon peaks at multiples of E_p are possible. With each order multiple plasmon interactions become more and more unlikely, therefore the plasmon peak intensity decreases. Moreover, plasmon oscillations are observed on every photoelectron line.

The following types of plasmons exist

- intrinsic plasmons [50, 267, 295] are created in the photoemission process, due to core hole-plasmon coupling
- extrinsic plasmons created by interactions of the emitted electron during its travel through the sample

The extrinsic plasmons are subdivided in the following two groups:

- Surface plasmons are caused by group oscillations of free electrons at the surface and have a lower frequency, approximately a factor of the square root of two, than the bulk plasmons.
- Bulk (or volume) plasmons have usually a higher intensity than the surface plasmons and arise from electron oscillations in the bulk [280, 296].

The intrinsic plasmon contribution to the spectra is small in most cases, with the intrinsic plasmons overlapping the extrinsic bulk plasmon peak [297, 298] and are not within the scope of this study. Therefore the intrinsic plasmon has not been separated from the extrinsic bulk plasmon. For plasmons the Mahan or DS line shape are also used see section 3.6 [50].

---

[i] The shake-up lines have often a higher intensity than the main peak of the core electron, therefore sometimes the shake-up line is considered to be the main line and the lower binding energy peak is called shake-off peak [291]

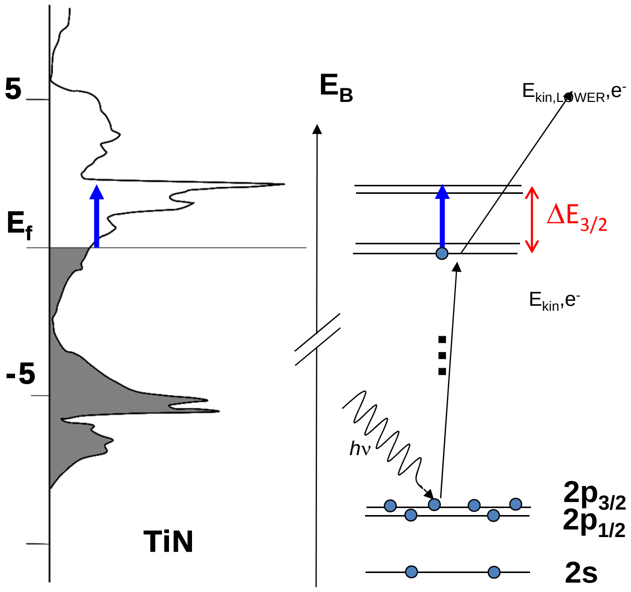

Figure 3.4: left side: projected DOS adopted from Marlo and Milman [305]. Right side: a sketch of the simplified shake-up process. Please note the sketch is a simple model which is not considering any changes in the potentials upon photo emission (Z+1) nor any changes in the valence band due to the excitation process, for details see text.

3.5 Shake-ups

Similar to Hüfner [50] the shake-up is defined in this work: any photoelectron peak on the lower binding energy side of the main line that can be understood by a discrete intrinsic electron-electron interaction.

Several models are found to describe the origin of the shake-up [50, 299–304]. The simplest way of looking at the shake-up is to consider it as an electron-electron process (fig. 3.4, right side). The emitting PE (e.g. from a Ti $2p_{3/2}$ orbital) excites an outer valence electron in previously unoccupied states and loses an energy ΔE that is given to the valence electron. This energy loss ΔE is equal to the binding energy difference between main and shake-up peak (see fig. 3.6). In this work this energy difference ΔE is also called shake-up energy. The energy difference ΔE corresponds to the energy difference of the valence electron before and after excitation, not considering any energy changes due to the created core hole. Projected density of states (pDOS) calculations (fig. 3.4, left side) reveal that this simple picture is only partially correct. The occupied and unoccupied states in a bulk TiN are not discrete and electrons can be excited from and into broader bands. This simple sketch does not consider any changes in the electrostatic potentials upon the creation of the core hole. The change in the electric field and a rearrangement of the outer electrons occurs instantly.

During the photoemission process an electron is emitted from an atom with the nuclear charge Z and a core hole is created. After photoemission, the core hole acts as an extra positive charge, and the electrons in the outer shells are subject to a Coulomb potential that can be described by a Z+1 approximation [306, 307]. The systems response of the photo hole is instantaneous and may result in two states: a ground state (main peak) and an excited state (shake-up).

Please note both final states are ionized Z+1 states.

In quantum mechanics the shake-up is explained by the wave functions describing the initial state and final state [301]. The excitation probability and hence the intensity of the photoelectron line depend on the overlap integral of the wave functions describing the initial and the final state. The overlap integral of the initial state before ionization and the lowest final state after ionization is always non-zero and results in the main photo electron line. For some materials (e.g. Ni and TiN) other overlap integrals are non-zero and are visible as a shake-up line. In a single Ti atom only a limited number of transitions of the valence electrons 3d into discrete finale states are allowed by the monopole selection rules (in this case only 3d→3d excitations). Single crystalline (sc-) TiN is a crystalline solid state material and forms broad hybridized Ti 3d-N 2p bands close to the Fermi level. As a result the selection rules are softened and more transitions into different final states are allowed. The shake-up process is no longer described by one initial eigenstate and one final state, but by a multitude of possible initial and final states. Additionally the valence electron excitation results again in a reorganization of the valence electrons, this time an even stronger perturbation in the valence band is created since the second photoelectron hole is located at the Fermi level. To calculate quantitatively the shake-up intensity and the energy difference ΔE it is required to perform time dependent (TD-) DFT or configuration interaction (CI) calculations, which are out of the scope of this thesis.

In literature [303, 308] the shake-up is often described with the Kotani-Toyozawa (KT) model (see fig. 3.5) to explain the shake-up state. In the KT model a localized orbital above the Fermi level and a broad band just below the Fermi level are present in the initial state. In the ground state the localized (e.g. d-) orbital is above the Fermi level and well separated from the highest occupied broad (e.g. hybridized s-p-) band. Due to the core hole generated by the photoionization the sharp d- band is pulled down below the Fermi level E_F and the delocalized p-d-hybrid level is only slightly lowered. The unfilled localized d-shell is now acting as an electron attractor. Two final states are possible: (1) one, where the d-orbital remains empty and the s-d-band is screening the two holes (the d- and the core hole) and (2) a second state, where the d-orbital is filled due to a charge transfer from the s-p-hybrid level. In the second case the localized d-orbital is completely filled, therefore fully screened and hence this state is called "well-screened" [309]. In the final state (1) the binding energy of the core electron is lower than in the state (2); therefore two peaks are observed, the shake-up and the main peak respectively [310]. The probability that those localized states are filled, depends on the population, the width and the amount by which they are lowered [311]. This charge transfer should not be confused with the chemical reaction between Ti and N where charge is transferred from Ti to N upon bond formation. This process is further not limited to a broad s-p-band as in CuF_2, but is transferable to other broad bands (e.g. the hybridized Ti 3d- N 2p orbital). Please note the KT model is just another description for the above described two final states (ground and excited ionized state). The main peak (2) is equal to the ground state in the Z+1 approximation and the shake-up is a result of exciting an electron from the occupied d-state into higher unoccupied s-p-states (1) that are again rearranged due to the

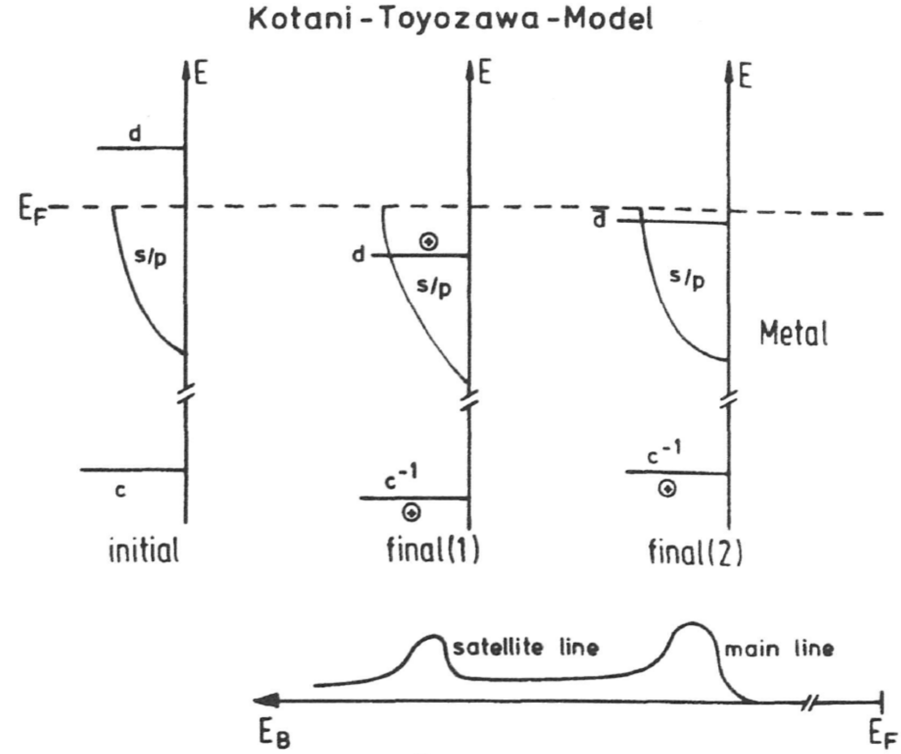

Figure 3.5: Sketch of the Kotani-Toyozawa model according to Hüfner [50]. Before photoionization the molecular orbitals are split in an unoccupied d-orbital and an occupied broad s-p-band (left). After the photoionization both bands, d- and s-p-orbital, are lowered, the bands overlap and two final states are possible. Either the d-orbital is fully screened by a charge transfer (right) or remains empty (middle), resulting in a main line and a shake-up line respectively.

now empty d-state. The exact nature of the ground and excited state remains uncertain until further TD-DFT is done, therefore in this work the two final states are not further specified.

3.6 Line shapes

Quantitative evaluation of the XPS spectra require a precise peak area determination, therefore it is essential to use the correct line shape to fit the peak. In order to find the correct line shape, a full understanding of what is causing and effecting the line shape is needed. Already a simple carbon C 1s peak is highly discussed and arises many different interpretations [312–314].

Doniach and Sunjic initially derived theoretical core line shapes [315]. The Doniach-Sunjic (DS) line shape has the numerical disadvantage that it is divergent, while the Mahan line shape [316] has a finite integral. The Mahan line shape is a combination of a Gaussian and a Lorentzian line shape. The reason for the Lorentzian part is the lifetime broadening (Heisenberg uncertainty principle), while the Gauss broadening originate from the response function of the instrument [317] and from phonon or vibrational excitation [ii]. Both line shapes, DS and Mahan, also contain an asymmetric shape term, which is caused by elastic scattering of the emitted photoelectrons in the conducting band. Obviously this asymmetry is more pronounced for metals since they have highly occupied conducting bands. The peak tail can also be used to analyze the electrons at the Fermi level [319]. A detailed comparison of the two line shapes discussed above can be found in [50]. All asymmetric peak shapes are moving intensities away from the area of observation, therefore they are sensitive to the background limits set by the user. In addition the DS background is ill defined [320], therefore a Gaussian Lorentzian product with a tail (GL(x)T(y)) Gaussian Lorentzian product used to describe the line shape (GL(x)) is commonly used for the line shape.

3.7 Background

In every spectrum there is also noise and, additionally, the intensity on both sides of the peak does not drop to zero. For a quantitative determination of the peak area this background (BG) has to be taken into account. To properly evaluate the spectrum of TiN accounting for all the issues mentioned above, the BG subtraction is of central importance. An incorrectly chosen BG causes wrong peak intensities and consequently results in misinterpretation of the data. In order to select the correct BG it is essential to understand its origin. Photoelectrons are emitted from depth up to 10 nm. On their way to the surface they undergo inelastic and elastic scattering. During these inelastic processes they lose energy and give rise to an increase in the count rate on the lower kinetic energy side of each peak [317]. Besides the inelastic scattering (extrinsic), also intrinsic effects (excitations due to the created core hole) participate in the rise of the BG [267]. Therefore a background correction is always required. A poor background subtraction will result in wrong interpretation (e.g. wrong peak ratio of Ti $2p_{3/2}$ to Ti $2p_{1/2}$), but a correct peak ratio does not necessarily mean a correct background [320]. For each material the background slope has to be either theoretically calculated or experimentally estimated [321]. Even for well know materials it is still a difficult and a highly discussed task to find the best approach for the background slope [322]. From simple BG subtractions, such as a linear BG [323] used for TiN and TiN_xO_y to a polynomial product of Shirley functions [324] numerous background subtractions are published. Most of these are available in common XPS evaluation programs.

All backgrounds should meet the data at the limit of the energy interval, which defines a set of peaks. Therefore the BG is always adjusted to a higher and lower energy limit of the peaks under investigation. Adjusting the background to only a single point would include always the noise of that particular point, therefore all background limits are usually routinely averaged by several energy points around the left and right side limit. The most commonly used backgrounds are briefly introduced in the following .

[ii] Phonons at zero temperature are Poisson distributed, for $n_{phon} >> 1$ the Poisson distribution can be approximated by a Gaussian distribution, [318]

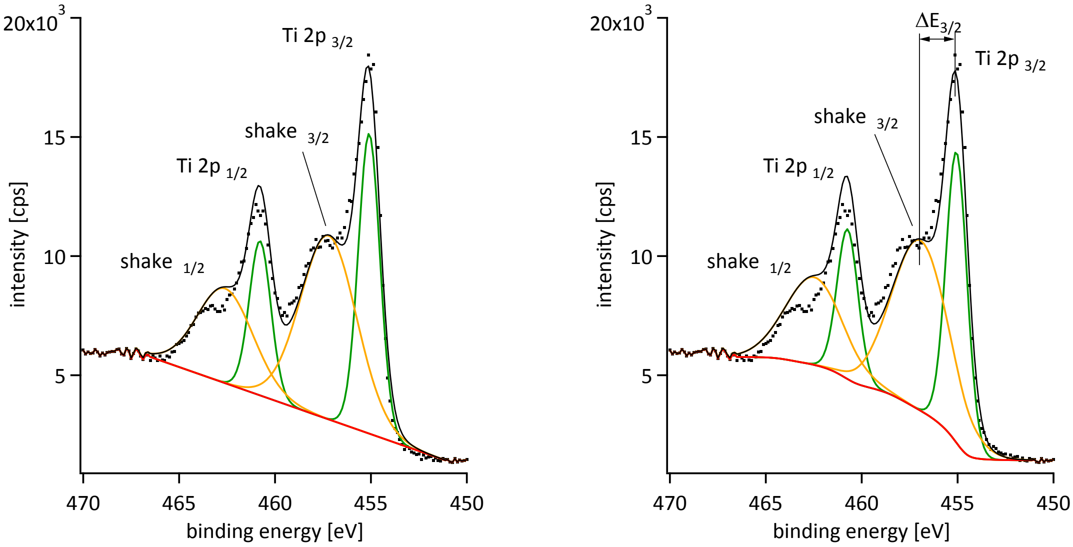

Figure 3.6: Detailed spectrum of Ti 2p with a linear BG (left) and a Shirley BG (right) subtraction over an energy range of 20 eV. Details on the the four peaks and different BG types will be discussed in section 7.2 and 7.3, respectively.

Linear background This background simply gives a linear line between the limits of the spectral region (see fig. 3.6, left side). The linear BG is often used for polymers and insulators, since hardly any increase in the BG is observed for these materials. Insulators have a big band gap and therefore show a low energy loss [267], i.e. no BG increase. This background has also been used already for TiN [325], but as will be seen in section 7.3, is not appropriate for any quantitative peak fitting in TiN.

Shirley background Probably the most commonly used BG type is the Shirley BG [324, 326] (see fig. 3.6, right side), which is widely used in the analysis of XPS data [267] and is also occasionally used for TiN [327–330]. The Shirley BG is an empirical background subtraction technique that iteratively adjusts the background as a function of the intensity of the photoelectron line. It is therefore proportional to the peak intensity and shows the highest slope at the peak center. For everyday practical applications it has the advantage that only a short energy range of 20 eV has to be recorded. It therefore cuts off intensities arising from shake-up or similar intrinsic contributions [331]. The algorithm is suitable for spectra that show only a small intensity increase when going from the low to high binding energy side of a peak; it is conveniently used as a BG for one or two non-overlapping peaks. The Shirley background corrected spectra ($F(E)$) of the kinetic energy E over an interval $[E_{min}, E_{max}]$ is given as:

$$F(E) = I(E) - k\int_{E_{min}}^{E_{max}} F(E')dE' \tag{3.2}$$

where $I(E)$ is the intensity at the kinetic energy E and k is adjusted in such a way that the BG adjusts to the spectrum at the lower energy side, $F(E_{min}) = 0$.

Sometimes also a Spline Shirley background is subtracted. In general it is strongly dissuaded to use Spline background subtraction. Any Spline function is manually adjusted, giving any imaginable background shape and results in the best case in an only wrong quantitative intensity.

Tougaard Background The Tougaard BG (see fig. 7.5) [317, 332, 333] is derived through purely physically sound arguments. It is based on the electron-electron interactions of the emitted electrons with the electrons in the solid. The latter redistribute, if a moving electron is present, which induces a small electric field, which then interacts with the emitted (moving) electron. The Tougaard BG uses the inelastic scattering cross section that is based on the dielectric response function and describes the interaction of the moving electron in the solid. A review of these processes is given in [268, 317, 332]. It has been shown in quantitative studies [317, 333–335] that a Tougaard BG is most suitable if the BG increases dramatically, such as metals, including TiN. This BG also has the advantage that it contains only the extrinsic background, so that the intrinsic peaks, such as shake-up and plasmons, can be easily identified after BG subtraction.

In the following the Tougaard BG is derived according to Tougaard [333] for the background corrected signal $F(E)$:

$$c \cdot F(E) = \frac{1}{\cos\theta}\left[\frac{L+\lambda\cos\theta}{\lambda L} I(E) - \int_{E}^{\infty} I(E')K(E'-E)dE'\right] \tag{3.3}$$

where $K(E)$ is the inelastic electron scattering cross section and L is adjusted to meet the data at the wide range on the low kinetic energy side E_{min} of the spectra.

The inelastic electron scattering cross sections $K(E)$ describes the interaction of the photoelectrons with the solid matter through which they are traveling. The acting forces depend on the electron distribution over the solid, hence $K(E)$ is a material-dependent parameter. The individual cross section [317] can either be theoretically calculated by using the dielectric response function or experimentally by Electron Energy Loss Spectroscopy (EELS). The universal cross section [iii] is introduced to overcome the necessity to determine the cross section for each individual material. According to Tougaard [336] it can be calculated by:

$$K(E) \cong \frac{1}{\lambda}\frac{B\,E}{(C+E^2)^2} \tag{3.4}$$

Since this BG contains only the kinetic energy E and two parameters B and C it is called Universal Two-parameter Tougaard background (U2T). Precise experiments were performed

---

[iii] note: Do not confuse with the Scofield cross section, the latter gives the number of electrons that are emitted by XPS, while the universal cross section describes the interaction of the photoelectrons with the electrons of the solid.

by Seah et al. [332] who derived the $K(E)$ by measuring the individual cross section of 59 elements and obtained $B = 681.2\,\text{eV}^2$ and $C = 355.0\,\text{eV}^2$. The factor B describes the linear inclination of the BG and increases with the amount of inelastic scattered electrons.

3.8 First principle method

Elemental quantifications are often performed using built-in sensitivity factors in commercial software packages. The quantitative concentrations of elements are calculated using sensitivity factors and the area intensities of the main and shake-up peak of each element [267, 337]. In this work the sensitivity factors used for the composition determination are derived from basic principles that take into account the inelastic mean free path (IMFP) [338–340], the geometry of the spectrometer, the transmission function [267], the asymmetry function [341] and the relative emission cross sections, the so-called Scofield's cross-sections. The latter describe the relative intensity of different elements and core shells compared to each other. Calculations for the Ti $2\text{p}_{1/2}$ and Ti $2\text{p}_{3/2}$ orbitals yield an area intensity ratio of 0.515 [342]. In the present work plasmon intensities are subtracted from the spectra for a correct evaluation of the shake-up intensity, but they are not included to calculate the quantitative elemental composition. In the following it is shown how the elemental concentration is received from the peak area and the above mentioned geometric and physical parameters.

The measured intensity I_A of a photoelectron line I_A of a given element A is expressed by [267, 337]:

$$\begin{aligned} I_A =& \sigma_A(h\nu) D(E_A) \int_0^{\pi} d\gamma \int_0^{2\pi} d\Phi L_A(\gamma) \cdot \\ & \cdot \int_{-\infty}^{\infty} \mathrm{d}x \int_{-\infty}^{\infty} \mathrm{d}y J_0(xy) \cos(\alpha)^{-1} T(xyz\Phi E_A) \int_0^{\infty} \mathrm{d}z N_A(xyz) \exp\Big(\frac{-z}{\lambda_B(E_A)\cos\Theta}\Big) \end{aligned} \tag{3.5}$$

where

- E_A is the kinetic energy of a photo electron line of a specific element A,
- $\sigma(h\nu)$ is the photo emission cross section, here the Scofield cross section is used, see sect. 3.8.2,
- $D(E_A)$ is the detector efficiency,
- $L_A(\gamma)$ is the asymmetry function and has been calculated according to Reilman et al. [341],
- $J_0(xy)$ is the X-ray flux at the position (x,y),
- α the angle between surface normal and incident beam,
- $T(xyz\Phi E_A)$ is the analyzer transmission function, which was determined on a regular basis by reference measurements,

- $N_A(xyz)$ is the atomic density,
- $\lambda_A(E_A)$ is the inelastic mean free path of photoelectrons with the kinetic energy E_A, see sect. 3.8.1,

The concentration c of an element A in a compound is given by the elements intensity I_A and the sum of all intensities I_{all}:

$$c_A = \frac{I_A}{I_{all}} \tag{3.6}$$

The X-ray flux J_0 and the detector efficiency $D(E_A)$ are assumed to be constant and can therefore be neglected in equation 3.5. The geometric parameter $\cos(\alpha)^{-1}$ also cancels out. The intensity I_A measured under an angle θ of emission (AOE) can therefore be expressed by:

$$I_A = N_A \cdot s_A \tag{3.7}$$

with the sensitivity factor

$$s_A = \sigma_A(h\nu)L_A(\gamma)T(E_A)\lambda_A \cos\Theta \tag{3.8}$$

All sensitivity factors s_A have been calculated for each elemental photo line before calculating the atomic concentration of each element by using equation 3.6.

3.8.1 Inelastic mean free path

The inelastic mean free path (IMFP) is defined in this thesis as the length λ within which the intensity of a signal decays with the depth of origin to $1/e$ of the its original intensity (see equation A.1). The IMFP depends strongly on the kinetic energy of the photoelectrons and the media, in which the electron is traveling in. The IMFP can either be assessed by elastic peak electron spectroscopy (EPES) or calculated [339, 343]. Elastic electron scattering strongly influences their intensity. It has been therefore been proposed by Gries and Werner [344] to use an attenuation length (AL) and an effective attenuation length (EAL) to describe the trajectory of the emitted electrons. Especially in X-ray Photoelectron Diffraction (XPD) elastic scattering occurs in certain crystalline directions. A precise determination of the EAL is beyond the scope of this work. The interested reader is referred to the review paper of Jablonski and Powell [345].

In this work the energy-dependent IMFPs have been calculated according to Tanuma et al. [338, 340] (TPP-2M). The results for electrons with a kinetic energy of ≈ 1030 eV are given in table 3.1

The IMFP of the bilayer systems investigated in this thesis is a combination of the IMFP from the bulk and the top layer. Since the difference between bulk and overlayer IMFP is negligible; therefore the IMFP of the top layer has been used. Besides other parameters the density of the

Material	IMFP according TPP-2M [nm]	IMFP from literature [nm]	literature
TiN	2.00	2.4 ± 0.1, 1.7	[339, 346]
Si	2.44	2.4 ± 0.15,2.75 ± 0.25	[347, 348]
Si_3N_4	2.41	1.9 ± 0.1, $1.6 - 2.36$	[346, 349]
AlN	2.43	$n.a.$	

Table 3.1: IMFP of different materials for electrons with a kinetic energy of ≈ 1030 eV are given. The values used were taken from [346] and errors were estimated, based on the data spreading in the plotted data.

material A (ρ_A) is also included in the TPP-2M formula. The measured density of the overlayers might be different from the literature values (sect. 5.8). The influence of the density ρ_A on the IMFP is small. The biggest difference between literature $\rho_{A,\text{lit}}$ and the XRR experiment $\rho_{A,\text{XRR}}$ is obtained for aluminum ($\rho_{\text{Al,XRR}} \approx 4.0\,\text{g/cm}^3$ versus $\rho_{\text{Al,lit}} \approx 3.3\,\text{g/cm}^3$) and results in a change of the IMFP of only 0.1 nm. The TPP-2M IMFP are typically calculated for bulk materials, and it must be assumed that for ultrathin films these values are not precise [339], especially if the thickness of the overlying material is lower than twice the IMFP.

3.8.2 Photoionization cross-sections

The Scofield's cross-sections are used to calculate the sensitivity factors s_A (see equation 3.7) and are calculated by using a Hartree-Slater model [342]. This model is based on a single particle in a central potential and considers only final states with a single vacancy. The Scofield's cross-sections are therefore *a priori* not calculated absolutely correctly for an excited final state, as it occurs during the shake-up process. However, the approximation of a neutral pure titanium atom instead of an ionized titanium atom of an TiN compound describes the situation well for most cases [268, 350], including this work. Following these findings the area ratio for spin orbit split peaks were set fix to the Scofield's cross-section [342].

3.9 Further surface effects

XPS is an intensively used technique in science and its experimental setups [271, 272, 351], and newly developed theories [352, 353], are comprehensive. Different surface effects can influence the intensity or the binding energy of the PE. Not all effects and theories can be considered in this work. In the following only a few effects are mentioned with reference to literature:

- surface or sample charging, charges induce an additional Coulombic field that interacts with the PE. Negatively charged regions result in higher kinetic energy (i.e. lower E_B) of the PE emerging from that region, positive charged regions result in a higher E_B. PE created far away from the charged area are not changed, since the Coulombic forces before and after transversing the charged area have an opposite sign [267]

- surface effects

  in an ideal crystal the surface atoms have a lower coordination number compared to the atoms in the bulk, as a result their binding energy is changed [267]

  electron excitations occur while the electron is either moving in a shallow region at the surface or in vacuum [352]

- intrinsic core hole effects, caused by the static core hole after photoionization resulting in a energy loss in the kinetic energy of the emitted electron [352, 354]. Note: This energy loss is due to the interaction of the photoelectron with the core hole during the emission and is not like in the shake-up due to an electron-electron interaction.
- "magic angle" of $\approx 35°$, under which the influence of the surface roughness (see sect. 5.6) can be neglected [355, 356]. It is shown that this angle is not universal and depends on the roughness [353, 357].

All these effects have the same influence on the main and the shake-up photoelectrons since they emerge from the same orbitals and have about the same kinetic energy.

3.10 XPS of TiN

This section is only an introductory section of XPS studies performed on TiN, which is required to understand why certain procedures as an *in situ* transfer were performed. A full discussion on the shake-up origin and a comparison to literature is found in section 7.8.

The first qualitative studies on the intensity of the shake-up feature over a wide range of composition of TiN_x ($0.5 < x < 1$) were done by Porte [310]. The group of Navinšek [328] was the first to report a quantitative value for the shake-up intensity of TiN; unfortunately the sample had been sputter cleaned before investigating. This is in fact problematic, as preferential sputtering of nitrogen is observed in TiN [176, 329], resulting in TiN_x with $x < 1$ and decreased shake-up intensity [310]. Therefore the shake-up intensity obtained in Navinšek's work is underestimated.

The quantification of the shake-up line intensity in TiN is jeopardized by oxygen. In the presence of oxygen in the sample TiO_xN_{1-x} is formed. A typical binding energy of the latter is located about 3 eV above that of the Ti 2p states and overlaps with the shake-ups of TiN [358]. Many papers assigned the shake-up to some kind of oxidized TiN_xO_y state [323, 359–361], therefore special care has been taken to keep the oxygen contamination to a minimum (see section 4.5). A pretreatment such as ion bombardment due to sputter cleaning not only alters the Ti/N ratio [86, 358], but will also cause point defects as described by [362]. Such procedures are therefore to be avoided not to alter the information contained in pristine TiN surfaces. To obtain TiN surfaces free of such artifacts and to avoid any of these detrimental effects, single-crystalline TiN layers were grown on MgO under oxygen-free conditions and transferred in situ to the XPS spectrometer.

Part II

Sample fabrication and characterization

It was almost as incredible
as if you fired a 15-inch shell
at a piece of tissue paper and
it came back and hit you.
— Lord Ernest Rutherford

In this way Lord Ernest Rutherford described his first backscattering experiments, that he also described as "the most incredible event that has ever happened to me in my life". Obviously not ballistic projectiles were shot on a tissue paper, but high energetic ions on a thin film. In this work thin layers of a few nm and different projectiles (X-rays and high energetic ions) are used to study the interface between bilayer systems. The thin films are fabricated by Unbalanced Magnetron Sputtering (UBMS) and characterized in detail.

The different fabrication processes are described earlier in section 2.3. This part of the thesis deals with the methods, parameters and characteristics of the deposition process. Chapter 4 describes the sample fabrication process, including the deposition geometry (sect. 4.1), the prerequisites for high temperature deposition (sect. 4.2) and the process parameters (sect. 4.3). Further the sample grounding (sect. 4.4) and the *in situ* transfer (sect. 4.5) are outlined.

In chapter 5 the different sample characterization methods are discussed. The main focus of this thesis are XPS investigations and hence the emphasis of the method description is on XPS theory. The basics of XPS (chapter 3), AR-XPS (sect. 5.3), AFM (sect. 5.6) and XPD (sect. 5.4) are explained and how they have been used in this work (5.1). All other techniques, that were only used to check if the prerequisites of the sample (as single crystallinity and oxygen-free) were met, are thus only sketched briefly in section 5.7 to 5.11.

4 Sample fabrication

All samples required superior fabrication conditions. The aim was to achieve oxygen-free, single crystalline (sc-) and stoichiometric TiN sublayers. The ultra-thin overlayers also had to be stoichiometric and oxygen-free. By means of Unbalanced Magnetron Sputtering (UBMS) at Ultra High Vacuum (UHV) (i.e. pressure $p < 10^{-9}$ mbar) and very high temperatures it is possible to deposit films of the required specifications. In the previous chapter in section 2.3 the basics of UBMS have already been explained briefly. The geometry of the deposition system influences the deposition rate and is described in sect. 4.1. The precautions used to perform high temperature depositions are explained in sect. 4.2. All fabrication parameters are summarized in section 4.3. During the XPS measurements the sample accumulates electrical charges, that can result in energy shifts in the XPS spectra. Thus the sample has been grounded to prevent any charging (sect. 4.4). In order to prevent contamination, the sample had been transfered *in-situ* in a Mobile Transfer Device (MTD) and its setup is outlined in section 4.5.

4.1 Deposition chamber

The deposition system used is an ATC 1500 F Sputtering System from AJA international Inc. (North Scituate, MA, USA). The vacuum chamber is equiped with four different targets ($\varnothing$= 50.8 mm). Their distance d_i to the substrate depends on which gun number i they are mounted. Due to the machine geometry the distance d_1 (and d_2) between gun #1 (and gun #2) and the substrate are $d_1 = d_2 = 105$ mm. Gun #3 (and #4) are further away from the substrate: $d_3 = d_4 = 118$ mm. The guns can be tilted, and hence the pathway of the emitted target atoms can be changed. The distances given are for a fixed angle that has been used for all samples. The magnetic field of the outer magnets of gun # 1 is defined as north, all other guns have their magnets mounted in the opposite direction. The magnetic field is hence in a closed field configuration between all guns and gun # 1. The z-position of the sample holder can be varied, but has also been set to a fixed value for all experiments, resulting in the distances given above. A higher distance between target and substrate causes lower deposition rates, as will be seen later (table 6.3).

All guns are equipped with pneumatically controlled shutters, the speed of opening and closing the shutter is adjustable and influences the determined deposition rate, especially for short deposition times below 5 s.

A detailed description of the system used in this thesis can be found in [12] and in the manufacturers manuals [363].

4.2 High temperature deposition

Very high temperatures are needed to deposited epitaxial samples, hence the sample and its holder have been heated to 800 °C [7]. This is made possible by the substrate holder being mounted on a heating block, where two high power bulbs are heating the samples. A thermocouple measures the temperature behind a protective glass approximately 10 mm away from the backside of the sample, hence the set temperature is not the exact substrate or sample temperature, the accuracy is empirically estimated to ±50 °C.

Since high temperatures and high vacuum are desired for the deposition process, equipment and processes had to be set up accordingly. After each venting of the system the chamber was baked out for two days at a temperature of around 100 °C at which mainly adsorbed water vaporizes. At higher temperature above 500 °C mainly hydrogen, but also small amounts of oxygen are degasing from the walls and parts (e.g. substrate shutter) inside the chamber. For TiN, which is highly sensitive towards oxygen, the chamber and sample holder had to be prepared with special care. Typically the sample holder including substrate was baked out overnight at 200 °C and then the temperature was slowly increased over 2 hours to 850 °C followed by a fast drop to 800 °C. Sample holder and substrate material have been chosen such that the outgasing is already reduced from the material side. The sample holder is made out of a black quartz glass (Vitreosil, Saint Gobain Glass) and has been designed to store two differently sized flat samples and a molybdenum sample plate where the sample is mounted for the *in-situ* transfer, as described in section 4.4. For the sample preparation presented in this thesis, a water and air cooling system has been designed to prevent the heating of the chamber walls. This could have resulted in further outgasing and a less clean HV environment that consequently would result in contaminated samples. Additionally Ti has been deposited on the chamber walls acting as a huge Ti sublimation pump since the highly reactive Ti basically absorbs any remaining contamination in the HV chamber. Following all these precautions and settings, pressures below $2.5 \cdot 10^{-9}$ mbar at 800 °C could be reached.

4.3 Deposition parameters

All samples have been prepared by reactive UBMS deposition from elemental targets in the same UHV chamber and under similar geometrical settings. The sample holder was rotated in order to prevent shadowing and to guarantee a uniform heating of the sample. Depending on the material system different deposition conditions have been employed, as indicated in the sample description.

The background pressure at the deposition temperature was below $4.0 \cdot 10^{-8}$ mbar for all samples. The pressure during deposition was set to $5 \cdot 10^{-3}$ mbar. The nitride films were produced at a gas composition of $Ar : N_2$ of about 2:1 (flow rates were 15 sccm and 8 sccm, resp.), all other layers were deposited in a pure Ar environment. The Ar gas had a purity of 6.0 (i.e. 99.99990%) and N_2 of 5.0 (99.9990%) and were additionally filtered by an *alphagas-purifier O_2-free (Air Liquide)*. Titanium, silicon and aluminum have been sputtered from elemental targets as summarized in table 4.1. The power density was 10 W/m^2. The TiN thickness was ≈ 30 nm in order to keep surface roughness at low levels [241].

Material	Ti	Si	Al
type/comments		p-type	
purity [%]	99.995	99.999	99.99
manufacturer	Kurt J. Lesker	EvoChem	Plasmaterials
thickness [mm]	6.35	3.175,bonded	6.35

Table 4.1: List of the targets used in this study.

(001)- or (111)- oriented magnesium oxide (MgO) was used as a substrate due to its small lattice mismatch with TiN (sect. 6.1), thus enabling epitaxial growth of TiN [65]. For the poly crystalline (pc-) TiN samples, Si wafers have been used. In order to obtain sc- TiN epitaxially grown on MgO, the depositions were carried out either at 800 °C without any bias or by applying a bias of approximately −75 V at 200 °C. For plasma conditions with no bias, the floating potential regulated itself to approximately 15 V. If not mentioned differently, no bias was applied on the substrate.

4.4 Sample grounding

The used MgO substrates are insulating, which can buildup electrostatic charges during the photoelectron process, resulting in a shift in the binding energy. Therefore neutralizers are commonly used to eliminate surface charging. There are two neutralizers in the XPS device used throughout this work to compensate surface charging of the sample: an electron source and an Ar^+ ion source. Both neutralizers are sources of oxygen contamination that increases over time. To overcome both problems (charging and oxygen contamination due to neutralizers) a Pt-frame is deposited on the substrate (see fig. 4.1) before mounting the MgO-substrate to the sample holder. In this way a sufficient electronic contact between the TiN film and the grounding of the sample holder is guaranteed.

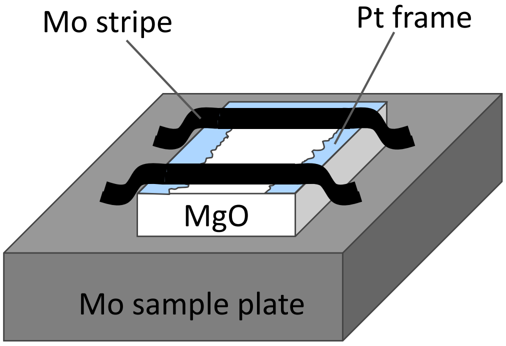

Figure 4.1: A priori the MgO substrate is covered with a Pt-frame and then fixed with two Mo stripes that are screwed on top of the sample holder.

4.5 Mobile transfer device

As mentioned in sect. 3.10 it is absolutely mandatory to have no oxygen contamination, neither in nor on the titanium nitride systems, since the overlap in the Ti 2p photo line of TiO_xN_y would severely effect the shake-up intensity. Sputter cleaning alters the surface and interface [268] and is therefore not an option. Hence the sample has to be transfered without breaking the UHV. Deposition chamber and XPS device are located in two different rooms, and for a sample transfer *in-situ* a Mobile Transfer Device (MTD) is essential. The newly designed MTD is composed of a connection part to mount the MTD to the different UHV systems, a storage compartment where the sample is stored during the transport, a volume (V1) between the storage compartment and the connection, device to handle and move the sample (i.e. wobble stick), a turbomolecular pump to evacuate the volume V1, an ion-getter pump to pump the storage, and a cart that allows to move the chamber. The MTD is first mounted to the deposition chamber, where it is loaded with the sample immediately after the deposition process. The complete device is unmounted from the deposition system and then moved and mounted to the XPS device. After pumping the connection part into UHV the sample can be moved *in-situ* into the XPS system. The overall design is laid out to connect the MTD also to other UHV instruments that are available at Empa (e.g. time of flight secondary ion mass spectrometer (TOF SIMS), low temperature atomic force microscope (LTAFM)).

In the beginning of this thesis a first MTD 1.0 (see fig. 4.2) was available[i]. In this earlier version, two valves were required and the sample was stored on a special shelf below the V1; the total inner volume was much bigger, and an angled construction reduced the pumping power of the pumps. A first series of experiments showed that the surface of the samples was significantly contaminated even though the samples were transfered with this MTD 1.0. Hence the transfer conditions had to be improved, and a new design for the MTD was developed. The second version of the MTD (see fig.4.3) was designed in such a way that the pumping time and the storage conditions were drastically improved. The whole inner surface was reduced, and the sample was stored directly on the linear transfer arm.

---

[i] The author would like to thank Saša Vranjković for developing the MTD 1.0, for the help with designing the MTD 2.0 and for all technical drawings.

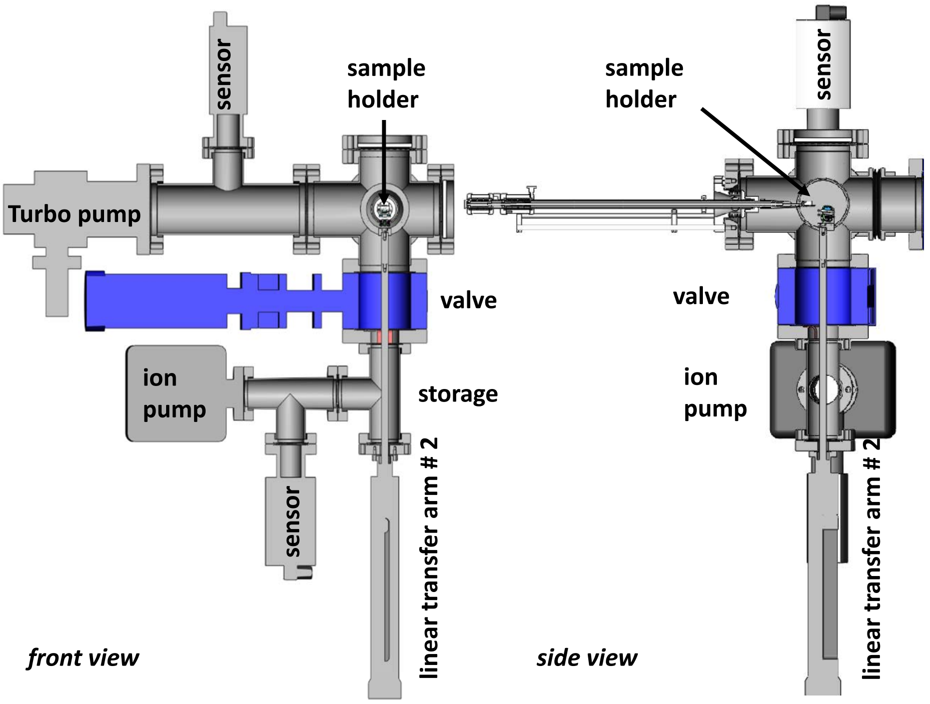

Figure 4.2: First version of the transfer chamber, technical drawing by Saša Vranjković.

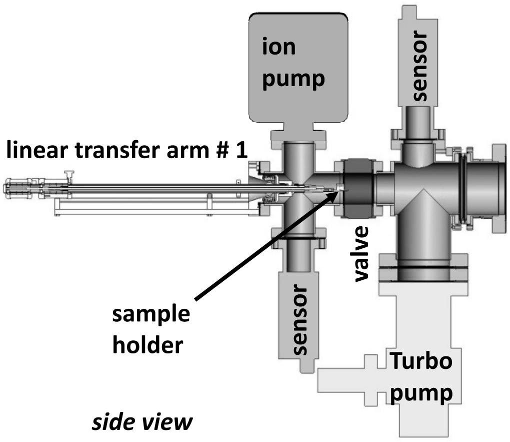

Figure 4.3: Second version of the transfer chamber, technical drawing by Saša Vranjković.

	MTD 1.0	MTD 2.0
inner surface	$2000\,\mathrm{cm}^2$	$850\,\mathrm{cm}^2$
time to reach 10^{-7} mbar	50 min	10 min
pressure in storage	$\approx 1\cdot10^{-8}$ mbar	$< 5\cdot10^{-10}$ mbar
pressure at transfer	$\approx 3\cdot10^{-7}$ mbar	$\approx 2\cdot10^{-8}$ mbar
transfer time	≈ 1.5 h	≈ 5 h
number of view ports	2	none

Table 4.2: Technical data of the transfer device. Inner surface excludes wobble stick, bellows and flange surfaces. Pressure in storage is the averaged pressure in the storage compartment between loading and unloading of the MTD. Pressure at transfer means the pressure in the volume V1 while the sample is transfered from the storage to the XPS sample plate.

In the first version the MTD was mounted to the XPS device and then only heated (with heating tapes) for a few minutes. After 1.5 hours the sample was transfered from storage to the XPS device. The storage pressure was in the range of a few 10^{-8} mbar and in the volume V1 at $\approx 3\cdot10^{-7}$ mbar. In version 2.0 the volume V1 could be heated longer, since the sample was safely stored not only at high vacuum (HV) but even at UHV conditions. Additionally the pump down time could be reduced by a factor of five. The new MTD 2.0 has a five times shorter pump down time than the first version.

The disadvantages of the new MTD 2.0 are a missing view port; however, with a little practice the wobble stick movement is nevertheless an easy task to transport the sample, especially since it is already mounted on the stick and does not need to be picked up (as it was the case in version 1.0). The advantage of design 2.0 is obviously the UHV storage ($< 5\cdot10^{-10}$ mbar [ii]) therefore even after several days no oxygen contamination is observed. This allows also a long heating cycle of the volume V1 resulting in better pressures during the actual transfer from the storage through the volume V1 into the XPS device. The UHV storage conditions and the lower pumping times are mainly a result of decreasing the inner surface of the device.

[ii] the sensors used in this thesis only capable of measuring pressures down to $5\cdot10^{-10}$ mbar.

5 Sample characterization

This study focuses on AR-XPS investigations performed on transition metal nitride interfaces. In the following, the XPS measurements are explained in detail. Previously the basics of XPS have been illustrated (sect. 3), together with the line types (sect. 3.3), especially plasmons (sect. 3.4) and shake-ups (sect. 3.5), as well as their line shape (sect. 3.6). The background heavily influences the shake-up quantification, as will be seen later, and thus different background subtractions have been compared (sect. 3.7). The analysis conditions used to record the XPS spectra are given in section 5.1. The constraints applied to the data are presented in section 5.2, followed by the description of the derived formalism to resolve bulk and interface signals (sect. 5.3).

In order to study the described systems via AR-XPS it is essential to have very well defined samples. XPS measurements are influenced by the surface roughness [364], crystallinity [365] and the elemental composition [267]. Hence the latter properties had to be determined. The crystallinity and its orientation have been confirmed by X-Ray Diffraction (XRD) (sect. 5.7) and Transmission Electron Microscopy (TEM)(sect. 5.10). The interface sharpness and the surface roughness have also been studied by TEM and Atomic Force Microscopy (AFM)(sect. 5.6), the latter was also used to analyze the overlayer coverage, i.e. to ascertain to what extend the sc-TiN is covered. The influence of the overlayer thickness on the interface shake-up ratio is studied in section 8.4.3. Thus it was essential to calculate the film thicknesses by extrapolating the deposition rates. These were obtained by measuring deposition time and film height using either a profilometer (sect. 5.11), X-Ray Reflectometry (XRR) (sect. 5.8), Rutherford Backscattering Spectrometry (RBS) or Elastic Recoil Detection Analysis (ERDA) (sect. 5.9). RBS and ERDA are also used to obtain the exact stoichiometry of the fabricated samples.

5.1 Analysis conditions in XPS

All XPS measurements were performed in a *Quantum2000* from *Physical Electronics* using a monochromatized AlK_α source (1486.6 eV). The X-ray spot has a diameter of 100 μm and is operated at a power of 25 W at 15 kV. The instrument's work function was adjusted to give a binding energy of 83.95 eV and a FWHM of 0.8 eV for the Au $4f_{7/2}$ peak (appendix D). The transmission function is calibrated for the angular resolved measurements on a regular time scale. The base pressure of the instrument was below $5 \cdot 10^{-9}$ mbar during the measurements presented here. All measurements were done in the fixed analyzer transmission mode (FAT). Survey scan spectra were recorded over a binding energy range from −5 eV to 1350 eV with an energy resolution of $\Delta E = 0.5$ eV (see fig. 7.1). Detailed spectra were recorded from 445 – 525 eV binding energy for Ti 2p (fig. 7.5), from 525 – 545 eV for O 1s (fig. 7.9) and from 392 – 413 eV for N 1s (fig. 7.7). The number of sweeps per region was 25 for O 1s, 4 for N 1s and varied for Ti 2p depending on the angle from 10 to 40 sweeps. For the energy region of Ti 2s and the valence band only one angle at 45° was used. For the detailed spectra a pass energy of $E_p = 58.7$ eV with an energy resolution of $\Delta E = 0.125$ eV was used. No ion or electron neutralizers were used, neither was argon sputtering considered as surface cleaning, since this would have altered the surface of TiN as described in [86, 358]. For each sample a minimum of two angle-resolved measurements has been performed. Each angle-resolved measurement contains 36 measurements at different angles of emission (AOE) ranging from 0° to 70° in steps of 2°. The acceptance angle of the electron analyzer was set to 4°. Since no carbon or argon was present in the samples, no reference binding energy was available for calibration. To overcome this deficit the work function at 45° (AOE) has been adjusted in such a way that the binding energy of Au $4f_{7/2}$ is found at 83.96 eV; the binding energies of gold are measured regularly before and after the measurements. The linearity of the binding energy scale (according to the ISO 15472 [366]) is checked on a monthly base by measuring Au 4f, Ag 3d and Cu 2p. Additionally the transmission function is corrected in the same time period.

For the first two years of this thesis, it was believed that the eucentric height of the sample holder was calibrated correctly, i.e. independent of the sample tilt the height z between measuring point and detector is constant. Unfortunately there is a change in z by 0.3 mm, which results in a loss of intensity towards low AOE see fig. 7.17. Obviously this resulted in completely wrong peak intensity ratios for those angles. All those measurements have been disregarded and ever since an Auto-z (i.e. automated height adjustment to the highest intensity) has been performed prior to each measurement.

5.2 Evaluation of the XPS spectra

The spectra have been evaluated using the CasaXPS software package (Version 2.3.16dev85) [320]. For BGs that show only a small increase underneath the peak, a Shirley or Linear BG subtraction is sufficient, therefore Shirley BGs have been used for N 1s and O 1s. The limits of the background are chosen in away that the peaks in the spectra are within the upper and lower limit and only integer values where chosen. The latter reduces the influence of the users personal taste or judgment. In table 5.1 a list of recommended BG limits and the BG type for different elemental lines are given.

A general reliable peak criterion for choosing one or two peaks is defined in [337]: If the FWHM is lower than 1.05 eV then one peak is assigned, if the FWHM is higher than 1.15 eV then two peaks are assigned, except if difference between the E_B of the two peaks compared to one peak was minimal, then only one peak was assigned. This criterion has been applied, where the difference between the E_B of one and two peaks was defined as to be smaller than 0.7 eV. Hence peaks that are closer than 0.7 eV, e.g. Si 2p doublet [367], are not resolved in this study. Plasmons and shake-ups are caused by more complex processes (see section 3.5 and 3.4), and therefore their FWHM was not constraint to the criterion mentioned above.

5.2.1 Background correction

Area	BG limits [eV]	BG type
Ti 2p	450-520	U2T
N 1s	394-402	S
O 1s	527 - 536	S
Si 2p in Si	97-104	S
Si 2p in Si_3N_4	99 - 106	S
Al 2p	69 - 79	S
Al 2s	115 - 126	S

Table 5.1: BG types are described in section 3.7. BG limits are given as the binding energy of the peak region.

The different BG types are introduced in section 3.7. The choice of BG type for O 1s, N 1s, Al 2p, Al 2s and Si 2p influences hardly the results, therefore the short-range Shirley BG can be used; while for Ti 2p it is essential to choose the U2T background (sect. 3.7). As will be discussed in section 7.3 the Shirley BG does not fulfill for Ti 2p the quantum mechanical requirements given by the Scofield's cross-sections.

In single crystalline materials the intensities of elastic and inelastic scattering events show a clear angle-dependent behavior due to X-ray photoelectron diffraction (see 5.4). The same accounts for bilayer systems where the distance that the emitted TiN photoelectrons travel through the sample depends on the angle of emission (AOE) . Hence the background will fluctuate (sect. 7.3), and the factor B (see eq. 3.4) is allowed to adjust the BG to the limits on the high BE side of the selected peak region, while the curvature given by C (eq. 3.4) is chosen to be fix to 355.0 eV^2.

A BG correction over the full range from 450 eV to 520 eV results, for certain angles, in a non-continuous BG, which is a non-physical situation. This discontinuity can be overcome by separating the BG region into two parts. For TiN the interval is divided in [450 eV, 495 eV] and [495 eV, 520 eV], for all overlayer systems the BG limits were set to [450 eV, 520 eV]. The background is also susceptible to noise, therefore a single data channel is not an appropriate method to evaluate the background. The noise of such a single channel is reduced by averaging over a few channels left and right of the selected data point. All area limits were averaged over

5 measuring points and no offsets were used. Especially for these studies the U2T BG has been implemented into CasaXPS by Neal Fairley[i].

5.2.2 Peak constraints

As will be shown in section 7.4 a standard Gauss-Lorentzian product line shape GL(20) is justified for peak fitting. To represent the entire Ti 2p spectrum, eight different peaks have been fitted using constraints that are based on physical principles of these peaks. Three peaks are identified, each spin-orbit split into doublets with total angular momentum number j of 1/2 and 3/2. The origin and the physical meaning of these peaks and their interdependence will be outlined in section 7.8. During the fitting process all positions on the binding energy scale were variable, i.e. no constraints were used for the binding energy. For TiN the only constraints of the fitting process were the FWHM of all 3/2 and 1/2 components, e.g. FWHM(Ti $2p_{3/2}$)=FWHM(Ti $2p_{1/2}$) as well as the area ratios of the main core level lines of Ti $2p_{1/2}$: Ti $2p_{3/2}$ were set to 0.515 as given by the Scofield's cross-sections [342] . All confinements for TiN are given in table 7.1. Since in bilayer systems the signal from the covered TiN is drastically reduced, additional constraints were applied to the fitting process. Besides the fixed FWHM (as in pure TiN) also shake-up areas, i.e. Area($shake_{1/2}$)= 0.515× Area($shake_{3/2}$) were correlated to each other. All other areas and FWHM were kept without any constraints. The Levenberg-Marquardt algorithm, implemented in CasaXPS, gives qualitatively the same result, meaning that all energy positions and peak areas show only a small variations from one angle to the next.

The N 1s line has been analyzed using two fitting curves, a GL(80) and a GL(30), allowing the separation of N-Ti and N-O, as described in section 7.2. All other energy lines have been evaluated using a GL(30).

5.3 Angle resolved-XPS (AR-XPS)

Angle Resolved X-ray Photoelectron Spectroscopy (AR-XPS) is the prime technique to differentiate between signals from the surface and the bulk [267, 328]. Low angles of emission θ (AOE) of 0° to 20° provide information that is primarily bulk sensitive, while those at high AOE (60° to < 90°) are surface sensitive (see fig. 5.1). AR-XPS is a non-destructive method that can easily be applied to get a qualitative difference between surface and buried layers; for a quantitative study some mathematical models have to be applied (see appendix A).

The angle of emission is defined as the angle between detector and the surface normal [368], i.e. at an AOE of 0°, where only electrons emitted perpendicular to the surface are detected [267]. In literature [27, 344, 369] also the term take-off angle (TOA) is used, the latter is defined as the angle between the surface plane and the detector (TOA=90°-AOE). The XPS system used

---

[i] The author would like to thank Neal Fairley of *Casa Software Ltd.* for implementing several new customized BG types into the software and for enlightening discussions on XPS.

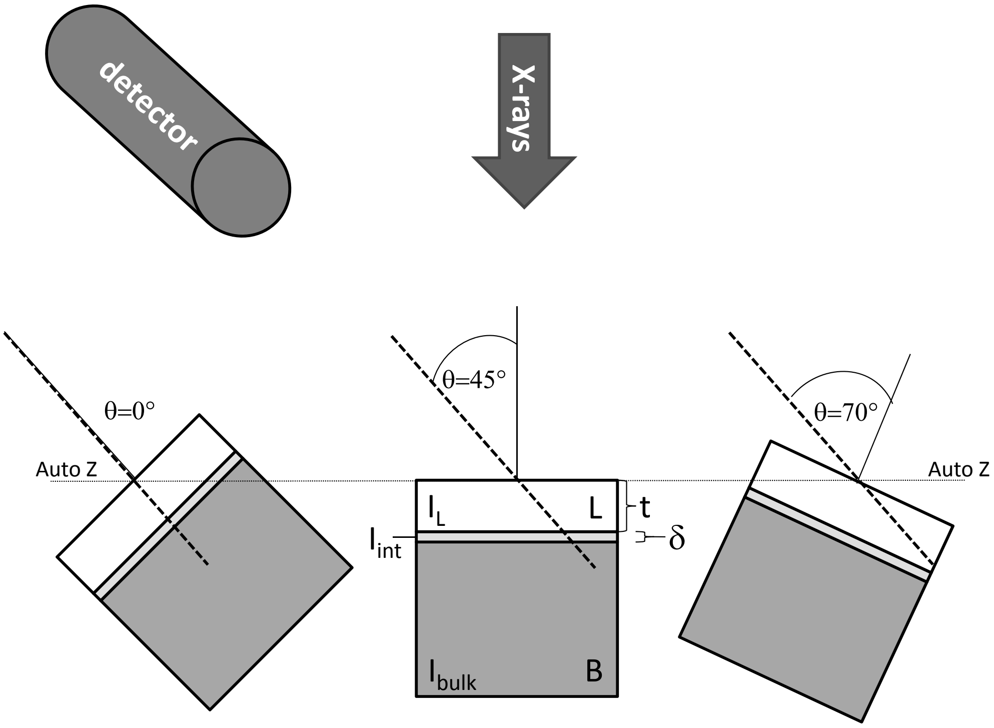

Figure 5.1: AR-XPS according to the setup in the system used in this work (*Phi instrument, Quantum2000*). The measuring geometry is sketched. The X-ray source always radiates from the top, the detector is fixed to an angle of 45° to the X-ray source. The sample is build-up of a bulk material B, an interface (*int*) and an overlayer material L, their intensities are I_{bulk},I_{int} and I_L respectively. The overlayer thickness and the interface thickness are defined as t and δ, respectively. The angle of emission (AOE) θ between the surface normal (solid line) and the detector direction (dashed line) is shown for three different sample rotations (from left to right: $\theta = 0°$, 45° and 70°). The dotted line indicates the sample height, which was always automatically corrected (Auto-z). The dashed line represents qualitatively from which depth the signals are picked up, for high AOE less bulk and more surface intensities are measured.

in this thesis tilts only the sample, and the angle between detector and X-ray source are kept constant at 45°.

5.3.1 Determination of the interface ratio r_i

The intensity changes of the shake-up at different interfaces are in the focus of this work, the absolute intensity is strongly influenced by the AOE and also by XPD effects (sect. 5.4). Therefore in the following only intensity ratios are used to overcome the angle-dependence of the intensities. An interface ratio r_i and a bulk ratio r_b are used to describe the intensity ratio of the shake-up and the main PE line intensity. The bulk ratio r_b is defined as the ratio of the shake-up intensity and main peak in the bulk material of TiN. If not stated else explicitly, then it is referred to the intensities of the 3/2 components (i.e. Ti $2p_{3/2}$ and $\text{shake-up}_{3/2}$). The interface ratio r_i is similarly defined as the ratio of the shake-up intensity and main peak intensity at the interface. r_i is assumed to be homogeneous within an interface region with a thickness δ. All ratios (especially r_i, r_b and R_m) are intensity ratios between the shake-up and main peaks, unless specifically mentioned. The measured ratio R_m (i.e. ratio between measured shake-up intensity and main peak intensity) is expressed as a function of the bulk ratio r_b and the interface ratio r_i by:

$$R_m = \frac{\frac{r_i}{1+r_i} f + \frac{r_b}{1+r_b} g}{\frac{1}{1+r_i} f + \frac{1}{1+r_b} g} \tag{5.1}$$

with

$$\begin{aligned} f &= 1 - g && (5.2) \\ g &= e^{-\delta/(\lambda \cos\Theta)} && (5.3) \end{aligned}$$

where λ is the IMFP, Θ is the AOE and δ is the interface thickness. The latter is defined as the thickness of a region at the interface where the shake-up intensity is altered due to interface effects. A detailed derivation of equation 5.1 is given in appendix A.

Another approach is to investigate the total intensity of the shake-up and the main lines separately and describing their intensity by an additional diffraction pattern function (eq. 5.4 in sect. 5.4).

5.3.2 Influence of the thickness on the measuring geometry

Section 8.4 shows that the XPS results are also influenced by the overlayer thickness t. Therefore it is essential to differentiate between real thickness effects and such effects that are induced into the measurement due to a changed measuring geometry. The latter is explained in this section.

The thickness of the overlying material changes the information depth of the different materials. Figure 5.2 sketches the information depth for two angles (blue: AOE= 0°; red: AOE>> 0°). The red areas indicate which sample volume is contributing with a higher intensity for high AOE compared to low AOE. The blue areas indicate from where more information is obtained at AOE= 0° compared to AOE>> 0°. The colors indicate the regions which are probed less or more in dependence of the angle. The highest intensity will always emerge from the sample surface, but for low AOE more depth information than for high AOE is found in the XPS signal.

For a pure TiN a low AOE reveals more depth information of the bulk TiN, while for high AOE more surface information is obtained (see left sketch in fig. 5.2). For a thin overlayer (e.g. AlN) with a thickness t_1 XPS signals from the overlayer and the underlying TiN are recorded

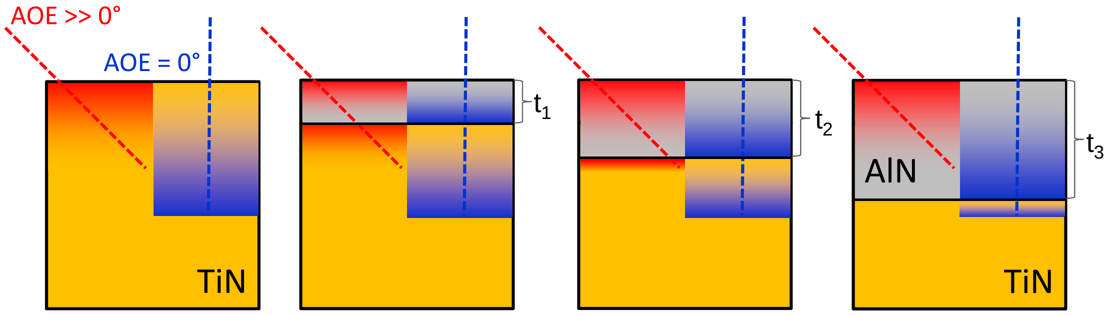

Figure 5.2: Comparison of the relative information depth of high AOE (red) compared to low AOE (blue). The information obtained from a TiN/AlN interface decreases with increasing thickness t of the overlying AlN film ($t_1 < t_2 < t_3$). TiN is drawn in orange and AlN in grey. For details see text.

(see second sketch from the left in fig. 5.2). High AOE (red) probe stronger the surface of the overlayer and the interface of the sublayer (TiN) but much less of the overlayer signal from the interfacial region. Low AOE (blue) provide more signal of the overlayer, including its interface region, the interface and more bulk information from the sublayer.

With growing overlayer thickness ($t_1 < t_2 < t_3$), the region from where the electrons are detected with respect to the position of the interface is changed. For high AOE (red) more and more "bulk" information from the overlayer is recorded, while the interface signal of the sublayer vanishes. For low AOE (blue) the observed sublayer region moves closer to the interface, while the overlayer information contains more bulk overlayer volume.

In both cases AR-XPS is probing a fixed volume, assuming the same IMFP. With increasing overlayer thickness the interface moves deeper and eventually lies too deep to be detected.

The influence of a lower AOE and an increasing thickness t on the Al 2s signal can be qualitatively separated (see fig. 5.3). For a lower AOE (blue in fig. 5.2) the Al 2s signal contains more information from the AlN "bulk" and more information from the AlN side of the TiN/AlN interface than for higher angles (red in fig. 5.2). In thicker overlayers the Al 2s signal contains also more information from the AlN "bulk", but less interface information compared to thinner layers. A similar qualitative comparison is applied to the Ti 2p signal (fig. 5.3).

5.4 X-Ray Photoelectron Diffraction (XPD)

In single-crystalline materials the emitted photoelectrons can undergo multiple *elastic* scattering resulting in interference patterns [266, 267, 365, 370–374]. Those patterns were first reported by Siegbahn [266] and Fadley et al. [370]. The wave field of the photoemitted electrons scatter at the surrounding atoms and undergo coherent interference. This is visible in intensity [375] and background fringes [376] that are dependent on the observation angles

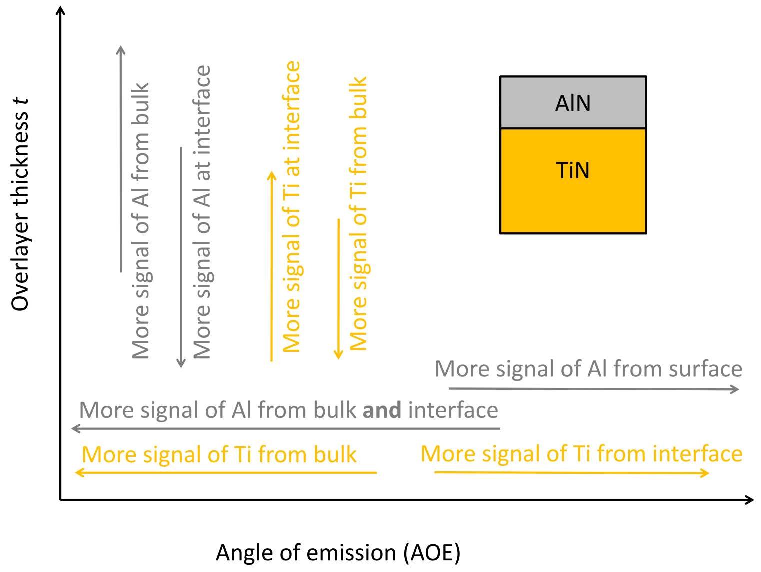

Figure 5.3: Influence of the information volume depending on the overlayer thickness and the AOE.

and electron energies. This elastic scattering of emitted photoelectrons induced by X-rays is called X-ray Photoelectron Diffraction (XPD). The interference patterns contain information on the scattering path lengths and thus on the relative position of emitting and scattering atoms [374]. Hence XPD is often used to investigate adsorbates on surfaces, epitaxial films and particles. The interference pattern can be generated by single or by multiple-scattering processes, the latter is important, especially for electron energies below 50 eV [375]. For high energetic electrons ($E_{kin} > 500$ eV) mainly 0^{th} order diffraction (forward focusing) occurs.

XPD patterns are recorded by setting the analyzer window to a certain kinetic energy and performing a full angle-scan over the azimuthal angle $\Phi = 0° - 360°$ with a sample tilt from $\chi = 0° - 90°$, similar to recording a pole figure (see sect. 5.7) [377]. With this setup the stereographic projection of the angular distribution, i.e. the intensities of a specified energy versus the two angles Φ, χ are recorded over the sample hemisphere. XPD has also been performed on sc-TiN (001) by Timm et al. [378]. Their results for a kinetic energy of $E_{kin} = 851.1$ eV, corresponding to the binding energy of the N 1s photoelectrons (when a Mg K α radition is used), are shown in fig. 5.4. The angular intensity distribution is assigned to the fcc structure of TiN. In this work an Al K α source is used for XPS. The Ti 2p photo electrons have therefore a kinetic energy of $E_{kin} > 1020$ eV and show mainly forward focusing [371]. Any higher order diffraction can be neglected and is also not observed in this study. In this thesis, the intensity of the forward focusing is described by the following semi-empirical derived equation:

$$I_{\text{FF}}(\theta) = I_0 + I_c \cos(\theta) + \sum_{i=1}^{n} I_{p,i} \cdot e^{-\left(\frac{\cos(\theta)-\cos(\theta_i)}{\sigma_i}\right)^2} \tag{5.4}$$

with $\cos(\theta_i) > 1$ and where I_0 is the intensity of the offset, I_c is the intensity of the Cosinus

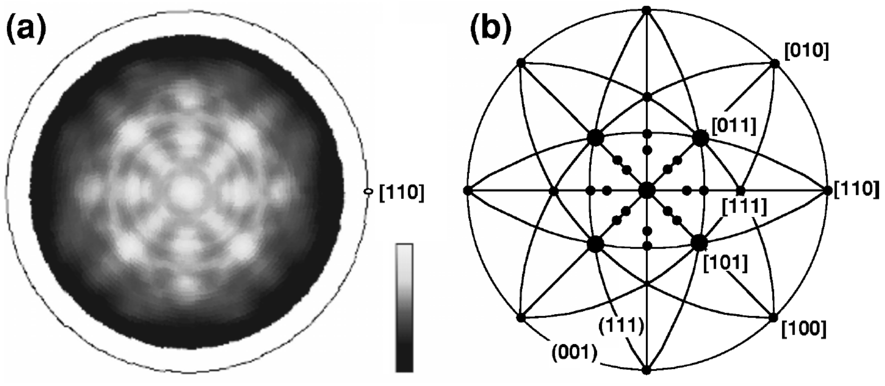

Figure 5.4: (a) XPD pattern of TiN (001) for N1s ($E_{kin} = 851.1eV$ over a range of $\chi = 0° - 78°$. (b) Stereographic representation of crystal directions (dots) and high density planes (lines) of a sc-TiN (001) surface. (reprint of Timm et al. [378])

decay, I_p is the intensity of the Gauss distributed peak i at the angle $\cos(\theta_i)$, and w is the FWHM of the Gauss distribution. Electrons originating from the final ground state (main) and the final excited state (shake-up) have approximately the same kinetics. Hence their XPD patterns are only slightly different. The focus of this study is to obtain knowledge on the shake-up intensity at different interfaces independent from XPD. The interference induced changes in the intensity in the main and shake-up peaks can be overcome by using their intensity ratio R_m (see sect. 5.5).

5.5 Models for the bulk ratio r_b

The oxygen-free bulk ratio r_b of the intensity of the shake-up and the main peaks are absolutely essential for the further interface investigations. As we will see below in sect. 8.5.2 a small change in the bulk ratio cannot only change the absolute values of the interface ratio r_i but also their qualitative interpretation. Therefore, five different ways of extrapolating the true bulk ratio for oxygen-free TiN are discussed below. The results and discussion of the different approaches can be found in section 7.6.

The bulk ratio is, due to the overlap of the binding energy of TiO_xN_y with the shake-up peak, strongly influenced by the oxygen concentration in the material under observation. From ERDA measurements of pure bulk TiN and from AR-XPS data of TiN samples covered with an oxidation barrier (Si_3N_4), it is known that the bulk itself is oxygen-free (below 0.2 atomic percent (at%)). Hence it can be assumed that oxygen is only present at the top of the sample, which enables the use of the following five models:

Averaging the ratio The most simple way of estimating a value for r_b is by averaging over all measured angles. This method ignores any changes of the ratio with the angle. All samples, especially the pure TiN samples, have a small but not negligible amount of oxygen on their surface even though the samples were transfered *in situ*.

Linear approach The measured intensity of the shake-up S_m overlaps with the $\mathrm{TiO_xN_y}$ contribution in the Ti 2p spectra. Therefore S_m can be expressed by:

$$S_m = I_S + I_{oxy} \tag{5.5}$$

where I_{oxy} is the intensity of the oxygen contribution and I_S is the intensity of the shake-up contribution. I_{oxy} is according to the first principal method 3.8 linear to the oxygen concentration (c_{oxy}) . It is therefore given by:

$$I_{oxy} = c_{oxy} \cdot I_{0,oxy} \tag{5.6}$$

The measured intensity ratio R_m is the fraction of measured shake-up intensity S_m and the measured main line intensity M_m and can be calculated by:

$$R_m = \frac{S_m}{M_m} = \frac{I_S + c_{oxy} \cdot I_{0,oxy}}{M_m} \tag{5.7}$$

A Levenberg-Marquardt algorithm is used to fit the measured date of R_m versus the oxygen concentration. For the measured main peak intensity M_m it is assumed that it is neither influenced by the oxygen concentration nor by the angle of emission and therefore being equal to the true main intensity $M_m = I_M$. The obtained values for I_S and I_M are then used to calculate the oxygen free bulk ratio r_b by:

$$r_b = \frac{I_S}{I_M} \tag{5.8}$$

This approach is not angle-dependent and uses only the oxygen concentration to determine the true bulk value.

Exponential Approach The following semi empirical approach was obtained by visual inspection of the plot of the measured ratio R_m versus the oxygen concentration (see fig. 7.21). R_m shows an slightly exponential behavior and increases with the oxygen concentration. A function for R_m is estimated with the fitting parameters a describing a linear part, b the exponential decay, and R_0 a virtual ratio by:

$$R_m = R_0 \left(1 - a \cdot e^{-b c_{oxy}}\right) \tag{5.9}$$

The oxygen free bulk ratio r_b is then easily obtained by setting $c_{oxy} = 0$ in eq. 5.9:

$$r_b = R_0 \left(1 - a\right) \tag{5.10}$$

This approach also considers only the influence of the oxygen concentration and ignores any changes due to the AOE.

XPD approach The intensities for the main Ti 2p and the shake-up are subject to forward focusing and are described by equation 5.4. The XPD approach uses the intensities I_{FF} of both main and shake-up. For $\Theta = 0°$ on the 0^{th} order forward focusing occures, its intensity is given by $I_{p,0}$ in equation 5.4. The bulk ratio is obtained by dividing $I_{p,0}$ of shake-up and main. The bulk ratio r_b is then calculated by:

$$r_b = \frac{I_{p,0}(\mathrm{shake-up}_{3/2})}{I_{p,0}(\mathrm{Ti\ 2p}_{3/2})} \tag{5.11}$$

Angle resolved approach This approach is based on the calculations done for AR-XPS measurements on bilayer system (sect. 5.3). The top layer $\mathrm{TiO_xN_y}$ is graded and has a thickness t_{oxy}. For pure TiN sample, the interface thickness δ (in eq. A.13) is interpreted as t_{oxy}. Hence equation 5.1 is used to fit the measured values depending on the angle by simply setting $t_{\mathrm{oxy}} = \delta$.

5.6 Atomic Force Microscopy

Atomic Force Microscopy (AFM) is a type of a scanning probe microscopy, where in the ideal case an atomically sharp tip is probing the sample surface. The tip is mounted at the end of a cantilever, and its bending is typically detected by a laser that is being reflected off the tip backside. The reflection is recorded by photodiodes that are attached to an electronic feedback loop. The forces that act on the tip, when it is brought into the proximity of the surface, are bending the cantilever and are detected by a movement of the laser reflection on the detector. The tip is rastered over the surface and gives a topography image of the sample with a very high resolution. For a more detailed description of AFM the reader is referred to standard textbooks on AFM [379, 380].

The commercial and atmospheric AFM used in the present work is a *NanoSurf Mobile S* [381]. All samples were stored in an desiccator to prevent water to diffuse into the hygroscopic MgO-substrate. All samples were measured with an atmospheric AFM within 24 hours after desiccator removal. The scans were performed in non-contact mode and no tip voltage was applied. The scans were controlled with an adaptive PID and two types of scans were performed: a wide range scan over $4 \times 4\ \mu\mathrm{m}^2$ with a line speed of 4 s/line and a small range of $0.5 \times 0.5\ \mu\mathrm{m}^2$ with a line speed of 1 s/line.

The "high resolution" scan head type was used with a height resolution of $\Delta z = 0.027$ nm and a lateral resolution $\Delta x = \Delta y = 0.15$ nm. The AFM tips used were *SuperSharpSilicon*^{TM} tips (type: *SSS-NCLR-20*) with a tip radius of typically 2 nm.

A parabolic BG subtraction has been performed on all images and the arithmetic average

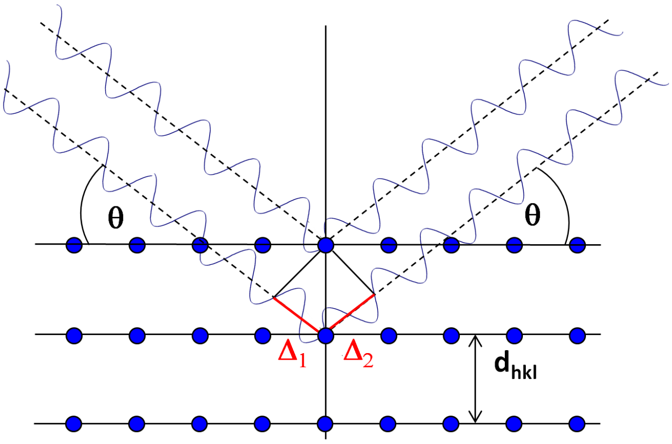

Figure 5.5: Sketch of the Bragg conditions for constructive interference.

surface roughness S_a has been calculated by:

$$S_a = \frac{1}{MN}\sum_{i=1}^{N}\sum_{j=1}^{M}\left|\bar{z} - z_{ij}\right| \tag{5.12}$$

where $\bar{z}$ is the averaged mean value of all heights z_{ij} and z_{ij} is the height at a position (i,j).

5.7 X-Ray Diffraction (XRD)

Probably the most important technique in crystallography is X-Ray Diffraction (XRD). The recorded diffraction patterns reveal information on the crystal structure, mean crystallite size, residual stress and distribution of orientations. The information depth is up to a few µm and is therefore of special interest in thin film characterization. In the following only the basics of this nondestructive technique are briefly explained. For more details please refer to textbooks on XRD [382–384].

Diffraction conditions

The concept of XRD is sketched in figure 5.5. Constructive interference is detected if the optical path length $\Delta = \Delta_1 + \Delta_2$ is equal to a multiple of the wavelength of the X-rays λ_x. Simple trigonometric calculations lead directly to Bragg's law that describes the relation for constructive interference:

$$n\lambda_x = 2d_{hkl}\sin\Theta \tag{5.13}$$

where d_{hkl} is the lattice constant for the (hkl) planes, n is an integer and Θ is the angle between sample surface and detector .

Commonly, the Bragg-Brentano setup is used, where the incident and diffracted beam have equal angles θ to the substrate normal. A *Siemens/Bruker, D5000* diffractometer has been used, which has a fixed X-ray source. Therefore the sample is turned by the angle Θ and the detector by 2Θ, hence the measurement is called a Θ/2Θ-scan. The X-ray source is a copper anode that emits mainly Cu radiation as $CuK_{\alpha,1}$, $CuK_{\alpha,2}$ and CuK_{β}. Also other X-ray ghost lines (sect. 3.3) with very low intensity are present, e.g. $TaK_{\alpha,1}$.

The obtained patterns can be compared to databases, e.g. JCPDS/ICDD (Joint Committee on Powder Diffraction Standards/ International Centre for Diffraction Data) or ICSD, FIZ Karlsruhe. In this way also the elemental composition and crystal phase of a material can be revealed.

Lattice mismatch

If a film grows on a substrate, and the deposited film has at least one crystallographic orientation equivalent to the substrate, we speak of epitaxy. If substrate and deposit are of the same material, then it is called homoepitaxy, else heteroepitaxy. The lattice constants in heteroepitaxial systems differ slightly, and hence both system have a lattice mismatch. The latter results in residual stress that can be compensated by defects in the crystallographic structure. The lattice mismatch f_{A-B} of two materials A and B , where A is usually the substrate, is calculated by:

$$f = \frac{d_B - d_A}{d_B} \tag{5.14}$$

where d_B and d_A are the lattice constants of the film and the substrate. The lattice mismatch can be used to calculate the coherency stress (see eq. 2.3).

Scherrer formula

The mean grain size d of crystallites can be calculated by the Scherrer equation [385, 386]:

$$d = \frac{K\lambda_x}{\beta \cos\Theta} \tag{5.15}$$

where d is the grain size, β is the FWHM of the 2Θ peak, and K is a shape factor . The latter varies with the actual crystallite shape and has typically a value of 0.9. The Scherrer formula underestimates the actual mean grain size, since other broadening effects are not considered, e.g. strain and instrumental broadening. The Scherrer formalism excludes also peak anisotropy, since typically only the (00l)-reflections are measured, i.e. if columnar growth occurs, then the length of the columns is obtained and not their width that could be much smaller. Scherrer's formula is only applicable for grain sizes up to about 100 – 200 nm due to the difficulty to differentiate between broadening of the crystallite size and broadening due to other factors [386].

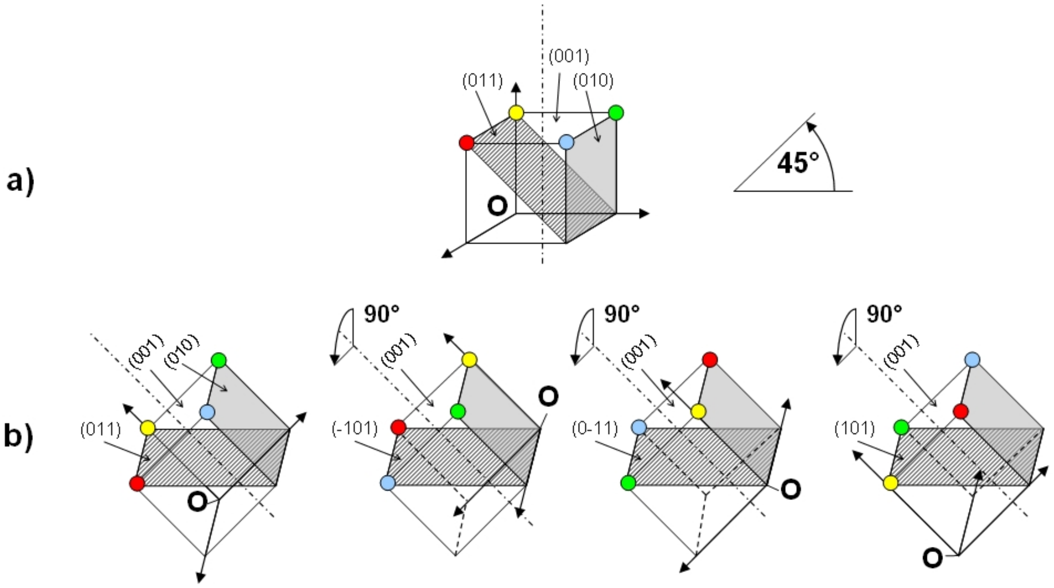

Figure 5.6: a) A fcc-crystal pointing in [001] direction shows no intensity for (110) planes, unless b) it is tilted by $\chi = 45°$ and rotated byϕ [387].

Pole figures

The texture, i.e. the distribution of the crystallographic orientations, is observed by pole figures. For fixed $\Theta/2\Theta$ angles only planes that fulfill Bragg's law and that are parallel to the sample surface participate in the diffraction intensity due to geometrical limitations (i.e. the scattering vector has to be parallel to the plane normal). These limitations are used to record a pole figure, where the $\Theta/2\Theta$ angles are kept fixed and the sample is tilted in χ and rotated in ϕ.

High intensities appear in the pole figure, when plane normals of the same family, are parallel to the angle bisector of incident and diffracted beam. Fixed $\Theta/2\Theta$ angles for a (110) plane of a fcc-crystal with its surface in [001] (fig. 5.6) are chosen. During the recording of the pole figure the sample is rotated around χ from 0° to 360° and after each spin tilted by angle of $\Delta\chi$. No intensity is detected for the <110> family, until the fcc (001) sample is tilted by $\chi = 45°$, here the sample is also rotated by ϕ and diffraction patterns appear every 90°. The (001) crystal has a four fold symmetry in [110], and hence four points/peaks are visible in the stereographic projection on the circle of $\chi = 45°$ (fig. 5.7).

Randomly oriented samples (here the intensity would be equally distributed over the full pole figure) or samples with a preferred orientation can be differentiated. Two scenarios are of special interest for thin film studies: bi- and uniaxial texture. In case that a film grows not only in the direction given by the substrate surface (e.g. 001), but all orientations of the substrate are copied then we speak of a biaxial texture. If the crystallites of the film point all in one

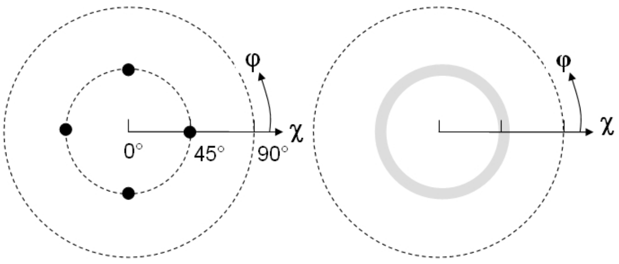

Figure 5.7: (110) pole figure for a fcc-(001) crystal for a biaxial grown film (*left*) and for uniaxial (*right*) [387].

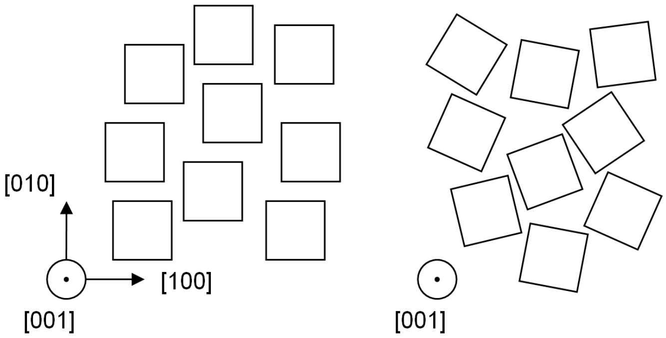

doo

Figure 5.8: Top view on bi- (*left*) and uniaxial (*right*) textures, in a Θ/2Θ scan only (001) diffractions appear.

direction, but are rotated around this axis [001] then a uniaxial texture is present (see fig. 5.8). The latter texture shows then not only four sharp peaks but rather a ring of intensity since for all ϕ angles at $\chi = 45°$ (110)-plane normals are parallel to the bisector of incident and diffracted beam. In order to differentiate between bi- and uniaxial growth a minimum of two pole figures has to be analyzed.

5.8 X-Ray Reflectometry (XRR)

XRR provides information on the layer thicknesses t in the range of 2 – 200 nm, the density ρ and the roughness S_a (0 – 2 nm) even of buried interfaces. In contrast to XRD, no crystallinity is required to perform XRR, and also multilayer systems can be studied. The only requisite is a difference in the refractive index of the layers. A schematic of the XRR geometry is shown in figure 5.9. Similar to XRD, interference fringes are induced by the difference of the optical path length Δ between a beam that is reflected at the sample surface (Point A) and at the interface (Point B). Below a certain critical angle Θ_c that is proportional to the square root of the density ρ, total reflection occurs. Again simple trigonometry can be used to calculate the conditions for interference fringes:

$$n\lambda_x = \Delta = 2t\sin\Theta_t \tag{5.16}$$

where Θ_t is the refracted angle described by Snell's law. The refraction depends also on the density ρ of the material and therefore simulations are required to determine the parameters t, ρ and S_a.

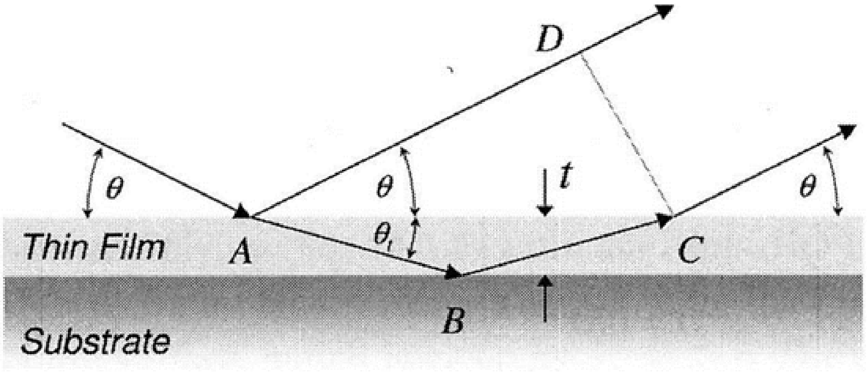

Figure 5.9: Sketch of the XRR basics, picture taken from [384]

5.9 High energetic ion scattering (RBS, ERDA)

In Rutherford Backscattering Spectrometry (RBS) the back scattering of high energetic particles (projectiles) is used to analyze the distribution of elements in a sample (target). Only projectiles with a lighter mass than the target atoms can be scattered backwards, hence light ions (typical He-ions) with energies in the MeV range are used. Conservation of momentum and energy allow to correlate the target and projectile mass to the energy of the back-scattered particles for a certain angle. The projectiles also lose energy during their travel through the material. This loss can be resolved and hence depth resolution is obtained [388, 389].

In Elastic Recoil Detection Analysis (ERDA) also ions in the MeV energy range are accelerated towards a sample, and target atoms are recoiled. Especially lighter elements are easily recoiled and hence ERDA is also sensitive to light elements such as hydrogen. The overlap in the spectrum of forward scattered (RBS) and elastically recoiled (ERDA) projectiles is resolved by either the $\Delta E - E$ or the Time Of Flight (TOF) method. In the former mentioned method, the specific energy loss ΔE through a thin layer is used to distinguish between forward- and backscattered ions with the same energy E. In TOF the particle velocity is used to categorize the particle mass [389].

All RBS and ERDA [390] experiments have been performed at the ETHZ Ion Beam Physics laboratory [ii]. For the RBS experiments a 2 MeV ^{4}He beam and a silicon PIN diode detector under 165 < degree are used and for ERDA a 13 MeV ^{127}I beam at an incident angle of 18 < degree. The RBS data have been analyzed with the RUMP software [391] and ERDA data with the DataFurnace code [392]. The results obtained by RBS and ERDA are presented in table 7.2.

[ii] Here the author would like to thank Max Döbeli from the Laboratory for Ion Beam Physics of ETHZ for measuring and analyzing the samples.

5.10 Transmission Electron Microscopy (TEM)

In Transmission Electron Microscopy (TEM) a focused electron beam is transmitted through a very thin sample. The electrons of the beam interact with the sample, and the transmitted electrons are recorded on a fluorescent screen or a digital camera. The basics of a TEM are similar to a conventional light microscope. However, a much higher resolution is obtained compared to a light microscope, since the accelerated electrons have a much smaller wavelength (a few pm) than visible light (several hundred nm). For more details on TEM the reader is referred to TEM textbooks by Williams and Carter [393].

The maximal sample thickness for TEM is around 100 nm, and for high resolution (HR-)TEM thickness of around 20 nm are required. Cross-sectional TEM samples were cut, mechanically ground, and manually polished (tripod method). The final refining has been done by ion milling the sample under a low-angle Ar beam in a *BalTec Res 101* ion miller. In this thesis a *JEM-2200FS (JEOL Ltd., Japan)* is used to obtain TEM images. The instrument has been operated at an acceleration voltage of 200 kV. A double tilt sample holder has been used to allow the tilting of the sample around two axes. Electron diffraction patterns of the MgO substrate have been used to orient the sample along the zone axes (001).

5.11 Profilometry

A profilometer measures the height and roughness of a sample with a scanning needle in contact. A stylus is moved laterally across the sample surface and the height of the stylus is transformed into a digital signal. By repeating several line scan the topography of the sample is measured. In this thesis a *Tencor P-10 surface Profiler* with a diamond stylus is used to obtain a line profile. The investigated samples were covered partially by a piece of Si-wafer during the deposition process. After removing the Si-wafer a step remains, the latter is measured and reveals the height between substrate and film. Since the stylus is in contact and forces between 1 and 100 mg act on the surface, hence the surface can be damaged or deformed.

Results and discussion Part III

There's plenty of room at the bottom.
- Richard P. Feynman

In this part of the thesis the results are presented and discussed. This part is divided in four chapters: chapter 6 deals with results of the general sample characteristics, in chapter 7 pristine TiN is analyzed using XPS, chapter 8 focuses on XPS results of bilayer systems and in chapter 9 interface polarization and hardness enhancement are discussed.

Before evaluating any XPS spectra it has to be verified, that all the fabricated samples are well defined, i.e. crystallinity (sect. 6.1), overlayer thickness (sect. 6.2), roughness (sect. 6.3) and interface structure (sect. 6.4) have to be known as precise as possible.

In chapter 7 XPS spectra of pristine TiN are presented. Each peak in the TiN spectrum is discussed regarding its position and intensity (sect. 7.1). The different components in the Ti 2p XPS spectra of TiN are shown in section 7.2. The background correction, which is important for a quantitative evaluation, is presented in section 7.3 and the line shape of Ti 2p in TiN is discussed in section 7.4. Photoelectrons (PE) emitted from sc-TiN samples undergo X-ray photoelectron diffraction (XPD), this results in visible oscillations in the PE intensity and the binding energy E_B (sect. 7.5). All information, gained from the above mentioned sections, is gathered and used to further evaluate the TiN samples. Five different models are discussed to obtain the bulk ratio r_b of the shake-up and main peak (sect. 7.6) and the origin of the shake-up is discussed (sect. 7.8).

The insight and basic results of the TiN sublayer are then used to evaluate interface systems in chapter 8. This chapter deals with TiN/Si, TiN/Si_3N_4 and TiN/AlN bilayer systems and their interface. In the first section of this chapter general information as oxygen concentration (sect. 8.3), sample and interface charging (sect. 8.4) are gathered. The interface thickness δ required to obtain the interface ratio r_i (as described in the suggested model, eq. A.23) is discussed in section 8.5.1. In section 8.6 the ratios r_i of the interfacial shake-up and main energy line are elucidated and the parameters influencing r_i are summarized and discussed in section 8.7.

The last chapter 9 of the results part deals with the expected interface polarization (sect. 9.1) and the effects contributing to an hardness enhancement (sect. 9.2).

6 General sample characteristics

For XPS experiments it is essential to know the systems under investigation very well. Surface and interface roughness, crystallinity, overlayer thickness and exact elemental composition have to be determined in order to give reliable conclusions on the shake-up properties.

First, the crystallinity and orientation of the bulk TiN had to be verified (sect.6.1). The overlayer thickness is a very important parameter in the shake-up ratio and needs to be determined precisely (sect. 6.2). To rule out effects due to surface and interface roughness, the samples have to be as flat as possible, therefore AFM measurements were done on different systems with different overlay materials and thicknesses (sect. 6.3). AFM measurements only reveal the surface of TiN before depositing an overlayer, hence TEM samples were prepared and investigated to verify that an atomically sharp interface is present (sect. 6.4).

6.1 Crystallinity of TiN

The crystallinity has been checked on selected samples by performing $\Theta/2\Theta$ scans and pole figure measurements (sect. 5.7). Therefore thick samples in the range of 500 nm were fabricated and investigated.

Figure 6.1 shows a $\Theta/2\Theta$ overview scan for TiN deposited on MgO(001) and MgO(111). The overview scan of TiN(001) reveals two double peaks, that are magnified again in the inlay. The highest peak in the XRD pattern is at $2\Theta = 42.924°$ representing the (002) planes of the substrate MgO ($CuK_{\alpha 1}$). A second peak accompanies the $CuK_{\alpha 1}$ peak of MgO(002), which is a result of the $CuK_{\alpha 2}$ that is always present in X-ray diffractograms where a Cu-X-ray tube is used. The TiN film in this sample has a thickness of approximately 500 nm, which is apparently not sufficient to block the substrate patterns. Also visible are the two diffraction patterns of the TiN lattice planes (002) at $2\Theta = 42.546°$ for $CuK_{\alpha 1}$ and at $2\Theta = 42.656°$ for $CuK_{\alpha 2}$. There are additionally very small peaks observed on the left side of the four main peaks, which are caused by various X-ray lines, e.g. $CuK_{\beta 1}$ at 38.614°. No further diffraction patterns are observed in this diffractogram indicating a single-crystalline epitaxial grow behavior of TiN on

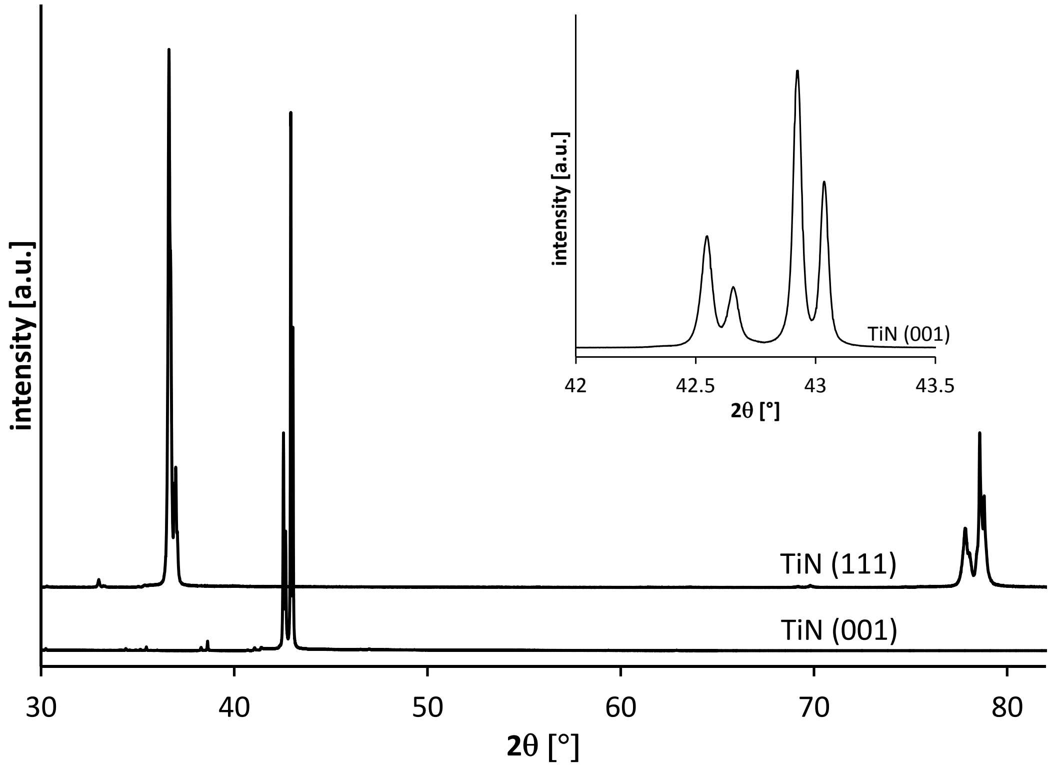

Figure 6.1: XRD Θ/2Θ overview scan for TiN (001) and TiN (111).

Mg(001).

In the XRD pattern of the TiN(111) sample the two diffractions (due to $CuK_{\alpha 1}$, $CuK_{\alpha 2}$) of the TiN(111) lattice planes are overlapping, but are resolved by fitting two Gauss distributions and $2\Theta = 36.621°$ for $CuK_{\alpha 1}$ and at $2\Theta = 36.726°$ for $CuK_{\alpha 2}$ are revealed. Next to the TiN(111) diffractions are also the MgO(111) patterns with a lower intensity (approx. 10% of MgO(001)) visible. Their $CuK_{\alpha 1}$ and $CuK_{\alpha 2}$ components cannot be resolved due to their low intensity. The TiN(111) sample has the same thickness of approximately 500 nm as the TiN(001) sample. The intensity ratio between TiN film and MgO substrate are reversed, since the intensity of the TiN(111) is approximately 70% of the TiN(002) peak [394], while the MgO(111) intensity is below 10% of the MgO(002) intensity [395]. In the TiN(111) samples also the diffraction reflexes of the (222) planes of TiN and MgO are observed between $2\Theta = 77.5°$ and $2\Theta = 79.0°$. Their intensity is, in accordance with Christensen [394], lower than that for the (111) lattice planes.

The lattice constants are calculated using equation 5.13 and are summarized and compared to literature in table 6.1.

Material	exp. d_{002} [Å]	Lit. d_{002} [Å]	literature
MgO	4.190 ± 0.010	4.211	[396]
TiN	4.255 ± 0.005	4.235	[397]

Table 6.1: Lattice constants for the (002) planes at room temperature are given and compared to literature.

Pole figures of TiN (001) and (111)

The texture of 500 nm thick TiN films grown at 800°C on MgO(001) and MgO(111) was evaluated by recording pole figures (sect. 5.7). The pole figures for the (002) planes were measured with $2\Theta = 42.510°$, for the (111) with $2\Theta = 36.663°$ and for (220) planes $2\Theta = 61.813°$. The samples were tilted by χ from 0° to 80° and rotated by ϕ from 0° to 360°.

The (002) pole figure of TiN(001) shows only one single peak at $\chi = 0°$ and $\phi = 0°$ indicating either uni- or biaxial epitaxial growth of TiN (sect. 5.7). The second pole figure for the (111) planes contains four peaks on the $\chi = 54.7°$ ring, the intensity maxima are well separated by $\Delta\phi = 90°$. It is therefore concluded that the TiN grows biaxially on the MgO(001) substrate. The broadening of the peaks along χ is due to the used slit geometry, if point apertures at the X-ray source and detector are used then round peaks are visible in the pole figure.

The diffraction patterns of the (002) planes in TiN(111) are observed if the sample is tilted by $\chi = 54.7°$. Under those conditions all peaks are heavily broadened due to the slit geometry and the (002) diffractions of the film and substrate cannot be separated. Therefore, the (022) planes were used to study the TiN(111) samples. The latter show one peak in the (111) (at $\chi = 0°$) and three peaks in the (022) pole figure on the $\chi = 35.3°$ ring. TiN(111) has a threefold symmetry in the <022> families, hence it is concluded that TiN grows also biaxial epitaxial on MgO(111).

The pole figures of TiN indicate that the film copies the exact crystal structure of the substrate if it is deposited under the conditions mentioned in section 4. This is in good agreement with the observations formerly reported [188, 254].

Influence of deposition temperature

Figure 6.4 shows the diffraction patterns of samples prepared at 800°C, 700°C and 600°C with no bias and at 200°C using a substrate bias voltage of −70 V. The position of the 2Θ peaks shifts for lower deposition temperatures to lower values revealing an increase in the lattice constant, i.e. the lattice is expanded in the direction of growth. This is most likely due to compressive stresses, which force the TiN lattice to adjust to the MgO substrate. The compressive stresses are parallel to the substrate resulting in a smaller lattice parameter in this direction. A compression parallel to the substrate results in an expansion of the lattice parameters in the direction of growth, which is the direction observed in a $\Theta/2\Theta$ scan.

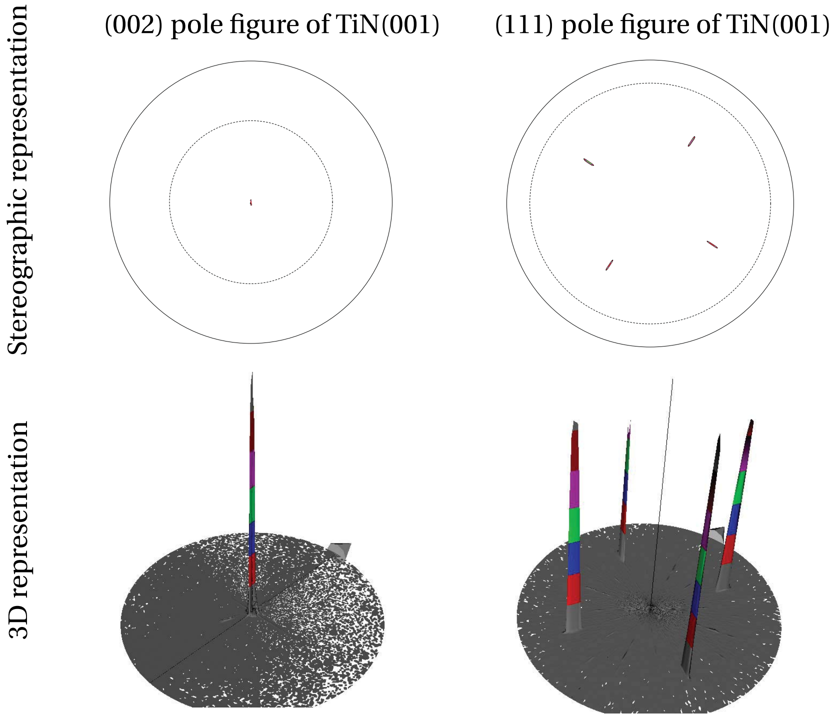

Figure 6.2: Pole figure pictures of TiN(001) in [002] (left) and [111] direction (right), top row are stereographic representations and bottom row the same pole figures in a 3D view.

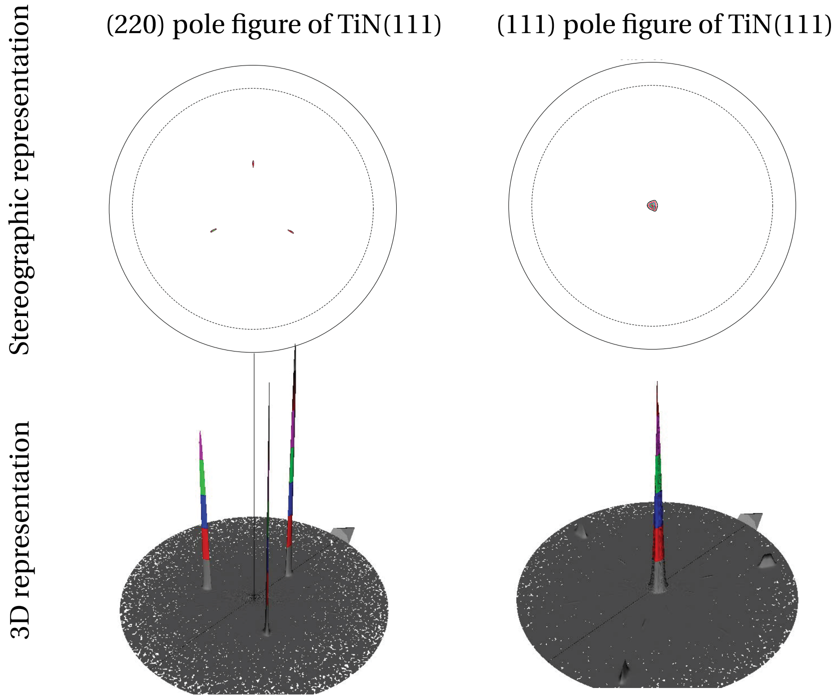

Figure 6.3: Pole figure pictures of TiN(111) in [022] (left) and [111] direction (right), top row are stereographic representations and bottom row the same pole figures in a 3D view.

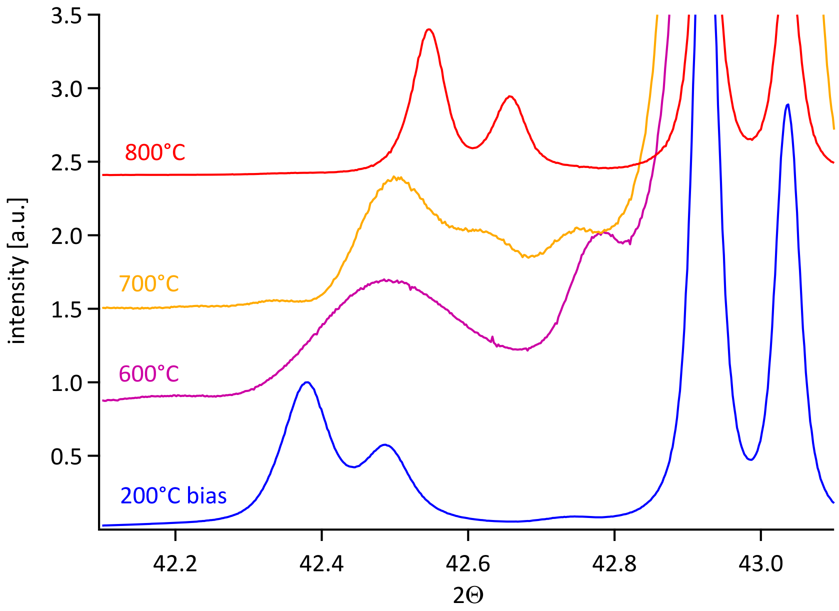

Figure 6.4: Θ/2Θ scans for TiN deposited at different temperatures.

The experimental lattice mismatch f_{exp} has been calculated for the (001) planes using the result from table 6.1 and equation 5.14. The theoretical lattice mismatch f_{theo} has been calculated using the thermal expansion coefficient α of 12.6×10^{-6} /K for MgO [398], 8.9×10^{-6} /K for TiN [399] and the lattice constants d from literature given in table 6.1. For these calculations it is assumed that the lattice parameters were constant in the investigated temperature interval, i.e. the lattice constants for TiN and MgO are calculated for the given temperature, but XRD is measured at room temperature (RT).

The hetero-epitaxial TiN on MgO decreases its lattice mismatch with increasing temperature. Already Karr et al. [254] has shown that the lattice mismatch decreases from $f_{exp} = 0.6\%$ at RT to $\approx 0.2\%$ at 750°C. The lattice mismatch calculations f_{theo} are in good agreement with the observations of Karr et al. [254] and show a decrease of the mismatch from 0.57% at RT to 0.32% at 800°C. The experimental results differ by a factor of 2.5 compared to Karr et al. [254] which is, considering the uncertainty of 0.010 Å, in good agreement with the thoeretical lattice mismatches. Experimental results and theoretical calculations, presented in this thesis, indicate that the TiN films form their fcc-structure with their lattice mismatch at the deposition temperature. This structure remains unaltered after sample cooling to RT.

Temperature	f_{exp} [%]	f_{theo} [%]	grain size d [nm]	film thickness t [nm]
TiN				
800°C	0.84	0.32	450	≈ 500
700°C	0.92	0.35	220	≈ 160
600°C	1.12	0.38	<150	≈ 50
200°C plus Bias	1.21	0.51	310	≈ 370
RT		0.57		

Table 6.2: Lattice mismatch of TiN grown at different temperatures. The film thicknesses were interpolated from deposition rates for TiN at 800°C.

The peak broadening is often used to determine the grain size d by applying the Scherrer formula 5.15. The instrumental peak broadening is not considered. The Scherrer formula is only applicable to unstrained grains smaller than 200 nm. The crystallites in here are neither unstrained nor smaller than 100 nm, therefore the absolute values (see table 6.2) are to be taken with precaution. Nevertheless the Scherrer formula describes qualitatively correctly the grain sizes behavior. The measured size refers to the size of the grains perpendicular to the surface, in this case only in [001] direction. AFM (sect.6.3) and TEM (sect.6.4) results clearly show that in fact a sc-TiN with no columns is present on the MgO samples. The fact that only (001) grain sizes are measured is also clearly seen, if the calculated grains sizes by Scherrer are compared to the film thickness (see table 6.2). Grain size and thickness agree well within the uncertainties given by the Scherrer formalism.

6.2 Overlayer thickness

There are several options to determine the thickness of deposited materials. Four techniques namely XRR, profilometry, AFM and RBS are presented and compared. The results of the deposition rates are summarized in table 6.3.

XRR experiments and simulations are used to obtain the film thickness as described in section 5.8. Only thin films can be analyzed with reflectometry measurements (typically between 10 nm and 200 nm) and precision of approximately 0.1 nm are possible with a simple XRR setup. The disadvantage is that a density contrast between overlying material and substrate is necessary, also neither the interface nor the surface should be rough. E.g. Si films on a Si-substrate show no density difference and hence cannot be investigated by XRR.

The easiest way to measure the thickness of thin films is using a profilometer (see sect. 5.11). The resolution of the profilometer given by the manufacturer is below 10 Å. However, considering the signal-to-noise ratio, the finite tip curvature and the deformation of the material during investigation it cannot be assumed that the device has a better resolution than a few tens of nm. Due to shadowing the step might be smeared out and result in the wrong thickness, therefore a line scan has to be performed over a wide range of a few µm. In order to have a good precision thick layers of a few hundreds to thousand nm have to be deposited, which can be a disadvantage, especially for materials with low deposition rate.

AFM measurements can also, at least qualitatively, give an estimate of the deposited layer thickness, especially if macroparticles are formed, or if the substrate is still visible in between the overlayer grains. Here the roughness of the thickest sample still showing the TiN sublayer is used to interpolate the deposition rate, see e.g. figure 6.7 top for Si_3N_4 and figure 6.11 bottom for Si.

RBS is also capable to resolve a film thickness if experiment and simulation are aligned correctly. The accuracy in the thickness for RBS is in general about 4%. The RBS experiments have the drawback that a high energy ion beam in the range of 1 – 3 MeV and hence a linear particle accelerator, is compulsory. Such accelerators are not found in most materials science labs. The samples in this work were sent to the ETH Laboratory for Ion Beam Physics, where the samples were analyzed.

In most XPS devices a sputter gun is present to perform depth profiling of the sample. If the sputter rate for ion, material, energy and incident angle is known, then the thickness can be estimated by recording a depth profile. The sputtering time necessary to sputter through a thin film is reported on the x-axis and the apparent atomic percentages of the elements are on the y-axis. These sputter rates depend strongly the XPS system used, therefore it is usually difficult to obtain calibrated sputter rates. Also the precision is rather low due to the slow decay in the elemental concentration and the fading out of the offset.

XRR is the preferred technique to evaluate thin film thicknesses due to its high precision and

Material	XRR	profilometer	AFM	RBS
TiN	1.7 ± 0.2			1.8 ± 0.1
Si	n.a.	10 ± 0.1	8.1 ± 1.0	
Si_3N_4	3.1 ± 0.1		3.1 ± 0.1	3.1 ± 0.1
Si_3N_4 (w/ Bias)	4.2 ± 0.1			
AlN (gun1)	2.0 ± 0.1		2.0 ± 0.5	
AlN (gun3)	1.4 ± 0.1	1.0 ± 0.2		

Table 6.3: Deposition rates of different techniques in nm/min. The growth rate for Si_3N_4 with Bias was obtained for a bias of −250 V.

facile operation. If, however, no XRR results could be obtained due to the limitations mentioned above, then profilometry was used to measure the deposit thickness. The comparison shows that the thickness determination agrees well among the different techniques.

Many parameters influence the deposition rate: applied power, pressure, magnetic field, sputtered material, temperature and the distance between targets and substrate are just some of the factors that are affecting the film thickness. Magnus et al. [42] showed that the substrate temperature between 200 °C and 600 °C has only a minor influence on the deposition temperature. All other parameters were kept constant as described in section 4. Due to internal multiuser machine management the targets have been shifted to different gun positions. Since the different position have different target-substrate distances and different magnetic fields, therefore the deposition rates differ, e.g. AlN deposited from gun 3 has a deposition rate of 2.0 ± 0.1 nm/min and from gun 1 of 1.4 ± 0.1 nm/min.

Another uncertainty in the thickness of the deposited films arises from the deposition time. The latter is not exact and may vary due to the shutter opening and closing. The error is estimated by up to 1 s, resulting in uncertainties up to of 0.17 nm for Si. The deposition rate is also not constant over time, since the race track depth of the target is also influencing the deposition rate slightly (sect. 2.3). The relation between track depth and deposition rate has not been determined. The overall error in the thickness is estimated to be up to 0.25 nm for materials with high deposition rates as Si, while for low deposition rates as for AlN and Si_3N_4 the error is estimated to be about 0.05 – 0.1 nm.

6.3 Topography measurements

It has been reported by De Bernardez et al. [400] and Yan et al. [364] that the surface roughness influences XPS measurements, hence prerequisites are flat inter- and surfaces. Therefore AFM imaging has been performed to gain insight on the interface and surface topography. The growth mode is not in the focus of this thesis, hence the growth behavior is not further discussed.

All surface topography measurements were done with an AFM as described in (sect. 5.6), the roughness S_a was calculated following equation 5.12. First, substrate and pristine TiN surfaces were measured (sect. 6.3.1), and then the different overlayer materials and their roughness in dependence of the film thickness (sect. 6.3.2) were studied. All AFM figures shown in the left column are scans of $4 \times 4\ \mu m^2$ and in the right column scans of $0.5 \times 0.5\ \mu m^2$. Please note: The shown AFM images are all scaled differently in order to see all features of all samples.

6.3.1 Substrate and TiN topography

Substrates were scanned by AFM before annealing them at 800 °C. AFM images of the substrates are shown in figure 6.5 and summarized in table 6.4. The pure MgO (001) substrate shows a roughness of 0.14 ± 0.05 nm, basically being atomically flat. The AFM images of TiN on MgO (001) also indicate what can be seen clearly in UHV-STM images of Karr et al. [241, 254], revealing that the morphology of TiN is dominated by growth mounds with a size of 40 – 100 nm [42].

Due to the problematic polishing process performed by the manufacturer [401] the MgO (111) substrates have a higher surface roughness of 0.46 ± 0.25 nm and deep grooves of up to 5 nm. The used Si-wafers (001) are as rough as MgO (111), but show rather roundish surface patterns compared to the scratches in MgO (111).

The TiN overlayers (shown in fig. 6.6) have a thickness of approximately 30 nm and were all deposited at 800 °C. TiN surfaces on MgO (001) and Si (001) substrate are fairly flat (0.18 ± 0.03 nm and 0.31 ± 0.05 nm respectively), while for TiN on MgO (111) a rough surface of $S_a = 1.2 \pm 0.3$ nm is observed. TiN grows epitaxially on MgO [231] at 800 °C. The reported surface roughness of TiN on Si varies over a wide range e.g. 0.27 nm [402] to up to 30 nm [39][i].The topography of TiN on MgO(111) shows grooves and a high roughness due to the already scratched substrate surface. Under the given conditions TiN wets Si quite well and hence the rough Si surface is flattened by the TiN layer. As described earlier in sect. 2.4 the film structure and hence the roughness are influenced by the process parameters.

material	roughness S_a [nm]
MgO (001)	0.14 ± 0.05
MgO (111)	0.46 ± 0.25
Si (001)	0.41 ± 0.13
TiN on MgO (001)	0.18 ± 0.03
TiN on MgO (111)	1.17 ± 0.33
TiN on Si	0.31 ± 0.05

Table 6.4: Roughness values are given in nm and calculated by equation 5.12 using only the $4 \times 4\ \mu m^2$ images and performing a parabolic background fit.

---

[i] Root mean square roughness is used, while in this thesis the arithmetic averaged roughness (sect. 5.12) is used.

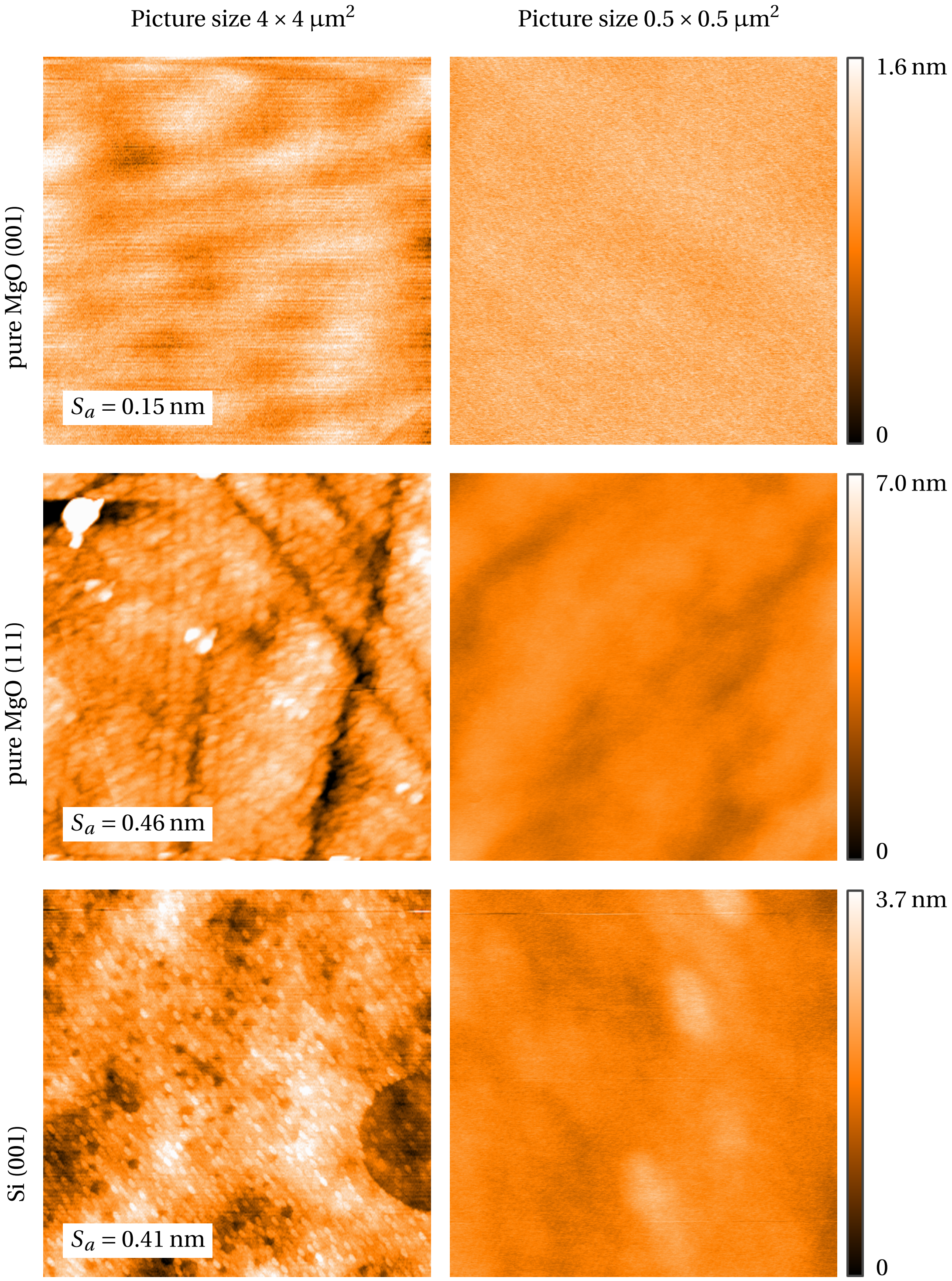

Figure 6.5: AFM images of pure MgO-substrate ((001) and in (111)) as well as Si (001) are shown.

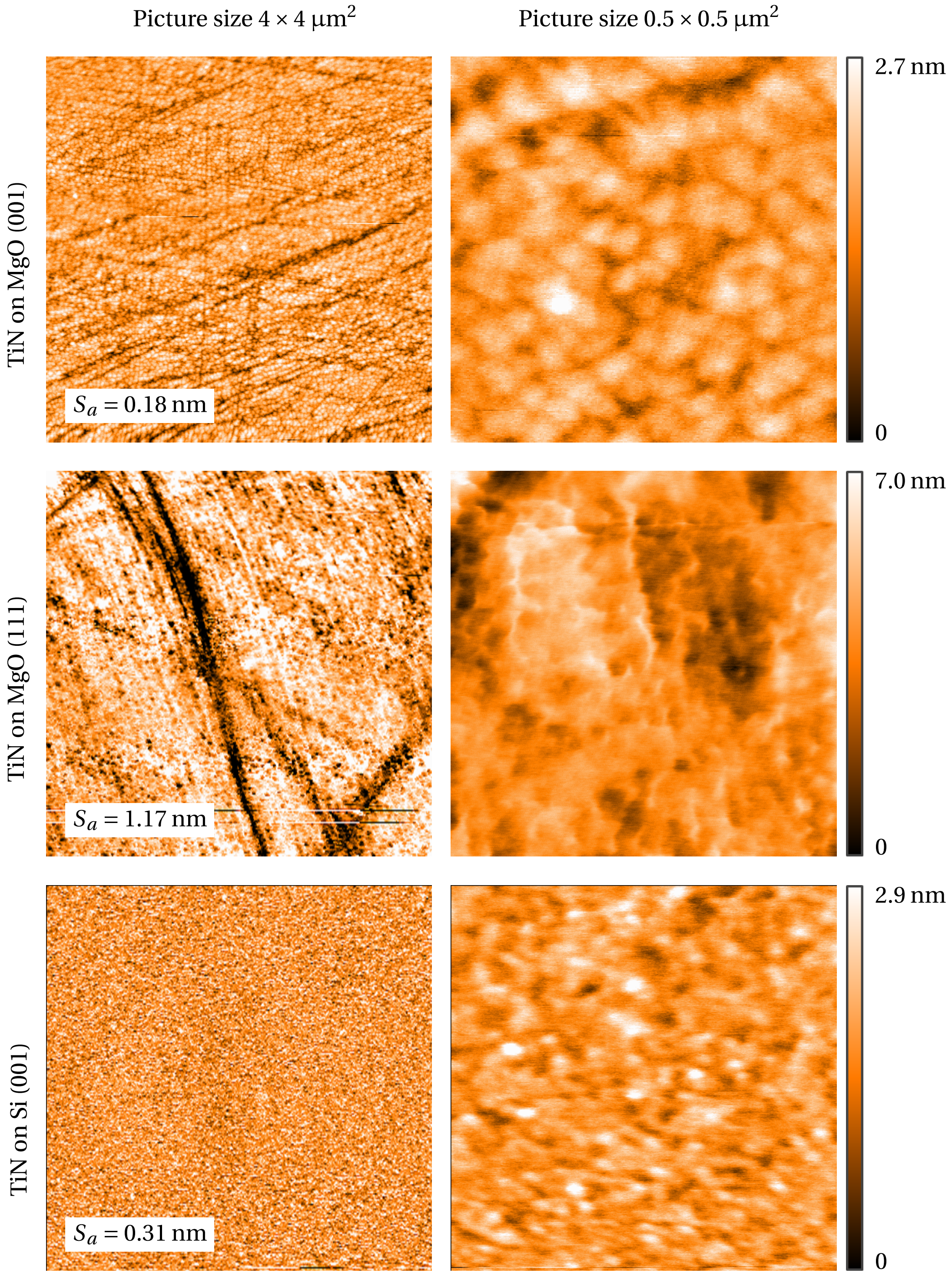

Figure 6.6: AFM images of TiN deposited on MgO(001) and MgO(111) as well as on Si(001) are shown.

6.3.2 Overlayer topography

Different overlayer films (AlN, Si_3N_4 and Si) were deposited on the TiN (001). The roughnes values are investigated for different overlayer thicknesses and in the case of Si also at different temperatures. It is shown that in the TiN/AlN and TiN/Si_3N_4 systems the roughness decreases with overlayer thickness, while Si bilayers show the opposite behavior.

Si_3N_4 overlayer topography

Thin Si_3N_4 films on TiN (001) show a leaf-like pattern that smears out with increasing layer thickness. Thicker Si_3N_4 overlayers show flat mounds and considerably lower roughness (fig.6.7). A direct comparison between Si_3N_4 film thickness and roughness is shown in figure 6.8. It is seen that the surface roughness decreases until a thickness of 1 nm is reached. Si_3N_4 films thicker than are considered atomically flat. The observed grooves in thin Si_3N_4 (e.g. for $t = 0.5$ nm, top left in fig. 6.7) look like the patterns in the TiN on MgO (001), that are only partially covered by thin Si_3N_4 films. The top layer first forms islands (Volmer-Weber growth) that grow and at one point are in contact and coalescence [230].

AlN overlayer topography

AlN films (fig.6.9) show a very similar topography as Si3N4, here a roughness below $S_a = 0.3$ nm is reached already for film thicknesses of 0.5 nm, indicating a better planar growth (Stranski-Krastanov or Frank-van-der Merwe growth) behavior for AlN than for Si_3N_4.

Si overlayer topography

The Si films on TiN show a completely different pattern(see 6.12, top and middle). Large islands of up to 250 nm are formed during deposition at 800 °C and are equally distribute over the full surface. Si deposited at 800 °C shows a minimum roughness of 2 nm that increases with the film thickness up to 8 nm (fig.6.12). At lower temperatures 500 °C (see 6.12,bottom) the mobility of the film-forming Si atoms is reduced and the formation of large islands is restrained.

6.4 TEM of TiN/Si_3N_4 multilayers

Within this thesis the TEM samples are used to obtain information on the interface topography and the TiN crystallinity. In figure 6.13 a multilayer TEM picture is presented (the sample has been prepared by Magdalena Parlinska[ii]). The sample was prepared under the same conditions as the bilayer systems where the growth direction is [001](sect. 4.3). The multilayer is composed of ≈ 4.0 nm thick TiN layers and Si_3N_4 interlayers with increasing thickness,

---

[ii] The author would like to thank Magdalena Parlinska for the sample preparation and the introduction to TEM.

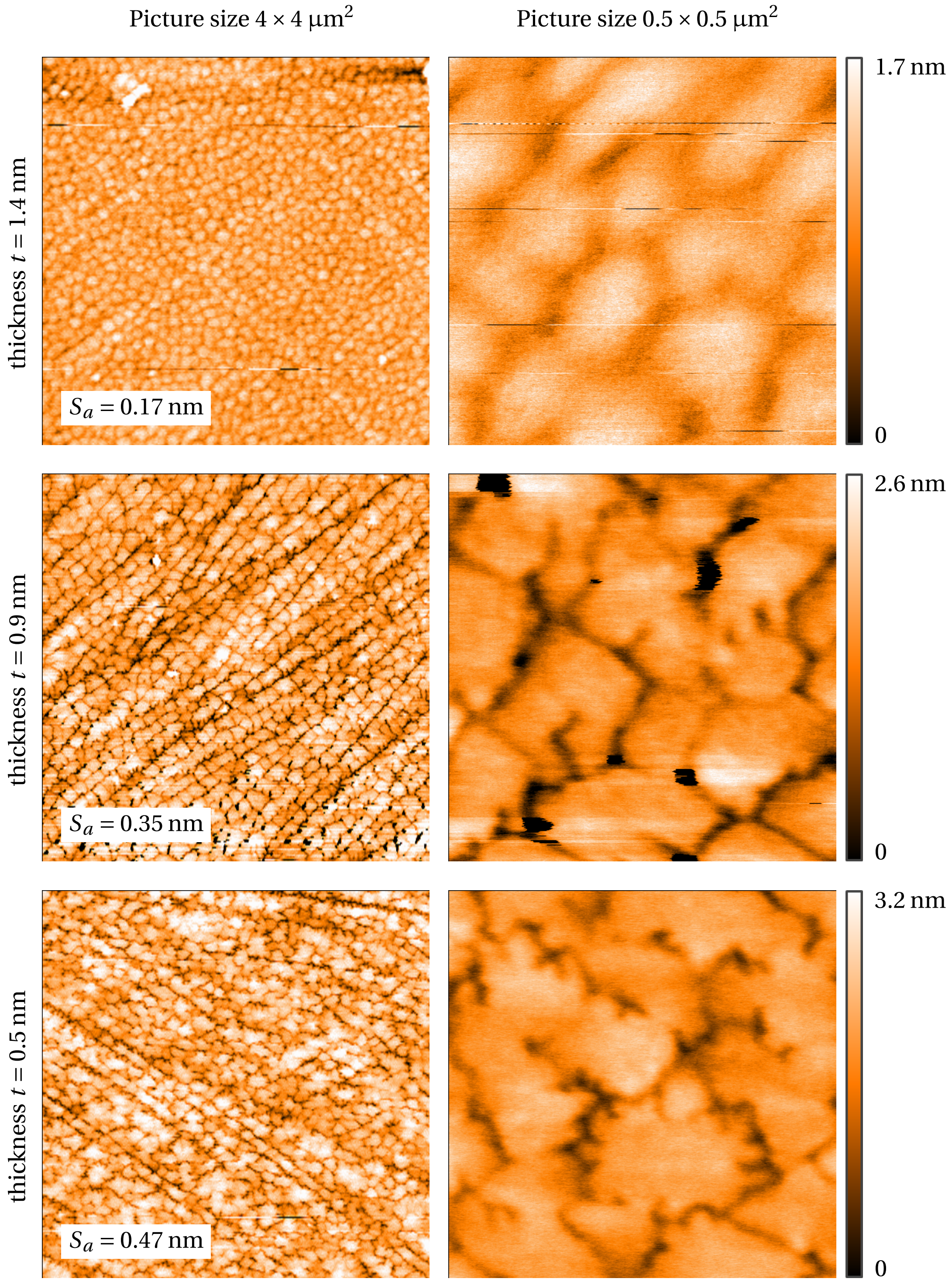

Figure 6.7: Si_3N_4 of different thicknesses deposited on TiN at 800 °C, roughness S_a is given as the averaged roughness of the particular sample. For details see text and figure 6.8. Note the different range scales.

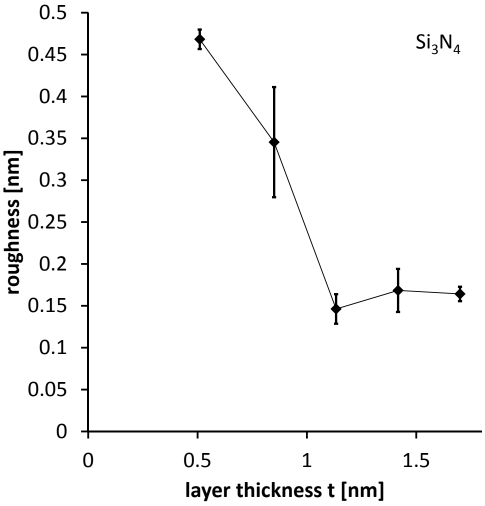

Figure 6.8: Roughness S_a of Si$_3$N$_4$ of different thicknesses t deposited on TiN (001).

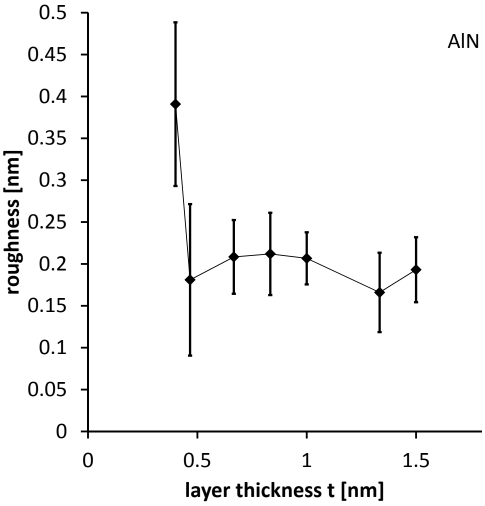

Figure 6.9: Roughness S_a of AlN of different thicknesses t deposited on TiN (001).

every second layer the Si$_3$N$_4$ layer thickness is increased by ≈ 0.3 nm. It is clearly seen that the sc-TiN continuesly grows epitaxially up to ≈ 0.6 nm thick Si$_3$N$_4$ interlayers. For thicker Si$_3$N$_4$ layers the TiN layers show grains with different orientations due to loss of coherence with the underlying Si$_3$N$_4$ layer. This is in agreement with the TEM studies reported by [188] who reported an epitaxial stabilization of cubic SiN$_x$ of up to ≈ 0.7 – 1.0 nm. The TEM picture shows further that the interface TiN/Si$_3$N$_4$ is atomically flat, which is essential for the following AR-XPS measurements.

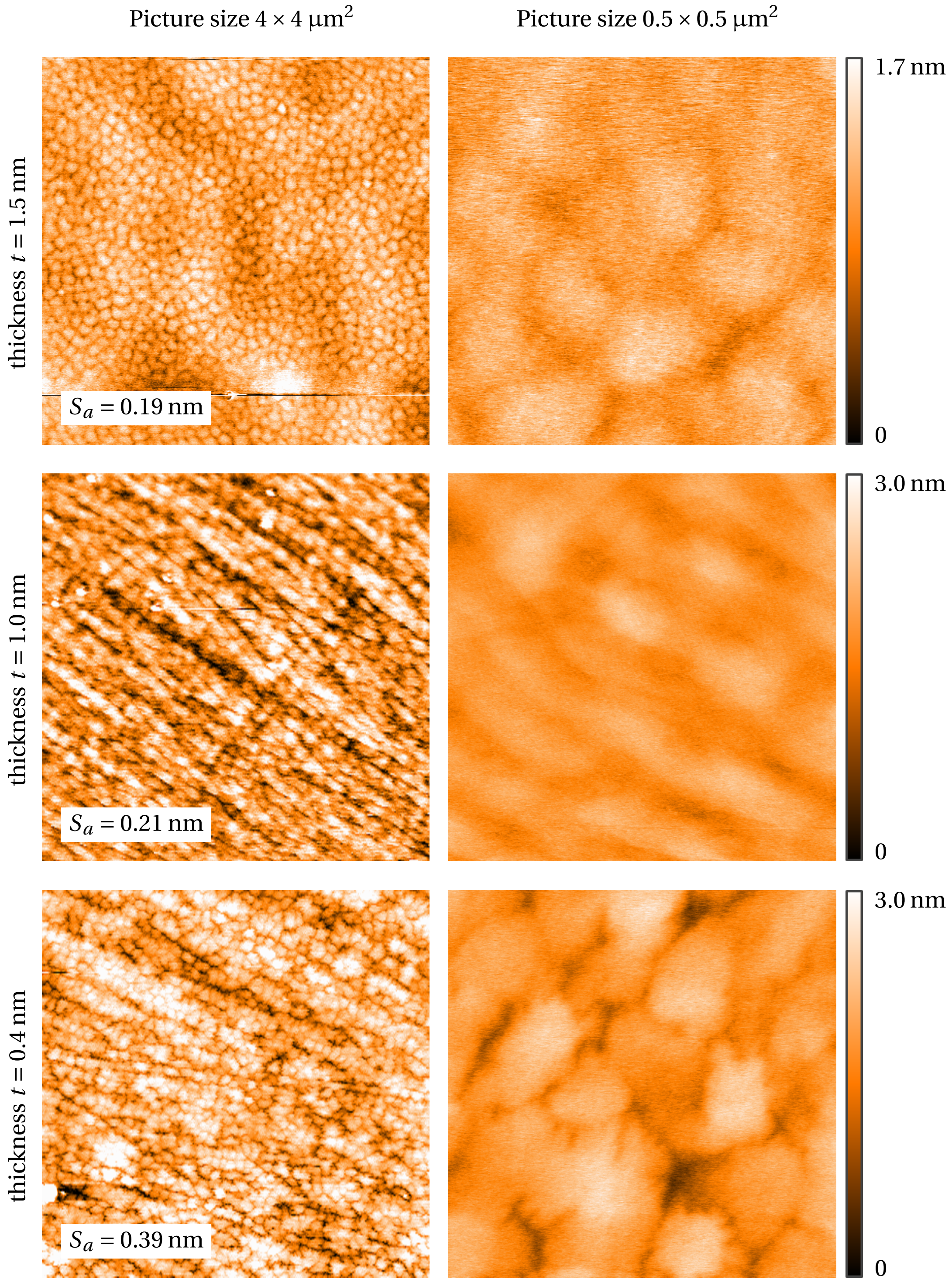

Figure 6.10: AlN of different thickness deposited on TiN at 800 °C, roughness S_a is given as the averaged roughness of the particular sample. For details see text and figure 6.9. Note the different range scales.

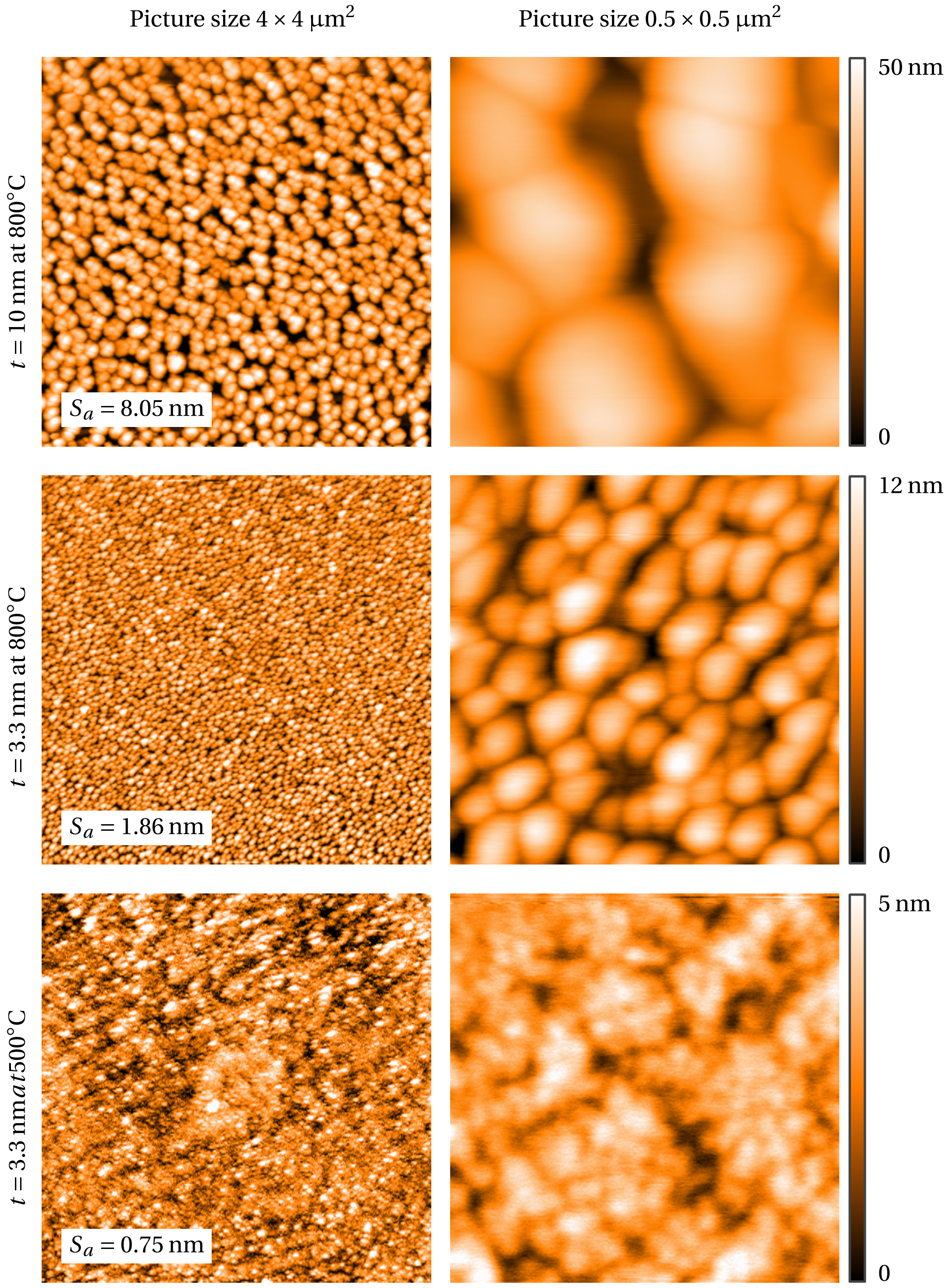

Figure 6.11: Si of different thickness deposited on TiN at 800 °C and at 500 °C, roughness S_a is given as the averaged roughness of the particular sample. For details see text and figure 6.12. Note the different range scales.

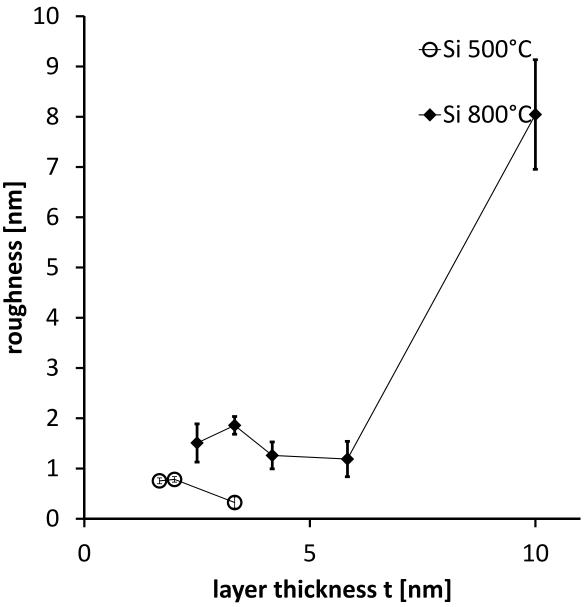

Figure 6.12: Roughness S_a of Si of different thickness t deposited on TiN (001) for two different deposition temperatures: 800 °C (diamonds) and 500 °C (circles).

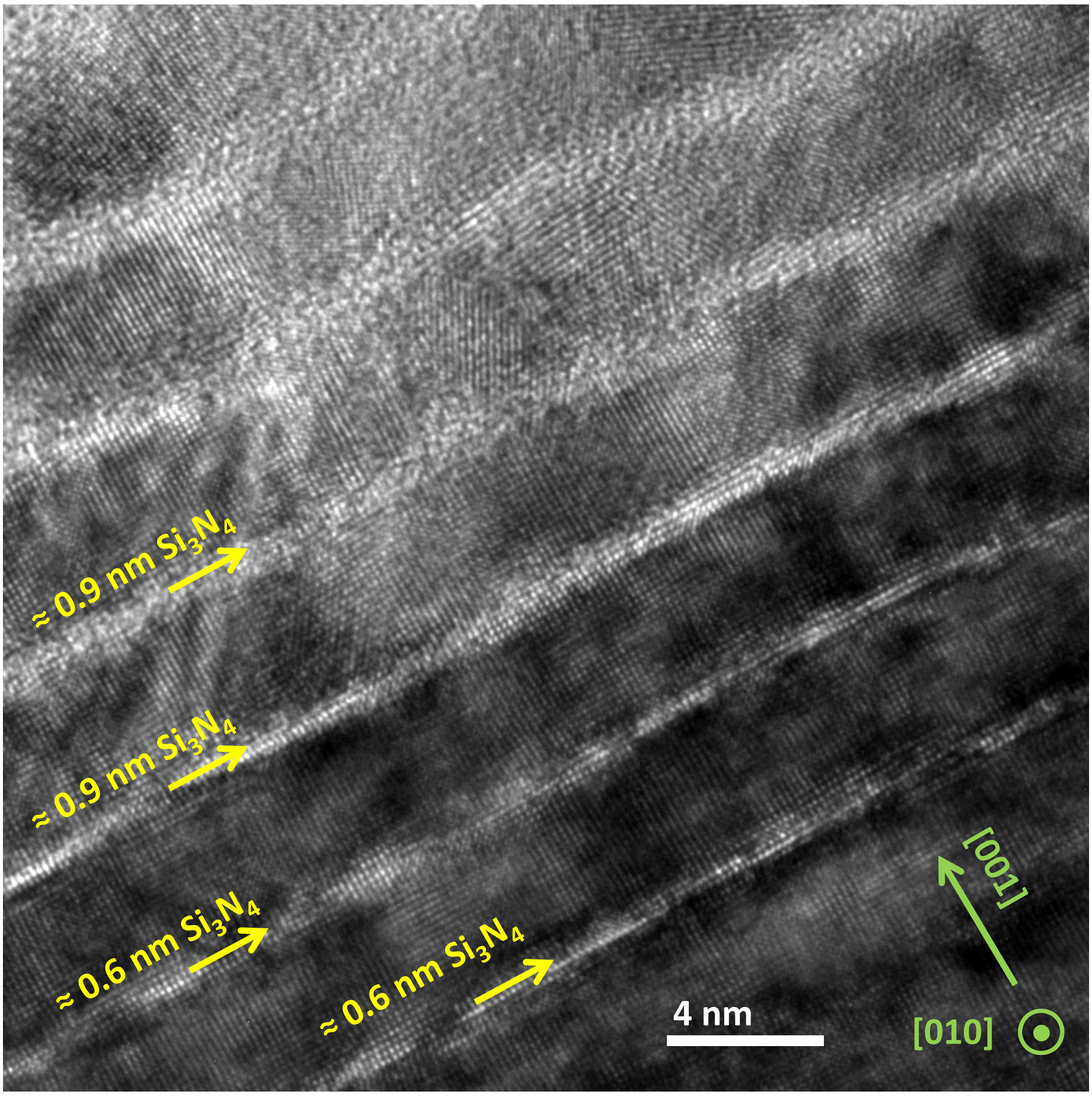

Figure 6.13: TEM image of a TiN/Si_3N_4 multilayer system, with a magnification of 600k.

7 XPS of pristine TiN

This chapter is the basis for the further evaluation of the bilayer systems(chapter 8). The shake-up of pristine TiN and its properties and dependences are required to resolve later an interface signal ratio r_i.

A quantitative evaluation of a XPS spectrum requires knowing the identity of all photoelectron (PE) peaks contributing to the total experimental spectrum ((sect. 7.1)). Additionally it is indispensable to properly reproduce the relative intensity, wherever it is dictated a priori by quantum mechanics, as e.g. in the case of multiplet splitting. Any fitting routine that does not appropriately reproduce such constraints, may lead to erroneous interpretations. The values of the peak intensities, as determined by fitting routines, are influenced by the choice of the background function, by overlapping peaks and also, in the case of single-crystalline materials, by photoelectron diffraction (XPD) effects. Therefore special care on the diffraction patterns, as explained in section 7.5 has to be taken before evaluating peak ratios.

All XPS spectra were recorded according to the description in 5.1. An overview spectrum is shown in 7.1. Each element contained in the sample, is represented by several photoelectron peak, which are discussed in the following section.

7.1 Binding energies of TiN

A XPS spectrum of stoichiometric TiN, recorded using monochromatic Al K_α radiation, is shown in figure 7.1: it contains the core level lines originating from Ti (Ti 2s, Ti 2p, Ti 3s, Ti 3p), those of N (N 1s) and surface contaminations of O (O 1s) as well as Auger transition lines from Ti and N and the Ti – N hybrid states close to the valence band. The Ti 2p peak (also see detailed spectra in fig. 7.5) shows a clear spin-orbit splitting of 5.74 ± 0.05 eV between Ti $2p_{3/2}$ and Ti $2p_{1/2}$. As mentioned above, an additional peak at lower kinetic energies is observed on the Ti 2p main peaks, called shake-up.

As described in section 5.1, no binding energy E_B reference peaks (e.g. C 1s or Ar 2p) were available; all binding energies are shown as measured. Several surface effects (e.g. surface

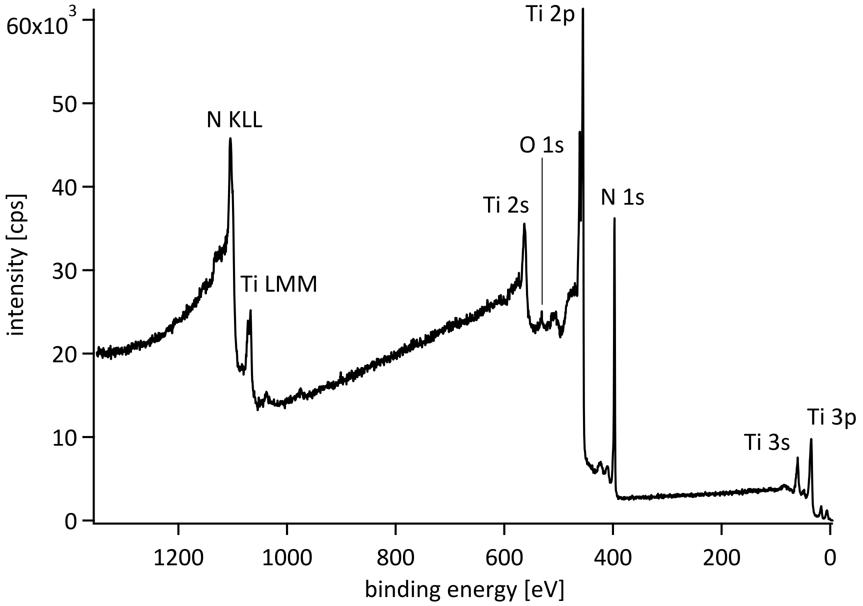

Figure 7.1: A full XPS spectrum of TiN containing Ti, N and a small amount of O.

charging or oxygen, see sect. 3.9) can cause a binding energy shift for different AOE. In the following the energy shifts due to oxygen, charging at the surface and instrumental influence are first studied for the case of polycrystalline (pc-)TiN. Additional shifts in the binding energy are resolved for sc-TiN samples, this is discussed in section 7.5.

A strong sample charging is not expected since the sample has been carefully grounded (sect. 4.4) and only a small energy shift of the spectra is observed (fig. 7.2). An instrumental influence on E_B is excluded, since the analyzer calibration is independent of the AOE[i] (Appendix D).

Fig. 7.2 shows how the binding energy E_B is influenced by the AOE, note values of $\Delta E_{B,oxy}$ and $\Delta E_{B,ch}$ are plotted in the right axis. The noise in a single angle-resolved scan (with 36 different angles) is quite high. Averaging over six angel resolved measurements resolves that E_B is affected by the AOE. An empirical function f_{EB}[ii] is chosen to fit the data (yellow line in fig. 7.2). The function contains an exponential decaying (black dotted line) and an exponential increasing function (black dashed line) to describe the influence of surface effects.

Oxygen is accumulated at the surface and results in an increase of $\Delta E_{B,oxy}$ =0.5 eV for high angles of emission, i.e. for information stemming from PE emitted close to the surface. The increase of $\Delta E_{B,oxy}$ is ascribed to surface oxides forming TiO_xN_{1-x}. Binding energies for TiO_xN_{1-x} between 455.4 eV [330] and 456.8 eV [309] were reported; they overlap with the shake-up and the main peak. The TiO_xN_{1-x} contribution has not been resolved due to the low

---

[i] Reference measurements on gold show an decrease from 0° to 70° of 0.05 eV and the standard deviation for the gold peak is 0.03 eV for an energy resolution of 0.125 eV.

[ii] $f_{EB} = E_0 + A\exp(\cos\Theta/a) + B\exp(-\cos\Theta/b)$; Θ = AOE, the parameters E_0, A, a, B and b have no direct physical meaning.

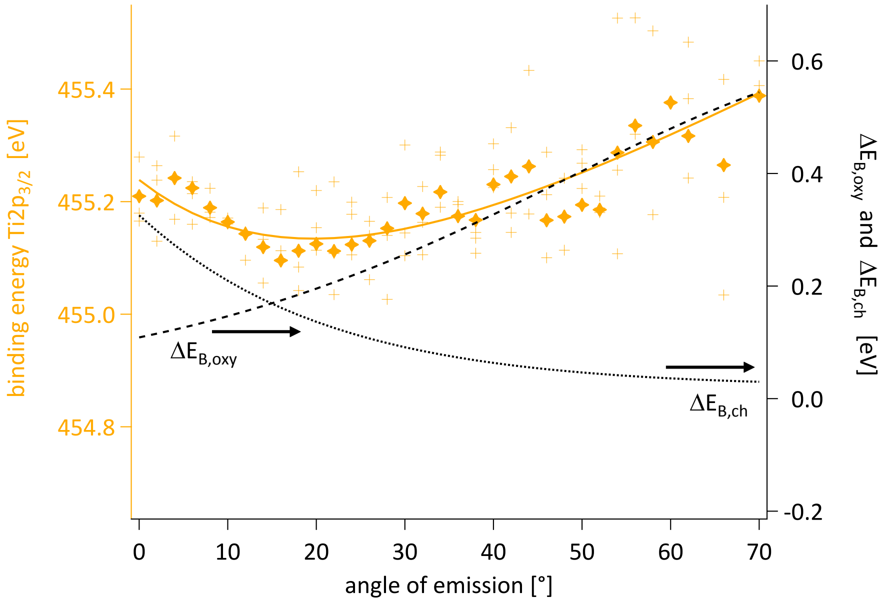

Figure 7.2: Binding energy for Ti $2p_{3/2}$ of polycrystalline TiN at different angles. Shown are six measurements (crosses) for each AOE, the averaged values (bold crosses) and two fit function describing the increase of E_B due to oxygen contaminations (black long dashed line) and due to surfaces effects (black small dashed line). See text for details.

oxygen content. This oxidized component of TiN was not subtracted from the spectra, which resulted in a small shift in the binding energy of the main TiN peak line.

Surface charging results in a decay of $\Delta E_{B,ch} = -0.3$ eV in the binding energy with increasing AOE. Johansson et al. [403] calculated a binding energy shift of −0.07 eV for Ti 2p and N 1s between surface Ti 2p atoms and bulk atoms due to a lower coordination of the atoms at the surface. The remaining decrease in E_B is assigned to a slightly negatively charged surface. All surface effects are hidden in the E_B signals. Increasing ($\Delta E_{B,oxy}$) and decreasing components ($\Delta E_{B,ch}$) influence each other, i.e. if the fit function describing $\Delta E_{B,oxy}$ is increased artificially then $\Delta E_{B,oxy}$ is decreased manually. Hence the obtained value are guidance value and cannot be considered as absolute.

More experimental support for charging and different surface termination is gained by analyzing the energy difference $\Delta E(\text{Ti } 2p_{3/2}, \text{N } 1s)$ between Ti $2p_{3/2}$ and N 1s core levels (see fig. 7.3). $\Delta E(\text{Ti } 2p_{3/2}, \text{N } 1s)$ reveals that for bulk sensitive angles (low AOE) both binding energies were shifting similarly. This indicates that the effect described by $\Delta E_{B,ch}$ is either due to sample charging and/or a different surface coordination.

The shifts are systematic and can therefore be either extrapolated or subtracted from the data. Surface and interface charging in bilayer systems are further revealed in section 8.4. The binding energy E_B is hardly influenced for AOE of 0°, surface charging, surface termination and oxygen effects are minimal at 0°. No energy referencing (e.g. to C 1s) is possible and

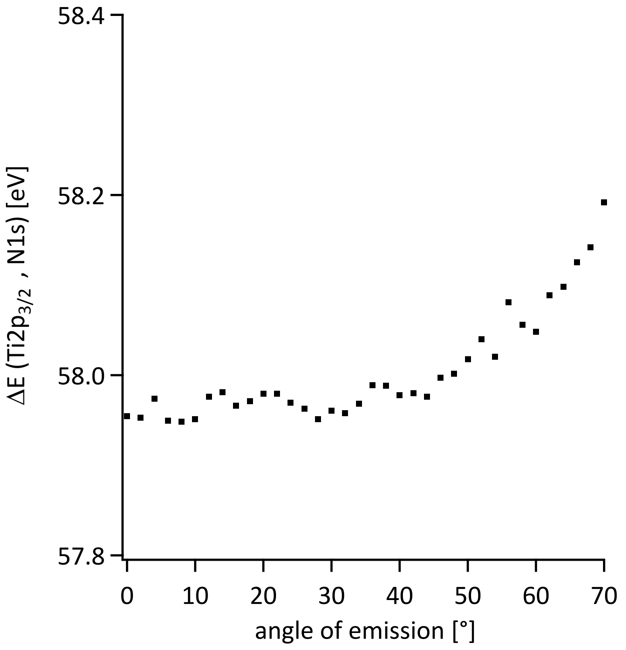

Figure 7.3: Binding energy difference ΔE(Ti $2p_{3/2}$, N 1s) between Ti $2p_{3/2}$ and N 1s averaged over three angle-resolved measurements, for angles below 45 degree no increase in ΔE is observed.

therefore the binding energy has been corrected by the oxygen offset $\Delta E_{B,oxy}$ at an AOE of 0° for all bulk E_B values in TiN as shown in table 7.1.

All analyzed sc-TiN(001) samples have a binding energy for Ti $2p_{3/2}$ of $E_B = 455.1 \pm 0.1$ eV. As a comparison to the above described angle-dependent treatment the binding energy for Ti $2p_{3/2}$ was plotted versus the oxygen concentration and extrapolated to a zero oxygen content binding energy (see fig. 7.4). In this way 455.0 ± 0.1 eV was obtained for the binding energy for the Ti $2p_{3/2}$ of oxygen-free TiN. A low oxygen concentration is mainly measured for low AOE and as a result both methods (E_B vs. AOE or E_B vs. c_{oxy}) are tantamount. For lower oxygen concentrations a smaller scattering of the binding energy data was found than for higher oxygen concentrations; the latter were measured mainly for high AOE and showed this deviation due to generally low intensities for those angles.

Table 7.1 summarizes all binding energies E_B for pure TiN(001) samples and all bilayer systems under investigation. The uncertainty shown in table 7.1 has been calculated using the standard deviation of the binding energies of four similarly fabricated TiN (001) samples. Within each measurement the error is higher, but was decreased by the above described fitting routine. The peak criteria as described in section 5.2 were applied. The shake-up and plasmon lines are very broad. The shake-up is an energy loss process, which is not from one single localized state to another, but rather a multitude of different excited states. Hence the shake-up is not one E_B peak but a convolution of many smaller peaks that cannot be resolved, this appears in the spectra as one broad energy line. Plasmon peaks are caused by exciting valence electrons into oscillating states with certain frequencies, there is also not one single frequency mode in which the excitation can occur. The convolution of frequencies results also in a peak broadening. For bilayer systems consisting of an overlayer on top of TiN the oxygen components (O-Ti and

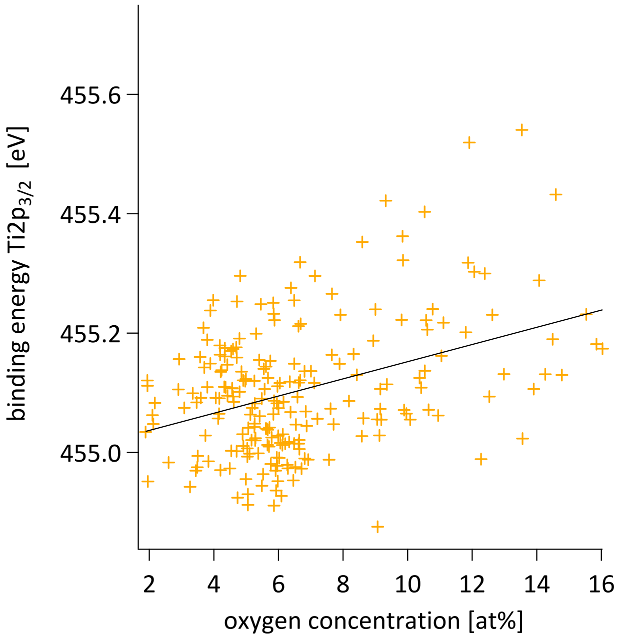

Figure 7.4: Binding energy of Ti 2p$_{3/2}$ versus the oxygen concentration for a sc-TiN sample measured several times at different angles of emission. An increase in the binding energy with the oxygen content (as measured by XPS) is observed.

O-N) are not resolved due to a low oxygen concentration, this results in broad oxygen energy lines.

There is also a binding energy shift with AOE in bilayer systems and this shift dependence additionally on the overlayer thickness *t*. A detailed analysis of this interface effect is found in section 8.4.

7.2 Ti 2p components in TiN

The binding energy E_B of Ti 2p$_{3/2}$ has been analyzed in detail in the previous section, in this section deals with the other components of the Ti 2p spectra as well as its background BG. For TiN the spin-orbit splitting energy between Ti 2p$_{3/2}$ and Ti 2p$_{1/2}$ is found at 5.83 ± 0.09 eV; the shake-up energy amounts to 2.16 ± 0.04 eV for the 3/2 shake-up. Both values were obtained by averaging over all measurements and are in agreement with literature data, where values between 5.5 eV and 5.9 eV for the spin orbit splitting and 2.3 eV to 2.8 eV for the shake-up are reported [327, 328, 330, 404]. If the oxygen concentration is high enough then the shake-up lines in TiN can be well separated from any TiO_xN_{1-x} contributions, which have a binding energy of about 3 eV above the Ti 2p states [358]. X-ray satellites (e.g. K_β) and ghost lines (X-ray lines stemming from contamination anode elements) can be ruled out as explanations for this contribution, since they would appear also in all XPS lines for all elements, which is not the case (see fig. 7.5, 7.7, 7.8 and 7.9). The shake-up feature is not correlated to a surface or bulk plasmon. The energy difference $\Delta E_{3/2}$ (and $\Delta E_{1/2}$) between the main Ti 2p$_{3/2}$ (and Ti 2p$_{1/2}$) peak and the shake-up depends on the electron total momentum *j*, for the two spin-orbit split states a shake-up energy of $\Delta E_{3/2} = 2.16 \pm 0.04$ eV and of $\Delta E_{1/2} = 1.78 \pm 0.07$ eV are measured

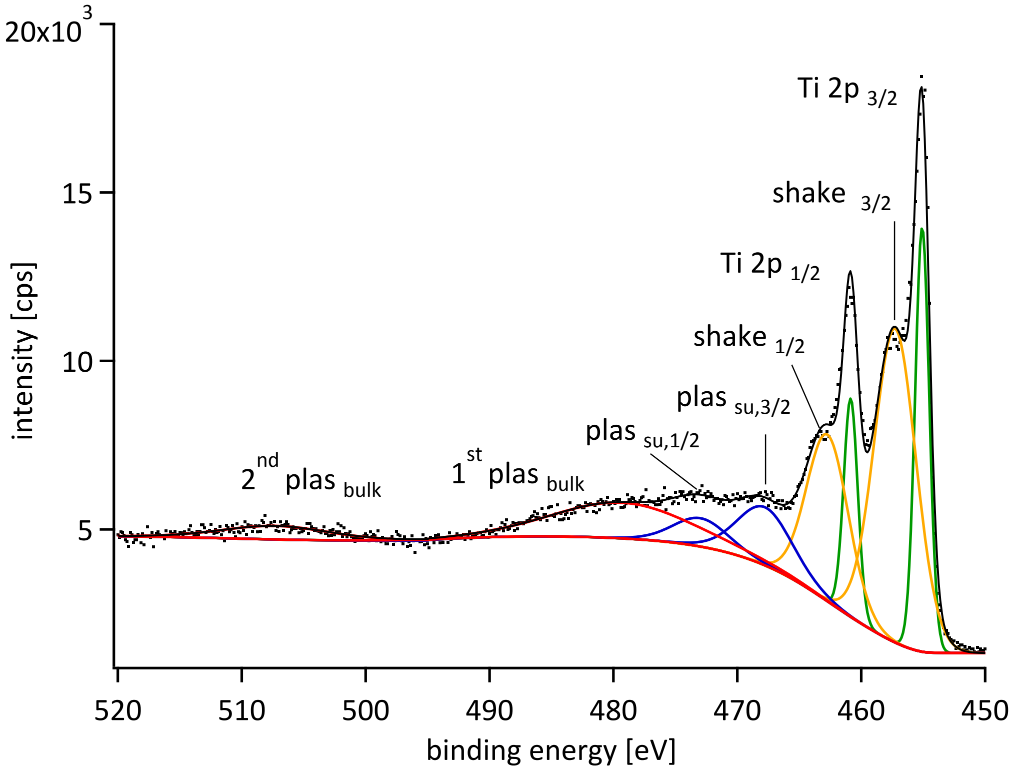

Figure 7.5: Detailed Ti 2p spectrum for TiN. A Tougaard BG subtraction is used and eight peaks (see text) are identified and quantitatively evaluated in consideration of boundary conditions. Constraints are described as in the text.

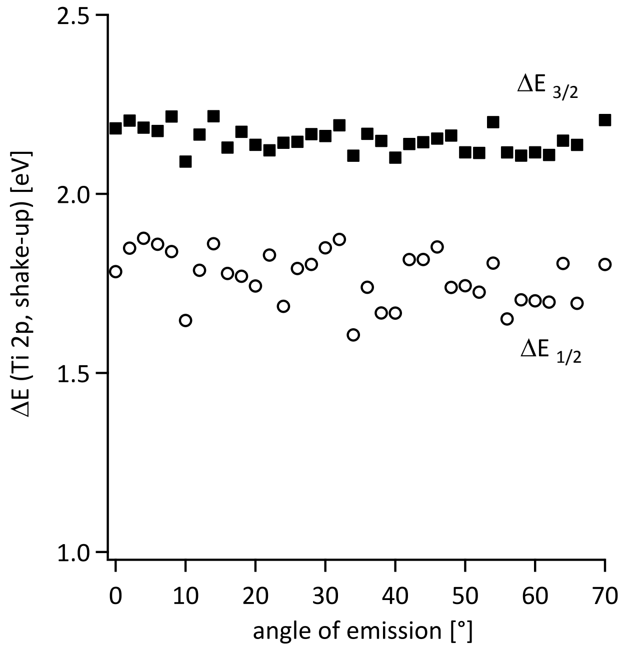

Figure 7.6: The shake-up energy depends on the spin-orbital splitting. For $\Delta E_{3/2}$ the shake-up energy is bigger and the fluctuations are lower than for $\Delta E_{1/2}$.

(see fig. 7.6). These values are constant for all angles indicating that ΔE is not influenced by surface or bulk properties, as for example by surface oxygen or surface plasmons. For $\Delta E_{1/2}$ the variance of the data points is larger than for $\Delta E_{3/2}$, since the shake-up$_{1/2}$ is strongly influenced by the surface plasmons that overlap in that energy area. The origin of this energy difference between $\Delta E_{3/2}$ and $\Delta E_{1/2}$ is discussed in detail below in section 7.8.

7.2.1 Surface and bulk plasmons

Besides the two main peaks and the two shake-up peaks, additional four peaks are visible after the spectral fitting procedure (sect. 5.2 and fig. 7.5). These peaks are caused by an interaction of surface and bulk plasmons with the emitted electrons. The two plasmon peaks at 467.51 ± 0.02 eV and 474.02 ± 0.14 eV showed an increased intensity with higher angle of emission (fig. 7.10), i.e. they are due to a surface phenomenon and are therefore interpreted as surface plasmons. They are separated by 6.51 ± 0.15 eV, which is similar to the spin-orbit splitting of the main Ti $2p_{3/2}$ and Ti $2p_{1/2}$ peaks. The splitting is not exactly the same as the spin orbit splitting of Ti 2p, but considering the fact that surface plasmon peaks are broad (FWHM=7.3 ± 1.4), this agreement seems satisfactory. The large width of the surface plasmon peaks is a result of each plasmon peak containing the main core level and the shake-up line; they are further strongly influenced by the even broader bulk plasmon peak (see below) due to overlapping. The energy loss due to surface plasmons between the center of mass of the Ti $2p_{3/2}$ main peak was 11.6 ± 0.7 eV. The same energy loss was observed for the Ti $2p_{1/2}$ components as well as for the shake-up peaks. This is exactly the same value of energy loss that was also observed for the Ti 2s core shells due to surface plasmons (see 7.8). Second order surface plasmons are not observed, as their intensity is too small, and their position overlaps

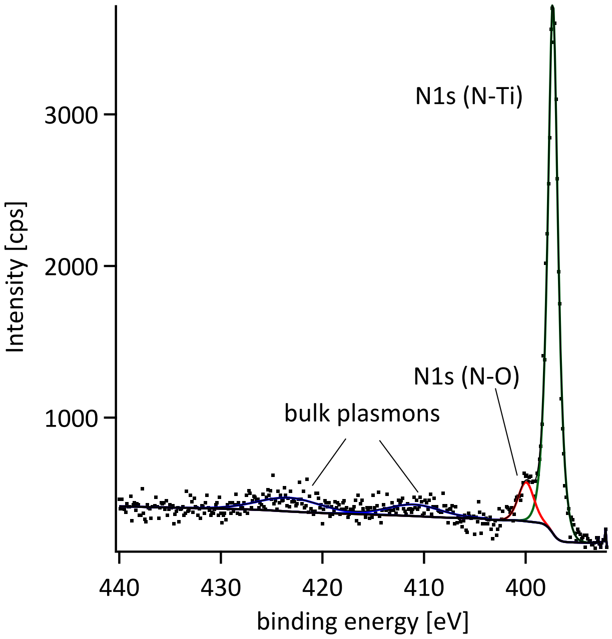

Figure 7.7: XPS spectrum of N 1s, from right to left: N 1s main peak, originating from N – Ti bonds and a minor N 1s peak from N – O bonds and two weak bulk plasmons.

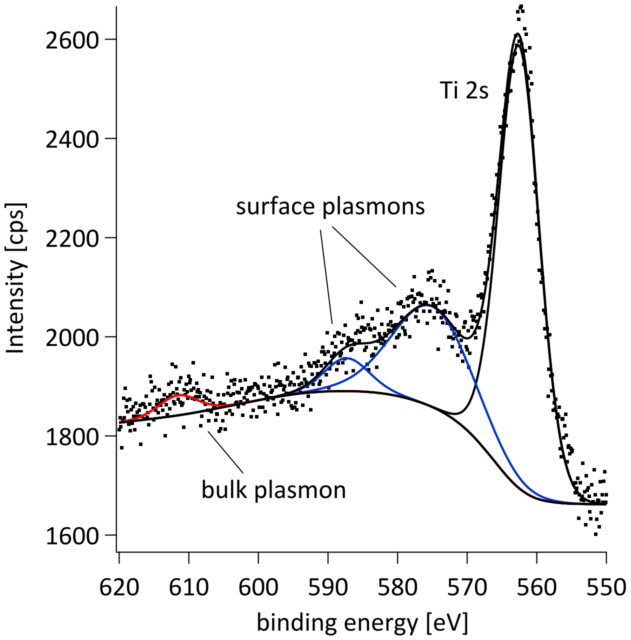

Figure 7.8: Ti 2s photoelectron lines, from right to left: Ti 2s main line, first order surface and first and second order bulk plasmon.

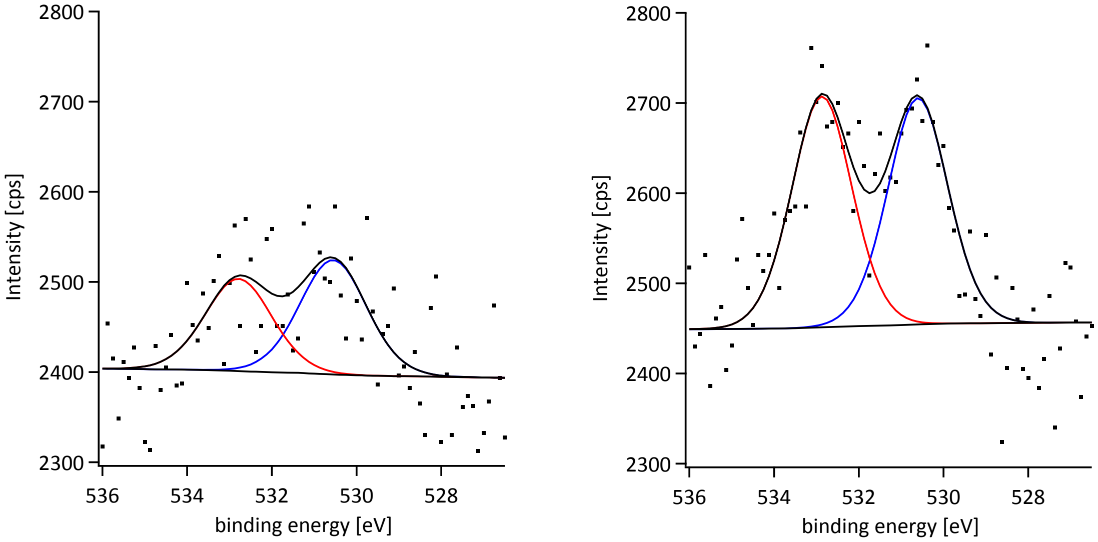

Figure 7.9: O 1s, the oxygen signal at an angle of emission of 20° after 2 hours (left) and after approximately 16 hours of measuring (right)

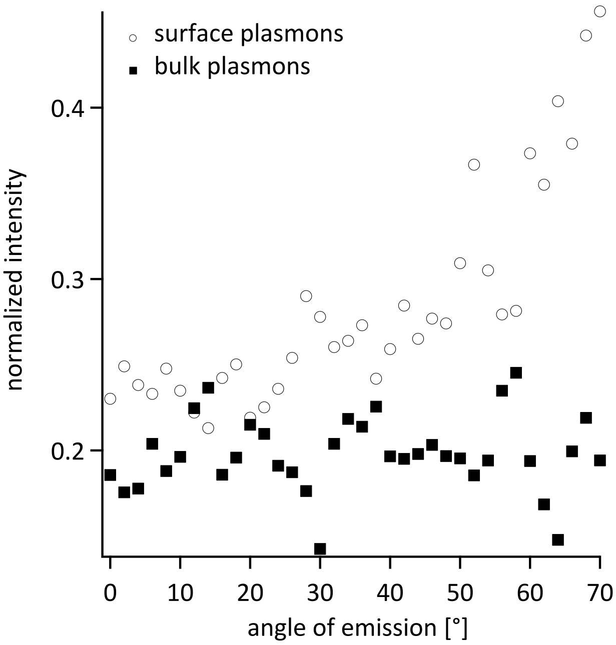

Figure 7.10: The intensity of the surface plasmons (circles) and of the bulk plasmons (squares) are shown for different angles of emission. The intensities of the two surface plasmons originating from the 3/2 and 1/2 components are summed up, the same accounts for the first and second order bulk plasmons. The surface and bulk plasmon intensities are further normalized. The intensity for the surface plasmon increases while that of the bulk plasmon stays constant over the entire range.

with the broad first bulk plasmon at 481.51 ± 0.76 eV. The first bulk plasmon is very broad (FWHM=10.5 eV) due to the fact that it contains all four peaks from the Ti 2p spectra (Ti $2p_{3/2}$, Ti $2p_{1/2}$ and their two shake-ups). The energy difference between the center of mass of the four major peaks at 458.2 ± 0.1 eV and the first and second bulk plasmon are 22.9 ± 0.4 eV and 49 ± 0.2 eV. The energy loss due to the second bulk plasmon is approximately twice that of the first bulk plasmon loss, indicating that it is a second order plasmon. This is in good agreement with the results for the first bulk plasmon reported in Strydom and Hofmann [361] (22.6 eV), and is a bit lower than in Soto [405] (24.7 eV). Further loss peaks, as described in [361] due to electron transition from N 2p to Ti 3d or Ti 4s, are not observed. Also for the low intensity Ti 2s peak at 562.5 ± 0.2 eV the plasmon peaks were observed with a kinetic energy lowered by 11.7 ± 0.3 eV, 26.2 ± 0.1 eV and 49.3 ± 0.2 eV. Those values correspond to first order surface and first and second order bulk plasmons (see 7.8). After the correct background correction the plasmon loss features can be clearly separated from the main peak and the shake-ups, despite the width of the plasmon loss features.

7.2.2 Nitrogen N 1s

The binding energies of the N 1s core level electrons in TiN originating from N bonded to Ti have been reported to lie between 396.6 eV to 397.4 eV; the values for N bonded to O rang from 395.8 eV to 402.5 eV [328, 358, 406, 407]; also other interpretations of additional peaks are given in literature [327, 369, 408]. A shoulder, causing an asymmetric peak shape, has been observed in the N 1s core level peak in TiN and other transition metal nitrides. Instead of using an asymmetric peak shape as reported in [328], a GL(80) line shape (see section 5.2.2) was used for the main peak and a second peak with GL(30) was fitted [12]. This allows the separation of the N – O contribution, which is masked when using a tail function. The main peak of N 1s, shown in fig. 7.7 has a binding energy of 397.08 ± 0.03 eV; it is accompanied by a smaller contribution with an approximately five to eight times lower intensity at 399.45 ± 0.12 eV (averaged over all samples). The main nitrogen peak is assumed to stem from N bonded to Ti and the second (smaller) peak is assigned to N bonded to O. Esaka et al. [409] resolved in TiN three energy lines for N 1s at 402.0 eV, 397.8 eV and 396.6 eV and correlated them to the three oxidation states N^{3-}, N^{2-} and N^{1-}. With increasing oxygen concentration the N^{3-}component increases and N^{1-} shifts to higher binding energies. Milošev [328] found also two N – O bond peaks at 400 eV and 396 eV and observed an increase of the intensity ratio $I(N-O_{400eV})/I(N^{3-})$ at lower AOE. Due to the low oxygen concentration it was not possible to identify the two N^{3-} and N^{2-} energy lines, and also no increase in the intensity ratio $I(N-O_{400eV})/I(N^{3-})$ could be observed. For low angles of emission the energy difference ΔE(Ti $2p_{3/2}$, N 1s) between titanium Ti $2p_{3/2}$ and nitrogen N 1s is 57.95 ± 0.03 eV (fig. 7.3). This is in agreement with Porte et al. [310], who reported approximately 58.3 eV for ΔE(Ti 2p,N 1s) in stoichiometric TiN and interpreted the increase with increasing nitrogen content as an enhanced charge transfer from Ti to N. A slight increase in ΔE(Ti $2p_{3/2}$, N 1s) by 0.2 eV for high angles of emission is due to surface oxygen, as shown in 7.3. Ti is less electronegative than N and hence the oxidized binding energy of Ti 2p shifts stronger than E_B of N 1s. This results in an increase in the energy

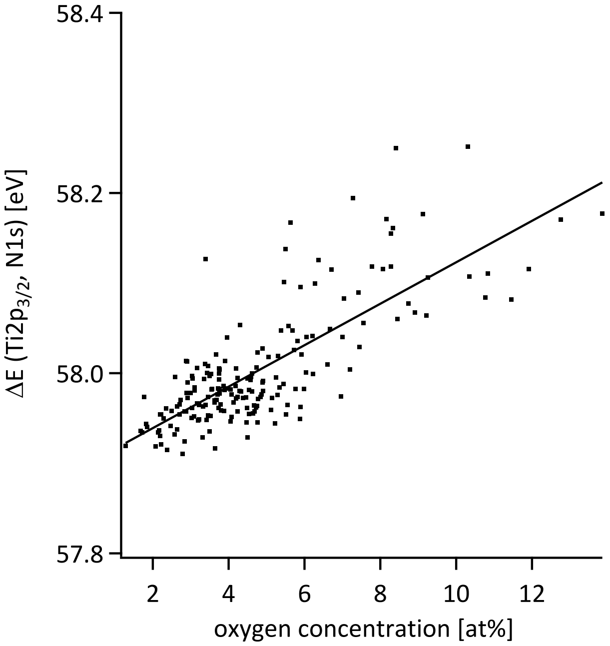

Figure 7.11: Binding energy difference ΔE(Ti $2p_{3/2}$, N 1s) between Ti $2p_{3/2}$ and N 1s; the increase in the binding energy difference is correlated to the oxygen content. Data obtained from one sample for several runs with different angles.

difference ΔE(Ti $2p_{3/2}$, N 1s) with increasing oxygen concentration. Saha and Tompkins [369] reported a shift in the N-Ti line from 395.7 eV to 397.1 eV, if TiN is oxidized. In this thesis the binding energy shift for the oxidized N-O states of the N 1s peak cannot be resolved, due to the low oxygen content in the fabricated samples.

For N 1s two plasmon peaks are observed at 12.8 ± 0.2 eV and at 26.0 ± 0.5 eV, see figure 7.7. Their energy loss is similar to that of the first order surface and bulk plasmon peaks of Ti 2p and Ti 2s, although the nitrogen plasmon peak intensity is much lower than of that from titanium.

7.2.3 Oxygen O 1s

The O 1s spectrum (given in fig. 7.9) consists of two peak components assigned to O – Ti at 530.80 ± 0.07 eV and to O – N at 532.99 ± 0.27 eV [350]. Here the binding energy is obtained by averaging over all measurements of all angles, the error is given by the standard deviation. In figure 7.12 the average for all 235 measurements with different angles of one sample is shown to illustrate the effect of averaging on the else very noisy measurements. Both components have about the same intensity, indicating that oxygen is bonded to equal parts to titanium and to nitrogen. The amount of oxygen at the surface and in the bulk material is small (below $0.2 at\%$ in the bulk), therefore the signal to noise ratio is over all angles low. In order to have a consistent peak fitting for such low intensity signals, the same FWHM for both O 1s peaks had

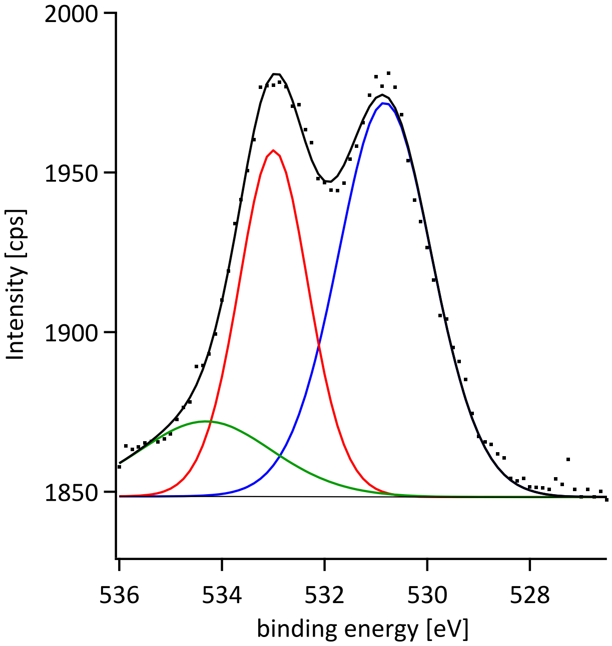

Figure 7.12: Averaged O 1s spectra of one sample for 235 measurements at different angles.

to be used. During the XPS measurements their intensities increased slowly (sect. 7.7). Due to the low intensity no binding energy shift depending on the angle can be resolved, and no interpolation to an AOE of 0° is performed: instead the binding energies are averaged over all angles and samples (fig. 7.12). A third peak can be identified, if the statistical quality is enhanced by averaging over more than 200 angle-resolved measurements. This photo line has a binding energy of 534.3 ± 0.5 eV, its intensity is $\approx 1at\%$, the interpretation of this peak is for such low intensities pure speculation and not in the scope of this study.

7.2.4 Valence band

The low binding energy spectrum, including the valence band region, is shown in fig. 7.13. About 16 eV below the Fermi level the N 2s states are observed, similar to Porte et al. [310] who reported 16.6 eV. The hybridized N 2p - Ti 3d states are found at 6 eV below the Fermi level and show a lower intensity compared to those reported by Porte, which is attributed to the lower oxygen concentration in the TiN deposited in this work. This band contains the covalent Ti – N bonds, which are considered the reason for the high mechanical hardness [410] and the high melting point of TiN [411]. The drop in the DOS towards lower binding energy between 6 eV and 11 eV is due to a complete hybridization of the N 2p and Ti 3d states. Around the Fermi level Ti $3d^1$ states contain delocalized electrons and give the material its relative high electrical conductivity [328].

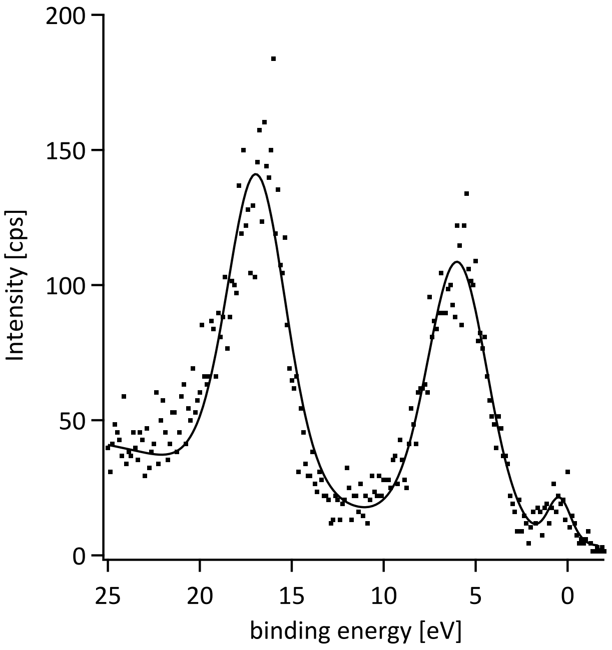

Figure 7.13: Valence band region of titanium nitride. The electronic states at the Fermi level originate from Ti 3d, at around 6 eV hybridized N 2p-Ti 3d states are found, and at around 16 eV N 2s states are present.

7.3 Background corrections

In section 3.7 the rising of a background (BG) has been explained and different BG types have been presented. In this section the advantages of the Universal Two-parameter Tougaard background (U2T) are elucidated and discussed.

Figure 3.6 present the Ti 2p spectra with a linear or a Shirley BG subtraction respectively. In both cases the BG limits were set to 451 – 466.5 eV. The onset of the linear BG at around 451 eV shows that the BG is higher than the measured count rate, which is not physical. Considering that this cut-off is part of the peak integral results in a big error for the integrated peak area. Also the shake – up$_{1/2}$ and Ti 2p$_{1/2}$ fits are overestimated, while the 3/2 components are underestimated. The Shirley BG gives the correct onset, but the 1/2 and 3/2 components are even more over- and underestimated respectively. Additionally the peak positions are shifted and do not represent the measured data. It is concluded that neither the linear nor the Shirley BG do fulfill the quantum mechanical requirements, which should yield area ratios for Ti 2p$_{1/2}$ and Ti 2p$_{3/2}$ of 0.515, as given by the Scofield's cross-sections [342]. A wrong set BG results also in a falsified binding energy. The fitted E_B for non-distinct peaks is slightly changed for different BGs, e.g. using a Shirley BG results in a energy difference in $\Delta E_{3/2}$ = 1.95 eV while a U2T BG gives $\Delta E_{3/2}$ = 2.16 eV (sect. 8.6.1).

An advanced technique to calculate the background functions was developed by Tougaard et al. [317, 333]. Applying the Tougaard BG to the Ti 2p spectrum (fig. 7.5) results in the correct Scofield ratio for all 1/2 and 3/2 components, even without setting them to a fixed value in the fitting parameters (see table 7.1). Additional peaks are revealed that are diminished by the linear or Shirley BG. Those peaks will be discussed later, first we focus on the background

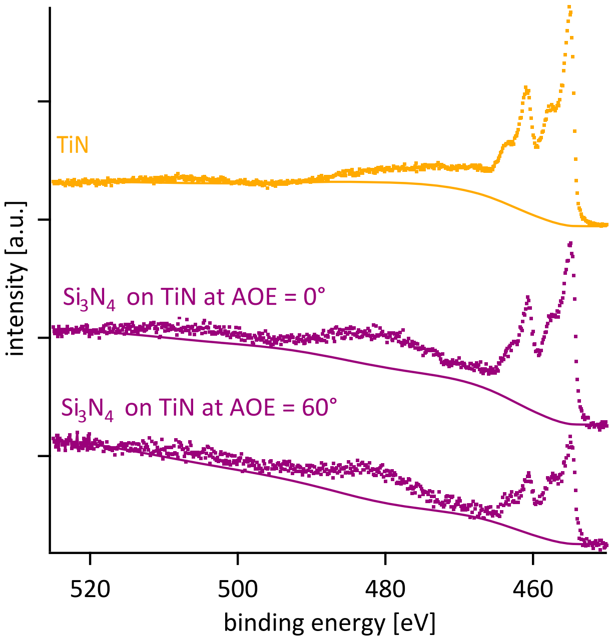

Figure 7.14: Intensity spectra of pure TiN and a TiN/Si_3N_4 bilayer system with 1.6 nm of Si_3N_4 .

description.

In the universal two-parameter Tougaard (U2T) BG (sect. 3.7), two parameters B and C for the inclination and the curvature of the BG are used; typically: $B = 681.2\,\mathrm{eV}^2$ and $C = 355.0\,\mathrm{eV}^2$ [332].

In figure 7.14 the results for pure TiN at an angle of emission of 0° and for TiN covered with 1.6 nm Si_3N_4 for AOE of 0° and 60° are plotted. The spectral intensity does not change for binding energies higher than 50 eV above the Ti $2p_{3/2}$ energy line. Under the same angle a Si_3N_4-covered TiN sample shows a higher increase in the BG than an uncovered TiN sample. The emitted Ti 2p electrons undergo more inelastic scattering while traveling through the Si_3N_4. This inelastic interaction causes a decrease in the kinetic energy of the PE and hence in an increase in the BG. For higher AOE the traveling length, the amount of inelastic scattering events and the BG increase. Therefore the factor B has been allowed to adjust the BG to the limits on the high BE side of the selected peak region, while the curvature given by C is chosen to be fix to $C = 355.0\,\mathrm{eV}^2$.

In single crystalline materials the intensity of elastic scattering events are enhanced in the crystallographic principal directions, and therefore the intensity shows a clear angle-dependent behavior. This phenomenon is called elastic forward scattering and results in the so-called X-ray Photoelectron Diffraction (XPD, see sect. 7.5). Along certain crystallographic directions high energy electrons undergo forward focusing, i.e. less inelastic and more elastic scattering occurs. This is not only seen in the intensity (fig. 7.17) that shows a clear angle dependence, but also in the BG parameter B (see fig. 7.15). For pristine sc-TiN clear diffraction patterns are observed in B. The averaged value for B in TiN is $657.1 \pm 19.9\,\mathrm{eV}^2$ in accordance with literature

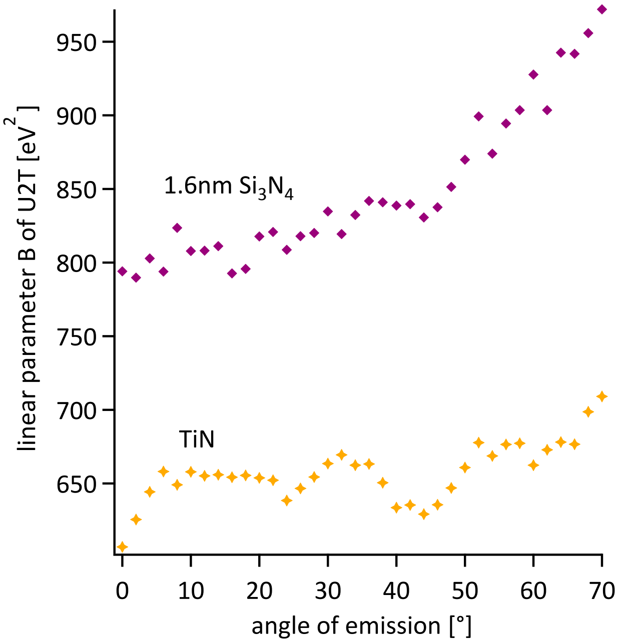

Figure 7.15: The BG parameter B reveals fluctuations that can be clearly correlated to XPD. Shown are B for pure TiN (cross) and TiN covered with 1.6nm thick Si_3N_4 overlayer (diamonds).

[332]. On the other side, for Si_3N_4 overlayers the diffraction patterns are strongly reduced, and the overall BG increases from $B = 800$ eV^2 to over $B = 950$ eV^2 from low AOE to high AOE.

7.4 TiN line shape

The exact line shape asymmetry of any given material cannot be calculated analytically; therefore the line shape of Ti 2p$_{3/2}$ and Ti 2p$_{1/2}$ in TiN is estimated by a reasonable modification of the line shape in pure Ti, which is considered below. All other elements have been analyzed using the line shapes given in 5.1.

Metallic titanium line shape The line shape of a XPS peak is strongly influenced by the valence band density of states. Typically metals show an asymmetric contribution at high binding energy, while insulators show symmetric line shapes [315, 412]. Figure 7.16 shows the spectrum of a sputter-cleaned oxygenfree Ti target. As discussed above a U2T BG has been subtracted, and three energies lines have been fitted: Ti 2p$_{3/2}$, Ti 2p$_{1/2}$ and a broad plasmon (compare to [280]). The latter is most likely not a single plasmon, but rather contains all kind of extrinsic losses (e.g. several surface and bulk plasmons). The line shape of the metallic Ti 2p peaks has been adjusted by the Chi square refinement, a shape described by a standard Gaussian-Lorentzian product [315, 316] combined with a tail T has been determined (sect. 3.6). For pure titanium the optimal peak shape of GL(20) T(0.65) has been found. The author is aware that the residual could be even further decreased by separating all components of the plasmon peak in their origin. For this purpose further measurements, e.g. High Kinetic Energy XPS (HIKE) would be required. The exact shape of the titanium peak is not within the scope of

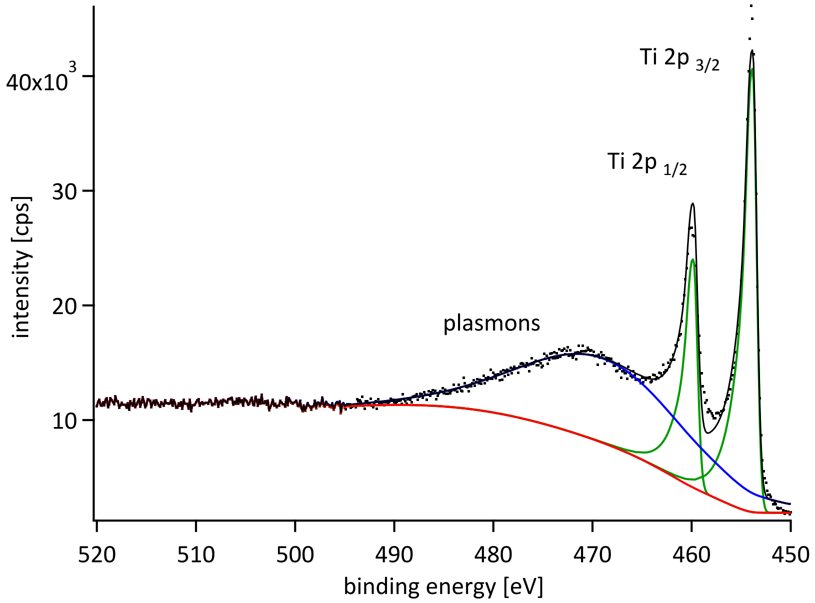

Figure 7.16: A Ti 2p spectrum of a pure Ti target after sputter cleaning is shown, the BG subtraction is a U2T.

this work.

Titanium nitride line shape The line shape is decisive for an accurate determination of the shake-up ratio r_b (eq. 5.1). Differences in r_b of up to a factor of three are found between e.g. GL(20) and GL(30)T(0.88) line shapes. Since the exact line shape of TiN could neither be extracted nor calculated, therefore the following approximation was used to describe the main Ti 2p peak in TiN: Pure titanium shows an asymmetric peak shape, as described above, with a tail value T of 0.65. Metallic Ti has four valence electrons in the $3d^2 4s^2$ configuration within a broad valence band of approximately 1 eV, leading to a tail formation, while TiN has a delocalized Ti $3d^1$ state at the Fermi level and a fully hybridized N 2p-Ti 3d band. Both bands are separated by a pseudo-gap of approximately 2.5 eV [305]. Only the delocalized Ti $3d^1$ states add up significantly to the tail intensity. Therefore in TiN only one valence electron instead of four (like in metallic Ti) can contribute to the tail, resulting in a decrease in the tail area of the Ti 2p line in TiN by about a factor of four. The intensity of the tail for metallic Ti is described by an exponential function $e^{-T \cdot E}$ with E being the kinetic energy. A decrease of the tail area a factor of four with respect to metallic Ti means an increase of the T value by a factor of four. The calculation to determine the peak tail can be found in the Appendix B. It is found that the tail decay is so strong for T values higher than 2.5 that it can be neglected, and the fit function becomes symmetric. Therefore a simple GL(20) without tail line shape is perfectly sufficient and has been used for the line shape of Ti 2p in TiN.

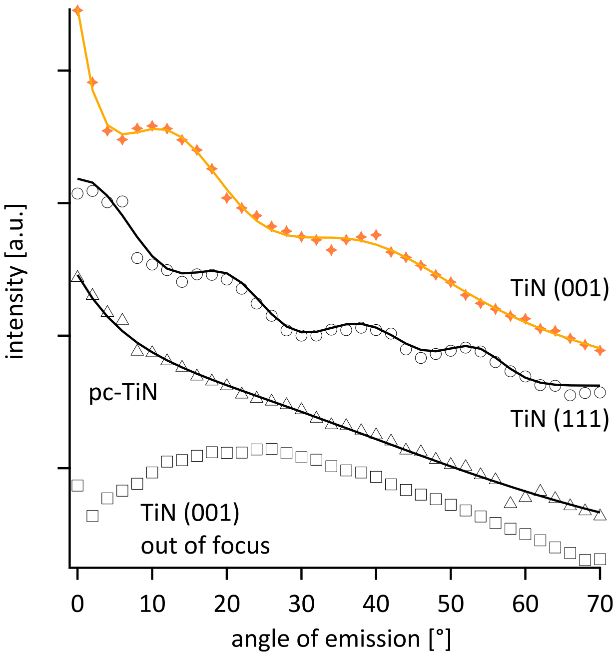

Figure 7.17: Ti 2p$_{3/2}$ intensities for sc- and pc- TiN samples. The intensities are scaled for a better representation. The plotted lines represent a fit function (eq. 5.4). data labeled TiN(001) and (111) represent sc-TiN layers with the surface normal being the crystalline orientation [001] and [111] respectively.

7.5 XPD patterns in TiN

As explained in section 5.4 forward focusing and diffraction occur for photoelectrons emitted from a single crystalline material such as sc-TiN. The intensity of photoelectron lines (e.g. Ti 2p$_{3/2}$) is modulated as a function of the AOE (see fig. 7.17). The patterns are correlated with the crystalline symmetry of the sample and vary therefore in AOE according to the crystal plane orientations of the sample under investigation. Photoelectrons of Ti2p$_{3/2}$ have a relatively high kinetic energy ($E_{kin} \approx 1031.5$ eV), well above 500 eV where the XPD patterns are generally dominated by forward focusing. All AR-XPS measurements of sc-TiN(001) samples are angle scans, where the sample is tilted around the [010] axis. Sc-TiN(001) samples (crosses, in fig. 7.17) show a maximum in the Ti 2p intensity at 0° and two local maxima at approximately 12° and 40°. This is in accordance with the observations of Timm et al. [378], shown in figure 5.4. The three maxima represent the forward focusing in [001], [104] and in [101]. Sc-TiN(111) (circles) has four maxima at about 0°, 20°, 38° and 53°, representing the forward focusing in [111], [112], [011] and [010]. Polycrystalline TiN (triangles) shows an initial decrease for angles above 10°, which continues linearly at lower rates for higher angles. As expected, no forward focusing is observed. A wrongly set focus of the analyzer entrance lens results in a diffuse intensity (squares), having only a shallow maximum for an AOE of 25°.

The intensities of the Ti 2p shake-up$_{3/2}$, Ti 2p$_{3/2}$ and N 1s of a sc-TiN(001) sample are shown in figure 7.18. The maxima in the [104] and in [101] direction for all three photoelectron lines are slightly different. Photoelectrons with a different origin and hence a different E_{kin} undergo a different kind of diffraction in XPD. This influence is small for the two XPD patterns of shake-up$_{3/2}$ and Ti 2p$_{3/2}$, where the difference in E_{kin} is only about 2.2 eV; their diffraction

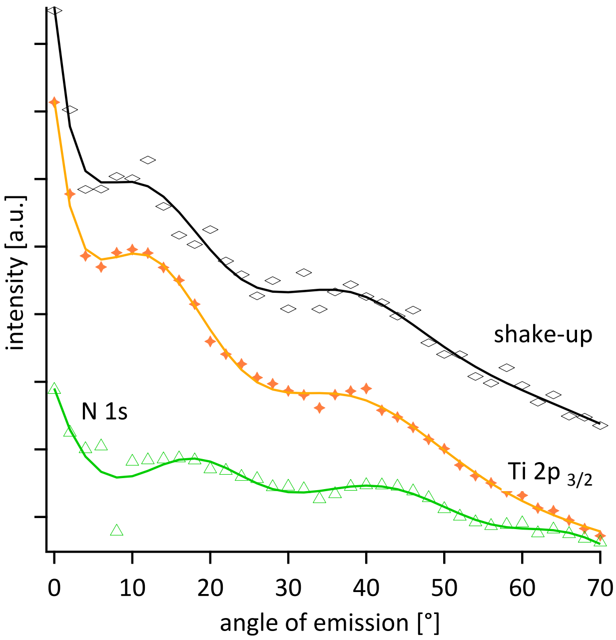

Figure 7.18: Intensities of TiN (001) photoelectrons of different origin with different E_{kin}.

patterns hardly differ. The slight difference of $\Delta\Theta \approx 1°$ in the fitted maxima is too large to be explained by the different E_B and therefore attributed to the low resolution in the AOE of the AR-XPS measurement[iii]. The uncertainty $\Delta\Theta$ between shake-up and main fit function is later carried on to the bulk ratio r_b and interface ratio r_i of the Ti 2p3/2 shake-up and main peak (eq. 5.11). The ratio of two oscillating functions, which are slightly shifted by $\Delta\Theta$ to each other, shows also oscillations. Those oscillations are partially filtered by the applied fitting routines (eq. 5.1, fig. 7.23).

N 1s photoelectrons show intensity maxima at 17°, 41° and 66°. The energy difference between electrons of N 1s and Ti $2p_{3/2}$ is about 80 eV and hence the diffraction pattern for N 1s are shifted compared to Ti $2p_{3/2}$. Consequently also the elemental concentration of nitrogen and titanium show XPD patterns (see fig. 7.26).

The BG is also angle-dependent (fig. 7.15). Minima are observed at 0°, 22° and 42° [413]. The BG value B represents the linear increase of inelastically scattered electrons, the minima occur at angles, where inelastic scattering is reduced and elastic scattering, i.e. forward focusing is enhanced. The BG at a certain energy E_x is the sum of all energy losses of all PE with a lower energy than E_x, hence the BG at Ti 2p also contains the N1s BG. In a forward focusing direction mainly elastic scattering occurs, resulting in a reduced BG. The minima in the BG at 0° and 42° of TiN(001) correspond to the intensity maxima at 0° and ≈ 40° of all Ti 2p and N 1s losses. The BG plateau between 10° and 20° is a result of a linear combination of the Ti 2p maxima at 12° and the N1s maxima at 17°. The minimum in B at 24° is most likely a outlier.

Not only the intensity and the background are influenced by XPD, but also the binding energy

---

[iii] AR-XPS scans were performed with a step size of 2°

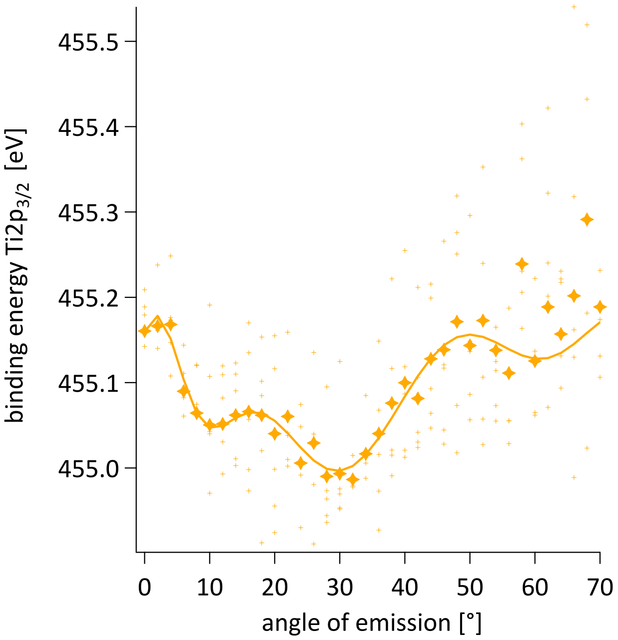

Figure 7.19: Binding energy patterns of sc-TiN as observed in six following experiments (thin crosses), averaged over all six measurements (bold crosses) and fit line from equation 5.4(line).

E$_B$. This diffraction effect is only visible after tedious experiments. It is shown for the energy line of Ti 2p$_{3/2}$ in what matter E_B is changed by the AOE in sc-TiN .

Figure 7.19 shows the binding energy of over 200 XPS measurements that are fitted to equation 5.4. Three local maxima and a global minimum at around 30° are observed. The binding energy for Ti 2p$_{3/2}$ in pc-TiN increases with the oxygen concentration and hence increases for high AOE, that is detecting more surface oxygen (sect. 7.1). This causes the increase of the electron binding energy at AOE above about 30°.The influence of the oxygen contamination on E$_B$ (as in pc-TiN observed) is excluded by subtraction the E$_B$ fit curve of a pc-TiN sample (fig. 7.2) from the E$_B$ fit curve of a sc-TiN sample (fig. 7.20).

The black line in fig. 7.20 represents the binding energy difference between sc-TiN(001) and pc-TiN. A negative value means that E$_B$ in sc-TiN is lower than in pc-TiN. Four local minima at 0°, 10°, 30° and 65° as well as three local maxima at 4°, 18° and 46° are observed. Minima in E$_B$ are approximately in the same crystalline directions as intensity maxima due to forward focusing (see fig. 7.17). The higher PE intensity in these directions is a result of more PE that stem from deeper regions in the sample, which are forward focused along certain crystallographic directions. Hence the change in E$_B$ might be correlated to a change in the depth information of the PE emerging from the bulk or the surface. Surface effects result in a higher E$_B$ at the surface as described in section 7.1. Oscillations in E$_B$ are observed in all single-crystalline samples investigated in this thesis (see fig. 7.20 and 8.6) and are result of different electron states at the surface/interface compared to the bulk.

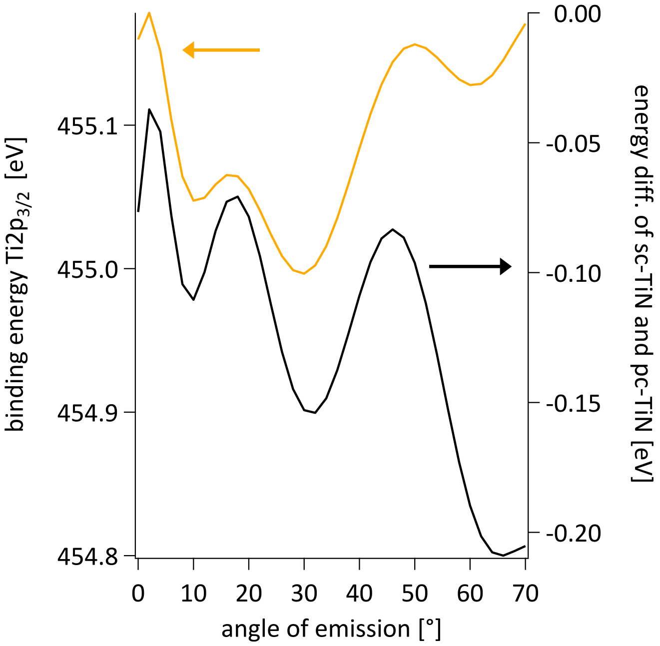

Figure 7.20: Fitted binding energy for Ti 2p$_{3/2}$ in sc-TiN (as shown in fig.7.19) and the energy difference between sc- and pc- TiN.

7.6 Bulk ratio r_b in sc-TiN

All fabricated samples are oxygen-free in the bulk, but have a slight oxygen contamination at the sample surface, even though all precautions as described in sect. 4.5 and 4.2 were met. The energy line of Ti 2p(Ti – O) in $\mathrm{TiO_xN_y}$ overlaps with the shake-up line, therefore the measured ratio R_m increases with the measured oxygen concentration (see figure 7.21).

Five different approaches to calculate the bulk ratio r_b of shake-up to main intensity can be used (sect. 5.5). These five methods are compared in the following and their results are shown in fig. 7.22.

- The averaged r_b is the simplest way of calculating the ratio. The disadvantage is that bulk and surface values for low and high AOE are averaged, i.e. the mean value contains also contributions of $\mathrm{TiO_xN_y}$ at the surface, that overestimate the value for r_b.
- The linear approach correlates the oxygen concentration with the bulk ratio r_b. The dotted line in fig. 7.21 represents the fit function for this linear approach. Inspection of measured data and line fit indicate that the fit value for the linear approach is also overestimated.
- An exponential approach was developed to better represent the data in dependence of the oxygen concentration. This method is purely empirical, but as will be seen in the next paragraphs, is sufficient to describe the bulk ratio.
- The XPD approach uses the angle-dependence of the forward focused intensities and uses the ratio of $I_{p,0}$ of shake-up to main (eq. 5.4). A slight difference in the diffraction

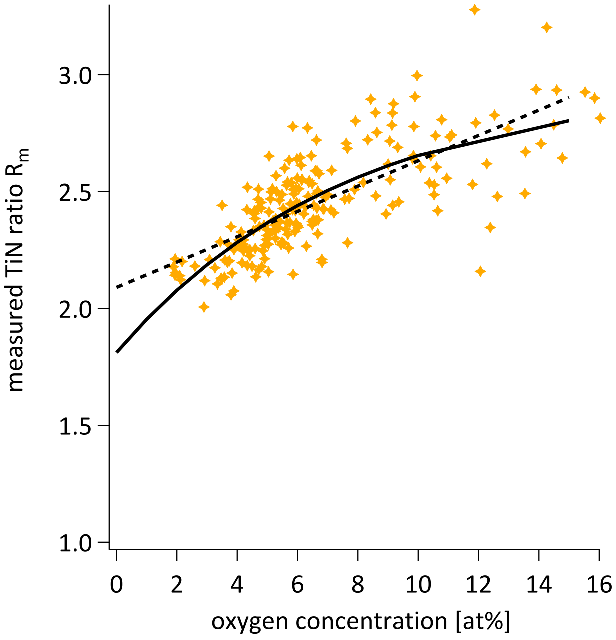

Figure 7.21: The bulk intensity ratio r_b between Ti $2p_{3/2}$ and shake-up$_{3/2}$ depends on the oxygen concentration. The doted line represent the linear fit approach, and the curved line represents the exponential approach (sect. 5.5). The oxygen concentration has been measured using the first principle method.

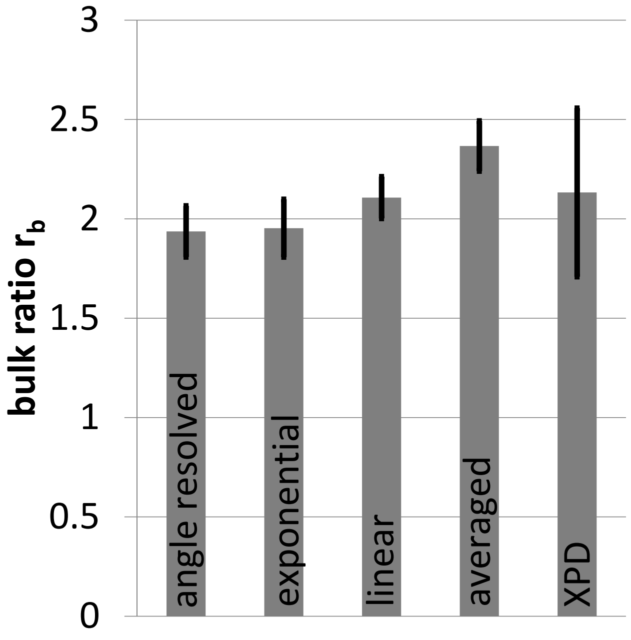

Figure 7.22: The oxygenfree bulk ratio r_b depends on the approach used to calculate the bulk value r_b.

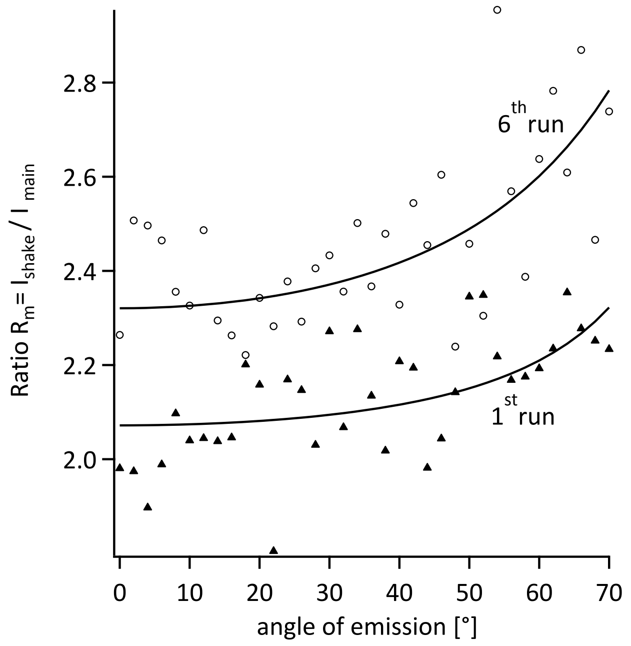

Figure 7.23: The area ratio $R_m = S_m/M_m$ increases with increasing angle of emission and also increases over time due to oxygen contamination. The ratios are shown for the first measurement directly after deposition (triangles) and after 72 hours in the spectrometer (empty circles).

patterns of main and shake-up (sect. 7.5) is expressed in a shift of the AOE by $\Delta\Theta$. This shift is carried on in this approach and results in an overestimated bulk value r_b with a high uncertainty (sect. 7.5).

- The angle-resolved approach is based on equation 5.1 and is further discussed in the following paragraphs.

The angle-resolved approach is not directly considering the effect of the oxygen concentration c_{oxy}, but since the measured c_{oxy} is dependent on the angle, hence the oxygen content is indirectly included. The time-dependence of the oxygen concentration is considered, since the influence of the slowly increasing oxygen contamination is neglected for each angle-resolved scan (AOE =0°-70°) .

Figure 7.23 shows the angular dependences of the measured area ratio R_m for pristine TiN. It increases for all measurements from low angles of emission to high angles, thus showing a surface sensitivity. As described above, a small oxygen contamination occurred during the measuring time, resulting in an increase in the thickness t_{oxy} of the oxygen-containing layer TiO_xNy. The thickness can be determined by applying equation 5.1 to the measured total ratio R_m while keeping the value for r_i fix. Figure 7.24 illustrates that the thickness t_{oxy} of the overlying surface contamination slowly increases over time. This increase causes an increase in the ratio R_m over time in figure 7.23. It is continuous with increasing exposure time. Applying the fitting of equation 5.1 to all measurements and all four TiN(001) samples resulted in a bulk ratio r_b of the shake-up to the main peak of 1.9 ± 0.1 for single-crystalline titanium nitride interpolated to pure and oxygen-free bulk TiN. The interpretation of the bulk ratio r_b and the shake-up origin will be discussed in detail below in sect. 7.8.

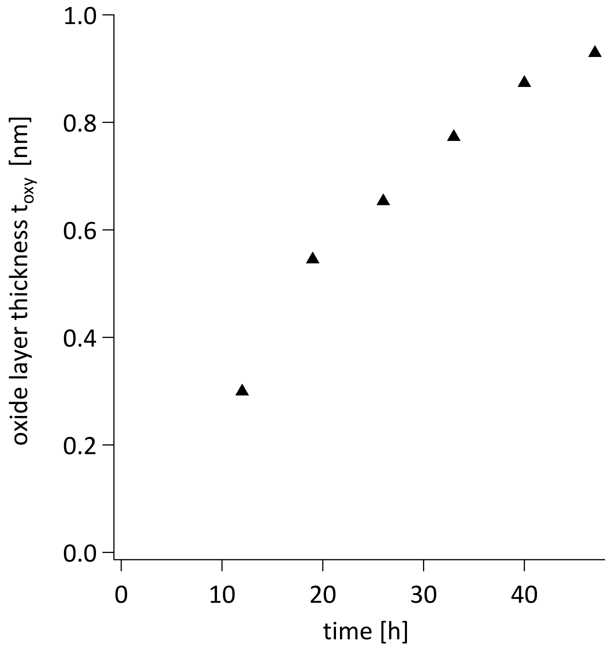

Figure 7.24: The thickness t_{oxy} of the oxygen contaminated layer increases slowly during the measuring time at $p = 4.5 \cdot 10^{-9}$ mbar. The oxidized layer thickness has been calculated as described in section 5.5.

All five experimental methods (fig. 7.22) result the same value for r_b within their accuracy. All methods are slightly overestimating the bulk ratio due to the surface contaminations. The lowest value for r_b and a small uncertainty is obtained for the angle-resolved method. Therefore in the following the bulk ratio r_b was derived according to the angle-resolved approach. Differences in r_b between pc- or sc-TiN in (001) or (111) are not observed, also TiN samples deposited with a bias of −75 V at 200 °C[iv] show the same bulk ratio r_b (fig. 7.25). An insufficient sample grounding (without a Pt frame, sect. 4.4) results in a high uncertainty, but nevertheless shows the same bulk ratio. Within the error margins all samples independent of orientation, grounding or bias show the same ratio r_b.

7.7 Elemental compositions

The elemental concentrations were determined as described in section 3.8, only intensity correction factors determined from basic principles were used, no additional adjustment factor was used. The results of the elemental concentration determinations are given in fig. 7.26. The composition ratio averaged over all angles and all samples was Ti/N = 1.0 ± 0.1, which is in perfect agreement with the RBS measurement (tab. 7.2).

The sc-TiN samples give rise to diffraction effects (sect. 7.5), that are observed as irregularities in the monotonous change of the photoelectron intensity of Ti 2p and of N 1s, as the observation angle is varied (see fig. 7.18). These non-uniform fluctuations cause oscillations in the elemental concentration (fig. 7.26). For high electron angles of emission the oxygen concen-

---

[iv] The biased TiN samples are nanocrystalline and exhibit compressive stresses, see sect. 6.1.

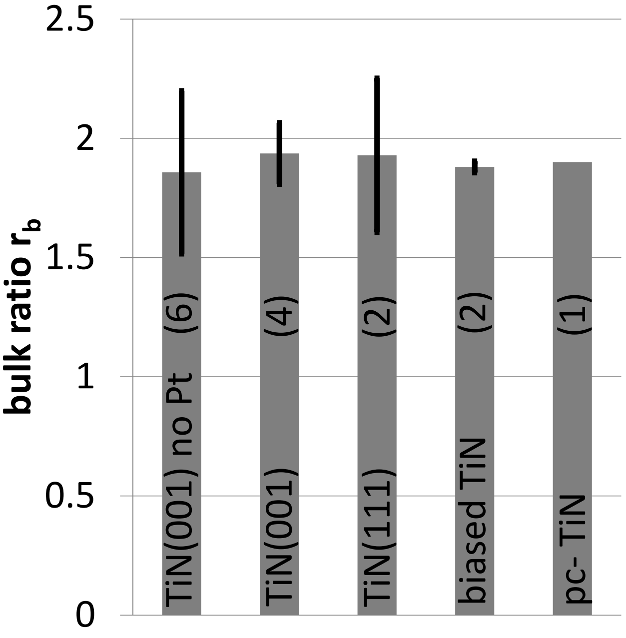

Figure 7.25: Bulk ratios of TiN samples deposited under different conditions. All samples are supported with a grounding Pt-frame, if not mentioned explicitly. F.l.t.r.:sc-TiN deposited without a grounding Pt-frame, sc-TiN(001), sc-TiN(111), sc-TiN(001) deposited with a bias and pc-TiN deposited on a Si-wafer. The numbers in brackets indicate how many samples were analyzed.

tration increases, indicating that it is accumulated only at the sample surface. It increases from 2 at% for an angle of emission of 0° to 12 at% for 70°. The oxygen amount additionally increased by about an additional 2 at% after 64 hours in the spectrometer at 5×10^{-9} mbar, illustrating that the oxygen content was hardly altered by the length of the measurement. Calibration measurements with ERDA showed oxygen concentrations below 0.2 at% in the bulk for samples that were fabricated under similar conditions. Therefore it must be assumed that the oxygen concentration in the bulk is heavily overestimated by the XPS measurements.

Figure 7.27 shows the calculated elemental concentration for different AOE of a TiN/Si bilayer system. Clearly the Si and O intensities increase with the AOE, while Ti and N decrease. This confirms that Si and O are located on top of TiN. Similar to the BG (see fig. 7.15) also the diffraction patterns in the concentration of elements is blurred and less pronounced than in sc-TiN (see fig. 7.26). The covering material does not crystallize in the same crystal structure, and hence more inelastic scattering occurs along the directions where forward focusing appears in pure TiN. In comparison to uncovered TiN also the oxygen concentration is lower for the less reactive overlayers Si and Si_3N_4 (not shown).

The Si_3N_4 and AlN bilayer systems show in general a similar behavior, the elemental concentration as obtained by XPS and ERDA are summarized in table 7.2.

7.8 Comparison of shake-up results with literature

Shake-Ups have been reported in various elements and compound e.g. [414], nickel Ni 1s [415][416], copper difluoride Cu 2p [417] and nitroanilines N1s [418]. The shake-up feature

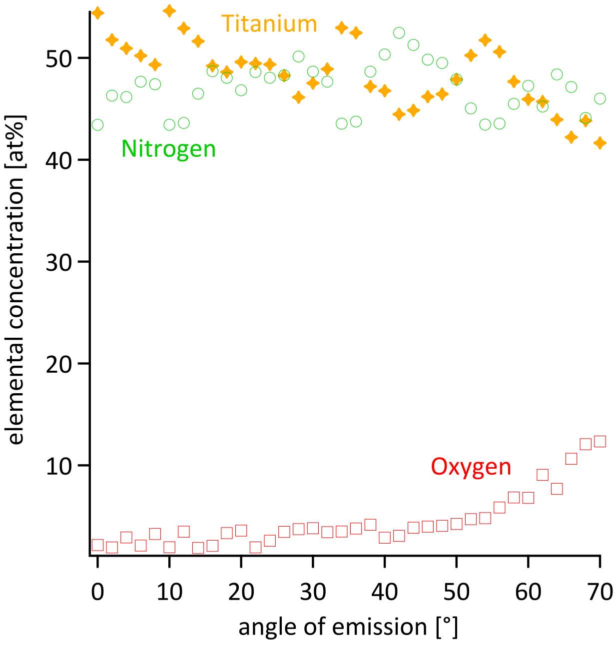

Figure 7.26: Elemental concentration of a sc-TiN grown on MgO(001) for different AOE, measured within the 12 h after deposition.

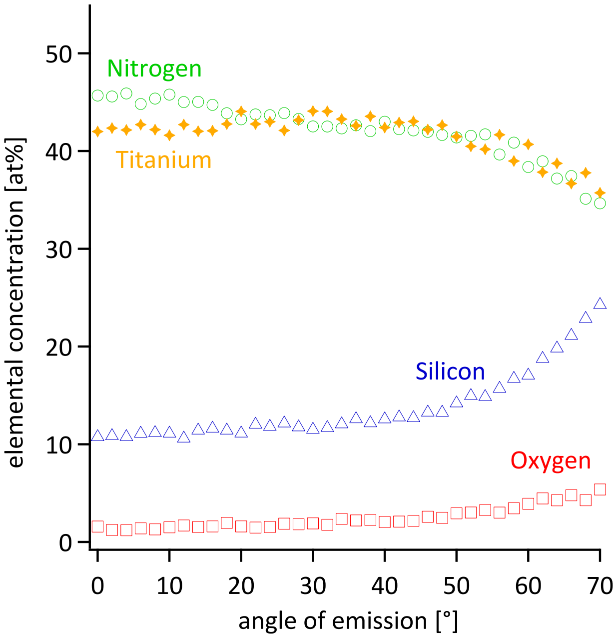

Figure 7.27: The elemental composition of bilayers system with a 2.9 nm thick Si film on TiN (001).

is always represented by an additional line peak on the higher binding energy side of the main peak and is caused due to two possible final states. Experiments indicate that the shake-up position and intensity convey important information on the materials properties. The previously mentioned (see reference) energy line types (main lines and plasmons) are well described and understood in detail. DFT calculations for those lines are straight forward and therefore easily accessible. All this is not the case for shake-ups. A full understanding of the process is only possible by time-dependent DFT calculations.

The most comprehensive studies on TiN using XPS have been done by Porte [310], Bertóti [358] and Milošev et al. [328]. Porte et al. were the first to study the intensity increase of the TiN shake-up qualitatively as the nitrogen content in TiN_x ($0.5 < x \leq 0.98$) increases. In that work all samples had undergone a "very slightly" argon etching prior to the XPS measurements, and a BG correction was performed; however, it is not mentioned what Ar^+ energy and sputter rate and what BG type were used. The oxygen content in the samples was about 1-2at% and also carbon species in unknown amounts were present on the surface. Bertóti et al. [358] used a Shirley background and experienced difficulties with the energy referencing due to the lack of carbon after sputter cleaning (Ar^+, 2.5 kV). The latter was required since up to 30at% of surface oxygen were present. Argon bombardment generally alters the surface, and the Shirley background causes less accurate peak ratios between the spin orbit split Ti $2p_{3/2}$ and Ti $2p_{1/2}$ deviating from the correct value of 0.515. This explains their observation of a lower than 0.5 ratio of Ti $2p_{3/2}$ and Ti $2p_{1/2}$. A few years later Bertóti [329] actually showed that the chosen BG severely affects the results, but quantitative determination remained uncertain. Milošev et al. were the first to report a quantitative value for the shake-up intensity, being 36% of the total intensity, while the core level intensity was 58% and the TiO_xN_y component in the Ti 2p spectra contributed to 7%. In their studies also a Shirley BG correction and sputter cleaning has been performed. The focus of that study was on the oxidizing process forming TiN_xO_y and on oxidation states in the Ti 2p spectra. In a second step Milošev used angle-resolved XPS, similar to the work presented here, for quantitative studies of the oxidation states; the ratio between shake-up and main peak was kept fixed at 0.6. These values are much lower than what is obtained from the angle-resolved measurements ($r_b = 1.9 \pm 0.1$). The samples of Milošev were sputter cleaned; however, preferential sputtering of N and O most likely led to understoichiometric TiO_xN_y (with x+y<1) [176, 329]. As described by Porte [310], a decrease in the N content is directly correlated with a reduced shake-up intensity, therefore Milošev's value can only be considered as a lower limit of the shake-up intensity. In addition the Shirley BG used in Milošev's work artificially reduces the intensity of the shake-up more than that of the main core level. To the author's knowledge only Milošev et al. [328] have reported a quantitative value for the ratio r_b of the shake-up and the main peak in TiN. Their value is below the observations made in this thesis. The difference is explained by the preferential sputtering (used by Milošev) resulting in substoichiometric TiN_x and therefore in a lower shake-up intensity. The XPS spectra of Delfino et al. [404] show also that in TiN the Ti $2p_{3/2}$ shake-up intensity is much higher than the main peak, but no numbers are given in there. From the spectra shown in Delfino et al. [404] it is guessed that also a Shirley or Linear BG correction has been performed. In this thesis the intensity ratio of the two main peaks (Ti $2p_{1/2}$ and Ti $2p_{3/2}$) was fixed according to Scofield, and a ratio of 0.49 ± 0.04 is observed for the spin orbit split shake-ups 3/2 and 1/2, which is the same value as for the main peak within the uncertainty margins. Therefore relative intensity difference between the 1/2 and 3/2 shake-up, as it is observed in Ni [416] is not observed in the experiments performed in this work. The discrepancy between the values reported in literature and those presented in this work can be attributed to energy scale referencing, oxygen contamination, sputter cleaning using high energy Ar^+ ions and an inappropriate background type. In many cases little or no information is given on the energy scale referencing procedures used. As shown in this work, the peak positions are significantly influenced by the oxygen concentration and sample charging at different angles (see fig. 7.2), explaining the scatter in the reported binding energies. Exposing the sample to air will immediately contaminate the sample surface, and sputter cleaning will result in preferential sputtering [329]. Transferring the samples ex-situ and sputter cleaning are therefore inappropriate to investigate TiN. In this work the influence of oxygen at the surface had been minimized by transferring the sample in situ and assessed by measuring at low angles of emission. Additionally special care had been taken to prepare TiN with very low oxygen contents in the bulk material ($0.2at\%$, measured by RBS). It has been shown that the Tougaard BG provides the most appropriate description, especially for samples with a step-like BG and for angle-dependent measurements. The Tougaard BG is calculated accounting for the extrinsic (inelastic scattering) and intrinsic excitations (e.g. due to screening) which can extend up to 50 eV above the main peak binding energy. A seeming disadvantage of Tougaard BG is that a wide range of spectra of up to 80 eV has to be recorded, while for Shirley BG corrections only a 20 eV spectrum is sufficient. However, a Shirley BG cannot account for surface and bulk plasmons intensities and their effect on the main peak intensity. These features with an energy loss of approximately 11 eV and 22 eV for first and second order bulk plasmons in the case for TiN are separated too far away from the main peaks to be accounted for in a Shirley BG. By choosing a Tougaard BG it is possible to attain the correct ratios for Ti $2p_{1/2}$ to Ti $2p_{3/2}$ as calculated by Scofield and the surface plasmons show the same multiplet splitting energy as the main Ti 2p peaks. For these reasons the Tougaard background correction algorithm is the best choice for an appropriate evaluation of TiN spectra.

7.9 Origin of the shake-up

In the investigations of Porte [310] on N-deficient TiN_x the origin the shake-up in TiN is described to a charge transfer. Porte observed that the shake-up feature increases with the nitrogen content; and that below a critical limit of $x < 0.8$ in TiN_x the shake-up feature disappears. It was argued that below that limit (x<0.8) the vacancy states can no longer form a band and become localized, and the wave function and the band do not overlap anymore [310]. This argumentation is tempting, but as described in section 3.5 TD-DFT or CI is required to gain further insight.

Shake-up energy ΔE The shake-up energy ΔE for TiN is reported between 2.2 eV and 2.8 eV [88, 310, 328, 330, 358]. In the present work, a value for $\Delta E = 2.16 \pm 0.04$ eV for the Ti $2p_{3/2}$ in oxygen free bulk sc-TiN is obtained. The discrepancies in literature are due to oxygen contaminations, sputtering cleaning and incorrect peak fitting. So far only the shake-up energy for the Ti $2p_{3/2}$ has been investigated. A clear difference between the $\Delta E_{3/2} = 2.16 \pm 0.04$ eV and $\Delta E_{1/2} = 1.78 \pm 0.07$ eV is found in the present work. Similar disparity between the two shake-ups energies have been observed in metallic nickel [416, 419]. In the case of nickel the shake-up feature is interpreted with two final states: a $2p^5 3d^9$ (shake-up) state and a state $2p^5 3d^{10}$ (main). The shake-up is composed of several multiplets, and the satellite energy was calculated using a Born-Haber cycle type approach. The calculations and experiments show a good agreement for the shake-up energies for Ni $2p_{3/2}$ (6.0 eV) and Ni $2p_{1/2}$ (4.6 eV) [416]. To the author's knowledge no similar calculations have been performed for TiN. The disparity of $\Delta E_{3/2}$ and $\Delta E_{1/2}$ in TiN can be explained by the coupling of core and valence band vacancy [420], resulting in two different shake-up energies depending how the holes or remaining core electrons of Ti $2p_{3/2}$ and Ti $2p_{1/2}$ couple with the valence electrons. While this explanation is suggestive, it is by far not sufficient for a complete description of the process: the transition amplitudes between occupied and unoccupied states, which describe the transition probabilities, as well as a reliable description (beyond the Kohn-Sham formalism) of the excited states would be necessary, but is not within the scope of this thesis. Nevertheless experimental results for ΔE are in the order of what can be explained by an process where the final state has excited electrons from occupied into initially unoccupied states.

Bulk ratio r_b The transition probabilities to excite an electron in unoccupied states has been calculated by Kochur and Popov [290] and Lowe et al. [421] for single Ti atoms. Their theoretical values should be in the order of the experimental data presented in this work. Kochur and Popov [290] calculated the transition probability for different elements and different shell excitations and obtained an increase in the shake up intensity with decreasing main quantum number, transition probabilities up to 0.5 are received in those DFT simulations. The probability for excited final states of the Ti 3d orbitals is calculated to be 0.1. Those calculations are for single atoms and not for solid states. Single atoms have discrete energy levels in which electrons are allowed to be excited. In solids those countable energies levels merge into broad energy bands. Wider bands and smaller energy gaps between those states allow more transitions into unoccupied states and result in higher probabilities/intensities for the shake-up process. A ratio $r_b = 1.9 \pm 0.1$ equals to a transition probability of 0.65, i.e. an increase by a factor of 7 which sounds reasonable for the widened bands.

7.10 Summary of the TiN results

In this chapter it was shown that the binding energies of TiN are influenced by oxygen contamination and surface effects (surface charging and termination), which result in an increase in the binding energy E_B towards higher and lower AOE (sect. 7.1). A self-consitent evaluation process was applied to the Ti 2p region of the TiN XPS spectra, and all components in the Ti 2p peak were resolved (sect. 7.2 and table 7.1). The shake-up energy depends on the core shell where the PE is emitted from, and $\Delta E_{3/2} = 2.16 \pm 0.04$ eV and of $\Delta E_{1/2} = 1.78 \pm 0.07$ eV were observed. Further it was found that the appropriate BG for the Ti 2p region in TiN is the Universal Two-parameter Tougaard background (U2T BG) (sect. 7.3), which also contains information on the crystalline structure of the sc-TiN sample. The Ti 2p line shape was estimated using a tail-approximation and a simple Gaussian-Lorentzian line shape GL(20) without a peak tail T was found to describe the line shape the best (sect. 7.4). XPD patterns were further resolved in PE intensities and in binding energies E_B (sect. 7.5). The change in E_B of sc-TiN might be correlated to a change in the depth information during the tilting of the sample around the AOE. High AOE detect more PE emitted from the surface region, which show a higher E_B due to the influence of surface oxygen. The bulk ratio r_b of shake-up and main PE line was calculated and a value of $r_b = 1.9 \pm 0.1$ was found. The bulk ratio r_b is independent from the method chosen to calculate it, but is heavily influenced by slight oxygen contaminations. The crystallinity (sc- or pc-), the crystallographic orientation ((001) or (111)) or an applied bias during the deposition have no influence on r_b. The oxygen contamination is located at the sample surface of the TiN samples and was compared to other bulk sensitive methods as RBS and ERDA (sect. 7.7). Therefore AR-XPS was successfully used to resolve the bulk ratio r_b in TiN. All obtained result of the TiN samples were compared to literature and the origin of the shake-up was discussed (sect. 7.8). It was explained that the shake-up is a direct result of a multitude of final excited states and that shake-up energy and intensity depend on the core shell from where the PE are emitted from.

system	assignment	binding energy [eV]	FWHM [eV]
sc-TiN(001)	Ti $2p_{3/2}$	455.1 ± 0.1	1.3 ± 0.1
	Ti $2p_{1/2}$	460.9 ± 0.1	*same as Ti* $2p_{3/2}$
	Shake-up$_{3/2}$	457.3 ± 0.1	3.8 ± 0.1
	Shake-up$_{1/2}$	462.9 ± 0.2	*same as shake-up*$_{3/2}$
	surface plasmon $_{3/2}$	467.8 ± 0.1	7.3 ± 1.4
	surface plasmon $_{1/2}$	474.0 ± 0.2	*same as surf. plas.*$_{3/2}$
	1^{st} bulk plasmon	481.2 ± 0.2	10.5 ± 1.9
	2^{nd} bulk plasmon	507.4 ± 0.1	10.6 ± 1.1
	N 1s (N-Ti)	397.2 ± 0.1	1.1 ± 0.1
	N 1s (N-O)	399.6 ± 0.1	2.3 ± 0.1
	O 1s (O-Ti)(*)	531.0 ± 0.5	2.2 ± 0.6
	O 1s (O-N)(*)	533.1 ± 0.3	*same as O 1s (O-Ti)*
Si bilayer	Ti $2p_{3/2}$	455.1 ± 0.3	1.3 ± 0.1
	Si 2p	99.4 ± 0.1	1.2 ± 0.1
	O 1s	532.2 ± 0.3	2.7 ± 0.6
Si_3N_4 bilayer	Ti $2p_{3/2}$	455.1 ± 0.2	1.3 ± 0.1
	Si 2p	101.9 ± 0.3	1.8 ± 0.1
	N 1s (N-Ti)	397.3 ± 0.2	1.4 ± 0.3
	N 1s (N-Si)	398.3 ± 0.5	2.5 ± 0.6
	O 1s	532.3 ± 0.3	2.4 ± 0.4
AlN bilayer	Ti $2p_{3/2}$	455.0 ± 0.1	1.3 ± 0.1
	Al 2p	73.6 ± 0.7	1.9 ± 0.3
	Al 2s	118.7 ± 0.4	1.9 ± 0.3
	N 1s (N-Me) (*)	397.1 ± 0.5	1.4 ± 0.1
	N 1s (N-O)	399.9 ± 1.6	1.7 ± 0.3
	O 1s	531.9 ± 0.7	2.8 ± 0.4

Table 7.1: Binding energies obtained as described in sect. 7.1, the uncertainties are determined by the standard deviation of four different samples, that were fabricated similarly. The given FWHM are the average over all measurements. FWHM in italic indicate that the FWHM was constraint to the mentioned peak. The values for the bilayer systems presented are averaged E_B over all angles and all measurements. (*)N 1s (N-Me) refers to Me = Al or Ti bonds (sect. 8.4).

Material	x in XPS	c_{oxy} in XPS [at%]	x in ERDA	c_{oxy} in ERDA [at%]
TiN_x	1.1 ± 0.1	2.4 ± 0.6	1.0 ± 0.02	< 0.2
SiN_x	1.34 ± 0.1	1.2 ± 0.2	1.33 ± 0.01	< 0.1
AlN_x	0.9 ± 0.1	4.0 ± 0.1	n.a.	n.a.

Table 7.2: Elemental compositions of different samples are compared. In some samples the oxygen concentration in the bulk TiN was close to the detection limit of ERDA <0.025at%, the results given are maximum oxygen concentrations in the bulk.

8 XPS investigations of bilayer systems

In this chapter the results for bilayer systems on sc-TiN(001) are presented, and the physics behind the shake-up feature are discussed. Section 8.1 investigates the overlayer structure using XPD, and it is verified that no perturbing factors are falsifying the shake-up intensity at the interface (sect. 8.2 and 8.3). In the following section 8.4 an interfacial charging is revealed, which depends on the thickness t of the overlying film.

In figure 8.1 small energy windows (30 eV) of wider spectra taken with a 80 eV width for an TiN/Si_3N_4 bilayer system with different AOE are shown. Biased Si_3N_4 bilayer systems refer to interface systems, where during the Si_3N_4 deposition a bias of −250 V has been applied at the substrate (see chapt. sec:Safabr). It is clearly seen in figure 8.1 that the shake-up intensity increases with increasing angle of emission (AOE). In bilayer systems the Ti PE signals of higher AOE contain more information from the TiN interface, therefore the increase of the shake-up intensity with higher AOE is directly correlated to a higher interfacial shake-up intensity.

These enhanced shake-up intensities are observed for different TiN interface bilayer systems. Figure 8.2 shows three different interface systems, TiN/AlN as well as biased and unbiased TiN/Si_3N_4 bilayers. It is observed that, depending on the overlayer material the shake-up intensity is altered. The shown spectra in figure 8.2 are detailed spectra of complete spectra of different bilayer system for one particular AOE. The following sections show, that it is essential to analyze all spectra of all AOE. The gained information is used to discuss the spectra of figure 8.2 in detail (sect. 8.7).

Seemingly the increased shake-up intensity is correlated to the TiN interface in the investigated bilayer systems. The interface ratio r_i of the shake-up to main peak of Ti $2p_{3/2}$ at the interface is calculated by applying the least square method to equation 5.1. The latter is strongly influenced by the interface thickness δ, which is discussed in section 8.5.1. In the second part of this chapter (sect. 8.6), it is shown that interface charging is influencing the shake-up energy of the systems (sect. 8.6.1). It is further explanied how the shake-up *intensity* is correlated to its *energy* (sect. 8.6.2). The correlation between shake-up energy and intensity is applied to the interface ratio r_i, and the influence of different overlayer systems and their overlayer

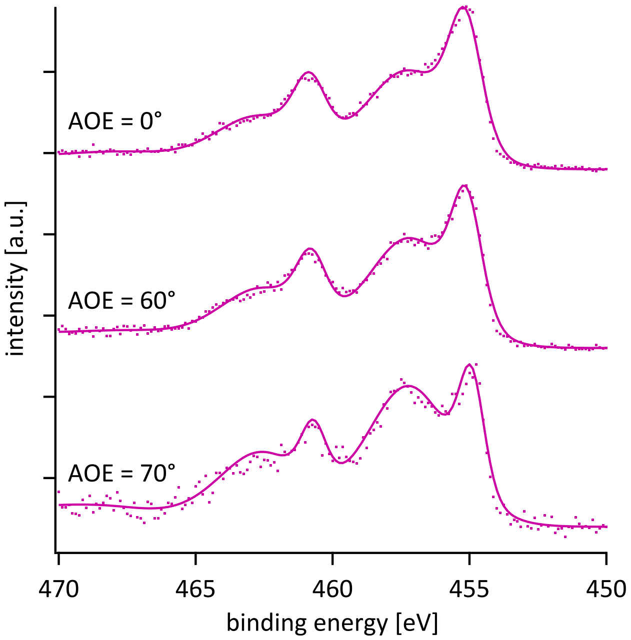

Figure 8.1: Details of Ti 2p spectra of a biased TiN/Si_3N_4 bilayer system, shown is only a short energy range over 30 eV of the full recorded spectrum (80 eV).

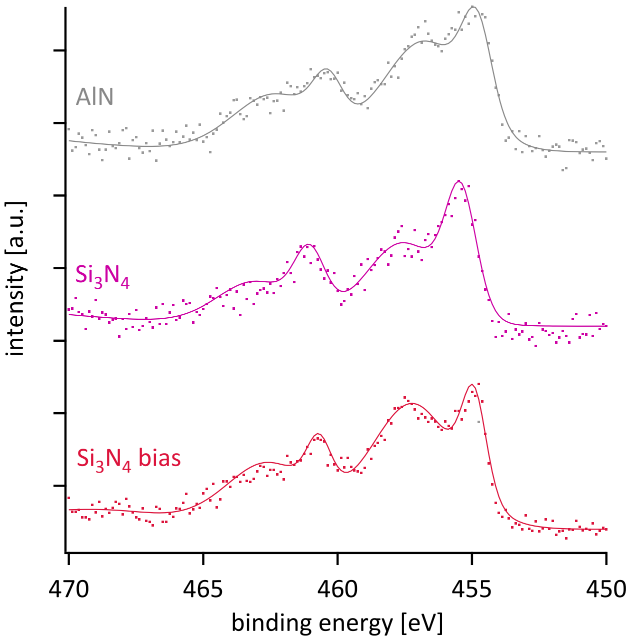

Figure 8.2: Normalized spectra at an AOE of 70° of AlN ($t = 1.3$ nm, grey), unbiased Si_3N_4 ($t = 1.4$ nm, violet) and biased Si_3N_4 ($t = 1.4$ nm, crimson) bilayer systems on sc-TiN(001) are compared.

thickness t is analyzed (sect. 8.6.3).

All results presented in the following refer to TiN (001) bilayer systems deposited at 800 °C, without substrate bias unless indicated otherwise. The different interface phenomena are demonstrated on the Ti $2p_{3/2}$ photoelectron (PE) line in this part of the thesis. The observations and explanations are, however, not limited to Ti $2p_{3/2}$, but also account for Ti $2p_{1/2}$. In this chapter only the obtained results are shown and explained regarding their physical context; a discussion of the results focusing on the bilayer systems is given in section 8.7.

8.1 XPD patterns in overlayers

Forward focusing (sect. 5.4) is clearly observed in pristine sc-TiN. XPD patterns are a versatile method to study the structure of thin films or structure of adsorbed molecules [365]. To properly measure XPD pole figures the sample has to be moved about the measured spot in a polar and azimuthal motion. The experimental system used in this thesis has only the option of rotating the sample along the AOE and is not designed to record XPD patterns. Nevertheless the limited range of tilt axis of the sample is capable of giving insight into the structure of the overlayer. It is not possible to derive the exact crystalline structure, but it can be differentiated between amorphous and crystalline materials. Figure 8.3 shows the area intensity of the Si 2p signal versus the AOE for Si_3N_4 bilayer systems. For each data point of the line more than five angle-resolved measurements were averaged and smoothed by averaging over the next neighbor. It is clearly seen that Si_3N_4 films with a thickness $0.5\,\mathrm{nm} < t < 0.7\,\mathrm{nm}$ on top of TiN (001) show an enhancement in the intensity of Si 2p for AOE $\leq 10°$. The higher intensity is caused by XPD and indicates a crystalline structure of Si_3N_4 for $t < 0.7\,\mathrm{nm}$. With increasing overlayer thickness the intensity of the XPD peak is damped and indicates a growth change from crystalline to amorphous Si_3N_4. If a substrate bias of −250 V is used then no XPD in the Si 2p intensity is observed, suggesting that crystalline growth is prevented by the enhanced ion energy under applied bias.

AlN overlayers show for thin ($t < 0.5\,\mathrm{nm}$) and thick films ($t = 1.5\,\mathrm{nm}$) XPD patterns (fig. 8.4). The diffraction patterns for different t differ in their position and intensity. This indicates that in AlN films the crystalline structures changes with increasing thickness. Si overlayers on TiN are not evaluated regarding their XPD patterns, since AFM results show that Si is not fully covering the TiN sublayer (sect. 6.3).

8.2 Binding energies of overlayer systems

The binding energies for the different interface systems are summarized in table 7.1. Full survey spectra and detailed spectra of all bilayer systems are found in appendix C. The main Ti $2p_{3/2}$ line lies for all bilayer system at 455.1 ± 0.3 eV. AR-XPS measurements revealed that oxygen is located at the surface of the overlayer (sect. 7.7). It is generally observed that overlayers reduce the oxygen contamination after deposition, and it has not been possible for

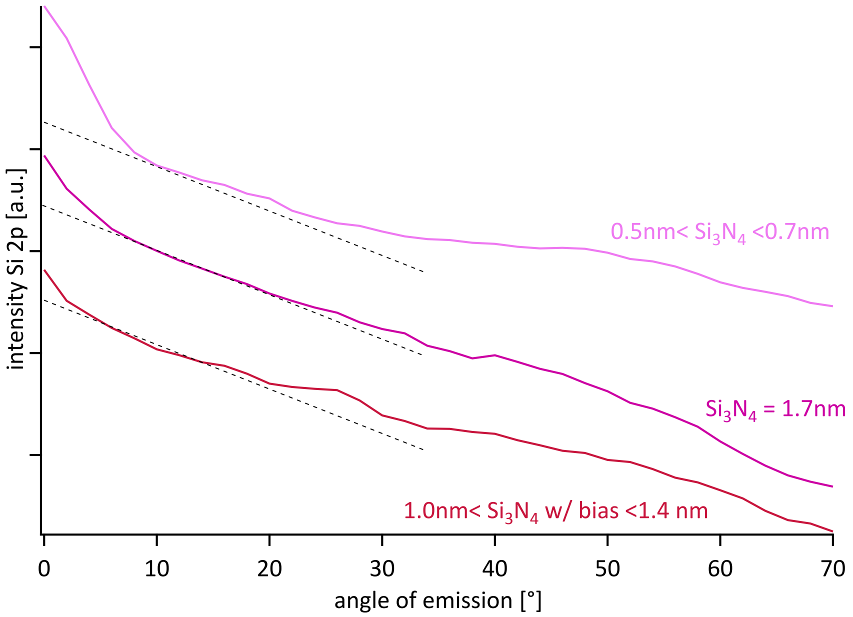

Figure 8.3: The intensity of the Si 2p PE line is compared for different Si_3N_4 overlayers, all shown values are averaged, smoothed and scaled. From top to bottom: three samples with 0.5 nm < t < 0.7 nm deposited at 800 °C without substrate bias, two samples with t = 1.7 nm at 800 °C without bias, three sample with 1.0 nm < t < 1.4 nm at 500 °C-800 °C with a bias of −250 V. The dashed lines are parallel and are guides for the eyes.

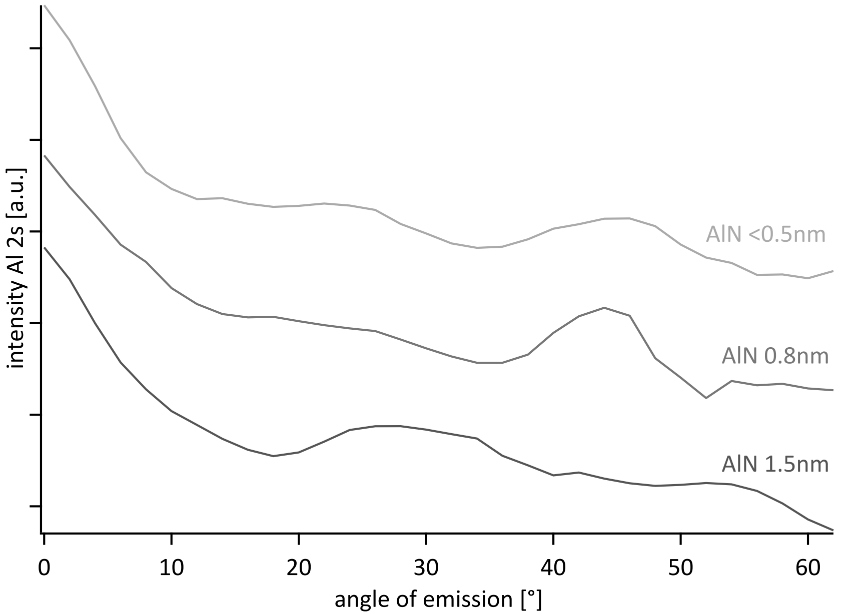

Figure 8.4: In AlN the intensity of the Al 2s signal shows a clear angle-dependences due to XPD. Presented are the results of normalized and smoothed data. The lines of 1.5 nm and 0.8 nm are obtained from one sample each, while for t < 0.5 nm the data had to be averaged over two samples due to the low count rate.

the bilayer systems to resolve two different oxygen components (O 1s (O-Ti) and O 1s (O-N)), as it was possible for pure TiN.

XPS spectra of TiN covered with Si (fig. C.2) show PE lines of Si 2p at 99.4 ± 0.1 eV for silicon and a pronounced oxygen O 1s energy line at 532.2 ± 0.3 eV [280]. For overlayers of Si_3N_4 (fig. C.4) the Si 2p line is found at 101.9 ± 0.3 eV indicating Si – N bonds [422]. The nitrogen binding energy can be separated in two peaks, one corresponding to N – Ti at 397.3 ± 0.2 eV (sect. 7.1) and a second peak of N – Si at 398.3 ± 0.5 eV [423, 424]. XPS spectra of TiN covered with AlN (see fig. C.6) have Al 2p and Al 2s lines at 73.6 ± 0.7 eV and 118.7 ± 0.4 eV, respectively. Both lines correspond to Al bonded to N [425]. Spin-orbit-splitting is only observed in Ti 2p, the energy split in Si 2p and Al 2p has been reported to be 0.6 eV [367] and 0.4 eV (respectively) [425], which is too small to be resolved (see peak criteria in sect. 5.2). Silicide energy lines are not found in the XPS spectra and indicate that there is no Ti-Si bonding.

8.3 Oxygen in bilayer systems

A big effort has been put into the experimental setup to keep the oxygen contamination as low as possible. Nevertheless, high surface oxygen concentrations (of up to 18 at%) are present in the samples with AlN or Si overlayers. In figure 8.5 the averaged oxygen concentration c_{oxy}[i] is plotted versus the overlayer thickness of different materials covering TiN (001).

Si_3N_4 bilayer systems have the lowest oxygen concentration, and the averaged oxygen content is slightly decreased with increasing Si_3N_4 overlayer thickness. The biased Si_3N_4 are in general showing a lower oxygen concentration than the unbiased systems. This is explained by a denser material due to higher ion energy under the applied bias [42, 426]. Si films on TiN reduce the overall oxygen concentration slightly compared to TiN. Si_3N_4 and Si show a higher oxidation resistance than the pure TiN and protect it, if fully covered, from being oxidized. AFM measurements (sect. 6.3) show clearly that Si is not completely covering the TiN sublayer for thin films. The open voids between the Si grains allows the oxidation of the TiN sublayer and results in a higher oxygen concentration in the TiN/Si system compared to fully covering TiN/Si_3N_4 systems.

In AlN bilayers the oxygen concentration is very high. Both TiN and AlN have highly reactive surfaces, which result in easily contaminated samples even under UHV conditions. Three data points stand out (empty gray circles), which are measured for thin overlayers with a thickness $t = 0.4 - 0.5$ nm. The binding energy for Al 2p in those three points is 74.3 ± 0.3 eV and for the thicker layers E_B is 73.0 ± 0.1 eV, while TiN shows no significant change in the binding energy, neither for thin ($E_B = 455.3 \pm 0.3$ eV) nor thicker AlN overlayers ($E_B = 455.0 \pm 0.1$ eV). This indicates that in the thin AlN films the detected oxygen is bonded to Al atoms and forms AlN_xO_y. AlN samples with $t \leq 0.5$ nm have oxygen contamination between 6 at% and 12

---

[i] c_{oxy} is averaged over the first angle-resolved scan, i.e. the first 36 measurements. Please note that the absolute oxygen values have a relative error of about 10%. c_{oxy} in this section is only used to explain qualitatively the oxygen influence, hence no further effort has been made to obtain exact values for c_{oxy}.

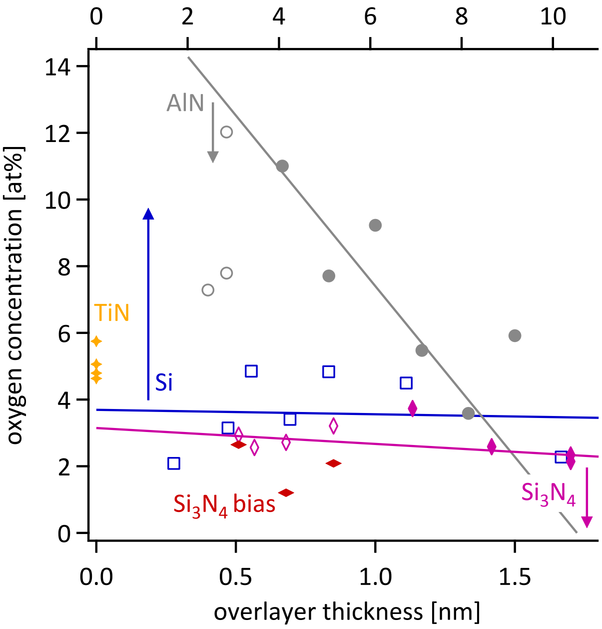

Figure 8.5: The oxygen concentration is shown as a function of the overlayer thickness of different materials. The plotted lines are linear fits of the data points. Presented are values for TiN (yellow stars), Si (blue squares), Si_3N_4 (purple diamonds), biased Si_3N_4 (tipped crimson diamonds) and AlN (gray circles). Data points represented by open symbols are neglected from the evaluation process (see fig. 8.9). Please note that the thickness scale for Si is plotted on the top axis, while the Al and Si_3N_4 thickness values are given on the bottom axis. Also note, there are two overlapping Si_3N_4 data points with a thickness of 1.7 nm.

at%. The thinnest sample ($t = 0.4$ nm) is not fully covering the TiN substrate, and hence the oxidation uptake of the sample surface lies between that of TiN and AlN. Samples with an AlN film of approximately 0.5 nm show a large statistical spread in their c_{oxy}. For very thin overlayers the relative error Δt_{rel} in the thickness is large ($\Delta t = 0.1$ nm $\rightarrow \Delta t_{\mathrm{rel}} = 20\%$, see sect. 6.2). The wide spread of c_{oxy} for $t \approx 0.5$ nm indicates a change of the surface morphology in that thickness range (see also sect. 6.3). Oxygen-free TiN/AlN interfaces with a thickness $t \leq 0.5$ nm could not be obtained under the available experimental conditions. Overlayers of AlN with a thickness $t < 0.5$ nm and of Si_3N_4 with $t \leq 1.0$ nm have an enhanced roughness ($S_a \geq 0.25$ nm) and do only partially cover the TiN sublayer (sect. 6.3). Hence they have to be evaluated separately in the evaluation process and are presented as open symbols in the data plots. All Si overlayers are excluded, since even $t \geq 10$ nm is not sufficient to have a closed cover on TiN. For the sake of completeness these thin overlayers, which do not fully cover the TiN sublayer, are partially shown as open blue squares in the data plots, but are not used in the further evaluation.

8.4 Sample charging and interfacial charging

The hurried reader is directly referred to the summarizing list in section 8.4.5, where the results of this section are summarized.

Figure 8.6 shows the binding energies E_B in a TiN/AlN bilayer system, which displays E_B of Al 2s and Ti $2p_{3/2}$ as a function of the AOE. It is clearly seen that bilayer systems with an AlN overlayer show an angular dependence of the binding energy E_B in the Al 2s and Ti $2p_{3/2}$ PE lines. For surfaces sensitive AOE (> 45°) the values for E_B scatter, slightly increase and oscillate. The effects causing changes of the binding energy with increasing AOE are explained in detail in section 7.5 and 7.1.

For AOE below 30° a clear increase in E_B with decreasing AOE is observed for both photoelectron lines (Al 2s and Ti $2p_{3/2}$). The increase between 30° and 0° of Al 2s is stronger than it is for Ti $2p_{3/2}$.

The shift of E_B not only depends on the AOE, but also on the film thicknesses of AlN. In figure 8.7 the extrapolated[ii] binding energy of Ti $2p_{3/2}$ and Al 2s are plotted versus the overlayer thickness t. It is clearly seen, that E_B at an AOE of 0° of Al 2s and Ti $2p_{3/2}$ decreases with the overlayer thickness t. The thickest sample with $t = 1.5$ nm shows a slight increase for Ti $2p_{3/2}$, also the value for Al 2s is higher than what is expected from the trend of the E_B curve of Al 2s.

A similar behavior is observed for TiN/Si_3N_4 interfaces, E_B also shows an angle dependence (not shown) and a thickness dependence (fig. 8.10). In the following first the change in E_B of the AlN bilayer systems is discussed and then explanations are given for the TiN/Si_3N_4 systems (sect. 8.4.4).

[ii] A linear fit function for values between 0° to 30° as indicated in fig. 8.6 is used.

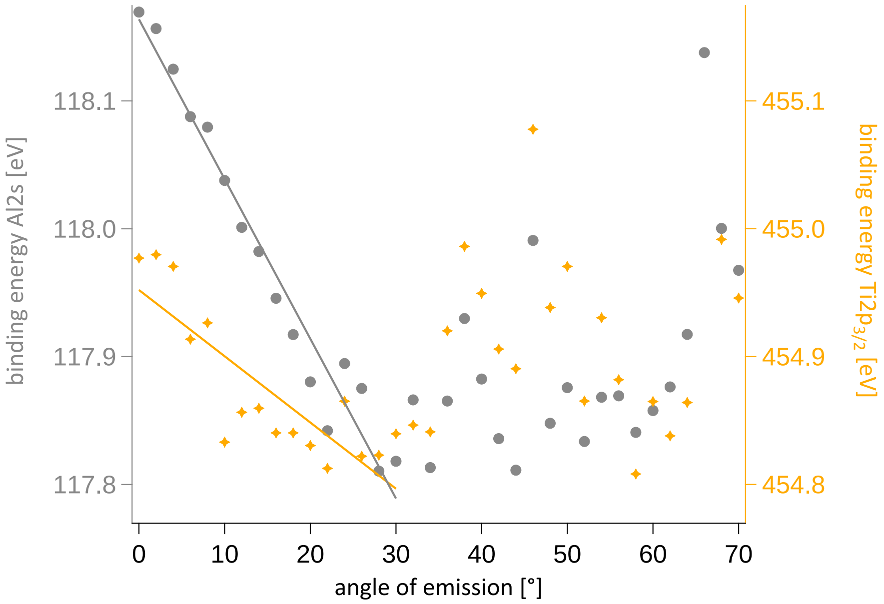

Figure 8.6: Binding energies of Al 2s and Ti 2p$_{3/2}$ are presented as a function of the AOE. The results are from a TiN/AlN bilayer system(t = 1.5 nm) and are averaged over three angle-resolved scans.

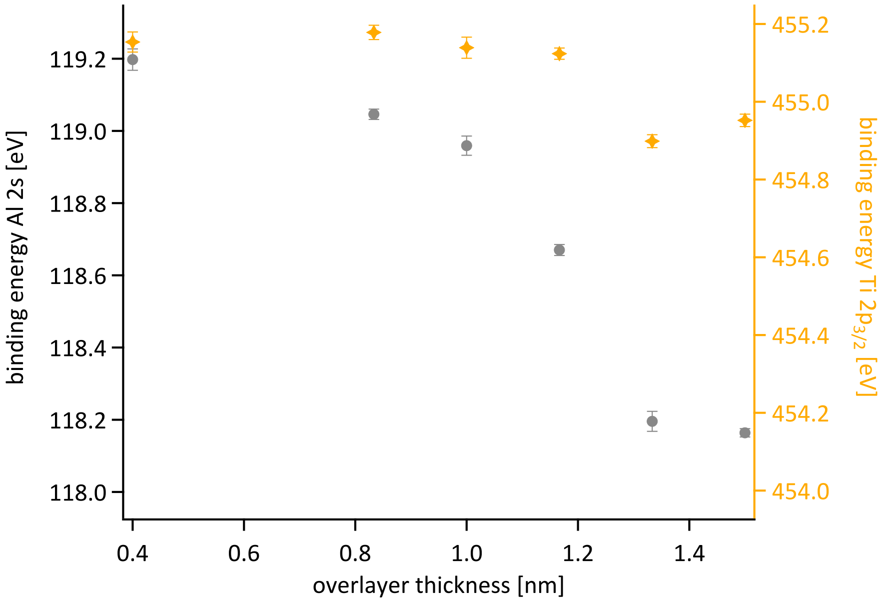

Figure 8.7: The binding energies E_B of Ti 2p$_{3/2}$ and Al 2s change with the thickness of the overlying AlN film. E_B are extrapolated to an AOE = 0°.

A systematic error due to an instrumental misalignment can be excluded (compare to section 7.1 and appendix D). An increase of E_B due to oxygen is also excluded since E_B shown in figure 8.7 is measured for bulk sensitive AOE only, and in these samples oxygen is observed mainly at the sample surface. The change in E_B correlated to surface oxygen is explained in the slight increase of E_B for higher AOE (see sect. 7.1 and 7.5).

For pure TiN a shift in E_B is observed and has been correlated to surface charging and a different surface coordination (sect. 7.1). A different surface coordination can be excluded at the interface, since it is assumed that all Ti atoms are terminated with six surrounding N atoms at the interface. A formation of a $Ti_{0.5}Al_{0.5}N$ phase at the interface is not expected from thermodynamical calculations [118–120](sect. 2.2.2). The hypothetical formation of $Ti_{0.5}Al_{0.5}N$ would also show no change in E_B . It has been shown that E_B for Al 2p in $Ti_{0.5}Al_{0.5}N$ alloys is equivalent to E_B of AlN (E_B (AlN)= 74.3 ± 0.3 eV) [88, 427].

Changes in the work function Φ of the substrate (see equation 3.1) have been reported for polymeric self-assembled monolayers (SAM) [428, 429] and result in a change of the measured E_B . However, an increase in the work function Φ of the substrate would results in a homogeneous lowering of E_B independent from the AOE.

The only remaining plausible explanation for the shift in E_B with the overlayer thickness is electrostatic charging. In the following the question is discussed whether this charge occurs in the complete sample (homogeneous charging), at the sample surface (surface charging) or at the interface (interfacial charging).

8.4.1 Homogeneous charging

Sample charging results in a shift in the binding energy of the PE lines. If the sample has an additional positive (negative) charge, then the additional Coulomb interaction can retard (accelerate) the electrons, i.e. a lowering (increasing) of E_{kin} of the emitted electrons. In the case of an *homogeneously* charged sample all PE lines should shift by approximately the same amount, i.e. energy differences between different photo lines remain constant. In figure 8.9 the energy difference ΔE_o, defined as the difference between the energy of Ti $2p_{3/2}$ and Al 2s in AlN (or Si 2p in the case of Si_3N_4) are displayed as a function of the overlayer thickness. It is clearly observed that the energy difference ΔE_o continuously increases with increasing overlayer thickness.

An explanation for the difference in the decrease of E_B could be that the core and valence orbitals are influenced differently due to the homogeneous charging. Al 2s electrons are closer to the Fermi level than the Ti $2p_{3/2}$ electrons and are more sensitive to the surrounding electron distribution and as a result are shifting slightly stronger than Ti $2p_{3/2}$. This is not the case in this bilayer system. A close comparison between figure 8.7 and 8.9 reveals that in fig. 8.7 the results of E_B for the sample with $t = 0.7$ nm are excluded. This sample has not been grounded with a Pt-frame (sect. 4.4), and therefore showed strong electrostatic charging in the spectrometer. (Binding energies of E_B(Ti $2p_{3/2}$)=461.1 eV and E_B(Al 2s)=124.9 eV were recorded for this sample without a Pt-frame.) The full spectrum shifts of more than 5 eV, but has no influence on the energy difference ΔE_o. Hence the increase in ΔE_o cannot be correlated to a *homogeneous* charging of the complete sample.

8.4.2 Surface charging

This paragraph deals with surface charging of only the AlN surface, in contrast to the next paragraph where a higher overlayer volume charging is discussed.

In general one would expect an increase in E_B for charged AlN overlayers, since AlN is an insulator [267] with a band gap between 5.4 eV and 6.3 eV [430, 431]. During the photoemission process electrons are emitted from the AlN overlayer and create PE holes. Those holes in the insulating AlN film are only slowly filled compared to the timescale of the photoemission process [428] and results in a positively charged AlN overlayer. This charge distribution interacts due to Coulombic forces with the PE of the AlN film and reduces their kinetic energy, i.e. increases E_B. If the charging is only located at the surface of AlN then E_B should increase with *increasing* AOE and not as it is observed with *decreasing* AOE.

Additionally surface charging would only result in an angle-dependent shift of the binding energy of Al 2s. The buried TiN signals would be not affected by a surface charging of AlN unless by a charge of opposite sign (i.e. accumulation of negative charge in TiN at the interface, see next section 8.4.3). Therefore surface charging can be ruled out.

8.4.3 Interfacial charging

Before discussing interfacial charging, it is essential to briefly review the influence of the overlayer thickness on the measurement geometry (sect. 5.3.2). A thicker overlayer results - in comparison to a thinner layer - in more information from the AlN "bulk"[iii] and more information from the TiN interface (fig. 5.3). In both PE lines (Ti $2p_{3/2}$ and Al 2s) E_B decreases with the increasing thickness t, i.e. E_B of Al 2s is lower in the bulk than it is at the interface, and E_B of Ti $2p_{3/2}$ is lower at the interface than it is in the bulk (fig. 8.8). At the same time the angle-resolved measurements show an increase in E_B with decreasing AOE (fig. 8.6), i.e. E_B of Al 2s is higher in the bulk and interface region than it is at the surface and E_B of Ti $2p_{3/2}$ is higher in the bulk than it is at the interface (fig. 8.8).

A negatively charged region results in a lowered E_B for PE emitted from this charged region (see section 8.4.1). Electrons emitted from a positively charged volume have an apparent higher E_B. The AR-XPS results and the change in E_B due to the thickness are hence indicating that the AlN interface region is positively charged and the TiN interface region has a negative charge accumulation.

[iii] "Bulk" in this context means a region not in the vicinity of the AlN surface or TiN/AlN interface.

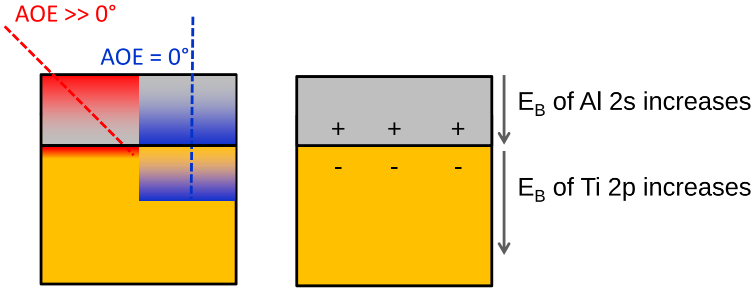

Figure 8.8: Sketch to describe the interface charging.

This charge accumulation is explained by the tendency of insulators such as AlN to charge positively as a consequence of the photoemission process. A charge build-up at an insulator/metal interface is balanced by charges of opposite sign in the metal [432]. Hence the positively charged AlN induces a negative charge accumulation at the TiN side of the interface. This interfacial charging is called *extrinsic* charging, since it is induced by an external photon source (X-rays).

The observed interfacial charging can also be explained by *intrinsic* interfacial charging. An intrinsic charge accumulation evolves at metal/semi-conductor contacts of bulk material. Band bending occurs at an interface of bulk metals and bulk semiconductors. The extent and the width of this band bending region are defined by the band gap, the work function, the Debye length and the depletion zone of the contact materials. The interfaces under investigation are thin and obey quantum size effects (QSE), i.e. for thin films in the range of the de Broglie wavelength of electrons, the electronic structure of the thin films is modified [433]. The determination of the exact electronic structure and hence the polarization requires theoretical calculations, which are beyond the scope of this thesis.

However, independent from any QSE, an interfacial charging is observed in these systems. In a macroscopic picture of the interface, electrons will flow from the valence band of the metal to the semiconductor or insulator (see sect. 2.2.2, fig. 2.3) and an electrostatic polarization is induced [27]. This intrinsic effect is heavily perturbated by applying an external electromagnetic field, hence it is assumed, that the intrinsic charging effect is rather small compared to the extrinsic charging. A separation of the intrinsic and extrinsic interfacial charging cannot be resolved with AR-XPS.

The decrease in the binding energy E_B with increasing overlayer thickness is correlated to the interfacial charging. The decrease in the Ti $2p_{3/2}$ energy line is less pronounced than it is for Al 2s. In the following this is explained by a much shorter depletion zone in TiN compared to AlN. The interfacial region of TiN/AlN has a gradient in the interfacial charging, which can at least on the "bulk" TiN side of the interface be explained by a depletion zone using band models. The depletion zone is described by the Debye length. For metals the Debye length is in general very small (<1 nm), while for insulators the Debye length can be several µm. The accumulated electrons on the TiN side of the interface are hence located within the first nm, while for AlN

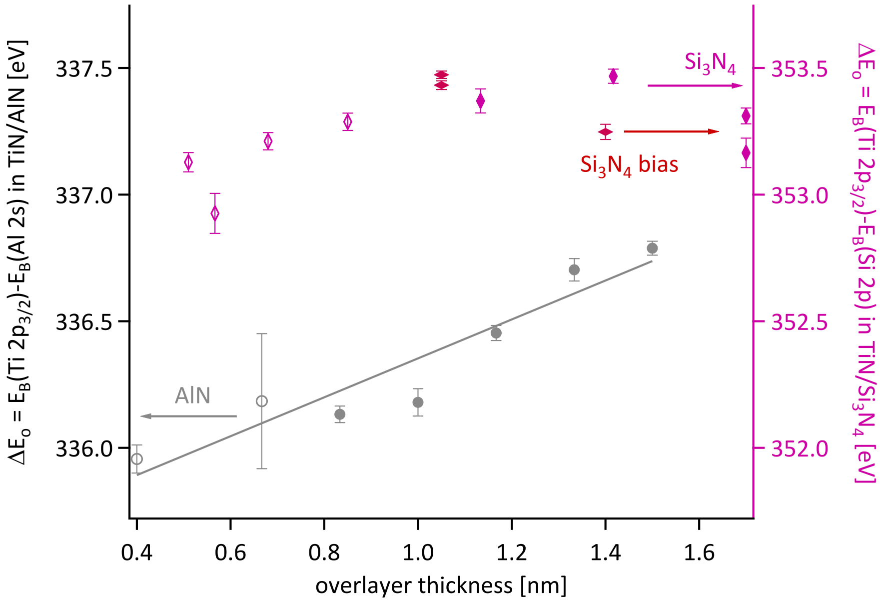

Figure 8.9: Binding energy difference of the photoelectron lines Al 2s - Ti $2p_{3/2}$ (gray) and Si 2p - Ti $2p_{3/2}$ (purple) versus the overlayer thickness covering TiN (001). The plotted line is a linear fit of the AlN data points. The same color code as in fig. 8.5 is used. Open symbols represent samples with a roughness of $S_a \geq 0.25$ nm (see introduction of this chapter).

photoelectron holes are created in the complete film. The angle-resolved measurement of the binding energy for TiN is probing more than just the first nm, also Ti $2p_{3/2}$ photoelectrons away from the depletion zone are detected. The influence on the binding energy is hence less pronounced in the Ti $2p_{3/2}$ than in the Al 2s, since AlN has a much larger charged volume that is detected by AR-XPS.

The energy difference ΔE_o of Ti $2p_{3/2}$ and Al 2s describes, independent from the description (QSE or macrosopic band models), the difference in the charging between overlayer and sublayer. ΔE_o is therefore a parameter that describes the interfacial charging.

8.4.4 Si_3N_4 systems

Si_3N_4 overlayers show also an angle dependence in E_B, which is similar to AlN bilayer systems explained by interfacial charging. The binding energies E_B of Si 2p and Ti $2p_{3/2}$ are decreasing until a thickness of 0.8 nm and from there on an increas occurs until the highest investigated thickness of 1.5 nm (fig. 8.10).

Section 8.1 shows that the first two to three monolayers of Si_3N_4 ($t < 0.7$ nm) have a different crystalline structure. DFT calculations by Marten et al. [194] and Ivashchenko et al. [195] indicate that those structures in first few monolayers are crystalline. The exact structure and composition is highly disputed (sect. 9.1), but all favored structures have either remaining free

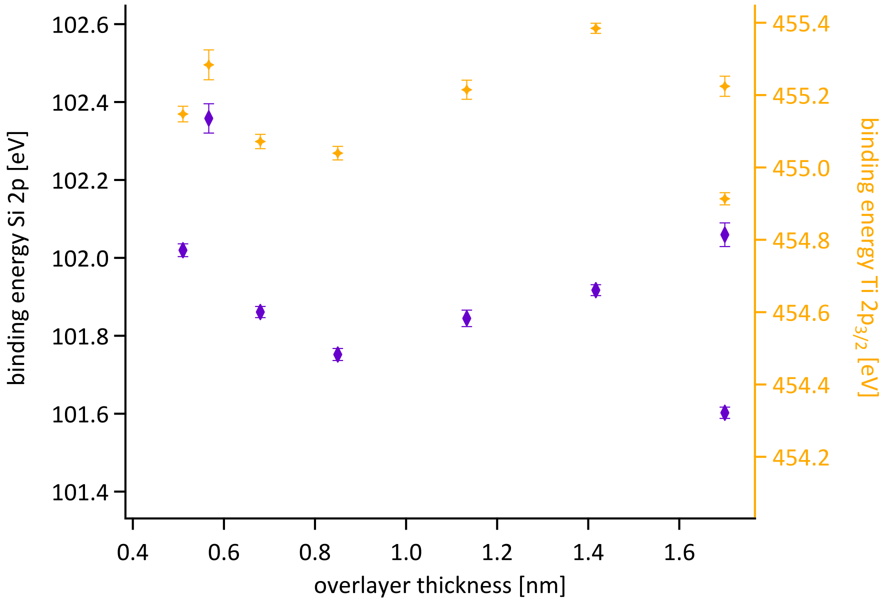

Figure 8.10: The binding energies E_B of Ti $2p_{3/2}$ and Si 2p change with the thickness of the overlying Si_3N_4 film.

charges at the Fermi level and can be considered as slightly metallic or have only a very small band gap. This unknown small band gap (sbg-) structure is in the following abbreviated as sbg-SiN_x . An explanation for the E_B decrease in thin SiN_x overlayers ($t \leq 0.8$ nm) could be that the thin sbg-SiN_x films are a semi-conductor and hence similar to AlN electrons accumulate at the TiN side of the interface while electron holes accumulate at the sbg-SiN_x side (see left side of figure 8.11). The change from decreasing to increasing E_B at $t \approx 0.8$ nm is an indication for a change in the Si_3N_4 structure.

The binding energy E_B of Si 2p and ΔE_o in TiN/Si_3N_4 systems increase between 0.8 nm and 1.4 nm. The decrease of E_B in AlN overlayer is explained by a positive interfacial charging of AlN. Following the argumentations presented for the AlN overlayer the increase in E_B of SiN_x between 0.8 nm and 1.4 nm is correlated to a negative interfacial charging. This might be explained with a shift of the charges to an interlayer between a sbg-SiN_x and an a-Si_3N_4 layer (see right side of figure 8.11). The a-Si_3N_4 layer has a much higher band gap of ≈4.9 eV [434] than the sbg-SiN_x structure resulting in a positive charge accumulation in the a-Si_3N_4 toplayer. The charge rearrange in sbg-SiN_x and TiN and is a result the binding energies of Si 2p and Ti $2p_{3/2}$ increase with increasing overlayer thickness.

The evaluation of Si_3N_4 overlayers thicker than 1.5 nm are again troublesome since the Ti $2p_{3/2}$ signal can hardly be resolved and strong deviations appear.

AFM measurement show that Si_3N_4 layers below $t \leq 0.8$ nm have a roughness of $S_a \geq 0.25$ nm and hence many effects can influence each other (e.g. oxygen contamination, island charging,

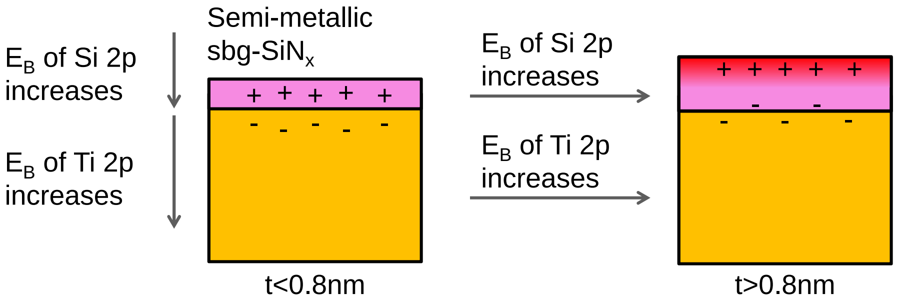

Figure 8.11: Sketch of SiN_x on TiN with different thickness. Left: $t < 0.8$ nm, right: $t > 0.8$ nm

sect. 6.3). Even though the E_B behavior with the overlayer thickness t could be explained with the different sbg-SiN_x structure in the first two ML, the higher roughness is an exclusion criterion that has to be considered. Hence all Si_3N_4 systems with a overlayer thickness below 1.0 nm are neglected from the further investigations since the higher roughness is disturbing the photoemission process and its evaluation. For the sake of completeness the results are shown in the figures as empty diamonds, but are not considered any longer in the evaluation or discussion of the results. The data for Si_3N_4 overlying films thicker than $t \geq 1.7$ nm is insufficient to give an exact statement on the charging situation, but can be still used for the evaluation of the interface ratio r_i (sect. 8.6).

In biased TiN/Si_3N_4 systems, where a substrate bias has been applied during the deposition of Si_3N_4, it is expected that the crystalline growth of sbg-Si_3N_4 is hindered. Already within the first monolayer an amorphous high band gap Si_3N_4 structure is formed. This should result in a higher interfacial charging (i.e. higher ΔE_o) in biased Si_3N_4 compared to unbiased Si_3N_4 systems. The few available data points are insufficient and more data is required for a precise statement regarding the charging situation in the biased TiN/Si_3N_4 interface.

8.4.5 Summary of sample and interface charging

In this subsection it has been shown that the increase of the binding energy E_B for lower AOE and the decrease in E_B of AlN as well as the increase of Si_3N_4 with increasing overlayer thickness are not correlated to:

- an instrumental misalignment
- forward focusing (see also sect.7.5)
- oxygen
- different interface coordination of TiN, AlN or Si_3N_4
- a formation of $Ti_{0.5}Al_{0.5}N$ or Ti_xSi_yN

- change in the work function of the substrate
- homogeneous sample charging
- surface charging of AlN or Si_3N_4

The change in the binding energies E_B is explained by extrinsic and intrinsic interface charging. In TiN/AlN bilayers systems the AlN overlayer charges positively, while electrons are accumulated at the TiN side of the interface. This interface polarization results in a decrease E_B of Al 2s and Ti $2p_{3/2}$ with increasing AlN film thickness. TiN/Si_3N_4 interfaces show a decrease in E_B for Si_3N_4 overlayers with an increasing thickness of up to 0.8 nm. For thicker Si_3N_4 films an increase in E_B is observed. The change in the binding energy behavior might be explained with a change in the growth pattern of Si_3N_4 at around 0.8 nm.

8.5 Interface model to describe r_i

The ratio r_i of shake-up and main peak intensity at the interface can be extracted from equation 5.1 using the least-square-method. r_i is a function of the AOE Θ, the IMFP λ, the bulk ratio r_b, the measured ratio R_m and the interface thickness δ. In order to have a reliable fitting process all parameters have to be either known (λ, r_b and δ) or are a variable (Θ) of the data R_m. The IMFP can be calculated according to section 3.8.1, and the bulk ratio r_b is obtained from experiments on pristine TiN (sect. 7.6). Hence all parameters except the interface thickness δ are known. The interface in this context is the region, in which the shake-up is influenced by the overlying material (see fig. 5.1). In the following subsection (sect. 8.5.1) the justification of the model of an interface thickness δ is investigated for shake-up ratios in bilayer systems. The uncertainties contained in the model are discussed in section 8.5.2, and it is explained why the values for r_i cannot be considered as absolute. In section 8.5.3 the influence of oxygen is analyzed.

8.5.1 Interface thickness δ

The model system as shown in fig. 5.1 assumes that there exists an interface region with a thickness δ. TEM studies elucidate that the interface of TiN and Si_3N_4 is atomically sharp (sect. 6.4). Hence it could be assumed that there is no extended interface region, i.e. $\delta = 0$. Inserting $\delta = 0$ in eq. 5.1 results in $R_m = r_b$, where R_m is the measured ratio and r_b the bulk ratio of pristine TiN. In this case the ratio of shake-up and main peak is constant over the full volume of the TiN sublayer. For this discussion the results are assumed to be independent from any XPD influence, and hence R_m is independent of the angle. The measured ratio R_m is obtained by averaging the ratio over the first 36 measurements, corresponding to a single angle scan from $\Theta = 0°$-$70°$. The averaged values for R_m are shown in figure 8.12. The error bars represent the standard deviation and are so high that they blur the data and make a clear statement impossible. Hence the averaged ratio is not a good choice to obtain significant results.

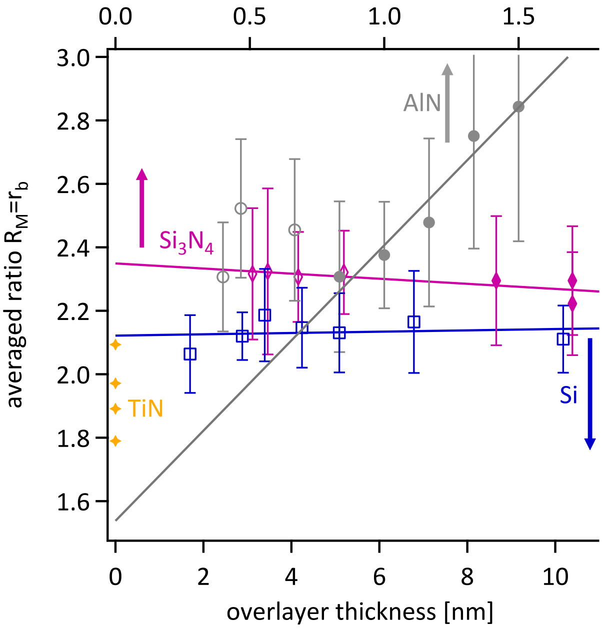

Figure 8.12: The ratio $R_m = r_b$ is plotted versus the overlayer thickness for $\delta = 0$. The same color code as in fig. 8.5 is used. Please note that the thickness scale for Si is plotted on the bottom axis, while the AlN and Si_3N_4 thickness values are given on the top axis.

Figure 8.13 shows the results for r_i as a function of δ, presented are the r_i values of three TiN/AlN samples of different thicknesses. The plotted points are obtained by fitting eq. 5.1 to the experimental data and using different values of δ in the fit function. The drawn fit curves express $r_i(\delta)$ as an exponential function (fig. 8.13). All AlN samples have in common that the interface ratio r_i increases with decreasing δ as well as with increasing overlayer thickness t. In the limit $\delta \to 0$ the interface ratio r_i results in $r_i(\delta) \to \infty$[iv] (compare also to fig. 8.14).

In the presented approach a critical interface thickness δ_c is defined; for interface regions thicker than δ_c the applied fit algorithm diverges (respectively r_i). Already in the vicinity of δ_c high values for r_i are obtained, which are physically meaningless. For AlN samples with a overlayer thickness $t = 0.8$ nm the interface thickness can be still chosen to be $\delta = 0.25$ nm, as is shown in figure 8.13. Films with $t = 1.0$ nm result for $\delta = 0.25$ nm in meaningless interface ratios r_i above 100 and for $t = 1.5$ nm the fit function diverges for $\delta = 0.25$ nm. Hence it is concluded that the critical interface thickness δ_c increases with the overlayer thickness t ($\delta_c \propto t$).

An empirical check of all measured results reveal that $\delta = 0.5$ nm is a value where the used fitting routine still converges for all samples. However, by choosing a fixed value for the interface ratio δ, uncertainties in the absolute values of r_i (sect. 8.5.2) are introduced to the evaluation process. If all data are evaluated with the parameter $\delta = 0.5$ nm, then the relation between $\Delta E_{3/2}$ and r_i is broken (sect. 8.6.2), which is an essential part of the shake-up theory (r_i should increase with decreasing $\Delta E_{3/2}$).

[iv] For $\delta \to 0$ eq. A.23 results in $R_m \approx r_i f + r_b g$ where $f \to 0$ and $g \to 1$, since the measured ratio R_m is always higher than the previously obtained bulk ratio r_b ($R_m > r_b$), hence $r_i \to \infty$ is obtained.

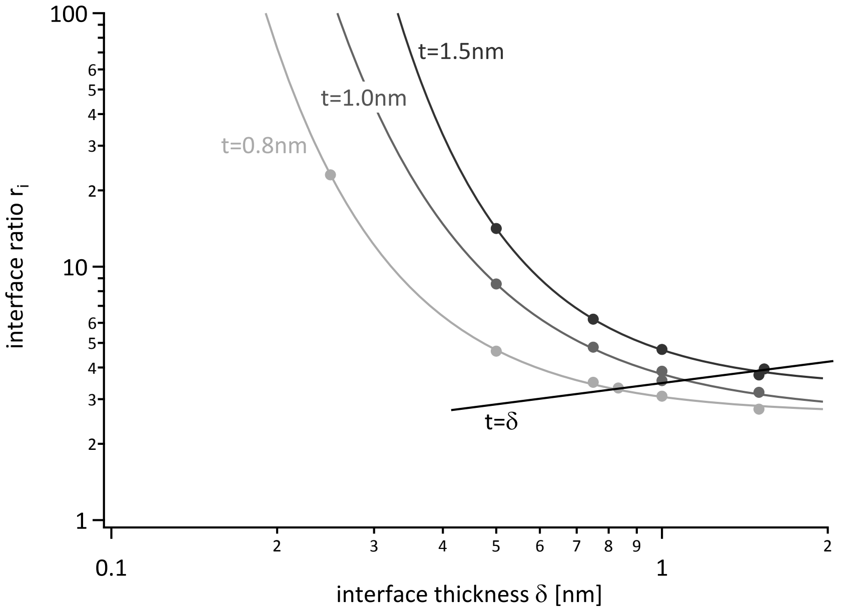

Figure 8.13: TiN/AlN bilayer system with different overlayer thicknesses t are compared to their interface ratio r_i, also shown is the curve for $t = \delta$.

Section 8.4.3 explains that charges are accumulated within the depletion zone at the interface. It is shown later in section 8.6.2 that the electron accumulation at the TiN side of the interface results in a decrease of the shake-up energy and influences the shake-up intensity. Hence it must be assumed that the depletion zone is the interface region where the shake-up properties are altered. The amount of interfacial charging and hence the width of the depletion zone depends on the overlayer thickness t (sect. 8.4.3). The width of the depletion zone cannot be determined exactly due to the complexity of QSE that occur at the interface. It can be assumed that the depletion zone at the TiN interface side is not wider than the positively charged region of the AlN or Si_3N_4 side of the interface. Therefore interface regions thicker than the covering film are physically not meaningful ($\delta \leq t$).

So far it has been shown in this section that $\delta_c < 0.5\,\text{nm} < \delta \leq t$. Best fitting results (lowest sum over all squared residual) are obtained for high δ[v]. Therefore it is reasonable to choose the highest value for δ, which is given by the overlayer thickness t ($\delta = t$).

For AlN bilayer systems with a thickness of $t \geq 0.8\,\text{nm}$ (see fig. 8.13) the ratio r_i is for all values of δ proportional to the overlayer thickness t. Also for $\delta = t$ the relation $r_i \propto t$ is still valid. TiN/Si_3N_4 bilayer systems show a similar behavior, where $r_i \propto t$ for overlying films with $t \geq 1.0\,\text{nm}$. Therefore the assumption $\delta = t$ can be used in a first approximation to evaluate the interface ratio r_i.

---

[v] if δ is allowed to adjust itself to R_m then the relation $\delta = 0.4e^{-1.7t} \approx 4t$ is obtained.

8.5.2 Uncertainties in interface ratios

All parameters (r_b, λ and δ) in the fit function (eq. 5.1) and the experimental data (R_m) have an error that contributes to the overall error of r_i. In this section the uncertainties due to these factors are revealed and discussed.

The self-consistent peak fitting procedure (sect. 5.2) used to extract the measured ratio R_m out of the Ti 2p spectrum is very precise for high intensity spectra. For high AOE ($\Theta > 50°$) the count rate decreases (fig. 7.20), and a low signal-to-noise ratio is obtained, i.e. the error ΔR_m depends on the AOE and is larger for high AOE. Longer measuring times[vi] are not feasible due to multiuser time management. XPD patterns are superimposing a clear interface signal and finally result in a highly disturbed measured shake-up ratio (fig. 8.17). An additional fit function would be required to modulate the curve due to XPD patterns (similar to sect. 7.5). The latter has been tested but cannot be resolved within this thesis. The diffraction patterns in r_i have not been considered in the fit algorithm (applying eq. 5.1 to the data), the fact that this is not resolved is also visible in the absolute sum of the quadratic deviation (goodness of fit), which remains as high as if the averaged values for r_i were used. The suggested formalism (eq. 5.1) results in higher absolute values for r_i and hence the relative errors are reduced.

The available experimental equipment does not allow a higher signal-to-noise ratio within the given time frame and hence the perturbing effects, can only be partially separated from the interface shake-up intensity. If all mentioned effects could be neglected, then the suggested fitting routine should find automatically the correct values for δ and r_i. In this case an appropriate error propagation will be possible and the error Δr_i can be approximated. The available data has those perturbing effects and hence the uncertainties in r_i can only be estimated. In the following the influence of a varying IMFP, δ and r_b are discussed.

The IMFP λ is calculated from theoretical data obtained from literature (sect. 3.8.1), and an error for this data is in general not given. A wide spread of IMFP values is found in literature, indicating that the IMFP is not precise. λ appears in the function A.23 of r_i only in combination with δ as a quotient δ/λ. Hence the error $\Delta\lambda$ is included in the error treatment of $\Delta\delta$.

Figure 8.14 shows a plot of the function $r_i(\delta, r_b)$ to illustrate the error due to the remaining two parameters r_b and δ. The function r_i changes hardly with r_b for large valueas of δ, while for small interface thicknesses $\delta \to 0$ the function shows a singularity. The error of r_i due to the uncertainty in r_b for values of $r_b = 1.9 \pm 0.1$, the value determined for TiN earlier, is considered small compared to the error due to the uncertainties in δ. In this work the interface thickness is set equal to the overlayer thickness $\delta = t$ (sect. 8.5.1). The minimal thickness, and hence the smallest interface thickness δ, used in this work is $t = \delta = 0.8$ nm. For $\delta = 0.8$ nm it is revealed from figure 8.14, that the error in r_i for $t \geq 0.8$ nm is rather small.

It is concluded that the uncertainties in the proposed fitting procedure to obtain r_i are reduced

---

[vi] In this thesis one angle-resolved scan lasted about 8 – 12 h, on each sample a minimum of 2 scans were performed.

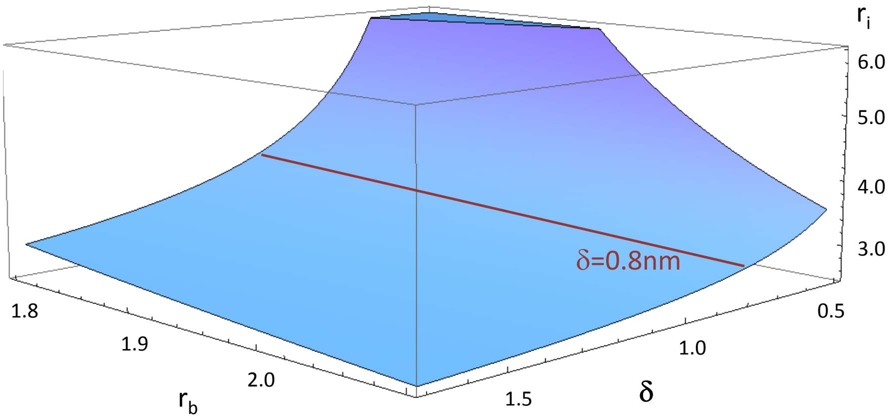

Figure 8.14: The interface ratio $r_i(\delta, r_b)$ is plotted as a function of the interface thickness δ and the bulk ratio r_b. The following values were used: $R_m = 2.3$, $\lambda = 2.4$ nm and $\Theta = 0°$. The red line indicates the values for $\delta = 0.8$ nm.

compared to the averaged values presented in figure 8.5. The influence of errors due to uncertainties in the bulk ratio r_b and the interface thickness δ (if $\delta \geq 0.8$ nm) are considered small and will not influence a qualitative interpretation of the data. A correct error propagation is not possible and therefore no error bars are shown for r_i. (In the following values are given for the interface ratio, please keep in mind that they can be used only for a qualitative evaluation.)

8.5.3 Oxygen influence on interface ratios

It has been shown in sect. 7.6 that oxygen interferes with the TiN shake-up signal. In this section the influence of oxygen on the shake-up ratio r_i at the interface is considered. The interface ratio r_i for different overlayer systems versus the averaged oxygen concentration c_{oxy} are presented in fig. 8.15. Additionally the semi-empirical function (eq. 5.9) is plotted, which describes the shake-up ratio as a function of c_{oxy} for pure TiN (fig. 7.21). All data points in the vicinity and below this semi-empirical curve can be explained completely with the oxygen content. Oxygen only influences the shake-up if it is within the TiN sublayer, surface oxygen bonded to Si or Al cannot contribute to the shake-up intensity.

The oxygen contamination is to a major part at the overlayer surface (compare to fig. 7.27 and sect. 8.3). The oxygen concentration c_{oxy} in fig. 8.15 is the overall concentration, and hence the oxygen contamination in the TiN sublayer is lower than the values given in figure 8.15. If only oxygen would influence the shake-up ratio, then the interface ratio r_i of Si_3N_4 would have to be below that of pure TiN, since pure TiN samples have a higher oxygen concentration than Si_3N_4 bilayers. Additionally AlN shows a decrease with the oxygen concentration, the opposite of what is expected for an oxygen correlation to the shake-up. Hence the high interface ratios for Si_3N_4 and AlN cannot be explained by the oxygen content at the interfaces. For Si overlayers the interface shake-up ratio is below that shown by the semi-empirically determined function

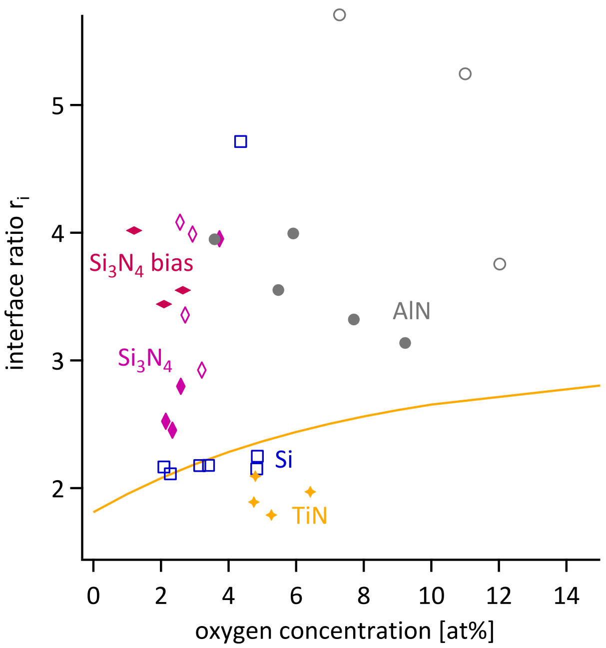

Figure 8.15: The interface ratio r_i is plotted versus the overall oxygen concentration c_{oxy}. Please note that for TiN the bulk ratio r_b has been used. The same color code as in fig. 8.5 is used.

that describes the oxygen influence at the TiN surface (eq. 5.9). Therefore the Si interface ratio r_i is explained by oxidation. TiN barely covered by Si oxidizes slowly, which results in an overestimated r_i. In the following the Si bilayer systems are not considered any further, since they neither form continuous nor oxygen-free interfaces.

8.6 Shake-up ratios r_i at different interfaces

The previous subsection 8.5 focuses on the procedure and the model to obtain r_i. This section deals with the results obtained from the applied fit algorithm and describes the physics behind the change in the interface ratio r_i.

The results for the measured ratio R_m of two different TiN/Si_3N_4 bilayer systems and the fit function $R_m(\Theta)$ (where Θ is the AOE) are plotted in figure 8.16 and 8.17. In the case of AlN as an overlying material the measured ratio R_m shows a clear difference between a 1.0 nm overlayer and a 1.5 nm layer of AlN (fig. 8.16). Si_3N_4 overlayers (fig. 8.17) are spreading wider and even though the quotient R_m of shake-up to main peak is used, diffraction pattern effects are still sensed in the measured ratio R_m. The XPD pattern is neglected by applying, similar to the evaluation of the bulk ratio, an exponential function for R_m, in this case eq. 5.1. It is in the nature of the function of R_m that it increases with the AOE independently from any XPD patterns. The measured data R_m scatter heavily around the fit function $R_m(\Theta)$ and the standard deviation increases for increasing AOE. For high AOE the signal intensity decreases (compare to fig. 7.18), hence induce a higher noise in the ratio R_m and result in a higher scattering for higher AOE. Most samples show an increase in R_m for $\Theta > 60°$, in some cases as shown in the sample with $t = 1.4$ nm in fig. 8.17 the intensity might even decrease due to XPD.

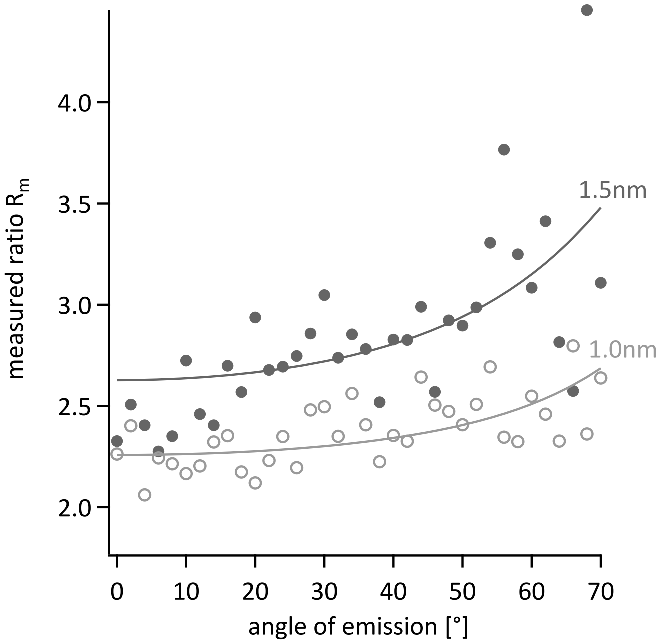

Figure 8.16: Results of angle-resolved measurements of TiN/AlN bilayers system with different diffraction patterns. Solid circles are for a thickness of $t = 1.5\,\text{nm}$ and empty circles correspond to $t = 1.0\,\text{nm}$.

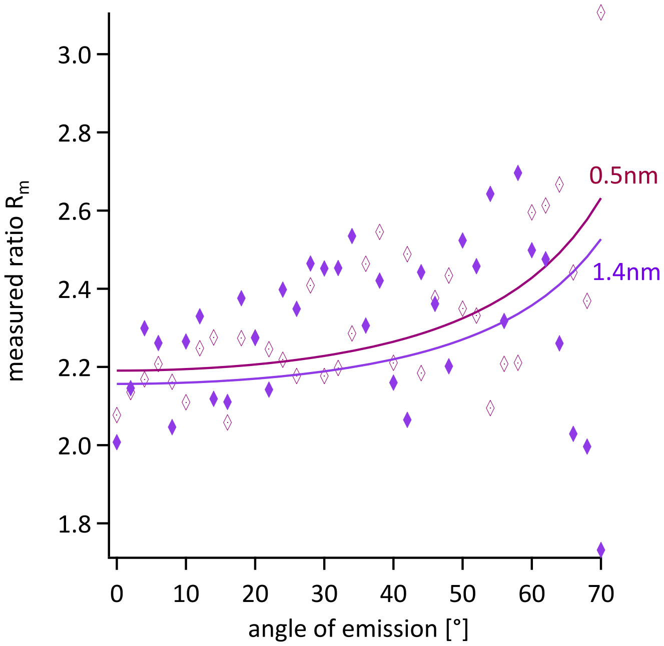

Figure 8.17: Results of angle-resolved measurements of TiN/Si_3N_4 bilayers system with different diffraction patterns. Solid diamonds are for a thickness of $t = 1.4\,\text{nm}$ and open diamonds correspond to $t = 0.5\,\text{nm}$.

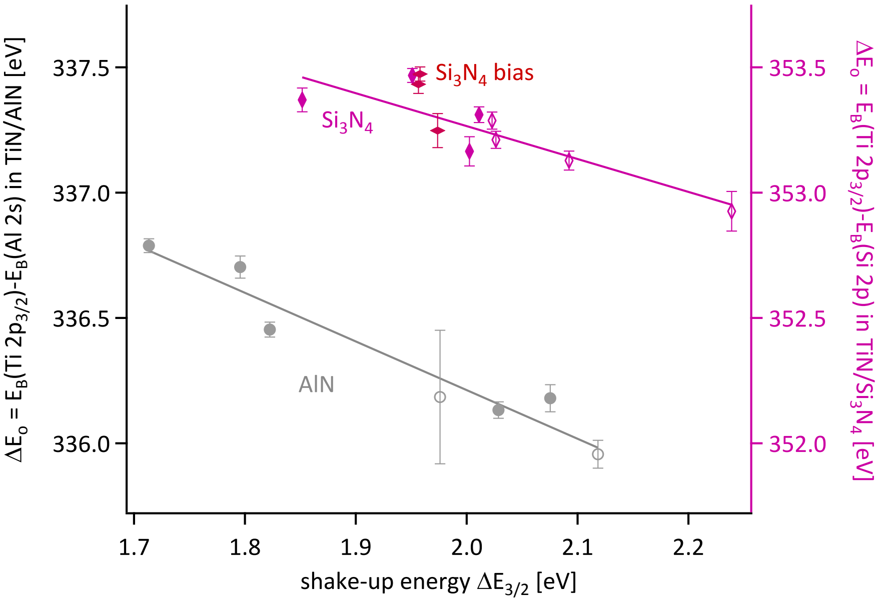

Figure 8.18: The shake-up energy $\Delta E_{3/2}$ and the energy difference ΔE_o between Ti $2p_{3/2}$ and Al 2s (or Si 2p) show a linear correlation. The same color code as in fig. 8.9 is used.

In pristine sc-TiN forward focusing occurs and the intensity I_{FF} (eq.5.4) shows maxima in preferred crystalline orientations, I_{FF} can be evaluated separately for the shake-up and the main peak (fig. 7.18). For overlayer systems this is an even more difficult task since the XPD pattern is damped by the overlayer passage, where electrons emitted from the sublayer TiN undergo inelastic scattering in e.g. Si_3N_4 . In principle it is possible to obtain an undiffracted ratio from the two fit values I_{FF} of shake-up and main, but the signal-to-noise rate of the XPS-device used in here is to low to exploit this approach.

8.6.1 Shake-up energy $\Delta E_{3/2}$ and interface charging

In section 8.4.3 it is shown and explained that interfacial charging occurs at TiN/Si_3N_4 and TiN/AlN interfaces. The energy difference ΔE_o between Ti $2p_{3/2}$ and Al 2s (or Si 2p) is a parameter that describes the electric potential between the charges at the interface. In this section the influence of the interfacial charging on the shake-up properties is investigated.

In figure 8.18 a clear correlation is revealed between the energy difference ΔE_o and the energy loss $\Delta E_{3/2}$ of the photoelectron due to the shake-up process. The shake-up energy $\Delta E_{3/2}$ decreases with increasing ΔE_o , which is proportional to the interfacial charging.

Figure 8.19 illustrates in a simple sketch of the valence band DOS of TiN (see also sect. 3.5) how interface charges can influence the shake-up energy $\Delta E_{3/2}$. In polarized metallic TiN the free electrons are partially occupying previously unoccupied states and reduce the distance between Fermi Energy and a pronounced maximum in the unoccupied states. The higher the

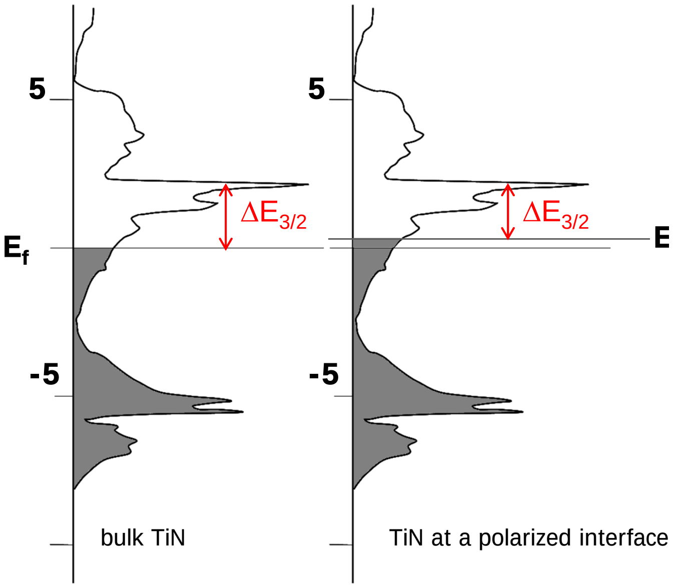

Figure 8.19: Sketch of a simple electron excitation model describing the shake-up process for bulk TiN and at a polarized interface. pDOS are adopted from Marlo and Milman [305].

interfacial charging the more free electrons are available to fill up more unoccupied states. Hence the shake-up energy $\Delta E_{3/2}$ required to excite electrons into the unoccupied states is reduced. In other words the energy difference $\Delta E_{3/2}$ between the two final states is directly correlated to energy difference ΔE_o of Ti 2p and Al 2s (or Si 2p), which is a valuable parameter to describe the interfacial charging.

The same trend is also observed for the unbiased and biased Si_3N_4 systems. It is remarkable that the correlation between interfacial charging ΔE_o and $\Delta E_{3/2}$ is independent from the quality (i.e. oxygen content and film coverage) or the structure of the sample.

This semi-classical approach explains the observations made regarding ΔE_o and $\Delta E_{3/2}$, but is not sufficient to explain the exact mechanisms behind the excitation process. Again TD-DFT calculations are required to gain more insight in the exact process.

8.6.2 Shake-up energy $\Delta E_{3/2}$ and intensity ratio r_i

The energy differences $\Delta E_{3/2}$ between the main and the shake-up peak is the energy required to promote an electron in the excited final state. The shake-up intensity is proportional to the transition probability from a ground state (main) to an excited state (shake-up). The shake-up process is quantum mechanically described by the time-dependent Schrödinger equation:

$$i\hbar\frac{\partial}{\partial t}\left|\psi(t)\right\rangle = H_t\left|\psi(t)\right\rangle \tag{8.1}$$

The solutions can only be approximated, e.g. by Dirac's perturbation theory (see e.g. Nolting [435]). The time-dependent 1st order transition probability $w_{ms}^{(1)}(t)$ from an initial (main) to a final state (shake-up) with the energies $E_m^{(0)}$ and $E_s^{(0)}$, respectively[vii], can be approximated [435] by:

$$w_{ms}^{(1)}(t) = \frac{1}{\hbar^2} \left| \int_o^t \langle E_s^{(0)} | \, H_{1,t_1} \, | E_m^{(0)} \rangle \exp\left(\frac{i}{\hbar} \left(\Delta E_{ms}^0 \right) t_1 \right) \mathrm{d}t_1 \right|^2 \tag{8.2}$$

where the shake-up energy is $\Delta E_{ms}^0 = E_s^{(0)} - E_m^{(0)}$. The equation 8.2 shows that the transition probability depends on the energy difference ΔE_{ms}^0, which the electron has to overcome. This is in agreement with the experiments, where the transition probability increases with decreasing $\Delta E_{3/2}$. For a further understanding of the correlation between $\Delta E_{3/2}$ and the shake-up ratio it is required to calculate the solutions for the above equation for all possible initial and final states. Those calculations are beyond the scope of this thesis.

The averaged function of $r_i(\Delta E_{3/2})$ over all systems (dashed line in fig. 8.20) is in good agreement with the uncovered TiN bulk values. All systems scatter slightly around this average. Unbiased and biased Si_3N_4 systems show a stronger decrease than AlN in the slope of $\Delta E_{3/2}$ versus r_i.

It has been discussed and explained that the values of r_i cannot be considered absolute (sect. 8.5.2). The interface ratio r_i depends on the interface thickness δ (see fig. 8.13) and on the quotient δ/λ, i.e. on t/λ (sect. 8.5.1). The difference in the inclination of $r_i(\Delta E_{3/2})$ is explained with uncertainties in δ/λ that arises due to the different IMFP, deposition rates and width of the depletion zone (i.e. δ) of the different systems.

In the case of Si_3N_4 overlayers, the applied bias results in denser materials and in the implantation of Argon (4at% in Si_3N_4 at a bias of -250 V). For denser materials a decrease in the IMFP λ is expected, which is not considered in the evaluation process. The deposition rates are flawed and result in an imprecise overlayer thickness t. Also the crude assumption $\delta = t$ is not absolute, since the depletion zone depends on the interface charging, which is not the same for different overlayer systems.

The qualitative correlation between r_i and $\Delta E_{3/2}$ has also been observed in the Ni shake-up peak [416], again for a detailed understanding of the shake-up process TD-DFT or CI calculations are required.

8.6.3 $\Delta E_{3/2}$ and r_i in TiN bilayer systems

The binding energy E_B of Ti 2p and Al 2s (or Si 2p) as well as their energy difference ΔE_o in TiN/AlN and TiN/Si_3N_4 bilayer systems depend on the thickness of the overlayer (sect. 8.4). Since ΔE_o , shake-up energy $\Delta E_{3/2}$ and intensity r_i are correlated (sect. 8.6.1), it is easily

---

[vii] the index (0) or (1) represents the 0th or 1st order in the series expansion used. Equation 8.2 cannot be used to calculate the exact transition probability, since neither initial nor final state are exactly known.

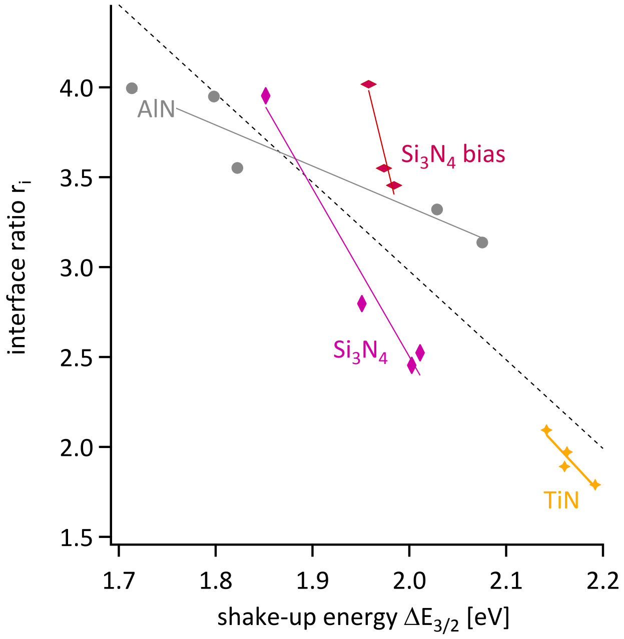

Figure 8.20: The shake-up energy $\Delta E_{3/2}$ versus the interface ratio r_i is shown for different bilayer systems. The dashed line represents the average over all samples independent from their overlying material or thickness. The bulk ratio r_b is also included for referencing. The same color code as in fig. 8.5 is used, lines are guides for the eyes.

concluded that $\Delta E_{3/2}$ and r_i must be influenced by the thickness t.

Figure 8.21 shows that the shake-up energy $\Delta E_{3/2}$ depends on the overlayer thickness t, similar to the binding energies of Ti 2p and Al 2s (or Si 2p). (Very thin films of AlN ($t < 0.8$ nm) and Si_3N_4 ($t < 1.0$ nm) are neglected from the evaluation for the reasons given in section 8.3.) The values obtained for $\Delta E_{3/2}$ of bilayer systems (see fig. 8.21) are all below the bulk values of pristine sc-TiN, where $\Delta E_{3/2}$ is 2.16 ± 0.04 eV (see fig. 7.6). Si_3N_4 bilayer systems show an increase in the shake-up energy $\Delta E_{3/2}$ with increasing overlayer thickness, while AlN bilayer systems reduce their $\Delta E_{3/2}$ with increasing overlayer thickness t. The shake-up energy of biased Si_3N_4 systems is almost constant. It is also clearly seen, that values of $\Delta E_{3/2}$ for thinner films (AlN $t \leq 0.8$ nm and Si_3N_4 $t < 1.0$ nm) scatter widely and do not fit in this description.

The decrease of $\Delta E_{3/2}$ in TiN/AlN bilayer systems with increasing t is explained with increasing charge accumulation ΔE_o at the interface (sect. 8.6.1). The increase of $\Delta E_{3/2}$ in TiN/Si_3N_4 systems is also correlated to an interfacial charging, which might be explained with a sbg-Si_3N_4 material in the first two monolayers of the Si_3N_4 grown on TiN(001) (sect. 8.4).

Figure 8.22 illustrates the results for the interface ratio r_i as a function of the overlayer thickness. All investigated bilayer systems reveal a higher r_i than the bulk ratio r_b for TiN. Fully covering AlN overlayers ($t \geq 0.8$ nm) have an enhanced interface ratio r_i that increases further with increasing thickness t. Si_3N_4 films on TiN decrease their ratio r_i with increasing thickness of Si_3N_4 over the full range of accessible thicknesses (for overlayer thicknesses higher than 1.7 nm the intensity of the Ti $2p_{3/2}$ PE line cannot be resolved sufficiently). The biased Si_3N_4 interface systems show no clear trend regarding the interface ratio r_i. The results of r_i depending on the overlayer thickness t are explained by a change in the interfacial charging (sect.

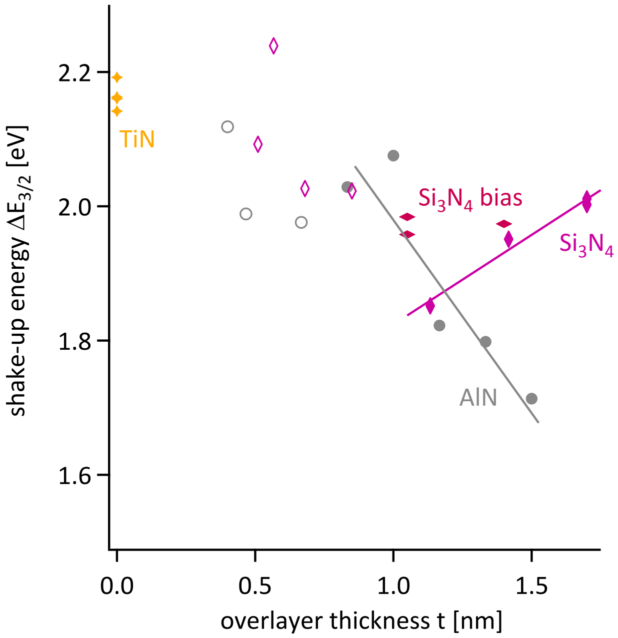

Figure 8.21: Energy differences $\Delta E_{3/2}$ of main and shake-up energy line versus the overlayer thickness are shown for different overlying materials. Empty symbols are not considered in the evaluation process (sect. 8.3). The same color code as in fig. 8.5 is used.

8.4), which alters $\Delta E_{3/2}$ (sect. 8.6.1) and hence influence the interface ratio r_i (sect. 8.6.2).

It is concluded that in all studied bilayer systems the interfacial charging depends on the thickness, morphology, crystalline structure and material of the overlying film. The energy difference ΔE_0 between Ti $2p_{3/2}$ and Al 2s (or Si 2p) is a valuable parameter describing the amount of interface charging. It is experimentally shown that the required shake-up energy $\Delta E_{3/2}$ to promote an electron in an excited state is correlated to the shake-up intensity ratio r_i. A lower energy difference $\Delta E_{3/2}$ results in a higher shake-up intensity. This relation between r_i and $\Delta E_{3/2}$ is independent of the overlying film material.

The gained insight on the physical mechanisms behind the shake-up process of the bilayer systems are summarized and discussed in the following section 8.7.

8.7 Discussion of bilayer systems

The shown results for the measured ratio R_m in figure 8.2 are only for one particular AOE=70° of each bilayer system. It is shown in the previous sections that many factors are influencing the R_m and that it is essential to evaluate an AR-XPS scan (0°-70°) in order to reveal the ratio r_i at different interfaces. High AOE (as used in fig. 8.2) have a low signal-to-noise ratio and therefore a measurement time of up to 45 min has been chosen. During this time the positions can slightly shift due to partial sample charging. As it is shown in the sections above, already small shifts of $\Delta E_B = 0.05$ eV are influencing the shake-up properties. The poor signal-to-noise ratio and the limited energy resolution are overcome by extrapolating the required data from many angle-resolved spectra.

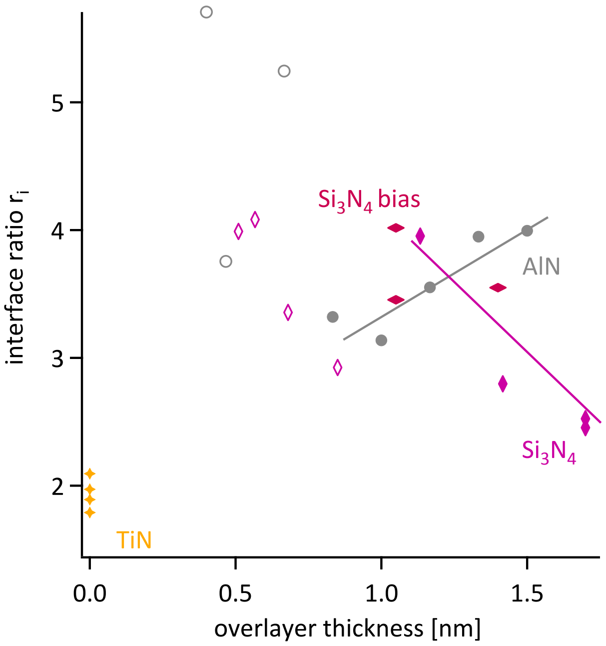

Figure 8.22: Interface ratios r_i as a function of the overlayer thickness t for interface systems on sc-TiN(001). For TiN the bulk ratio r_b is used. Lines are guides for the eyes. The same color code as in fig. 8.5 is used.

In the following subsections the results for each bilayer system are summarized and discussed.

8.7.1 Si overlayers

The TiN/Si bilayer systems studied show even for very thick 10 nm overlayer of Si still a fairly strong Ti 2p signal from the sublayer TiN. The depth information in standard XPS with an X-ray energy of 1486.6 eV is limited to approximately 4 – 5 nm and decays exponentially. Hence it is not expected that a strong Ti signal buried below a 10 nm overlayer is observed. AFM scans reveal that Si forms big islands on TiN(001), which do not fully cover TiN (sect. 6.3) when deposited at 800 °C. Lowering the deposition temperature to 500 °C decreases the roughness, but still results in an only partial coverage of the TiN sublayers. As a result TiN is directly observed past the 10 nm thick islands. Hence it is not surprising that the measured results for the shake-up (i.e. binding energy E_B and shake-up ratio r_i at the interfaces) are not much different from those obtained from pristine TiN (sect. 8.2 and 8.5.3). Compared to TiN only slightly lower oxygen concentration c_{oxy} and a slightly higher interface intensity (i.e. r_i) are found. The increase in r_i is a consequence of the oxidation of the uncovered areas of TiN (fig. 8.5). The evaluation of the Si films shows that it is essential to have uniform and fully covering overlayers to obtain reliable data for the interface interpretation. The prepared and investigated Si bilayers systems cannot add any information to the understanding of shake-ups at interfaces.

8.7.2 AlN overlayers

AlN layers on TiN with a thickness $t \geq 0.8$ nm are atomically flat ($S_a < 0.25$ nm, sect. 6.3) and hence, in contrast to Si overlayers, are flat enough to study the TiN/AlN interface by AR-XPS. The AlN overlayers have a high oxygen concentration at the surface due to the fairly high reactivity of AlN. It has been shown (sect. 8.5.3) that oxygen in the AlN layer is neither influencing the interface ratio r_i nor the energy differences $\Delta E_{3/2}$ (loss due to shake-up), the binding energy E_B or the energy difference ΔE_o between Ti $2p_{3/2}$ and Al 2s (sect. 8.4). XPD patterns indicate that all overlayers of AlN show a crystalline structure. The diffraction patterns and hence the AlN structures change from AlN film thicknesses of $t \leq 0.5$ nm to $t \geq 1.5$ nm.

To properly extract information on the materials system TiN/AlN, one has to differentiate between the sample charging (visible in E_B shift of all PE lines) and the charging at the interface region (observed in ΔE_0, sect. 8.4). ΔE_o is used to show that electrons are accumulated at the TiN/AlN interface and that the electron density at the interface increases with the AlN thickness t. With increasing electron density the energy difference $\Delta E_{3/2}$ decreases (sect. 8.6.1). Additionally the shake-up ratio r_i at the interface is increasing with decreasing shake-up energy $\Delta E_{3/2}$ for all overlayers (sect. 8.6). Therefore it is concluded that ΔE_o , $\Delta E_{3/2}$ and r_i are probing the electron density between the overlayer and the sublayer independent from the sample charging. AlN is a strong insulator for all known structures having a band gap of either 5.4 eV (zinc-blende) [430, 431], 5.8 eV (rocksalt) [203] or 6.3 eV (wurzite)[430, 431]. Due to the photoemission process the AlN overlayer is charged positively and this induces negative charges on the TiN side of the interface.

XPD patterns (sect. 8.1) show that AlN growth proceeds in a crystalline structure on TiN (001). The diffraction pattern changes for AlN thicker than $t > 0.8$ nm. The latter is explained with the formation of a stabilized rocksalt structure in superlattices of AlN/TiN(001) with an AlN layer thickness up to $t = 2.0$ nm, thicker interlayers of AlN crystallize in the hexagonal phase [154].

8.7.3 Si_3N_4 overlayers

The TiN/Si_3N_4 systems deposited have a partially similar behavior as the TiN/AlN bilayers. The averaged oxygen concentration is fairly low (below 4 at%), and the interface ratio r_i is above the values that can be explained with an oxygen contamination alone. AFM roughness measurements suggest that only samples with thickness $t > 1.0$ nm are flat enough to be analysed by AR-XPS, hence only a small window from $t > 1.0$ nm to $t < 1.7$ nm can be investigated. Thicker samples do not provide enough intensity from the TiN sublayer to obtain reliable data within a limited time frame. The binding energy E_B and the energy difference ΔE_o increase for thickness from 0.8 nm to 1.4 nm.

The decrease for a Si_3N_4 layer thickness of up to 0.8 nm is explained with theoretical considerations and experimental results that suggest that Si_3N_4 bilayer systems form in the first two

ML a small band gap (sbg-)SiN_x layer of a crystalline form of SiN_x (sect. 8.1), which might even behave metallic [194, 195]. In this case only a small interface charging between the SiN_x overlayer and the TiN sublayer will evolve. In this work it is proposed that the charged region shifts with increasing film thickness ($t \geq 0.8$ nm) away from the TiN/sbg-SiN_x interface region. It is suggested that after the termination of the first two monolayers, where a small band gap (sbg-)SiN_x is formed, an amorphous (a-) Si_3N_4 high band gap structure continues to grow. Due to the different band gaps in between the different SiN_x and Si_3N_4 structures the interface charge will move from the TiN/sbg-SiN_x interface towards a sbg-SiN_x/Si_3N_4 interface region (sec. 8.4).

The biased Si_3N_4 systems show no crystalline phase in the XPD pattern of Si 2p, and hence no SiN_x interlayer of presumably metallic character forms. The biased layer of Si_3N_4 is insulating and charges can build up immediately. This is observed in a thickness-independent shake-up energy $\Delta E_{3/2}$ of biased Si_3N_4 (fig. 8.21), at least for the small range of investigated thickness t.

For a comparison of the interface ratio r_i of biased and unbiased Si_3N_4 films more data is required. A precise statement regarding the charging situation and the shake-up intensity cannot be given based on the limited experimental data. However, it is expected that the amorphous high band gap Si_3N_4 structure results in a higher interfacial charging than for the sbg-SiN_x , which will be visible in an enhanced interface ratio r_i in the biased systems.

9 Effects of hardness enhancement

In section 8.4 it is shown that the shake-up intensity is strongly influenced by an intrinsic and extrinsic interface charging. Patscheider et al. [27] suggested that intrinsic interface polarization, probed by the shake-up intensity, results in an hardness enhancement in the TiN/Si_3N_4 nanocomposites. In the following section 9.1 it is argued that the suggested hardness enhancement due to interface polarization is most unlikely for thin one to two ML thick SiN_x interlayers.

9.1 Polarisation at the interface

The band model approach, as used by Patscheider et al. [27], is a continuum model used to describe an ideal infinite crystal. In an infinite three-dimensional crystal the high number of orbitals are so close that they overlap and form broad bands, separated by band gaps, which indicate forbidden energy regions. Most microscopic sized bulk systems can be considered as infinitely sized and the band model describes the electronic properties sufficiently. In the case of TiN/Si_3N_4 nanocomposites, where only a few monolayers of Si_3N_4 are separating the TiN grains, the Si_3N_4 cannot be described any longer as infinite in all dimensions. On the nanoscale the SiN_x matrix can be approximated as a two dimensional layer with a 0.5 nm thickness. Such a system would be physically described as a two-dimensional quantum well, resulting in discrete energy values [433, 436–438]. Hence the band model, as it is used in Patscheider et al. [27], is not a suitable description for this problem.

In section 8.6.2 it is shown that the shake-up intensity increases with the interfacial charging (i.e. polarization). Further it is explained that the intrinsic and extrinsic charge contributions cannot be separated (sect. 8.4), but only the intrinsic interfacial charging can contribute to the hardness enhancement. Following the argumentation of Patscheider et al. [27] the interface charging probed by the shake-up intensity is correlated to the hardness. This argumentation is not consistent with the obtained results in this thesis. The argumentation of Patscheider [47] implies that the intrinsic contributions of the interfacial charging are contributing to the shake-up intensity. If it is assumed that the shake-up is probing mainly the intrinsic interfacial charging, then the hardness should increase in a similar way as the polarization. This is not the case since the reported nanohardness enhancement has its maximum for SiN_x interlayers of one to two ML, while the polarization increases continuously at least until a thickness of ≈ 0.8 nm is reached.

According to Patscheider et al. [27] the polarization at the TiN/Si_3N_4 interface is a consequence of charge accumulation at TiN grain boundaries due to a lower highest occupied level in Si_3N_4. It has been shown by Hao et al. [76] on TiN(111)/SiNx/TiN(111) interfaces that in the case of β-like Si_2N_3, not only the Si 3p- N 2p form hybridized orbitals, but also the N atoms form hybridized bonds with the Ti atoms [187]. There is a high electron density in the Ti 3d orbitals [439, 440] at the Fermi level causing a metallic character of the interface system [187]. First principle calculations also favor other structures for the SiN_x interlayer [194, 195, 203], showing a similar metallic behavior for the reported SiN_x arrangement. Projected density of states (pDOS) calculations show further that Si_3N_4 layers between a stack of TiN with a Si_3N_4 thickness of three ML have in the second ML only a small band gap of $E_g \approx 1$ eV [194], while the first layers of both sandwich structures have a residual electron DOS at the Fermi level. The hardness enhancement is obtained for thicknesses of approximately two ML, where a metallic interface is expected and no polarization can form. The polarization picture as described by Patscheider et al. [27] is not suitable any longer for such highly hybridized metallic orbitals, where a Ti-N-Si hybrid orbital is formed at the TiN/Si_3N_4 interface. Even the term interface is difficult in this context; a clear plane separating Si_3N_4 and TiN cannot be drawn, since both phases share a N atom.

To summarize, the shake-up intensity cannot directly be correlated to an hardness enhancement, since intrinsic and extrinsic interfacial charging cannot be separated. Further it is argued that the suggested polarization by Patscheider et al. [27] most likely does not persist in TiN/Si_3N_4 interface systems, since the applied band model is not suitable for a structure with thickness of one to two ML, and since all favored interlayer structures have metallic states in the pDOS at the Fermi level or have at least a small band gap [194, 195, 203]. In such slightly metallic SiN_x interlayers no polarization can assemble and also no polarization strengthening can participate in the hardness enhancement of TiN/Si_3N_4 nanocomposites.

The question remains, where does the hardness enhancement originates from? In the following section 9.2 the effects contributing to the hardness are listed and discussed.

9.2 Contributing effects

In sect. 2.2.2 it has been explained that "bulk hardening effects" are not contributing to the hardness enhancement of nanocomposites. In this section it is discussed which and to what amount "thin film hardening effects" are participating in the total hardness of a nano composite containing two phases. The calculations below are only approximations intended to show qualitatively which effects are contributing under what conditions and to which extent.

Si_3N_4 has the possibility to grow in different structures and different orientations on top of the grain. In this approach only two orientations of the c-axis of the $\alpha-$ and $\beta-$ Si_3N_4 are considered: parallel ($\|$) and orthogonal ($\perp$) to the surface normal. *Ab initio* interface studies suggest several structures for the Si_3N_4 interlayer (sect. 2.2.4), three structures (α-, β- and c-Si_3N_4 system) are chosen to calculate the hardness of the nanocomposite, the used values are found in the appendix E (tab. E.1). For the c-Si_3N_4 system a lower (l) and an upper (up) limit is estimated to show how strong the hardness is deviating due to the wide range of reported hardness H, Young's modulus E and shear modulus G.

TiN/Si_3N_4 systems grow epitaxially under certain conditions [441], and hence fulfill the prerequisite for coherency stress τ_{coh} (eq. 2.3). Epitaxial growth only occurs for systems with a small lattice mismatch f, only for $f < 0.1$ the coherency stress is considered in the hardness calculations. Most superhard nanocomposites were deposited at elevated temperature (> 200 °C) [15, 115, 161, 422, 442], and thermal stress τ_t (eq. 2.4) will hinder the deformation process. Nanocomposites show a random orientation (i.e. no texture), therefore no texture effects are present [19, 81, 183]. Grain boundary sliding has been reported [111, 164, 166, 168] to be the dominating effect in uni-phase nanocrystalline film deformation. For nanocomposites it is assumed that the combination of two appropriate materials (i.e. high coherency) results in a strong interface, where grain boundary sliding is hindered [86, 443–445]. Hence the Koehler stress (eq. 2.6), as it is observed in multilayer systems, is applied to the hardness calculations of the nanocomposites, since dislocation movement through the interface material will be impeded in a similar way as in multilayers. Polarization strengthening is not used, since its existence in these nanocomposites is doubtful, as explained in sect. 9.1.

The Vickers hardness is further approximated by $H \approx 3\sigma$ [446–448], where σ is the yield stress. The latter is calculated by Schmidt's law that correlates the shear stress τ_s to yield stress σ using: $\sigma = \tau_s/m$ where m is the Taylor factor [449] with $m \approx 0.3$ for polycrystalline TMN with a B1-structure [183]. In this work the total hardness (H_{tot}) of the nanocomposite is approximated by:

$$H_{tot} = H_{coh} + H_t + H_K \tag{9.1}$$

where H_{coh} is the hardness enhancement due to coherency stress τ_{coh} (eq. 2.3), H_t is the hardness induced due to thermal stress τ_t (eq. 2.4) and H_K is the hardness increase due to Koehler stress (eq. 2.6) where $H_K = H_k + H_A$ and H_A is the hardness of the material A containing the dislocation activity (see appendix E).

Figure 9.1 reveals the results for the hardness approximations. The columns are divided in the stress components contributing to the total hardness. The gray shaded area represents the expected maximum hardness according to Fischer-Cripps et al. [28]. Black lines represent actual experimental data of TiN/Si_3N_4 nanocomposites from different groups fabricated under different conditions. The nanohardness values of the group of Vepřek [81, 82], who claimed hardness of more than 100 GPa, are not included here. Their reported results are disputed,

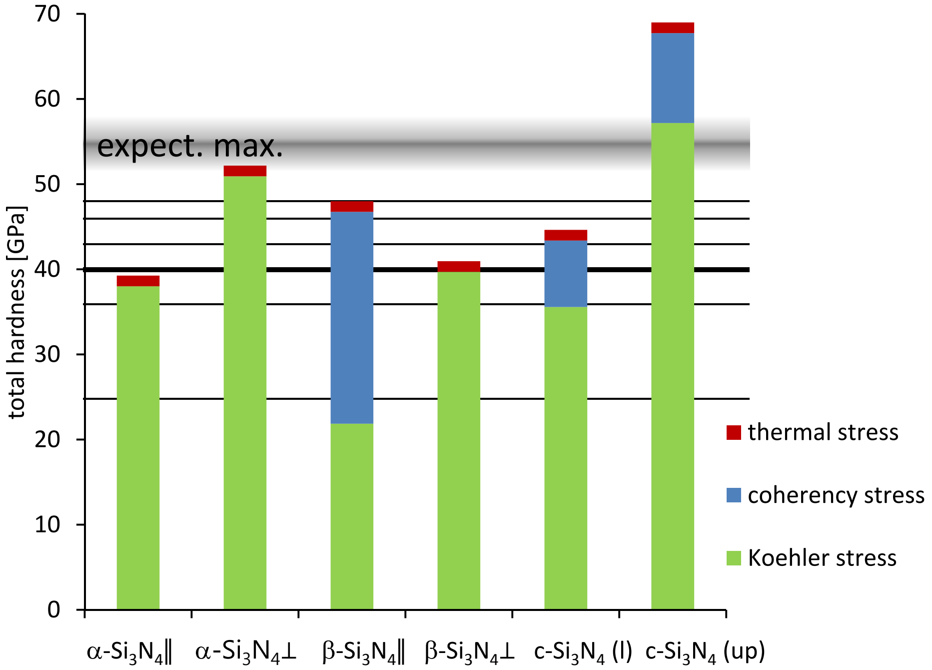

Figure 9.1: Different approximations for the total hardness of a nanocomposite with an α-Si_3N_4, β-Si_3N_4 and c-Si_3N_4 matrix between the nc-TiN grains. For α- and β- Si_3N_4 the hardness is calculated for parallel ∥ and orthogonal ⊥ growth behavior. In the case of c-Si_3N_4 a lower (l) and an upper (up) approximation for β-Si_3N_4 are estimated. All parameters used are found in table E.1 and the obtained hardness values are shown in table E.2. Experimental results from literature are marked by lines: at 55 GPa the expected maximum hardness [28] (shaded area); experimental maximum hardness data from different source are given at: 48 GPa [115], 46 GPa [15], 42 GPa [20], 40 GPa [422, 450, 451], 36 GPa [161], 25 GPa [452] (black lines, line thickness represents amount of literature with equal value). Please note, experimental settings (as deposition technique, temperature, bias etc.) are different for different publications. Nanohardness values obtained by the group of Veprek are not shown, due to their most likely heavily overestimated hardness [28].

since the claimed superhardness could not be reproduced, and it has been claimed that the measurement procedure of Veprek et al. [81, 82] shows some deficiencies and is hence overestimated by a factor of approximately two [28].

The Si_3N_4 hardness is an important factor in approximating the Koehler hardness (green). Using a low hardness value 30 GPa [453] or a high value 47 GPa [156] for the c-Si_3N_4 structure results directly in a lower (l) and an upper (up) hardness for the nanocomposite. The coherency stress (blue) is an effect of the lattice mismatch, and only participates if the mismatch is not so large that dislocations are introduced. For α-Si_3N_4 (∥ and ⊥) and β-Si_3N_4 (⊥) the lattice mismatch is above 0.2, and hence the coherency stress is not considered for those systems. The hardness increase due to thermal stress (red) contributes only to a minor part and is approximately 1.25 GPa for all samples.

Reviewing experimental data from the literature indicates that the experimental maximum hardness for TiN/Si_3N_4 nanocomposites is $H_{tot} \leq 48$ GPa, being more than a factor of two below the values of Vepřek's group. Real nanocomposites have not only one phase with one certain orientation between their grains (see fig. 2.4), but form different crystalline structures between the nc- grains. The interface structure depends on the adjacent grain orientation. The gap at grain junctions probably results in amorphous Si_3N_4 depots, and the grain-grain distances are not everywhere uniform. A multitude of different structures is expected, with the most prominent one being β- and c-Si_3N_4 . The averaged value of 49 GPa of all considered structures is in qualitative agreement with experimental data.

Note: Applying Schmidt's law and the Taylor factor are estimations that account only for isotropic materials and introduce some uncertainties [183]. The author is aware that the hardness values are an estimate that only explains qualitatively the observed hardness, but in a sufficient way.

The synthezised c-Si_3N_4 has been reported to be the third-hardest material after diamond and c-BN [454]. Hence the superhardness enhancement is explained by the stabilization of the c-Si_3N_4 phase for thin interlayer thicknesses [194, 195]. An additional hardening effect (as e.g. interface polarization) is not required to explain the observed phenomena.

Conclusions Part IV

Anyone who has never made a mistake
has never tried anything new.
- Albert Einstein

10 Conclusions

The aim of this thesis was to investigate the shake-up feature in the XPS spectra, specifically in the Ti 2p PE line of TiN interfaces to determine properties of bilayers of TiN with semiconducting and insulating overlayers. The background of this work was to investigate an assumed intrinsic interface polarization and utilize the quantitative description of the interface polarization to explain the hardness enhancement in TiN/Si_3N_4 nanocomposites.

The thesis' outcome is that the observed shake-up intensity changes are correlated to an intrinsic and an extrinsic polarization, which is induced due to the photoemission process. A self-consistent method for the TiN spectra evaluation is presented and a formalism to calculate the interface ratio r_i of shake-up and main peak is derived. Results for the bulk r_b and interface ratio r_i are presented and put into a physical context. A method has been found to change the shake-up energy. It is experimentally shown that the shake-up intensity increases with decreasing shake-up energy.

It is further explained why an intrinsic interface polarization in TiN/Si_3N_4 nanocomposites is unlikely. Values of nanohardness are summarized from literature and compared to hardness estimations using known hardness enhancement effects. It is shown that no additional hardness effect such as interface polarization is require to estimate the hardness of TiN/Si_3N_4 nanocomposites.

In order to gather the results described above many experimental, analytical and technical problems were solved and new approaches were tried. The achievements of this thesis are briefly presented in the following sections, describing:

- experimental improvements (sect. 10.1),
- data evaluation of TiN XPS spectra and a formalism to reveal the interface ratio r_i (sect. 10.2),
- XPS results of pristine oxygen-free TiN (sect. 10.3),
- interface characteristics (sect. 10.5),
- the shake-up origin and parameters influencing shake-up energy and intensity (sect. 10.4) and
- the interface polarization in TiN/Si_3N_4 nanocomposites, as well as effects contributing to the hardness (sect. 10.6).

10.1 Experimental achievements

In this work, unbalanced magnetron sputter deposition has been used to fabricate bilayer systems of TiN/AlN, TiN/Si_3N_4 and TiN/Si. The deposition process has been optimized to obtain oxygen-free TiN layers and oxygen-free bilayer systems. Any oxygen contamination results in a disturbing TiO_xN_y line, rendering the evaluation of the shake-up ratio problematic. Therefore oxygen contaminations have been kept at a minimum by transferring the samples in situ between deposition and analysis. An ultra high vacuum (UHV) transfer chamber has been designed and assembled to transfer the deposited samples without breaking the UHV. The design was chosen to reduce the pumping time and to guarantee pressures in the storage compartment below 5×10^{-10} mbar.

The encountered experimental problems (e.g. sample grounding) are described and have been successfully solved. Different techniques have been used to obtain information on bulk (XRD, RBS, XPD), surface (AFM, XRR, XPS) and interface (TEM, XPS) properties. The results obtained using these techniques verify that the TiN samples are single crystallinity (sc-) and oxygen-free, and the interfaces are atomically sharp.

10.2 Data processing

A self-consistent evaluation fitting routine of the XPS spectra of TiN is presented and used to evaluate the spectra of sc-TiN in detail. A big effort has been put in the correct identification of all peaks in the Ti 2p spectra, as well as deriving their peak shape and their intensities. It is found that the Tougaard BG in combination with Gauss-Lorentzian product line shapes (GL(20)) are describing the Ti 2p spectra well. The spin-orbit split main peaks Ti $2p_{1/2}$ and Ti $2p_{3/2}$, their corresponding shake-up features as well as first and second order bulk and surface plasmons are evaluated fulfilling the requirements to the intensity ratios of the spin-orbit split peak, its shake-up losses and plasmon losses.

Angle resolved measurements were used to extract the oxygen-free bulk ratio r_b of TiN bulk (shake-up to main peak ratio). The ratio r_b is obtained by extrapolation of AR-XPS spectra to oxygen-free conditions without having to use a damaging sputter cleaning procedures. Five different models have been suggested and compared to obtain the bulk ratio r_b. Additionally, an empirical equation is developed to express the bulk ratio r_b as a function of the oxygen content c_{oxy}.

10.3 Conlusions on pristine TiN

The sc-TiN has been thoroughly characterized by XRD polefigures, AFM and TEM imaging. A precise knowledge of effects influencing the XPS results of sc-TiN is essential, since sc-TiN is used as the sublayer for the bilayer system, and all interface signals have to be separated from the bulk properties. The bulk ratio of shake-up and main intensity is revealed by using an angle-resolved approach, where a value of $r_b = 1.9 \pm 0.1$ is extrapolated.

The bulk ratio is within the uncertainties independent of the crystalline structure of TiN, i.e. independent of the orientation ((001) or (111)) and independent of the degree of crystallinity (sc- or pc-). Also no difference in the bulk ratio is observed for TiN samples deposited with or without an applied substrate bias. An insufficient sample grounding results also to the same bulk ratio, but shows a much higher scattering in the shake-up ratio due to time-dependent fluctuations in the sample charging.

The shake-up energy depends on the total angular momentum of the emitted PE, for electrons emitted from Ti $2p_{1/2}$ a shake-up energy of $\Delta E_{1/2} = 1.78 \pm 0.07$ eV and for Ti $2p_{3/2}$ of $\Delta E_{3/2} = 2.16 \pm 0.04$ eV are found. XPD patterns are observed and angle-dependent patterns are resolved in the PE line intensities, the background and binding energy.

10.4 Conclusion shake-up

The obtained shake-up energy and intensity for bulk sc-TiN is explained by two final states of the ionized Ti atom in a crystalline network. A simple electron excitation model describes the changes in the shake-up energy qualitatively and the difference in $\Delta E_{1/2}$ and $\Delta E_{3/2}$ are explained by core hole-valence band coupling [420] (sect. 7.10). The obtained shake-up intensities for pristine TiN are above the expected values received by DFT calculations [290] for excitation process in single atoms. The higher intensity has been explained with band broadening and an reduced excitation energy (sect. 7.8). For a complete quantitative description of the shake-up feature it is required to perform further computational simulation (TD-DFT or CI).

Different overlayers on sc-TiN are used to change the shake-up energy at the interface. Hence a method is found that allows the fine tuning of the shake-up energy by varying the overlayer thickness or the overlayer material. The TiN interface studies reveal clearly that the shake-up energy decreases with increasing interfacial charging (sect. 8.4). Further it is revealed that a decreasing shake-up energy results in an increase in the shake-up ratio r_i (sect. 8.6.2). The gained insight on the shake-up feature is utilized to characterize the different bilayer systems (sect. 8.6.3).

10.5 Conclusion on bilayer systems

Different layer morphologies in TiN/Si_3N_4 , TiN/AlN and TiN/Si bilayers are observed using AFM. Si films deposited on TiN are not fully covering the TiN sublayer and exhibit island growth. Completely covering TiN/Si layers could not be prepared. Si_3N_4 and AlN films deposited on a TiN sublayer show atomically flat overlayers for Si_3N_4 films thicker than 1 nm and for AlN films thicker than 0.5 nm. TEM images verify that the prepared TiN/Si_3N_4 interfaces are atomically flat.

XPD patterns obtained using XPS reveal that AlN films grow epitaxially on sc-TiN(001) and that the crystalline structure changes between 0.8 nm and 1.5 nm. Si_3N_4 overlayers show similar XPD patterns indicating an epitaxial growth pattern for layers thinner than 0.7 nm, while thicker Si_3N_4 or biased Si_3N_4 films grow amorphous.

AR-XPS data illustrate that TiN/AlN and TiN/Si_3N_4 interfaces are charging, the resulting interfacial charging is altered by the overlayer structure and thickness. An interfacial charging modifies the shake-up energy. It is experimentally shown that a decrease in the shake-up energy is directly correlated to an increase in the shake-up intensity. Hence the overlayer thickness can be used to fine tune the shake-up energy and intensity.

10.6 Conclusions on interface polarization and superhardness

The observed polarization on the TiN/AlN and TiN/Si_3N_4 bilayer systems during the photoemission process is extrinsic and intrinsic. The difference between intrinsic and extrinsic interfacial charging cannot be resolved with AR-XPS.

In this thesis it is explained that the proposed band model to describe the interface polarization [27] is not appropriate. Recent DFT calculations [194, 195] indicate metallic or at least small band gap SiN_x structures for the first two monolayers of Si_3N_4 grown on TiN(111), and therefore no *intrinsic* interface polarization can build up at those interface.

The maximum hardness enhancement H_{tot} due to coherency stress, thermal stress and Koehler stress has been estimated and compared to literature. All reported hardness maxima for TiN/Si_3N_4 nanocomposites are found between 25 GPa and 48 GPa (with the exception of

Vepřek et al. [82], who reported values above 100 GPa). The estimated maximum hardness depends on the assumed interface structure and is between approximately 40 GPa and approximately 70 GPa. These calculated values are for ideal systems. It must be assumed that the interface structures in real nanocomposite systems are not ideal and are a mixture of different structures, which depend on the adjacent grain orientations. The estimated hardness values describe well the experimental data and no further hardness enhancement effect, as interface polarization, is required.

Nomenclature

α	thermal expansion coefficient
α_A, α_B	the thermal expansion coefficients of material A and B
$\bar{z}$	averaged mean value of all heights z_{ij}
β	FWHM of the 2Θ peak in XRD
χ	angle by which the sample in pole figures is tilted
Δ	optical path length
δ	interface thickness
$\Delta\mathrm{E}_{1/2}$	energy difference between the main and the shake-up peake of Ti $2\mathrm{p}_{1/2}$
$\Delta\mathrm{E}_{3/2}$	energy difference between the main and the shake-up peake of Ti $2\mathrm{p}_{3/2}$, also called shake-up energy
$\Delta\Theta$	shift between the maxima of main and shake-up in the XPD patterns
ΔE_o	energy difference between the PE lines of core holes of two materials indicating the interface charging
λ	inelastic mean free path
λ_x	wavelength of the X-rays
ν_A, ν_B	Poisson ratio of material A and B
Φ	work function, see eq. 3.1
ϕ	angle by which the sample in pole figures is rotated
ρ	density of the material
ρ_A	density of the material A
σ	yield stress

τ_k	maximum stress to move a dislocation through an interface
τ_s	shear stress
τ_t	thermal stress of a layer A in contact with layer B
τ_K	Koehler stress
Θ	in XPS: see AOE; in XRD: angle between sample surface and detector
Θ_s	angle between interface and slip plane
Θ_t	refracted angle described by Snell's law
A	contact area
B	universal parameter of the U2T, linear inclination
C	universal parameter of the U2T, describing the curvature
c_{oxy}	oxygen concentration
d	grain size
d_c	critical grain size, transition from HP to iHP
d_t	distance that an emitted electron travels through the solid
d_{hkl}	lattice constant for the (hkl) planes
d_i	distance between substrate and target in gun # i
E or E_{kin}	kinetic energy; E can also refer to the Young's modulus
f	total misfit
$F(E)$	background corrected spectra
f_{A-B}	lattice mismatch of two materials A and B
f_{exp}	experimental lattice mismatch
f_{theo}	theoretical lattice mismatch
G_A, G_B	shear modulus of material A and B respectively
H	hardness
H_0	intrinsic hardness
H_A	hardness of the material A containing the dislocation activity
H_K	hardness increase due to Koehler stress

H_{coh}	hardness enhancement due to coherency stress τ_{coh}
H_{tot}	total hardness
H_t	hardness induced due to thermal stress τ_t
$I(E)$	intensity at the kinetic energy E
I_0	intensity of the offset
I_A	measured intensity of an element A
I_c	intensity of the Cosinus decay
I_m	measured intensity signal
I_p	intensity of the Gauss distributed peak i at the angle $\cos(\theta_i)$
I_0	intensity of a pure element at the place of origin
I_{int}	interface intensity of a signal emerging from an interface
I_{oxy}	intensity of the oxygen contribution
I_S	intensity of the shake-up contribution
K	a shape factor used in the Scherrer equation
k	fitting parameter for the Shirley background
$K(E)$	inelastic electron scattering cross section
k_{HP}	material dependent strengthening coefficient
L	fitting parameter to adjust the background to its limits
m	Taylor factor
M_m	measured intensity of the main photoelectron line
n	an integer
p	pressure in mbar
P_{max}	maximum load
R_0	virtual ratio used for fitting
r_b	ratio of the shake-up intensity and main peak in the bulk material
r_i	ratio at the interface of the shake-up intensity and main peak intensity
R_m	ratio of the measured area intensity of the shake-up S_m and the main intensity M_m

S_a	arithmetic average surface roughness
S_m	measured intensity of the shake-up
T	exponential decaying tail value used to describe the line shape
T_m	melting temperature of the film
x	depth from where a signal emerges
z_{ij}	height at a position (i,j)
$\Delta\mathrm{E}$	an energy difference, if not described explicitly then it refers to the energy difference between shake-up and main peak
$\mathrm{E_F}$	Fermi level
$\mathrm{E_B}$	binding energy
a	linear fitting parameter
a-	X-ray amorphous
AFM	Atomic Force Microscopy
AFM	Atomic Force Microscopy
AL	attenuation length
AOE	angle of emission θ between detector and the normal to the sample surface
AR-XPS	Angle Resolved X-ray Photoelectron Spectroscopy
at%	atomic percent
B	element that is only contained in the bulk, e.g. Ti
b	exponential fitting parameter
bct	body-centered tetragonal
BG	background
c-	cubic
CVD	Chemical Vapor Deposition
DFT	Density Functional Theory
DOS	density of states
DS	Doniach-Sunjic line shape

EAL	effective attenuation length
EELS	Electron Energy Loss Spectroscopy
EPES	elastic peak electron spectroscopy
ERDA	Elastic Recoil Detection Analysis
ERDA	Elastic Recoil Detection Analysis
ESCA	Electron Spectroscopy for Chemical Analysis
fcc	face-centered cubic
FEM	finite element method
FRS	Frank-Read source
GL(x)	Gaussian Lorentzian product used to describe the line shape
HIKE	High Kinetic Energy XPS
HP	Hall-Petch
HR-TEM	High Resolution TEM
HV	high vacuum
iHP	inverse Hall-Petch
IMFP	inelastic mean free path
j	total angular momentum number
L	element that is only contained in the overlying material, e.g. Si
LEED	Low-Energy Electron Diffraction
LTAFM	low temperature atomic force microscope
MD	molecular dynamic
MgO	magnesium oxide
ML	monolayer, please note footnote in section 2.2.4
MTD	Mobile Transfer Device
nc-	nanocrystalline
pc-	poly crystalline
pDOS	projected DOS

PE	photoelectron
PES	Photoelectron Spectroscopy
PVD	Physical Vapor Deposition
QMD	quantum molecular dynamics
QSE	quantum size effects
RBS	Rutherford Backscattering Spectrometry
RT	room temperature
sbg-SiN_x	small band gap SiN_x , (sect. 8.4.4)
sc-	single crystalline
STM	Scanning Tunneling Microscopy
SZM	Sputter Zone Model
T	temperature during the deposition process
TEM	Transmission Electron Microscopy
TMN	transition metal nitride
TOA	take-off angle
TOF	Time Of Flight
TOF SIMS	time of flight secondary ion mass spectrometer
U2T	Universal Two-parameter Tougaard background
UBMS	Unbalanced Magnetron Sputtering
UHV	Ultra High Vacuum: $p < 10^{-9}$ mbar
UPS	Ultraviolet Photoelectron Spectroscopy
V1	volume between the storage and the connection part in the mobile transfer device
w-	wurtzite
XPD	X-ray Photoelectron Diffraction
XPS	X-ray Photoelectron Spectroscopy
XRD	X-Ray Diffraction
XRR	X-Ray Reflectometry
z	height of the sample in the XPS device

Bibliography

[1] Krzysztof Lukaszkowicz. Review of Nanocomposite Thin Films and Coatings Deposited by PVD and CVD Technology, Nanomaterials. InTech, Available from: http://www.intechopen.com/books/nanomaterials/review-of-nanocomposite-thin-films-and-coatings-deposited-by-pvd-and-cvd-technology, 2011.

[2] R. Hauert and J. Patscheider. From alloying to Nanocomposites—Improved performance of hard coatings. Adv. Eng. Mater., 2(5):247–259, May 2000.

[3] PRweb. Global coatings market to reach 8.7 billion gallons and US$107 billion by the year 2017, according to new report by global industry analysts, inc. web, March 2012.

[4] Coatings World. New study anylyzes world market for nanocoatings, March 2012.

[5] Nanostructured coatings. applications and markets to 2015. http://nanoposts.moonfruit.com, January 2011.

[6] European Commission. Commission recommendation of 18 october 2011 on the definition of nanomaterial text with EEA relevance, Nov. 2011.

[7] J. E Sundgren and H. T. G. Hentzell. A review of the present state of art in hard coatings grown from the vapor phase. J. Vac. Sci. & Technol. A, 4(5):2259–2279, 1986.

[8] S. Veprek. The search for novel, superhard materials. J. Vac. Sci. & Technol. A, 17(5):2401–2420, 1999.

[9] J. Musil. Hard and superhard nanocomposite coatings. Surf. Coat. Technol., 125(1–3):322–330, March 2000.

[10] Sam Zhang, Deen Sun, Yongqing Fu, and Hejun Du. Recent advances of superhard nanocomposite coatings: a review. Surf. Coat. Technol., 167(2–3):113–119, April 2003.

[11] R. Hauert. An overview on the tribological behavior of diamond-like carbon in technical and medical applications. Tribol. Intl., 37(11):991–1003, 2004.

[12] Aude Pelisson. Al-Si-N Transparent Hard Nanostructured Coatings. PhD thesis, University of Basel, 2009.

[13] A.D. Pogrebnyak, A.P. Shpak, N.A. Azarenkov, and V.M. Beresnev. Structures and properties of hard and superhard nanocomposite coatings. Physics-Uspekhi, 52:29, 2009.

[14] H. Hu, L. Onyebueke, and A. Abatan. Characterizing and modeling mechanical properties of nanocomposites–review and evaluation. J. Miner. Mater. Char. Eng., 9(4):275–319, 2010.

[15] Sam Zhang and Xiaomin Zhang. Toughness evaluation of hard coatings and thin films. Thin Sol. Films, 520(7):2375–2389, January 2012.

[16] Yongjun Tian, Bo Xu, and Zhisheng Zhao. Microscopic theory of hardness and design of novel superhard crystals. Int. J. Refract. Met. Hard Mater, 33(0):93–106, July 2012.

[17] J. A. Thornton. High rate thick film growth. Annu. Rev. Mater. Sci., 7(1):239–260, 1977.

[18] F. Vaz, L. Rebouta, P. Goudeau, J. Pacaud, H. Garem, J. P. Rivière, A. Cavaleiro, and E. Alves. Characterisation of Ti(1-x)SixNy nanocomposite films. Surf. Coat. Technol., 133-134:307–313, November 2000.

[19] Jörg Patscheider, Thomas Zehnder, and Matthieu Diserens. Structure-performance relations in nanocomposite coatings. Surf. Coat. Technol., 146-147:201 – 208, 2001.

[20] Zhiquan Guo, Gurdial Blugan, René Kirchner, Mike Reece, Thomas Graule, and Jakob Kuebler. Microstructure and electrical properties of Si3N4/TiN composites sintered by hot pressing and spark plasma sintering. Ceram. Int., 33(7):1223–1229, September 2007.

[21] Xuejie Liu, Yuan Ren, Xin Tan, Shiyang Sun, and Engelbert Westkaemper. The structure of Ti–Si–N superhard nanocomposite coatings: ab initio study. Thin Sol. Films, 520(2):876–880, November 2011.

[22] R.F. Zhang and S. Veprek. Phase stabilities of self-organized nc-TiN/a-Si3N4 nanocomposites and of TixSixNy solid solutions studied by ab initio calculation and thermodynamic modeling. Thin Sol. Films, 516(8):2264 – 2275, 2008.

[23] Tobias Marten, Eyvaz I. Isaev, Björn Alling, Lars Hultman, and Igor A. Abrikosov. Single-monolayer SiNx embedded in TiN: a first-principles study. Phys. Rev. B, 81(21):212102, June 2010.

[24] Stan Vepřek, Stephen G. Prilliman, and Simon M. Clark. Elastic moduli of nc-TiN/a-Si3N4 nanocomposites: Compressible, yet superhard. J. Phys. Chem. Solids, 71(8):1175–1178, August 2010.

[25] M. Parlinska-Wojtan, S. Meier, and J. Patscheider. Transmission electron microscopy characterization of TiN/SiNx multilayered coatings plastically deformed by nanoindentation. Thin Sol. Films, 518(17):4890–4897, June 2010.

[26] D. Craciun, N. Stefan, G. Socol, G. Dorcioman, E. McCumiskey, M. Hanna, C.R. Taylor, G. Bourne, E. Lambers, K. Siebein, and V. Craciun. Very hard TiN thin films grown by pulsed laser deposition. Appl. Surf. Sci., (0), 2011.

[27] Jörg Patscheider, Niklas Hellgren, Richard T. Haasch, Ivan Petrov, and J. E. Greene. Electronic structure of the SiN_x/TiN interface: A model system for superhard nanocomposites. Phys. Rev. B, 83(12):125124, March 2011.

[28] A.C. Fischer-Cripps, S.J. Bull, and N. Schwarzer. Critical review of claims for ultra-hardness in nanocomposite coatings. Philos. Mag., 92(13):1601–1630, 2012.

[29] S. Vepřek, A. Niederhofer, K. Moto, T. Bolom, H. D. Männling, P. Nesladek, and A. Dollinger, G.and Bergmaier. Composition, nanostructure and origin of the ultrahardness in nc-TiN/a-Si3N4/a- and nc-TiSi2 nanocomposites with HV=80 to >=105 GPa. Surf. Coat. Technol., 133-134: 152 – 159, 2000.

[30] Jan Procházka, Pavla Karvánková, Maritza G. J. Vepřek-Heijman, and Stan Vepřek. Conditions required for achieving superhardness of >= 45GPa in nc-TiN/a-Si3N4 nanocomposites. Mater. Sci. & Eng. A, 384(1-2):102 – 116, 2004.

[31] Florian Kauffmann, Baohua Ji, Gerhard Dehm, Huajian Gao, and Eduard Arzt. A quantitative study of the hardness of a superhard nanocrystalline titanium nitride/silicon nitride coating. Scr. Mater., 52(12):1269 – 1274, 2005.

[32] Florian Kauffmann, Gerhard Dehm, Veit Schier, Alexander Schattke, Thomas Beck, Stéphane Lang, and Eduard Arzt. Microstructural size effects on the hardness of nanocrystalline TiN/amorphous-SiNx coatings prepared by magnetron sputtering. Thin Sol. Films, 473(1):114 – 122, 2005.

[33] Stan Vepřek, Maritza G.J. Vepřek-Heijman, Pavla Karvankova, and Jan Prochazka. Different approaches to superhard coatings and nanocomposites. Thin Sol. Films, 476(1):1 – 29, 2005.

[34] Hans Söderberg, Magnus Odén, Tommy Larsson, Lars Hultman, and Jon M Molina-Aldareguia. Epitaxial stabilization of cubic-SiNx in TiN/SiNx multilayers. Appl. Phys. Lett., 88(19):191902–191902–3, May 2006.

[35] E. Lewin, P.O.Å. Persson, M. Lattemann, M. Stüber, M. Gorgoi, A. Sandell, C. Ziebert, F. Schäfers, W. Braun, J. Halbritter, S. Ulrich, W. Eberhardt, L. Hultman, H. Siegbahn, S. Svensson, and U. Jansson. On the origin of a third spectral component of C1s XPS-spectra for nc-TiC/a-C nanocomposite thin films. Surf. Coat. Technol., 202(15):3563–3570, April 2008.

[36] P. Rinke, M. Winkelnkemper, A. Qteish, D. Bimberg, J. Neugebauer, and M. Scheffler. Consistent set of band parameters for the group-III nitrides AlN, GaN, and InN. Phys. Rev. B, 77(7):075202, 2008.

[37] Qing-Miao Hu, Krisztina Kádas, Sture Hogmark, Rui Yang, Börje Johansson, and Levente Vitos. Hardness and elastic properties of covalent/ionic solid solutions from first-principles theory. J. Appl. Phys., 103(8):083505–083505–9, April 2008.

[38] J.S. Jeng and J.S. Chen. Effects of substrate bias and nitrogen flow ratio on the surface morphology and binding state of reactively sputtered ZrNx films before and after annealing. Appl. Surf. Sci., 255:8263–8269, 2009.

[39] Yingxue Xi, Huiqing Fan, and Weiguo Liu. The effect of annealing treatment on microstructure and properties of TiN films prepared by unbalanced magnetron sputtering. J. Alloys Compd., 496(1–2):695–698, April 2010.

[40] Nai-Yuan Ku. Thermal stability of Zr-Si-N nanocomposite hard thin films. Master's thesis, Linköping University, Institute of Technology, 2010.

[41] Erik Lewin, Mikael Råsander, Mattias Klintenberg, Anders Bergman, Olle Eriksson, and Ulf Jansson. Design of the lattice parameter of embedded nanoparticles. Chem. Phys. Lett., 496 (1-3):95 – 99, 2010.

[42] F. Magnus, A.S. Ingason, S. Olafsson, and J.T. Gudmundsson. Growth and in-situ electrical characterization of ultrathin epitaxial TiN films on MgO. Thin Sol. Films, 519(18):5861–5867, July 2011.

[43] Benny André, Erik Lewin, Ulf Jansson, and Urban Wiklund. Friction and contact resistance of nanocomposite Ti–Ni–C coatings. Wear, 270(9–10):555–566, April 2011.

[44] A. Rizzo, M.A. Signore, L. Mirenghi, L. Tapfer, E. Piscopiello, E. Salernitano, and R. Giorgi. Sputtering deposition and characterization of zirconium nitride and oxynitride films. Thin Sol. Films, 520(9):3532–3538, February 2012.

[45] Xiaoping Hu, Huijuan Zhang, Jiawei Dai, Geyang Li, and Mingyuan Gu. Study on the superhardness mechanism of Ti–Si–N nanocomposite films: Influence of the thickness of the Si3N4 interfacial phase. J. Vac. Sci. & Technol. A, 23(1):114–117, 2005.

[46] Yu-Hsia Chen, Kitty W Lee, Wen-An Chiou, Yip-Wah Chung, and Leon M Keer. Synthesis and structure of smooth, superhard TiN/SiNx multilayer coatings with an equiaxed microstructure. Surf. Coat. Technol., 146-147(0):209–214, September 2001.

[47] Jörg Patscheider. Nanocomposite hard coatings for wear protection. MRS Bull., 28(03):180–183, 2003.

[48] Lars Hultman, Javier Bareno, Axel Flink, Hans Soderberg, Karin Larsson, Vania Petrova, Magnus Oden, J. E. Greene, and Ivan Petrov. Interface structure in superhard TiN-SiN nanolaminates and nanocomposites: Film growth experiments and ab initio calculations. Phys. Rev. B, 75(15): 155437, 2007.

[49] Ingvar Lindgren. Chemical shifts in x-ray and photo-electron spectroscopy: a historical review. J. Electron Spectrosc. Relat. Phenom., 137-140:59–71, July 2004.

[50] Stefan Hüfner. Photoelectron spectroscopy: principles and applications. Springer, 2003. ISBN 9783540418023.

[51] A. Grill. Diamond-like carbon: state of the art. Diamond Relat. Mater., 8(2):428–434, 1999.

[52] A. A. Voevodin and J. S. Zabinski. Superhard, functionally gradient, nanolayered and nanocomposite diamond-like carbon coatings for wear protection. Diamond Relat. Mater., 7(2):463–467, 1998.

[53] N. H. Cho, K. M. Krishnan, D. Veirs, M. D. Rubin, C. B. Hopper, B. Bhushan, and D. B. Bogy. Chemical structure and physical properties of diamondlike amorphous carbon films prepared by magnetron sputtering. J. Mater. Res., 5(11):2543–54, 1990.

[54] C. A. Charitidis. Nanomechanical and nanotribological properties of carbon-based thin films: A review. Int. J. Refract. Met. Hard Mater, 28(1):51–70, 2010.

[55] William D. Sproul, Paul J. Rudnik, and Carl A. Gogol. The effect of target power on the nitrogen partial pressure level and hardness of reactively sputtered titanium nitride coatings. Thin Sol. Films, 171(1):171–181, April 1989.

[56] U. Helmersson, S. Todorova, S. A. Barnett, J. and E. Sundgren, L. C. Markert, and J. E. Greene. Growth of single-crystal TiN/VN strained-layer superlattices with extremely high mechanical hardness. J. Appl. Phys., 62(2):481 –484, July 1987.

[57] P. B Mirkarimi, L. Hultman, and S. A Barnett. Enhanced hardness in lattice-matched single-crystal TiN/V0.6Nb0.4N superlattices. Appl. Phys. Lett., 57(25):2654–2656, December 1990.

[58] Sung Hoon Kim, Young Joon Baik, and Dongil Kwon. Analysis of interfacial strengthening from composite hardness of TiN/VN and TiN/NbN multilayer hard coatings. Surf. Coat. Technol., 187 (1):47–53, October 2004.

[59] Laurence Vel, Gérard Demazeau, and Jean Etourneau. Cubic boron nitride: synthesis, physicochemical properties and applications. Mater. Sci. & Eng. B, 10(2):149–164, October 1991.

[60] Takashi Taniguchi, Minoru Akaishi, and Shinobu Yamaoka. Mechanical properties of polycrystalline translucent cubic boron nitride as characterized by the vickers indentation method. J. Am. Ceram. Soc., 79(2):547–549, May 1996.

[61] Natalia Dubrovinskaia, Vladimir L Solozhenko, Nobuyoshi Miyajima, Vladimir Dmitriev, Oleksandr O Kurakevych, and Leonid Dubrovinsky. Superhard nanocomposite of dense polymorphs of boron nitride: Noncarbon material has reached diamond hardness. Appl. Phys. Lett., 90(10): 101912–101912–3, March 2007.

[62] S L Qiu and P M Marcus. Structure and stability under pressure of cubic and hexagonal diamond crystals of C, BN and Si from first principles. J. Phys.: Condens. Matter, 23(21):215501, June 2011.

[63] S. H. Fleming. U.S. Patent 109,879,4, 1912.

[64] C. D Reedy. CHEMICAL VAPOR DEPOSITION COATINGS ON TITANIUM. U.S. Patent 3,787,223, 1974.

[65] J.-E. Sundgren, B.-O. Johansson, and S.-E. Karlsson. Mechanisms of reactive sputtering of titanium nitride and titanium carbide I: influence of process parameters on film composition. Thin Sol. Films, 105(4):353 – 366, 1983.

[66] T. Sato, M. Tada, Y.C. Huang, and H. Takei. Physical vapor deposition of chromium and titanium nitrides by the hollow cathode discharge process. Thin Sol. Films, 54(1):61–65, October 1978.

[67] Kazuo Nakamura, Konosuke Inagawa, Kazuyuki Tsuruoka, and Souji Komiya. Applications of wear-resistant thick films formed by physical vapor deposition processes. Thin Sol. Films, 40: 155–167, January 1977.

[68] F.V. Bernus, H. Freller, and K.G. Günther. Vapour-deposited films and industrial applications. Thin Sol. Films, 50:39–48, May 1978.

[69] Jeanine T. DeMasi-Marcin and Dinesh K. Gupta. Protective coatings in the gas turbine engine. Surf. Coat. Technol., 68-69:1–9, December 1994.

[70] Sankar Moni Borah, Arup Ratan Pal, Heremba Bailung, and Joyanti Chutia. Optimization of plasma parameters for high rate deposition of titanium nitride films as protective coating on bell-metal by reactive sputtering in cylindrical magnetron device. Appl. Surf. Sci., 254(18):5760–5765, July 2008.

[71] Hsyi-En Cheng and Yao-Wei Wen. Correlation between process parameters, microstructure and hardness of titanium nitride films by chemical vapor deposition. Surf. Coat. Technol., 179(1): 103–109, February 2004.

[72] A. Mumtaz and W. H Class. Color of titanium nitride prepared by reactive dc magnetron sputtering. J. Vac. Sci. & Technol., 20(3):345–348, March 1982.

[73] S. Niyomsoan, W. Grant, D. L. Olson, and B. Mishra. Variation of color in titanium and zirconium nitride decorative thin films. Thin Sol. Films, 415(1-2):187–194, August 2002.

[74] Li Shizhi, Shi Yulong, and Peng Hongrui. Ti-Si-N films prepared by plasma-enhanced chemical vapor deposition. Plasma Chem. Plasma Process., 12(3):287–297, 1992.

[75] Stan Veprěk. Superhard nanocomposites: Recent progress in the understanding of their preparation and properties and large-scale industrial applications in dry and fast machining. In "International Conference on Nanotechnology and Advanced Materials 2007", 2007.

[76] Shiqiang Hao, Bernard Delley, Stan Veprek, and Catherine Stampfl. Superhard nitride-based nanocomposites: Role of interfaces and effect of impurities. Phys. Rev. Lett., 97(8):086102, 2006.

[77] A.G. Dias, J.H. van Brenda, P. Moretto, and J. Ordelman. Development of TiN-Si3N4 nano composite coatings for wear resistance applications. J. Phys. IV, 5:C5–831, 1995.

[78] Heon-Jin Choi, Kyeong-Sik Cho, June-Gunn Lee, and Young-Wook Kim. R-Curve behavior of silicon Nitride–Titanium nitride composites. J. Am. Ceram. Soc., 80(10):2681–2684, January 1997.

[79] F.-J. Haug, P. Schwaller, J. Wloka, J. Patscheider, A. Karimi, and M. Tobler. Stoichiometry dependence of hardness, elastic properties, and oxidation resistance in TiN/SiNx nanocomposites deposited by a hybrid process. J. Vac. Sci. & Technol. A, 22(4):1229–1234, 2004.

[80] Frédéric Deschaux-Beaume, Thierry Cutard, Nicole Fréty, and Christophe Levaillant. Oxidation of a silicon nitride-titanium nitride composite: Microstructural investigations and phenomenological modeling. J. Am. Ceram. Soc., 85(7):1860–1866, July 2002.

[81] A. Niederhofer, P. Nesládek, H. D. Männling, K. Moto, S. Veprek, and M. Jílek. Structural properties, internal stress and thermal stability of nc-tin/a-si3n4, nc-tin/tisix and nc-(ti1-yalysix)n superhard nanocomposite coatings reaching the hardness of diamond. Surf. Coat. Technol., 120-121:173 – 178, 1999.

[82] S. Veprek, A. Niederhofer, K. Moto, P. Nesládek, H. Männling, and T. Bolom. Nanocomposites Nc-TiN/a-Si3N4/a- and Nc-TiSi2 with hardness exceeding 100 GPa and high fracture toughness. MRS Online Proc. Lib., 581:null, 1999.

[83] Chunsheng Lu, Yiu-Wing Mai, and Yao-Gen Shen. Recent advances on understanding the origin of superhardness in nanocomposite coatings: A critical review. J. Mater. Sci., 41(3):937–950, 2006.

[84] W. J. Meng, X. D. Zhang, B. Shi, R. C. Tittsworth, L. E. Rehn, and P. M. Baldo. Microstructure and mechanical properties of Ti–Si–N coatings. J. Mater. Res., 17(10):2628–2632, 2002.

[85] S. Veprek, H.-D. Männling, P. Karvankova, and J. Prochazka. The issue of the reproducibility of deposition of superhard nanocomposites with hardness of >=50 gpa. Surf. Coat. Technol., 200 (12-13):3876 – 3885, 2006.

[86] S. Veprek and S. Reiprich. A concept for the design of novel superhard coatings. Thin Sol. Films, 268(1-2):64 – 71, 1995.

[87] Inger-Lise Tangen, Yingda Yu, Tor Grande, Ragnvald Høier, and Mari-Ann Einarsrud. Preparation and characterisation of aluminium nitride–titanium nitride composites. J. Eur. Ceram. Soc., 24 (7):2169–2179, June 2004.

[88] P.W. Shum, Z.F. Zhou, K.Y. Li, and Y.G. Shen. XPS, AFM and nanoindentation studies of Ti1-xAlxN films synthesized by reactive unbalanced magnetron sputtering. Mater. Sci. & Eng. B, 100(2): 204–213, July 2003.

[89] P.J. Martin, A. Bendavid, J.M. Cairney, and M. Hoffman. Nanocomposite Ti–Si–N, Zr–Si–N, Ti–Al–Si–N, Ti–Al–V–Si–N thin film coatings deposited by vacuum arc deposition. Surf. Coat. Technol., 200(7):2228–2235, December 2005.

[90] Hans-Jürgen Bargel and Günter Schulze. Werkstoffkunde. Gabler Wissenschaftsverlage, January 2009.

[91] M. Holleck. Material selection for hard coatings. J. Vac. Sci. & Technol. A, 4:2661–2669, 1986.

[92] H. Holleck and V. Schier. Multilayer PVD coatings for wear protection. Surf. Coat. Technol., 76–77, Part 1(0):328–336, November 1995.

[93] Frank H.W. Löffler. Systematic approach to improve the performance of PVD coatings for tool applications. Surf. Coat. Technol., 68–69(0):729–740, December 1994.

[94] H Holleck. Surface engineering: science and technology I : proceedings of the symposium sponsored by the Materials Processing and Manufacturing Division of The Minerals, Metals & Materials Society, held during the 1999 TMS Annual Meeting in San Diego, California, February 28-March 4, 1999, volume Division, Minerals, Metals and Materials Society. Materials Processing and Manufacturing and Meeting, Minerals, Metals and Materials Society. Minerals, Metals & Materials Society, January 1999.

[95] H.O. Pierson. Handbook of refractory carbides and nitrides, 1996.

[96] Z. Y. Liu, Xiaoju Guo, Julong He, Dongli Yu, and Yongjun Tian. Comment on “Hardness of covalent and ionic crystals: First-Principle calculations”. Phys. Rev. Lett., 98(10):109601, March 2007.

[97] K. Ono. Solid-Solution strengthening. Pergamon Press, Encyclopedia of Materials Science and Engineering., 6, 1986.

[98] William D. Callister and William D. Callister, Jr. Fundamentals of Materials Science and Engineering: An Interactive e . Text, 5th Edition. Wiley, 5 edition, December 2000. ISBN 047139551X.

[99] H.W. Liu and Q. Gao. The equivalence between dislocation pile-ups and cracks. Theor. Appl. Fract. Mech., 12(3):195–204, February 1990.

[100] P.M. Anderson and C. Li. Hall-Petch relations for multilayered materials. Nanostruct. Mater., 5 (3):349–362, March 1995.

[101] E O Hall. The deformation and ageing of mild steel: III discussion of results. Proc. Phys. Soc. B, 64(9):747–753, September 1951.

[102] N. J. Petch. The cleavage strength of polycrystals. J. Iron Steel Inst., 174:25, 1953.

[103] J.C.M. Li and Y.T. Chou. The role of dislocations in the flow stress grain size relationships. Metallurg. Mater. Trans., 1(5):1145–1159, 1970.

[104] C.E. Carlton and P.J. Ferreira. What is behind the inverse Hall–Petch effect in nanocrystalline materials? Acta Mater., 55(11):3749–3756, June 2007.

[105] J. Musil. Nanostructured Coatings. Nanostructure science and technology. Springer, New York, 2006. ISBN 0-387-25642-3.

[106] E. Arzt. Size effects in materials due to microstructural and dimensional constraints: a comparative review. Acta Mater., 46(16):5611–5626, October 1998.

[107] S.C. Tjong and Haydn Chen. Nanocrystalline materials and coatings. Mater. Sci. & Eng. R, 45 (1–2):1–88, September 2004.

[108] Padmanabhan, G. Dinda, H. Hahn, and H. Gleiter. Inverse Hall–Petch effect and grain boundary sliding controlled flow in nanocrystalline materials. Mater. Sci. & Eng. A, 452-453:462–468, 2007.

[109] Desai, P. Millett, and D. Wolf. Is diffusion creep the cause for the inverse Hall–Petch effect in nanocrystalline materials? Mater. Sci. & Eng. A, 493(1-2):41–47, 2008.

[110] C S Pande and K P Cooper. Nanomechanics of Hall–Petch relationship in nanocrystalline materials. Progr. Mater. Sci., 54(6):689–706, 2009.

[111] Jakob Schiøtz, Francesco D. Di Tolla, and Karsten W. Jacobsen. Softening of nanocrystalline metals at very small grain sizes. Nature, 391(6667):561–563, February 1998.

[112] Y.G. Zheng, H.W. Zhang, Z. Chen, C. Lu, and Y.-W. Mai. Roles of grain boundary and dislocations at different deformation stages of nanocrystalline copper under tension. Phys. Lett. A, 373(5): 570–574, January 2009.

[113] E. W. Taylor. Miner. Mag., 28:718, 1949.

[114] Sam Zhang, Deen Sun, Yongqing Fu, and Hejun Du. Toughening of hard nanostructural thin films: a critical review. Surf. Coat. Technol., 198(1–3):2–8, August 2005.

[115] F Vaz, L Rebouta, Ph Goudeau, T Girardeau, J Pacaud, J.P Riviére, and A Traverse. Structural transitions in hard Si-based TiN coatings: the effect of bias voltage and temperature. Surf. Coat. Technol., 146–147(0):274–279, September 2001.

[116] A. Flink, T. Larsson, J. Sjölén, L. Karlsson, and L. Hultman. Influence of Si on the microstructure of arc evaporated (Ti,Si)N thin films; evidence for cubic solid solutions and their thermal stability. Surf. Coat. Technol., 200(5–6):1535–1542, November 2005.

[117] Zhiyun Pan, Zhihu Sun, Zhi Xie, Junhua Xu, Isao Kojima, and Shiqiang Wei. Interfacial intermixing of TiN/Si 3 n 4 super-hard multilayer films studied by fluorescence x-ray absorption fine structure. J. Phys. D: Appl. Phys., 39(13):2796–2802, July 2006.

[118] R.F. Zhang and S. Veprek. On the spinodal nature of the phase segregation and formation of stable nanostructure in the Ti–Si–N system. Mater. Sci. & Eng. A, 424(1–2):128–137, May 2006.

[119] M.A. Auger, R. Gago, M. Fernández, O. Sánchez, and J.M. Albella. Deposition of TiN/AlN bilayers on a rotating substrate by reactive sputtering. Surf. Coat. Technol., 157(1):26–33, August 2002.

[120] Xinyu Zhang, Zhouwen Chen, Shiliang Zhang, Riping Liu, Haitao Zong, Qin Jing, Gong Li, Mingzhen Ma, and Wenkui Wang. Electronic and optical properties of rock-salt aluminum nitride obtained from first principles. J. Phys.: Condens. Matter, 19(42):425231, October 2007.

[121] S. Christiansen, M. Albrecht, H. P. Strunk, and Stan Veprek. Microstructure of novel superhard nanocrystalline-amorphous composites as analyzed by high resolution transmission electron microscopy. Journal of Vacuum Science & Technology B: Microelectronics and Nanometer Structures, 16(1):19–22, 1998.

[122] P Zeman, R Čerstvý, P.H Mayrhofer, C Mitterer, and J Musil. Structure and properties of hard and superhard Zr–Cu–N nanocomposite coatings. Mater. Sci. & Eng. A, 289(1–2):189–197, September 2000.

[123] Robert C. Cammarata, Henry Ehrenreich, and Frans Spaepen. Chapter 1 generalized thermodynamics of surfaces with applications to small solid systems. In Solid State Physics, volume Volume 61, pages 1–75. Academic Press, 2009. ISBN 0081-1947.

[124] V Ramaswamy, W.D Nix, and B.M Clemens. Coherency and surface stress effects in metal multilayers. Scr. Mater., 50(6):711–715, March 2004.

[125] S. Labat, F. Bocquet, B. Gilles, and O. Thomas. Stresses and interfacial structure in Au–Ni and Ag–Cu metallic multilayers. Scr. Mater., 50(6):717–721, March 2004.

[126] T. Tsakalakos. Special mechanical properties of very thin films. Le Journal de Physique Colloques, 49(C5):C5–707–C5–717, October 1988.

[127] B. J Daniels, W. D Nix, and B. M Clemens. Effect of coherency stresses on the hardness of epitaxial Fe(001)/Pt(001) multilayers. Appl. Phys. Lett., 66(22):2969–2971, May 1995.

[128] S. I. Rao and P. M. Hazzledine. Atomistic simulations of dislocation–interface interactions in the Cu-Ni multilayer system. Philos. Mag. A, 80(9):2011–2040, 2000.

[129] Junhua Xu, Masao Kamiko, Yaomin Zhou, Ryoichi Yamamoto, Geyang Li, and Mingyuan Gu. Superhardness effects of heterostructure NbN/TaN nanostructured multilayers. J. Appl. Phys., 89(7):3674–3678, April 2001.

[130] Junhua Xu, Koichiro Hattori, Yutaka Seino, and Isao Kojima. Microstructure and properties of CrN/Si3N4 nano-structured multilayer films. Thin Sol. Films, 414(2):239–245, July 2002.

[131] Hans Söderberg, Magnus Oden, Jon M. Molina-Aldareguia, and Lars Hultman. Nanostructure formation during deposition of TiN/SiNx nanomultilayer films by reactive dual magnetron sputtering. J. Appl. Phys., 97(11):114327, 2005.

[132] J. S. Koehler. Attempt to design a strong solid. Phys. Rev. B, 2(2):547–551, July 1970.

[133] D. J. Bacon, D. M. Babnett, and R. O. Scattebgood. On the anisotropic elastic field of a dislocation segment in three dimensions. Philos. Mag. A, 39(2):231–235, 1979.

[134] Philip C. Yashar and William D. Sproul. Nanometer scale multilayered hard coatings. Vacuum, 55(3–4):179–190, December 1999.

[135] E.S. Pacheco and T. Mura. Interaction between a screw dislocation and a bimetallic interface. J. Mech. Phys. Sol., 17(3):163–170, June 1969.

[136] S. L. Lehoczky. Retardation of dislocation generation and motion in Thin-Layered metal laminates. Phys. Rev. Lett., 41(26):1814–1818, December 1978.

[137] A K Head. Edge dislocations in inhomogeneous media. Proc. Phys. Soc. B, 66(9):793–801, September 1953.

[138] S. L Lehoczky. Strength enhancement in thin-layered Al-Cu laminates. J. Appl. Phys., 49(11): 5479–5485, November 1978.

[139] X. Chu, M. S. Wong, W. D. Sproul, S. L. Rohde, and S. A. Barnett. Deposition and properties of polycrystalline TiN/NbN superlattice coatings. In 38th National Symposium of the American Vacuum Society, volume 10, pages 1604–1609. AVS, 1992.

[140] M. Shinn, L. Hultman, and S.a. Barnett. Growth, structure, and microhardness of epitaxial TiN/NbN superlattices. J. Mater. Res., 7(04):901–911, 1992.

[141] K. K Shih and D. B Dove. Ti/Ti-N Hf/Hf-N and W/W-N multilayer films with high mechanical hardness. Appl. Phys. Lett., 61(6):654–656, August 1992.

[142] S. I. Rao, P. M. Hazzledine, and D. M. Dimiduk. Interfacial strengthening in Semi-Coherent metallic multilayers. MRS Online Proc. Lib., 362:null, 1994.

[143] P.b. Mirkarimi, S.a. Barnett, K.m. Hubbard, T.r. Jervis, and L. Hultman. Structure and mechanical properties of epitaxial TiN/V0.3Nb0.7N(100) superlattices. J. Mater. Res., 9(06):1456–1467, 1994.

[144] W. M. C Yang, T. Tsakalakos, and J. E Hilliard. Enhanced elastic modulus in composition-modulated gold-nickel and copper-palladium foils. J. Appl. Phys., 48(3):876–879, March 1977.

[145] T. Tsakalakos and J. E Hilliard. Elastic modulus in composition-modulated copper-nickel foils. J. Appl. Phys., 54(2):734–737, February 1983.

[146] R. C Cammarata, T. E Schlesinger, C. Kim, S. B Qadri, and A. S Edelstein. Nanoindentation study of the mechanical properties of copper-nickel multilayered thin films. Appl. Phys. Lett., 56(19): 1862–1864, May 1990.

[147] B. M. Davis, D. N. Seidman, A. Moreau, J. B. Ketterson, J. Mattson, and M. Grimsditch. ‘‘Supermodulus effect’’ in Cu/Pd and Cu/Ni superlattices. Phys. Rev. B, 43(11):9304–9307, April 1991.

[148] A. Fartash, Eric E. Fullerton, Ivan K. Schuller, Sarah E. Bobbin, J. W. Wagner, R. C. Cammarata, Sudha Kumar, and M. Grimsditch. Evidence for the supermodulus effect and enhanced hardness in metallic superlattices. Phys. Rev. B, 44(24):13760–13763, December 1991.

[149] F. Zeng, Y. Gao, L. Li, D.M. Li, and F. Pan. Elastic modulus and hardness of Cu–Ta amorphous films. J. Alloys Compd., 389(1–2):75–79, March 2005.

[150] Jiawan Tian, Zenghu Han, Qianxi Lai, Xiaojiang Yu, Geyang Li, and Mingyuan Gu. Two-step penetration: a reliable method for the measurement of mechanical properties of hard coatings. Surf. Coat. Technol., 176(3):267–271, January 2004.

[151] U. Harms and R. B. Schwarz. Anomalous modulus and work function at the interfaces of thin films. Phys. Rev. B, 65(8):085409, February 2002.

[152] D. Wolf and J. F. Lutsko. Structurally induced supermodulus effect in superlattices. Phys. Rev. Lett., 60(12):1170–1173, March 1988.

[153] Junhua Xu, Geyang Li, and Mingyuan Gu. The microstructure and mechanical properties of TaN/TiN and TaWN/TiN superlattice films. Thin Sol. Films, 370(1–2):45–49, July 2000.

[154] A. Madan, I. W. Kim, S. C. Cheng, P. Yashar, V. P. Dravid, and S. A. Barnett. Stabilization of cubic AlN in epitaxial AlN/TiN superlattices. Phys. Rev. Lett., 78(9):1743–1746, March 1997.

[155] M. Vila, D. Caceres, and C. Prieto. Mechanical properties of sputtered silicon nitride thin films. J. Appl. Phys., 94(12):7868–7873, 2003.

[156] Cenk Kocer, Naoto Hirosaki, and Shigenobu Ogata. Ab initio calculation of the ideal tensile and shear strength of cubic silicon nitride. Phys. Rev. B, 67(3):035210, January 2003.

[157] D. M. Mattox. Particle bombardment effects on thin-film deposition: A review. J. Vac. Sci. & Technol. A, 7(3):1105–1114, 1989.

[158] André Anders. A structure zone diagram including plasma-based deposition and ion etching. Thin Sol. Films, 518(15):4087–4090, May 2010.

[159] L. Hultman. Thermal stability of nitride thin films. Vacuum, 57:1–30, 2000.

[160] Paul H. Mayrhofer, Christian Mitterer, Lars Hultman, and Helmut Clemens. Microstructural design of hard coatings. Progr. Mater. Sci., 51(8):1032–1114, November 2006.

[161] Chi-Lung Chang, Chao-Te Lin, Pi-Chuen Tsai, Wei-Yu Ho, and Da-Yung Wang. Influence of bias voltages on the structure and wear properties of TiSiN coating synthesized by cathodic arc plasma evaporation. Thin Sol. Films, 516(16):5324–5329, June 2008.

[162] H Van Swygenhoven, A Caro, and D Farkas. A molecular dynamics study of polycrystalline fcc metals at the nanoscale: grain boundary structure and its influence on plastic deformation. Mater. Sci. & Eng. A, 309–310(0):440–444, July 2001.

[163] A. Hasnaoui, P.M. Derlet, and H. Van Swygenhoven. Interaction between dislocations and grain boundaries under an indenter – a molecular dynamics simulation. Acta Mater., 52(8):2251–2258, May 2004.

[164] Jakob Schiøtz and Karsten W Jacobsen. A maximum in the strength of nanocrystalline copper. Science, 301(5638):1357–1359, May 2003.

[165] Christian Brandl, Peter M. Derlet, and Helena Van Swygenhoven. Strain rates in molecular dynamics simulations of nanocrystalline metals. Philos. Mag., 89(34-36):3465–3475, 2009.

[166] H.-H. Fu, D.J. Benson, and M.A. Meyers. Analytical and computational description of effect of grain size on yield stress of metals. Acta Mater., 49(13):2567–2582, August 2001.

[167] R Schwaiger, B Moser, M Dao, N Chollacoop, and S Suresh. Some critical experiments on the strain-rate sensitivity of nanocrystalline nickel. Acta Mater., 51(17):5159–5172, October 2003.

[168] Y.J. Wei and L. Anand. Grain-boundary sliding and separation in polycrystalline metals: application to nanocrystalline fcc metals. J. Mech. Phys. Sol., 52(11):2587–2616, November 2004.

[169] D.H. Warner, F. Sansoz, and J.F. Molinari. Atomistic based continuum investigation of plastic deformation in nanocrystalline copper. Int. J. Plast., 22(4):754–774, April 2006.

[170] J.E. Carsley, J. Ning, W.W. Milligan, S.A. Hackney, and E.C. Aifantis. A simple, mixtures-based model for the grain size dependence of strength in nanophase metals. Nanostruct. Mater., 5(4): 441–448, May 1995.

[171] Ning Wang, Zhirui Wang, K.T. Aust, and U. Erb. Effect of grain size on mechanical properties of nanocrystalline materials. Acta Metall. Mater., 43(2):519–528, February 1995.

[172] A.A. Nazarov. On the pile-up model of the grain size-yield stress relation for nanocrystals. Scr. Mater., 34(5):697–701, March 1996.

[173] Hans Conrad and Jagdish Narayan. On the grain size softening in nanocrystalline materials. Scr. Mater., 42(11):1025–1030, May 2000.

[174] David J Benson, Hsueh-Hung Fu, and Marc André Meyers. On the effect of grain size on yield stress: extension into nanocrystalline domain. Mater. Sci. & Eng. A, 319–321(0):854–861, December 2001.

[175] L. Capolungo, C. Jochum, M. Cherkaoui, and J. Qu. Homogenization method for strength and inelastic behavior of nanocrystalline materials. Int. J. Plast., 21(1):67–82, January 2005.

[176] Ning Jiang, H.J. Zhang, S.N. Bao, Y.G. Shen, and Z.F. Zhou. XPS study for reactively sputtered titanium nitride thin films deposited under different substrate bias. Phys. B, 352(1-4):118 – 126, 2004.

[177] Hyoung Seop Kim and Yuri Estrin. Phase mixture modeling of the strain rate dependent mechanical behavior of nanostructured materials. Acta Mater., 53(3):765–772, February 2005.

[178] Jianqiu Zhou, Zhenghui Li, Rongtao Zhu, Yuanling Li, and Zhenzhong Zhang. A mixtures-based model for the grain size dependent mechanical behavior of nanocrystalline materials. J. Mater. Process. Technol., 197(1–3):325–336, February 2008.

[179] Babak Farrokh and Akhtar S. Khan. Grain size, strain rate, and temperature dependence of flow stress in ultra-fine grained and nanocrystalline Cu and Al: Synthesis, experiment, and constitutive modeling. Int. J. Plast., 25(5):715–732, May 2009.

[180] Garritt J. Tucker, Shreevant Tiwari, Jonathan A. Zimmerman, and David L. McDowell. Investigating the deformation of nanocrystalline copper with microscale kinematic metrics and molecular dynamics. J. Mech. Phys. Sol., 60(3):471–486, March 2012.

[181] H. S Kim. A composite model for mechanical properties of nanocrystalline materials. Scr. Mater., 39(8):1057–1062, 1998.

[182] S. Veprek, M. Haussmann, S. Reiprich, Li Shizhi, and J. Dian. Novel thermodynamically stable and oxidation resistant superhard coating materials. Surf. Coat. Technol., 86–87, Part 1(0):394–401, December 1996.

[183] Xi Chu and Scott A Barnett. Model of superlattice yield stress and hardness enhancements. J. Appl. Phys., 77(9):4403–4411, May 1995.

[184] Hsueh-Hung Fu, David J. Benson, and Marc André Meyers. Computational description of nanocrystalline deformation based on crystal plasticity. Acta Mater., 52(15):4413–4425, September 2004.

[185] K.S Kumar, H Van Swygenhoven, and S Suresh. Mechanical behavior of nanocrystalline metals and alloys. Acta Mater., 51(19):5743–5774, November 2003.

[186] Chihiro Iwamoto and Shun-ichiro Tanaka. Interface nanostructure of brazed silicon nitride. J. Am. Ceram. Soc., 81(2):363–368, 1998.

[187] Shiqiang Hao, Bernard Delley, Stan Veprek, and Catherine Stampfl. Superhard Nitride-Based nanocomposites: Role of interfaces and effect of impurities. Phys. Rev. Lett., 97(8):086102, 2006.

[188] Hans Söderberg, Jens Birch, Lars Hultman, and Magnus Odén. RHEED studies during growth of TiN/SiNx/TiN trilayers on MgO(001). Surf. Sci., 601(11):2352 – 2356, 2007.

[189] R. F. Zhang, A. S. Argon, and S. Veprek. Understanding why the thinnest SiN_x interface in transition-metal nitrides is stronger than the ideal bulk crystal. Phys. Rev. B, 81(24):245418, June 2010.

[190] B. Alling, E. I. Isaev, A. Flink, L. Hultman, and I. A. Abrikosov. Metastability of fcc-related Si-N phases. Phys. Rev. B, 78(13):132103, October 2008.

[191] Björn Alling. A Theoretical Study of Disorder and Decomposition in Multinary Nitrides Hard Coatings Materials. PhD thesis, ÉCOLE POLYTECHNIQUE FÉDÉRALE DE LAUSANNE, 2009.

[192] Aude Pelisson. internal communication.

[193] Jan Procházka. Superharte TiN/Si_3N_4 Nanokomposite durch reaktive Magnetronzerstäubung kombiniert mit chemischer Gasphasenabscheidung. PhD thesis, Technische Universität München, Institut für Chemie, Anorganische Materialien, 2003.

[194] Tobias Marten, Björn Alling, Eyvaz I. Isaev, Hans Lind, Ferenc Tasnádi, Lars Hultman, and Igor A. Abrikosov. First-principles study of the SiN_x/TiN(001) interface. Phys. Rev. B, 85(10):104106, March 2012.

[195] V. I. Ivashchenko, S. Veprek, P. E. A. Turchi, and V. I. Shevchenko. Comparative first-principles study of TiN/SiN_x/TiN interfaces. Phys. Rev. B, 85(19):195403, May 2012.

[196] Ming-Show Wong, Gwo-Yih Hsiao, and Sheng-Yu Yang. Preparation and characterization of AlN/ZrN and AlN/TiN nanolaminate coatings. Surf. Coat. Technol., 133–134(0):160–165, November 2000.

[197] M.A. Auger, O. Sanchez, C. Ballesteros, M. Jergel, M. Aguilar-Frutis, and C. Falcony. TiN/AlN bilayers and multilayers grown by magnetron co-sputtering. Thin Sol. Films, 433(1–2):211–216, June 2003.

[198] F.H. Mei, N. Shao, J.W. Dai, and G.Y. Li. Coherent growth and superhardness effect of AlN/TiN nanomultilayers. Mater. Lett., 58(27–28):3477–3480, November 2004.

[199] A. Karimi, G. Allidi, and R. Sanjines. Relative orientation of the constituents on the degree of crystallographic coherence in AlN/TiN superlattices. Surf. Coat. Technol., 201(7):4062–4067, December 2006.

[200] I. W Kim, Quan Li, L. D Marks, and S. A Barnett. Critical thickness for transformation of epitaxially stabilized cubic AlN in superlattices. Appl. Phys. Lett., 78(7):892–894, February 2001.

[201] V. Pankov, M. Evstigneev, and R. H Prince. Enhanced stability of rocksalt-type AIN phase in AIN/TiN superlattices synthesized by room-temperature pulsed laser deposition. J. Appl. Phys., 92(8):4255–4260, October 2002.

[202] D. Chen, X.L. Ma, and Y.M. Wang. Thickness-dependent structural transformation in the AlN film. Acta Mater., 53(19):5223–5227, November 2005.

[203] R. F. Zhang, S. H. Sheng, and S. Veprek. Mechanical strengths of silicon nitrides studied by ab initio calculations. Appl. Phys. Lett., 90(19):191903, 2007.

[204] H. Schmidt and M. Mennig. Wet coating technologies for glass, November 2000.

[205] John E. Mahan. Physical Vapor Deposition of Thin Films. Wiley-Interscience, 1st edition, February 2000. ISBN 0471330019.

[206] H.O. Pierson. Handbook of chemical vapor deposition (CVD) - principles, technology and applications (2nd edition), 1999.

[207] D.M. Dobkin and M.K. Zuraw. Principles of Chemical Vapor Deposition. Springer, 1st edition, April 2003. ISBN 1402012489.

[208] Ludvik Martinu and Daniel Poitras. Plasma deposition of optical films and coatings: A review. J. Vac. Sci. & Technol. A, 18(6):2619–2645, 2000.

[209] S. M. Rossnagel. Thin film deposition with physical vapor deposition and related technologies. J. Vac. Sci. & Technol. A, 21(5):S74–S87, 2003.

[210] Donald M. Mattox. Handbook of Physical Vapor Deposition (PVD) Processing. William Andrew, May 2010.

[211] P. J. Kelly and R. D. Arnell. Magnetron sputtering: a review of recent developments and applications. Vacuum, 56(3):159–172, March 2000.

[212] Jeon G Han. Recent progress in thin film processing by magnetron sputtering with plasma diagnostics. J. Phys. D: Appl. Phys., 42(4):043001, February 2009.

[213] K. Sarakinos, J. Alami, and S. Konstantinidis. High power pulsed magnetron sputtering: A review on scientific and engineering state of the art. Surf. Coat. Technol., 204(11):1661–1684, February 2010.

[214] Daniel J Kester and Russell Messier. Phase control of cubic boron nitride thin films. J. Appl. Phys., 72(2):504–513, July 1992.

[215] John L Vossen. Thin Film Processes. Academic Press, New York, 1978.

[216] Donald Leonard Smith. Thin-Film Deposition: Principles and Practice. McGraw-Hill Professional, March 1995.

[217] John A Venables. Introduction to Surface and Thin Film Processes. Cambridge University Press, Cambridge, 2000. ISBN 0-521-62460-6.

[218] Milton Ohring. Materials Science of Thin Films. Milton Ohring, 2002.

[219] Albano Cavaleiro. Nanostructured Coatings. Nanostructure science and technology. Springer, New York, 2006. ISBN 0-387-25642-3.

[220] Peter M Martin. Handbook of Deposition Technologies for Films and Coatings Science, Applications and Technology. Elsevier, Oxford, 3rd ed edition, 2010. ISBN 978-0-8155-2031-3.

[221] T. Q. Li, S. Noda, Y. Tsuji, T. Ohsawa, and H. Komiyama. Initial growth and texture formation during reactive magnetron sputtering of TiN on si(111). J. Vac. Sci. & Technol. A, 20(3):583–588, 2002.

[222] F. C. Frank and J. H. van der Merwe. One-Dimensional dislocations. III. influence of the second harmonic term in the potential representation, on the properties of the model. Proc. R. Soc. London.A, 200(1060):125–134, December 1949.

[223] F. C. Frank and J. H. van der Merwe. One-Dimensional dislocations. II. misfitting monolayers and oriented overgrowth. Proc. R. Soc. London.A, 198(1053):216–225, 1949.

[224] F. C Frank and J. H Van Der Merwe. One-Dimensional dislocations. I. static theory. Proc. R. Soc. London.A, 198(1053):205–216, August 1949.

[225] I. N. Stranski and L. Krastanov. Zur theorie der orientierten ausscheidung von ionenkristallen aufeinander. In Sitzungsber. Akad. Wiss. Wien. Math.-Naturwiss., volume 146, pages 797–810, 1938.

[226] M. Volmer and A. Weber. Keimbildung in übersättigten gebilden. Z. Phys. Chem., 119:277–301, 1926.

[227] K. Jagannadham, J. Narayan, R. Chowdhury, Z. Tsvetanka, and P. Tiwari. Domain epitaxial growth of TiN/Si(001), TiN/GaAs(001), and Si/TiN/Si(001) heterostructures by laser physical vapor deposition: Theory and experiment. J. Electron. Mater., 23(9):861–874, 1994.

[228] B.A. Movchan and A.V. Demchishin. Phys. Met. Metallogr., 28:83, 1969.

[229] John A. Thornton. The microstructure of sputter-deposited coatings. J. Vac. Sci. & Technol. A, 4 (6):3059–3065, 1986.

[230] P.B Barna and M Adamik. Fundamental structure forming phenomena of polycrystalline films and the structure zone models. Thin Sol. Films, 317(1–2):27–33, April 1998.

[231] L. Hultman, S.A. Barnett, J.-E. Sundgren, and J.E. Greene. Growth of epitaxial TiN films deposited on MgO(100) by reactive magnetron sputtering: The role of low-energy ion irradiation during deposition. J. Cryst. Growth, 92(3–4):639–656, October 1988.

[232] R. Banerjee, K. Singh, P. Ayyub, M. K. Totlani, and A. K. Suri. Influence of the Ar/N2 ratio on the preferred orientation and optical reflectance of reactively sputter deposited titanium nitride thin films. J. Vac. Sci. & Technol. A, 21(1):310–317, 2003.

[233] Sadao Adachi and Mitsutoshi Takahashi. Optical properties of TiN films deposited by direct current reactive sputtering. J. Appl. Phys., 87(3):1264–1269, February 2000.

[234] G. S. Chen, J. J. Guo, C. K. Lin, Chen-Sheng Hsu, L. C. Yang, and J. S. Fang. Evaluation of radio-frequency sputter-deposited textured TiN thin films as diffusion barriers between copper and silicon. J. Vac. Sci. & Technol. A, 20(2):479–485, 2002.

[235] L.A. Cyster, D.M. Grant, K.G. Parker, and T.L. Parker. The effect of surface chemistry and structure of titanium nitride (TiN) films on primary hippocampal cells. Biomol. Eng., 19(2–6):171–175, August 2002.

[236] H. Ljungcrantz, M. Odeén, L. Hultman, J. E. Greene, and J.-E. Sundgren. Nanoindentation studies of single-crystal (001)-, (011)-, and (111)-oriented TiN layers on MgO. J. Appl. Phys., 80(12):6725, 1996.

[237] T. Q. Li, S. Noda, H. Komiyama, T. Yamamoto, and Y. Ikuhara. Initial growth stage of nanoscaled TiN films: Formation of continuous amorphous layers and thickness-dependent crystal nucleation. J. Vac. Sci. & Technol. A, 21(5):1717–1723, 2003.

[238] Min-Ku Lee, Hee-Soo Kang, Whung-Whoe Kim, Joung-Soo Kim, and Won-Jong Lee. Characteristics of TiN film deposited on stellite using reactive magnetron sputter ion plating. J. Mater. Res., 12(09):2393–2400, 1997.

[239] Li-Jian Meng and M.P. dos Santos. Characterization of titanium nitride films prepared by d.c. reactive magnetron sputtering at different nitrogen pressures. Surf. Coat. Technol., 90(1–2): 64–70, March 1997.

[240] H.Q. Lou, N. Axén, R.E. Somekh, and I.M. Hutchings. Effect of deposition conditions on the characteristics of reactively sputtered titanium nitride films. Surf. Coat. Technol., 90(1–2):123–127, March 1997.

[241] Brian W Karr, I. Petrov, David G Cahill, and J. E Greene. Morphology of epitaxial TiN(001) grown by magnetron sputtering. Appl. Phys. Lett., 70(13):1703–1705, March 1997.

[242] J P Zhao, X Wang, Z Y Chen, S Q Yang, T S Shi, and X H Liu. Overall energy model for preferred growth of TiN films during filtered arc deposition. J. Phys. D: Appl. Phys., 30(1):5–12, January 1997.

[243] U. C Oh and Jung Ho Je. Effects of strain energy on the preferred orientation of TiN thin films. J. Appl. Phys., 74(3):1692–1696, August 1993.

[244] J. H Je, D. Y Noh, H. K Kim, and K. S Liang. Preferred orientation of TiN films studied by a real time synchrotron x-ray scattering. J. Appl. Phys., 81(9):6126–6133, May 1997.

[245] G. Abadias and Y. Y Tse. Diffraction stress analysis in fiber-textured TiN thin films grown by ion-beam sputtering: Application to (001) and mixed (001)+(111) texture. J. Appl. Phys., 95(5): 2414–2428, March 2004.

[246] Joshua Pelleg, L.Z. Zevin, S. Lungo, and N. Croitoru. Reactive-sputter-deposited TiN films on glass substrates. Thin Sol. Films, 197(1–2):117–128, March 1991.

[247] Laurette Combadiere and Jean Machet. Reactive magnetron sputtering deposition of TiN films. I. influence of the substrate temperature on structure, composition and morphology of the films. Surf. Coat. Technol., 88(1–3):17–27, January 1997.

[248] P. Patsalas, C. Charitidis, and S. Logothetidis. The effect of substrate temperature and biasing on the mechanical properties and structure of sputtered titanium nitride thin films. Surf. Coat. Technol., 125(1-3):335 – 340, 2000.

[249] J. E Greene, J. -E Sundgren, L. Hultman, I. Petrov, and D. B Bergstrom. Development of preferred orientation in polycrystalline TiN layers grown by ultrahigh vacuum reactive magnetron sputtering. Appl. Phys. Lett., 67(20):2928–2930, November 1995.

[250] L. Hultman, J. -E Sundgren, J. E Greene, D. B Bergstrom, and I. Petrov. High-flux low-energy (approx. 20 eV) N+2 ion irradiation during TiN deposition by reactive magnetron sputtering: Effects on microstructure and preferred orientation. J. Appl. Phys., 78(9):5395–5403, November 1995.

[251] I. Petrov, F. Adibi, J. E Greene, L. Hultman, and J. -E Sundgren. Average energy deposited per atom: A universal parameter for describing ion-assisted film growth? Appl. Phys. Lett., 63(1): 36–38, July 1993.

[252] B. Rauschenbach and J. W Gerlach. Texture development in titanium nitride films grown by Low-Energy ion assisted deposition. Cryst. Res. Technol., 35(6-7):675–688, November 2000.

[253] J. W Gerlach, U. Preckwinkel, H. Wengenmair, T. Kraus, and B. Rauschenbach. Biaxial alignment of TiN films prepared by ion beam assisted deposition. Appl. Phys. Lett., 68(17):2360–2362, April 1996.

[254] Brian W. Karr, David G. Cahill, I. Petrov, and J. E. Greene. Effects of high-flux low-energy ion bombardment on the low-temperature growth morphology of TiN(001) epitaxial layers. Phys. Rev. B, 61(23):16137–16143, June 2000.

[255] G. Abadias, Y. Y Tse, Ph Guérin, and V. Pelosin. Interdependence between stress, preferred orientation, and surface morphology of nanocrystalline TiN thin films deposited by dual ion beam sputtering. J. Appl. Phys., 99(11):113519–113519–13, June 2006.

[256] S Mahieu, D Depla, and R De Gryse. Modelling the growth of transition metal nitrides. J. Phys. Conf. Ser., 100(8):082003, March 2008.

[257] E. Jiran and C. Thompson. Capillary instabilities in thin films. J. Electron. Mater., 19(11):1153–1160, 1990.

[258] Emmanouil Frantzeskakis. Analysis of potential applications for the templated dewetting of metal thin films. Thesis, Massachusetts Institute of Technology, Dept. of Materials Science and and Engineering, 2005.

[259] S. V. Dudiy and B. I. Lundqvist. Wetting of TiC and TiN by metals. Phys. Rev. B, 69(12):125421, March 2004.

[260] Joseph Antoine Ferdinand Plateau. Statique expérimentale et théorique des liquides soumis aux seules forces moléculaires. Gauthier-Villars, 1873.

[261] L. Rayleigh. On the instability of jets. Proc. London Math. Soc., s1-10(1):4–13, November 1878.

[262] Amanda L Giermann and Carl V Thompson. Solid-state dewetting for ordered arrays of crystallographically oriented metal particles. Appl. Phys. Lett., 86(12):121903–121903–3, March 2005.

[263] H. Hertz. Ueber einen einfluss des ultravioletten lichtes auf die electrische entladung. Ann. Phys., 267(8):983–1000, January 1887.

[264] Wilhelm Hallwachs. Ueber den zusammenhang des electricitätsverlustes durch beleuchtung mit der lichtabsorption. Ann. Phys., 273(8):666–675, January 1889.

[265] Albert Einstein. On a heuristic viewpoint concerning the production and transformation of light. Ann. Phys., 17:132–148, 1905.

[266] Kai Siegbahn. ESCA applied to free molecules. North-Holland Pub. Co., 1970.

[267] D. Briggs and T. Grant. Surface Analysis by Auger and X-Ray Photoelectron Spectroscopy. IM-Publications, 2003.

[268] M. P. Seah, I. S. Gilmore, and S. J. Spencer. Quantitative XPS: I. analysis of x-ray photoelectron intensities from elemental data in a digital photoelectron database. J. Electron Spectrosc. Relat. Phenom., 120(1-3):93 – 111, 2001.

[269] Standard terminology relating to surface analysis, designation e673-03.

[270] P. D. Innes. On the velocity of the cathode particles emitted by various metals under the influence of rontgen rays, and its bearing on the theory of atomic disintegration. Proc. R. Soc. London.A, 79(532):442–462, 1907. ISSN 09501207.

[271] Dmitry Zemlyanov. Electron spectroscopy: A new window opens. Nat. Nanotechnol., 6(10): 612–613, October 2011.

[272] D. Frank Ogletree, Hendrik Bluhm, Gennadi Lebedev, Charles S Fadley, Zahid Hussain, and Miquel Salmeron. A differentially pumped electrostatic lens system for photoemission studies in the millibar range. Rev. Sci. Instrum., 73(11):3872–3877, November 2002.

[273] E. Rutherford. The scattering of α and β particles by matter and the structure of the atom. Philos. Mag., 6:21, 1911.

[274] N. Bohr. On the constitution of atoms and molecules. Philos. Mag. 6, 26:1–25, 1913.

[275] H. G. J. Moseley. XCIII. the high-frequency spectra of the elements. Philos. Mag. 6, 26(156): 1024–1034, 1913. ISSN 1941-5982.

[276] H. Moseley. Atomic models and x-ray spectra. Nature, 92:554ff, January 1914.

[277] K. Siegbahn, C. Nordling, A. Fahlman, K. Nordberg, J. Hedman, G. Johansson, T. Bergmark, S. Karlsson, I. Lindgren, and B Lindberg. Atomic, molecular and solid state structure studied by means of electron spectroscopy. Nova Acta Reg Soc Sct Upsaliensis, 20:1, 1967.

[278] J. G. Jenkin, R. C. G. Leckey, and J. Liesegang. The development of x-ray photoelectron spectroscopy: 1900-1960. J. Electron Spectrosc. Relat. Phenom., 12(1):1 – 35, 1977.

[279] Noel H. Turner and John A. Schreifels. Surface analysis: X-ray photoelectron spectroscopy and auger electron spectroscopy. Anal. Chem., 70(12):229–250, 1998.

[280] John F. Moulder, William F. Stickle, Peter E. Sobol, and Kenneth D. Bomben. Handbook of X-ray Photoelectron Spectroscopy. Physical Electronics Inc., 1992.

[281] Lise Meitner. Über die Entstehung der β-Strahl-Spektren radioaktiver Substanzen. Z. Phys. A, 9 (1):131–144, 1922.

[282] Académie des sciences (France). comptes rendus hebdomadaires des séances de l'Académie des sciences / publiés... par MM. les secrétaires perpétuels. 1835-1965. http://visualiseur.bnf.fr/CadresFenetre?O=NUMM-3133&I=2182&M=tdm.

[283] C. G. H. Walker, C. A. Anderson, A. McKinley, N. M. D. Brown, and A. M. Joyce. A combined AES, resonant photoemission and EELS study of in-situ grown titanium nitride. Surf. Sci., 383(2-3): 248–260, July 1997.

[284] A. Barrie, I.W. Drummond, and Q.C. Herd. Correlation of calculated and measured 2p spin-orbit splitting by electron spectroscopy using monochromatic x-radiation. J. Electron Spectrosc. Relat. Phenom., 5(1):217 – 225, 1974.

[285] J. Hedman, P.-F. Hedén, C. Nordling, and K. Siegbahn. Energy splitting of core electron levels in paramagnetic molecules. Phys. Lett. A, 29(4):178–179, May 1969.

[286] C. S. Fadley, D. A. Shirley, A. J. Freeman, P. S. Bagus, and J. V. Mallow. Multiplet splitting of Core-Electron binding energies in Transition-Metal ions. Phys. Rev. Lett., 23(24):1397–1401, December 1969.

[287] C. S. Fadley and D. A. Shirley. Multiplet splitting of Metal-Atom electron binding energies. Phys. Rev. A, 2(4):1109–1120, October 1970.

[288] V.P. Sachenko and V.F. Demekhin. Satellites of the x-ray spectra. J. Exper. Theor. Phys. (USSR), 49: 765–769, 1965.

[289] Thomas A. Carlson, C. W. Nestor, Thomas C. Tucker, and F. B. Malik. Calculation of electron Shake-Off for elements from Z=2 to 92 with the use of Self-Consistent-Field wave functions. Phys. Rev., 169(1):27–36, May 1968.

[290] Andrei G. Kochur and Vitali A. Popov. Shake up and shake off probabilities for L-, M-, and N-electrons in atoms with Z=3 to 60. Radiat. Phys. Chem., 75(11):1525–1528, November 2006.

[291] Wolfgang Schattke. Solid-State Photoemission and Related Methods: Theory and Experiment. John Wiley & Sons, December 2008.

[292] David Bohm and David Pines. A collective description of electron interactions: III. coulomb interactions in a degenerate electron gas. Phys. Rev., 92(3):609–625, November 1953.

[293] Y. Baer and G. Busch. X-Ray photoemission from aluminum. Phys. Rev. Lett., 30(7):280–282, February 1973.

[294] C. J. Powell and J. B. Swan. Origin of the characteristic electron energy losses in aluminum. Phys. Rev., 115(4):869–875, 1959.

[295] A. M. Bradshaw, W. Domcke, and L. S. Cederbaum. Intrinsic and extrinsic plasmon coupling in x-ray photoemission from core states of adsorbed atoms. Phys. Rev. B, 16(4):1480–1488, 1977.

[296] R. H. Ritchie. Plasma losses by fast electrons in thin films. Phys. Rev., 106(5):874, June 1957.

[297] W. J. Pardee, G. D. Mahan, D. E. Eastman, R. A. Pollak, L. Ley, F. R. McFeely, S. P. Kowalczyk, and D. A. Shirley. Analysis of surface- and bulk-plasmon contributions to x-ray photoemission spectra. Phys. Rev. B, 11(10):3614, May 1975.

[298] M. Kurth, P. C. J. Graat, and E. J. Mittemeijer. Determination of the intrinsic bulk and surface plasmon intensity of XPS spectra of magnesium. Appl. Surf. Sci., 220(1-4):60–78, 2003.

[299] R. Manne and T. Åberg. Koopmans' theorem for inner-shell ionization. Chem. Phys. Lett., 7(2): 282–284, October 1970.

[300] K.S. Kim and R.E. Davis. Electron spectroscopy of the nickel-oxygen system. J. Electron Spectrosc. Relat. Phenom., 1(3):251–258, 1972.

[301] Marion A. Brisk and A.D. Baker. Shake-up satellites in x-ray photoelectron spectroscopy. J. Electron Spectrosc. Relat. Phenom., 7(3):197–213, 1975.

[302] Sven Larsson. Satellites in ESCA inner-shell spectra of 3d0 transition metal complexes. J. Electron Spectrosc. Relat. Phenom., 8(3):171–178, 1976.

[303] Akio Kotani and Haruhiko Ogasawara. Theory of core-level spectroscopy of rare-earth oxides. J. Electron Spectrosc. Relat. Phenom., 60(4):257–299, December 1992.

[304] M. Ohno and P. Decleva. Satellites of the 2s and 2p XPS spectra of TiCl_4. Phys. Rev. B, 49(2): 818–825, January 1994.

[305] M. Marlo and V. Milman. Density-functional study of bulk and surface properties of titanium nitride using different exchange-correlation functionals. Phys. Rev. B, 62(4):2899–2907, July 2000.

[306] Nils Mårtensson and Börje Johansson. Core level binding energy shifts between free and condensed atoms. Sol. Stat. Commun., 32(9):791–794, December 1979.

[307] W. L. Jolly. Electron Spectroscopy. North-Holland, Amsterdam, 1972.

[308] Hüfner. Very High Resolution Photoelectron Spectroscopy, volume 715. Springer Berlin Heidelberg, Berlin, Heidelberg, 2007. ISBN 978-3-540-68130-4.

[309] John C. Fuggle and Santos F. Alvarado. Core-level lifetimes as determined by x-ray photoelectron spectroscopy measurements. Phys. Rev. A, 22(4):1615, October 1980.

[310] Louis Porte, Laurent Roux, and Jean Hanus. Vacancy effects in the x-ray photoelectron spectra of TiN_x. Phys. Rev. B, 28(6):3214–3224, 1983.

[311] J. C. Fuggle, M. Campagna, Z. Zolnierek, R. Lässer, and A. Platau. Observation of a relationship between Core-Level line shapes in photoelectron spectroscopy and the localization of screening orbitals. Phys. Rev. Lett., 45(19):1597–1600, November 1980.

[312] Javier Díaz, Guido Paolicelli, Salvador Ferrer, and Fabio Comin. Separation of the sp^3 and sp^2 components in the C1sphotoemission spectra of amorphous carbon films. Phys. Rev. B, 54(11): 8064–8069, 1996.

[313] J. M Conny and C. J Powell. Standard test data for estimating peak parameter errors in x-ray photoelectron spectroscopy III. errors with different curve-fitting approaches. Surf. Interf. Anal., 29(12):856–872, December 2000.

[314] De-Quan Yang and Edward Sacher. Carbon 1s x-ray photoemission line shape analysis of highly oriented pyrolytic graphite: The influence of structural damage on peak asymmetry. Langmuir, 22(3):860–862, 2005.

[315] S. Doniach and M. Sunjic. Many-electron singularity in x-ray photoemission and x-ray line spectra from metals. J. Phys. C, 3(2):285–291, 1970.

[316] G.D. Mahan. Many-body effects on x-ray spectra of metals. In Frederick Seitz Henry Ehrenreich and David Turnbull, editors, Advances in Research and Applications, volume 29 of Solid State Physics, pages 75 – 138. Academic Press, 1974.

[317] Sven Tougaard. Universality classes of inelastic electron scattering cross-sections. Surf. Interf. Anal., 25(3):137–154, 1997.

[318] Stephen Evans. Curve synthesis and optimization procedures for x-ray photoelectron spectroscopy. Surf. Interf. Anal., 17(2):85–93, February 1991.

[319] J.C.W. Folmer and D.K.G. de Boer. XPS core level line shapes in metallic compounds: A probe for the nature of the electrons at the fermi level. Sol. Stat. Commun., 38(12):1135–1138, June 1981.

[320] Neal Fairley and Alan Carrick. The Casa Cookbook. Fairley, Neal and Carrick, Alan, 2005.

[321] S Tougaard. Algorithm for analysis of low-energy-resolution REELS; determination of inelastic electron scattering cross-sections and applications in quantitative XPS. Surf. Sci., 464(2–3): 233–239, October 2000.

[322] J. E. Castle. Module to guide the expert use of x-ray photoelectron spectroscopy by corrosion scientists. J. Vac. Sci. & Technol. A, 25(1):1–27, 2007.

[323] C. Ernsberger, J. Nickerson, T. Smith, A. E. Miller, and D. Banks. Low temperature oxidation behavior of reactively sputtered tin by x-ray photoelectron spectroscopy and contact resistance measurements. J. Vac. Sci. & Technol. A, 4(6):2784–2788, 1986.

[324] D. A. Shirley. High-Resolution X-Ray photoemission spectrum of the valence bands of gold. Phys. Rev. B, 5(12):4709, June 1972.

[325] Y.L. Jeyachandran, Sa.K. Narayandass, D. Mangalaraj, Sami Areva, and J.A. Mielczarski. Properties of titanium nitride films prepared by direct current magnetron sputtering. Mater. Sci. & Eng. A, 445-446:223 – 236, 2007.

[326] János Végh. The shirley background revised. J. Electron Spectrosc. Relat. Phenom., 151(3): 159–164, May 2006.

[327] N. Heide, B. Siemensmeyer, and J. W Schultze. Surface characterization and electrochemical behaviour of nitrogen- and carbon-implanted titanium. Surf. Interf. Anal., 19(1-12):423–429, June 1992.

[328] I. Milošev, H.-H. Strehblow, B. Navinšek, and M. Metikoš Huković. Electrochemical and thermal oxidation of TiN coatings studied by XPS. Surf. Interf. Anal., 23(7–8):529–539, July 1995.

[329] I. Bertóti. Characterization of nitride coatings by XPS. Surf. Coat. Technol., 151-152:194 – 203, 2002.

[330] A. Glaser, S. Surnev, F.P. Netzer, N. Fateh, G.A. Fontalvo, and C. Mitterer. Oxidation of vanadium nitride and titanium nitride coatings. Surf. Sci., 601(4):1153 – 1159, 2007.

[331] P. Steiner, H. Höchst, and S. Hüfner. XPS investigation of simple metals. Z. Phys. B, 30(2):129–143, June 1978.

[332] M. P. Seah, I. S. Gilmore, and S. J. Spencer. Background subtraction: II. general behaviour of REELS and the tougaard universal cross section in the removal of backgrounds in AES and XPS. Surf. Sci., 461(1-3):1–15, August 2000.

[333] S. Tougaard. Composition depth information from the inelastic background signal in XPS. Surf. Sci., 162(1-3):875–885, October 1985.

[334] M P (NPL) Seah, S J Spencer, F Bensebaa, I Vickridge, H Danzebrink, M Krumrey, T Gross, W Oesterle, E Wendler, B Rheinländer, Y Azuma, and M Suzuki S Tanuma D W Moon H J Lee Hyun Mo Cho H Y Chen A T S Wee T Osipowicz J S Pan W A Jordaan R Hauert U Klotz C van der Marel M Verheijen Y Tamminga C Jeynes P Bailey (CCLRC) S Biswas U Falke N V Nguyen D Chandler-Horowitz J R Ehrstein D Muller J A Dura I Kojima, N Suzuki. Critical review of the current status of thickness measurements for ultrathin SiO2 on Si part V: Results of a CCQM pilot study. Surf. Interf. Anal., 36 (9):1269–1303, 2004.

[335] M. Repoux. Comparison of background removal methods for XPS. Surf. Interf. Anal., 18(7): 567–570, July 1992.

[336] S. Tougaard. Practical algorithm for background subtraction. Surf. Sci., 216(3):343–360, June 1989.

[337] Antonella Rossi. Lectures on quantitative surface analysis, ETH Zürich, Switzerland.

[338] S. Tanuma, C. J Powell, and D. R Penn. Calculations of electron inelastic mean free paths for 31 materials. Surf. Interf. Anal., 11(11):577–589, August 1988.

[339] G. G. Fuentes, E. Elizalde, F. Yubero, and J. M. Sanz. Electron inelastic mean free path for Ti, TiC, TiN and TiO2 as determined by quantitative reflection electron energy-loss spectroscopy. Surf. Interf. Anal., 33(3):230–237, 2002.

[340] S. Tanuma, C. J Powell, and D. R Penn. Calculations of electron inelastic mean free paths. Surf. Interf. Anal., 37(1):1–14, January 2005.

[341] Robert F. Reilman, Alfred Msezane, and Steven T. Manson. Relative intensities in photoelectron spectroscopy of atoms and molecules. J. Electron Spectrosc. Relat. Phenom., 8(5):389–394, 1976.

[342] J. H. Scofield. Hartree-Slater subshell photoionization cross-sections at 1254 and 1487 eV. J. Electron Spectrosc. Relat. Phenom., 8(2):129–137, 1976.

[343] S. Tanuma, C. J. Powell, and D. R. Penn. Calculation of electron inelastic mean free paths (IMFPs) vii. reliability of the tpp-2m imfp predictive equation. Surf. Interf. Anal., 35(3):268–275, 2003.

[344] W. H Gries and W. Werner. Take-off angle and film thickness dependences of the attenuation length of x-ray photoelectrons by a trajectory reversal method. Surf. Interf. Anal., 16(1-12): 149–153, July 1990.

[345] A. Jablonski and C. J. Powell. The electron attenuation length revisited. Surf. Sci. Rep., 47(2-3): 33–91, June 2002.

[346] Ronald Powell and Stephen M. Rossnagel. Pvd for Microelectronics: Sputter Desposition to Semiconductor Manufacturing. Academic Press, October 1998.

[347] W. H Gries. A universal predictive equation for the inelastic mean free pathlengths of x-ray photoelectrons and auger electrons. Surf. Interf. Anal., 24(1):38–50, January 1996.

[348] J. Zemek, P. Jiricek, A. Jablonski, and B. Lesiak. Elastic electron backscattering from silicon surfaces: effect of surface roughness. Surf. Interf. Anal., 34(1):215–219, 2002.

[349] R. Jung, J. C. Lee, G. T. Orosz, A. Sulyok, G. Zsolt, and M. Menyhard. Determination of effective electron inelastic mean free paths in SiO2 and Si3N4 using a Si reference. Surf. Sci., 543(1): 153–161, 2003.

[350] R. J Ward and B. J Wood. A comparison of experimental and theoretically derived sensitivity factors for XPS. Surf. Interf. Anal., 18(9):679–684, September 1992.

[351] Sari Granroth, Weine Olovsson, Erik Holmström, Ronny Knut, Mihaela Gorgoi, Svante Svensson, and Olof Karis. Understanding interface properties from high kinetic energy photoelectron spectroscopy and first principles theory. J. Electron Spectrosc. Relat. Phenom., 183(1–3):80–93, January 2011.

[352] N. Pauly and S. Tougaard. Surface and core hole effects in x-ray photoelectron spectroscopy. Surf. Sci., 604(13-14):1193–1196, July 2010.

[353] S. Oswald and F. Oswald. A promising concept for using near-surface measuring angles in angle-resolved x-ray photoelectron spectroscopy considering elastic scattering effects. J. Appl. Phys., 109(3):034305–034305–11, February 2011.

[354] N. Pauly and S. Tougaard. Calculation of the angular distribution of the surface excitation parameter for Ti, Fe, Cu, Pd, Ag, and Au. Surf. Interf. Anal., 40(3-4):731–733, 2008.

[355] P.L.J Gunter, O.L.J Gijzeman, and J.W Niemantsverdriet. Surface roughness effects in quantitative XPS: magic angle for determining overlayer thickness. Appl. Surf. Sci., 115(4):342–346, August 1997.

[356] Wolfgang S. M Werner. Magic angle for surface roughness for intensity ratios in AES/XPS. Surf. Interf. Anal., 23(10):696–704, September 1995.

[357] J. Zemek. Electron spectroscopy of corrugated solid surfaces. Anal. Sci., 26(2):177–186, 2010.

[358] I. Bertóti, M. Mohai, J. L. Sullivan, and S. O. Saied. Surface characterisation of plasma-nitrided titanium: an XPS study. Appl. Surf. Sci., 84(4):357 – 371, 1995.

[359] Kevin S Robinson and Peter M. A Sherwood. X-Ray photoelectron spectroscopic studies of the surface of sputter ion plated films. Surf. Interf. Anal., 6(6):261–266, December 1984.

[360] T. Brat. Characterization of titanium nitride films sputter deposited from a high-purity titanium nitride target. Journal of Vacuum Science & Technology B: Microelectronics and Nanometer Structures, 5:1741, November 1987.

[361] I.leR. Strydom and S. Hofmann. XPS and EELS study of the valence band electronic structure of TiN and (Ti, Al)N coatings as influenced by the deposition parameters. Vacuum, 41(7-9): 1619–1623, 1990.

[362] A. J. Perry. On the existence of point defects in physical vapor deposited films of TiN, ZrN, and HfN. J. Vac. Sci. & Technol. A, 6(3):2140, 1988.

[363] A300 Series, A3CV & CTM magnetron sputtering sources; Installation and Operation Manual. AJA international, PO Box 246, 809 Country Way North Scituate, MA 02060, USA, 2004.

[364] Y.L. Yan, M.A. Helfand, and C.R. Clayton. Evaluation of the effect of surface roughness on thin film thickness measurements using variable angle XPS. Appl. Surf. Sci., 37(4):395–405, August 1989.

[365] C. Westphal. The study of the local atomic structure by means of x-ray photoelectron diffraction. Surf. Sci. Rep., 50(1-3):1 – 106, 2003. ISSN 0167-5729.

[366] International Organization for Standardization. Surface chemical analysis – x-ray photoelectron spectrometers – calibration of energy scales. Technical report, ISO 15472:2010, 2010.

[367] C. H. F. Peden, J. W. Rogers, N. D. Shinn, K. B. Kidd, and K. L. Tsang. Thermally grown Si3N4 thin films on Si(100): Surface and interfacial composition. Phys. Rev. B, 47(23):15622–15629, June 1993.

[368] E42 Committee. Terminology relating to surface analysis. Technical report, ASTM International, 2003.

[369] Naresh C Saha and Harland G Tompkins. Titanium nitride oxidation chemistry: An x-ray photoelectron spectroscopy study. J. Appl. Phys., 72(7):3072–3079, October 1992.

[370] C.S. Fadley, R.J. Baird, W. Siekhaus, T. Novakov, and S.Å.L. Bergström. Surface analysis and angular distributions in x-ray photoelectron spectroscopy. J. Electron Spectrosc. Relat. Phenom., 4(2):93–137, 1974.

[371] William F. Egelhoff. X-Ray photoelectron and auger electron forward scattering: A new tool for surface crystallography. Crit. Rev. Solid State Mater. Sci., 16:213–235, January 1990.

[372] Scott A. Chambers. Epitaxial film crystallography by high-energy auger and x-ray photoelectron diffraction. Adv. Phys., 40(4):357–415, August 1991.

[373] D P Woodruff and A M Bradshaw. Adsorbate structure determination on surfaces using photoelectron diffraction. Rep. Prog. Phys., 57(10):1029–1080, October 1994.

[374] D.P. Woodruff. Surface structural information from photoelectron diffraction. J. Electron Spectrosc. Relat. Phenom., 178–179(0):186–194, May 2010.

[375] D.P Woodruff. Photoelectron diffraction: past, present and future. J. Electron Spectrosc. Relat. Phenom., 126(1–3):55–65, October 2002.

[376] R. Opitz, S. Löbus, A. Thissen, and R. Courths. An angle-scanned photoelectron diffraction (XPD) study of the growth and structure of ultrathin Fe films on Au(001). Surf. Sci., 370(2-3):293–310, January 1997.

[377] J. Osterwalder, T. Greber, A. Stuck, and L. Schlapbach. Experimental full-solid-angle substrate photoelectron-diffraction data at 1-keV energies: Implications for photoelectron holography. Phys. Rev. B, 44(24):13764–13767, December 1991.

[378] R. Timm, P. R Willmott, and J. R Huber. Parallel epitaxy of TiN(100) thin films on si(100) produced by pulsed reactive crossed-beam laser ablation. Appl. Phys. Lett., 71(14):1966–1968, October 1997.

[379] Ernst Meyer, Hans Josef Hug, and Roland Bennewitz. Scanning Probe Microscopy: The Lab on a Tip. Springer, 2004.

[380] Peter Eaton and Paul West. Atomic Force Microscopy. Oxford University Press, USA, May 2010. ISBN 0199570450.

[381] Operating Instructions; Mobile S; Version 1.6. Nanosurf, Nanosurf AG Gräubernstrasse 12-14 4410 Liestal Switzerland, 2007.

[382] H. Jagodzinski and H. Jagodzinski. H. p. klug und l. e. alexander: X-ray diffraction procedures for polycrystalline and amorphous materials, 2. Auflage. John Wiley & Sons, New York-Sydney-Toronto 1974. Ber. Bunsen Ges. Phys. Chem., 79, 79(6, 6):553, 553–553, 553, June 1975.

[383] C. Suryanarayana and M. Grant Norton. X-Ray Diffraction: A Practical Approach. Springer, 1998.

[384] Mario Birkholz, Paul F. Fewster, and Christoph Genzel. Thin film analysis by X-ray scattering. Wiley-VCH, 2006. ISBN 9783527310524.

[385] P. Scherrer. Göttinger Nachr. Math. Phys., 2:98–100, 1918.

[386] Uwe Holzwarth and Neil Gibson. The scherrer equation versus the 'Debye-Scherrer equation'. Nat. Nanotechnol., 6(9):534–534, August 2011.

[387] Dominik Jaeger, Jörg Patscheider, and Aude Pelisson. Praktikum iii, departement materialwissenschaften, p6 texturuntersuchungen-polfiguren. Technical report, ETHZ and Empa Dübendorf, 2011.

[388] Wei-Kan Chu, James W. Mayer, and Marc-A. Nicolet. Backscattering spectrometry. Academic Press, 1978. ISBN 9780121738501.

[389] Henning Bubert and Holger Jenett, editors. Surface and Thin Film Analysis: A Compendium of Principles, Instrumentation, and Applications. Wiley-VCH, May 2002. ISBN 3527304584.

[390] C. Kottler, M. Döbeli, F. Glaus, and M. Suter. A spectrometer for low energy heavy ion ERDA. Nucl. Instr. Meth. Phys. Res. B, 248(1):155–162, July 2006.

[391] Lawrence R. Doolittle. A semiautomatic algorithm for rutherford backscattering analysis. Nucl. Instr. Meth. Phys. Res. B, 15(1–6):227–231, April 1986.

[392] C Jeynes, N P Barradas, P K Marriott, G Boudreault, M Jenkin, E Wendler, and R P Webb. Elemental thin film depth profiles by ion beam analysis using simulated annealing - a new tool. J. Phys. D: Appl. Phys., 36(7):R97–R126, April 2003.

[393] David B. Williams and C. Barry Carter. Transmission Electron Microscopy. Springer, 2009.

[394] A.N. Christensen. A neutron diffraction investigation of single crystals of titanium carbide, titanium nitride, and zirconium nitride. Acta Chem. Scand. Ser. A, 29:563–568, 1975.

[395] S. Sasaki, K. Fujino, and Y. Takeuchi. X-ray determination of electron-density distributions in oxides, MgO, MnO, CoO, and NiO, and atomic scattering factors of their constituent atoms. Proc. Japan Acad., 55:43–48, 1979.

[396] Massimo Boiocchi, Franca Caucia, Marcello Merli, Danilo Prella, and Luciano Ungaretti. Crystal-Chemical reasons for the immiscibility of periclase and wüstite under lithospheric p, t conditions. Eur. J. Mineral., 13(5):871–881, January 2001.

[397] Masashi Hasegawa, Takehiko Yagi, Masashi Hasegawa, and Takehiko Yagi. Systematic study of formation and crystal structure of 3d-Transition metal nitrides synthesized in a supercritical nitrogen fluid under 10 GPa and 1800 k using diamond anvil cell and YAG laser heating. ChemInform, 37, 37(4, 4):no–no, January 2006.

[398] Milo A Durand. The coefficient of thermal expansion of magnesium oxide. Phys., 7(8):297–298, August 1936.

[399] K. Aigner, W. Lengauer, D. Rafaja, and P. Ettmayer. Lattice parameters and thermal expansion of Ti(CxN1-x), Zr(CxN1-x), Hf(CxN1-x) and TiN1-x from 298 to 1473 k as investigated by high-temperature x-ray diffraction. J. Alloys Compd., 215(1–2):121–126, November 1994.

[400] L.S De Bernardez, J Ferrón, E.C Goldberg, and R.H Buitrago. The effect of surface roughness on XPS and AES. Surf. Sci., 139(2–3):541–548, April 1984.

[401] K. Peters (CrysTec GmbH). communication via email 2010.

[402] Young-Ki Lee, Jung-Yeul Kim, You-Kee Lee, Min-Sang Lee, Dong-Kun Kim, Duck-Yong Jin, Tae-Hyun Nam, Hyo-Jun Ahn, and Dong-Koo Park. Surface chemistry of non-stoichiometric TiNx films grown on (1 0 0)Si substrate by DC reactive magnetron sputtering. J. Cryst. Growth, 234 (2–3):498–504, January 2002.

[403] L. I. Johansson, H. I. P. Johansson, and K. L. Håkansson. Surface-shifted N 1s and C 1s levels on the (100) surface of TiN and TiC. Phys. Rev. B, 48(19):14520, November 1993.

[404] M. Delfino, J. A. Fair, and D. Hodul. X-ray photoemission spectra of reactively sputtered TiN. J. Appl. Phys., 71(12):6079, 1992.

[405] G Soto. AES, EELS and XPS characterization of Ti(C, N, O) films prepared by PLD using a ti target in N2, CH4, o2 and CO as reactive gases. Appl. Surf. Sci., 233(1–4):115–122, June 2004.

[406] H.Z. Wu, T.C. Chou, A. Mishra, D.R. Anderson, J.K. Lampert, and S.C. Gujrathi. Characterization of titanium nitride thin films. Thin Sol. Films, 191(1):55–67, October 1990.

[407] P. Prieto, L. Galán, and J. M. Sanz. Electronic structure of insulating zirconium nitride. Phys. Rev. B, 47(3):1613–1615, January 1993.

[408] P. Prieto. X-ray photoelectron spectroscopy study of the difference between reactively evaporated and direct sputter-deposited TiN films and their oxidation properties. J. Vac. Sci. & Technol. A, 13(6):2819, November 1995.

[409] F. Esaka, K. Furuya, H. Shimada, M. Imamura, N. Matsubayashi, H. Sato, A. Nishijima, A. Kawana, H. Ichimura, and T. Kikuchi. Comparison of surface oxidation of titanium nitride and chromium nitride films studied by x-ray absorption and photoelectron spectroscopy. J. Vac. Sci. & Technol. A, 15(5):2521–2528, September 1997.

[410] Rointan Framroze Bunshah. Handbook of hard coatings: deposition technologies, properties and applications. William Andrew, 2001.

[411] Boris Navinšek, J. Brguljan, and M. Peternel. Optimization of surface morphology and tool material for tin (PVD) efficiency in a given tribo-system. Materialwiss. Werkstofftech., 20(5): 166–173, May 1989.

[412] A. Barrie. 27th conference on analytical chemistry and applied spectroscopy, Cleveland, USA. In Preprints, 1976.

[413] Fumihiko Matsui, Tomohiro Matsushita, Mie Hashimoto, Kentaro Goto, Naoyuki Maejima, Hirosuke Matsui, Yukako Kato, and Hiroshi Daimon. Negative photoelectron diffraction replica in secondary electron angular distribution. J. Phys. Soc. Jpn., 81(1):013601, 2012.

[414] Kai Siegbahn. ESCA applied to free molecules. North-Holland Publishing, 1969.

[415] T. Novakov. X-ray photoelectron spectroscopy of solids; evidence of band structure. Phys. Rev. B, 3(8):2693–2698, 1971.

[416] O. Karis, S. Svensson, J. Rusz, P. M. Oppeneer, M. Gorgoi, F. Schäfers, W. Braun, W. Eberhardt, and N. Mårtensson. High-kinetic-energy photoemission spectroscopy of Ni at 1s: 6-eV satellite at 4 eV. Phys. Rev. B, 78(23):233105, December 2008.

[417] A. Rosencwaig, G. K. Wertheim, and H. J. Guggenheim. Origins of satellites on Inner-Shell photoelectron spectra. Phys. Rev. Lett., 27(8):479, 1971.

[418] S. Pignataro, A. Foffani, and G. Distefano. Esca study of some chromium complexes: ionization energies and multi-peak structure of the spectra. Chem. Phys. Lett., 20(4):350–355, June 1973.

[419] A. Bosch, H. Feil, G.A. Sawatzky, and N. Mårtensson. Core hole satellites in Ni and Au Ni. Sol. Stat. Commun., 41(4):355–357, January 1982.

[420] David P. Spears, Helmut J. Fischbeck, and Thomas A. Carlson. Satellite structure in the x-ray photoelectron spectra of rare gases and alkali-metal halides. Phys. Rev. A, 9(4):1603–1611, April 1974.

[421] J. A. Lowe, C. T. Chantler, and I. P. Grant. Ab initio determination of satellite intensities in transition-metal photoemission spectroscopy using a multiconfiguration framework. Phys. Rev. A, 83(6):060501, June 2011.

[422] M. Diserens, J. Patscheider, and F. Lévy. Improving the properties of titanium nitride by incorporation of silicon. Surf. Coat. Technol., 108-109(1-3):241–246, October 1998.

[423] J. R. Shallenberger, D. A. Cole, and S. W. Novak. Characterization of silicon oxynitride thin films by x-ray photoelectron spectroscopy. In Papers from the 45th National Symposium of the American Vacuum Society, volume 17, pages 1086–1090. AVS, 1999.

[424] Priyanka Singh, S.M. Shivaprasad, M. Lal, and M. Husain. Angle-dependent XPS analysis of silicon nitride film deposited on screen-printed crystalline silicon solar cell. Sol. Energy Mater. Sol. Cells, 93(1):19–24, January 2009.

[425] Leland Rosenberger, Ronald Baird, Erik McCullen, Gregory Auner, and Gina Shreve. XPS analysis of aluminum nitride films deposited by plasma source molecular beam epitaxy. Surf. Interf. Anal., 40(9):1254–1261, 2008.

[426] Zhigang Xie, Adolph Miller Allen, Mei Chang, Phillip Wang, and Tza-jing Gung. Control of bombardment energy and energetic species toward a superdense titanium nitride film. J. Vac. Sci. & Technol. A, 28(6):1326–1329, 2010.

[427] Harish C. Barshilia, K. Yogesh, and K.S. Rajam. Deposition of TiAlN coatings using reactive bipolar-pulsed direct current unbalanced magnetron sputtering. Vacuum, 83(2):427–434, September 2008.

[428] Heejoon Ahn, Michael Zharnikov, and James E. Whitten. Abnormal pinning of the fermi and vacuum levels in monomolecular self-assembled films. Chem. Phys. Lett., 428(4–6):283–287, September 2006.

[429] Nagaiyanallur V. Venkataraman, Stefan Zürcher, Antonella Rossi, Seunghwan Lee, Nicola Naujoks, and Nicholas D. Spencer. Spatial tuning of the metal work function by means of alkanethiol and fluorinated alkanethiol gradients. J. Phys. Chem. C, 113(14):5620–5628, 2009.

[430] I. Vurgaftman, J. R Meyer, and L. R Ram-Mohan. Band parameters for III–V compound semiconductors and their alloys. J. Appl. Phys., 89(11):5815–5875, June 2001.

[431] I. Vurgaftman and J. R Meyer. Band parameters for nitrogen-containing semiconductors. J. Appl. Phys., 94(6):3675–3696, September 2003.

[432] D. R. Baer, M. H. Engelhard, D. J. Gaspar, A. S. Lea, and C. F. Windisch. Use and limitations of electron flood gun control of surface potential during XPS: two non-homogeneous sample types. Surf. Interf. Anal., 33(10-11):781–790, 2002.

[433] W B Su, C S Chang, and Tien T Tsong. Quantum size effect on ultra-thin metallic films. J. Phys. D: Appl. Phys., 43(1):013001, January 2010.

[434] Tamotsu Hashizume, Shinya Ootomo, Takanori Inagaki, and Hideki Hasegawa. Surface passivation of GaN and GaN/AlGaN heterostructures by dielectric films and its application to insulated-gate heterostructure transistors. In Papers from the 30th Conference on the Physics and Chemistry of Semiconductor Interfaces, volume 21, pages 1828–1838. AVS, 2003.

[435] W. Nolting. Grundkurs Theoretische Physik 5/2. Springer, 2006.

[436] C. Miao, H. Lu, X.Z. Du, Y. Li, R. Zhang, and Y.D. Zheng. InGaN/GaN multi-quantum-well planar metal-semiconductor-metal light-emitting diodes. Electron. Lett., 44(6):441 –442, 2008.

[437] J. Zhou, Y. L Hao, Z. J Yang, and G. Y Zhang. Resonant tunneling effect in metal-semiconductor-metal ultraviolet detectors grown with AlGaN/GaN multi-quantum-well interlayer. Appl. Phys. Lett., 89(5):053514–053514–3, August 2006.

[438] S. M. Sze and Kwok Kwok Ng. Physics of semiconductor devices. John Wiley and Sons, 2007.

[439] J. Redinger, P. Weinberger, and A. Neckel. Theory of angle-resolved photoemission for in general disordered complex lattices: applications to the off-normal emission from TiNx (100). Theor. Chim. Acta, 71(6):479–487, July 1987.

[440] C. Stampfl, W. Mannstadt, R. Asahi, and A. J. Freeman. Electronic structure and physical properties of early transition metal mononitrides: Density-functional theory LDA, GGA, and screened-exchange LDA FLAPW calculations. Phys. Rev. B, 63(15):155106, March 2001.

[441] Hans Söderberg, Magnus Odén, Axel Flink, Jens Birch, Per O.Å. Persson, Manfred Beckers, and Lars Hultman. Growth and characterization of TiN/SiN(001) superlattice films. J. Mater. Res., 22: 3255–3264, 2007.

[442] P.C. Wo, P.R. Munroe, Z.F. Zhou, K.Y. Li, and Z.H. Xie. Effects of TiN sublayers on the response of TiSiN nanocomposite coatings to nanoidentation and scratching contacts. Mater. Sci. & Eng. A, 527(16–17):4447–4457, June 2010.

[443] F. Vaz and L. Rebouta. Superhard nanocomposite ti-si-n coatings. In Materials science forum, volume 383, page 143–150, 2001.

[444] S. Neralla, D. Kumar, S. Yarmolenko, and J. Sankar. Mechanical properties of nanocomposite metal–ceramic thin films. Composites Part B: Engineering, 35(2):157–162, March 2004.

[445] S. Vepřek, P. Nesládek, A. Niederhofer, F. Glatz, M. Jílek, and M. Šíma. Recent progress in the superhard nanocrystalline composites: towards their industrialization and understanding of the origin of the superhardness. Surf. Coat. Technol., 108–109(0):138–147, October 1998.

[446] D. Tabor. J. Inst. Met., 62:307, 1951.

[447] J. Cahoon. An improved equation relating hardness to ultimate strength. Metallurg. Mater. Trans. B, 3(11):3040–3040, 1972.

[448] Thomas H Courtney. Mechanical behavior of materials. McGraw-Hill, New York, 1990. ISBN 0070132658 9780070132658.

[449] G. J. Taylor. Journal Institute of Metals, 62:307, 1938.

[450] R. Chandra, Davinder Kaur, Amit Kumar Chawla, N. Phinichka, and Z.H. Barber. Texture development in Ti–Si–N nanocomposite thin films. Mater. Sci. & Eng. A, 423(1–2):111–115, May 2006.

[451] A.C. Fischer-Cripps, P. Karvánková, and S. Vepřek. On the measurement of hardness of super-hard coatings. Surf. Coat. Technol., 200(18–19):5645–5654, May 2006.

[452] M. Dudek, O. Zabeida, J. E. Klemberg-Sapieha, and L. Martinu. Effect of substrate bias on the micro-structure and properties of nanocom-posite titanium nitride–based films. Journal of Achievements in Materials and Manufacturing Engineering Selected full texts, 37(2):416–421, 2009.

[453] Emmanuel Soignard, Maddury Somayazulu, Jianjun Dong, Otto F Sankey, and Paul F McMillan. High pressure-high temperature synthesis and elasticity of the cubic nitride spinel γ-Si3N4. J. Phys.: Condens. Matter, 13(4):557–563, January 2001.

[454] J Z Jiang, F Kragh, D J Frost, K Støahl, and H Lindelov. Hardness and thermal stability of cubic silicon nitride. J. Phys.: Condens. Matter, 13(22):L515–L520, June 2001.

[455] Andreas Zerr, Markus Kempf, Marcus Schwarz, Edwin Kroke, Mathias Göken, and Ralf Riedel. Elastic moduli and hardness of cubic silicon nitride. J. Am. Ceram. Soc., 85(1):86–90, 2002.

[456] Boris Kiefer, Sean R. Shieh, Thomas S. Duffy, and Toshimori Sekine. Strength, elasticity, and equation of state of the nanocrystalline cubic silicon nitride γ-Si3N4 to 68GPa. Phys. Rev. B, 72 (1):014102, July 2005.

[457] Rolf Haug. Advances in Solid State Physics. Springer, January 2008.

[458] Andreas Zerr, Gerhard Miehe, George Serghiou, Marcus Schwarz, Edwin Kroke, Ralf Riedel, Hartmut Fuesz, Peter Kroll, and Reinhard Boehler. Synthesis of cubic silicon nitride. Nature, 400 (6742):340–342, July 1999. ISSN 0028-0836.

[459] D. Chakraborty and J. Mukerji. Effect of crystal orientation, structure and dimension on vickers microhardness anisotropy of β-, α-Si3N4, α-SiO2 and α-SiC single crystals. Mater. Res. Bull., 17 (7):843–849, July 1982.

[460] O Yeheskel and Y Gefen. The effect of the α phase on the elastic properties of Si3N4. Mater. Sci. & Eng., 71(0):95–99, May 1985.

[461] Xinwen Zhu and Yoshio Sakka. Textured silicon nitride: processing and anisotropic properties. Sci. Technol. Adv. Mater., 9(3):033001, July 2008.

[462] Ping Yang, Hoong-Kun Fun, Ismail Ab. Rahman, and Mohd.Idiris Saleh. Two phase refinements of the structures of α-Si3N4 and β-Si3N4 made from rice husk by rietveld analysis. Ceram. Int., 21(2):137–142, 1995.

A Interface maths

In the following formulae the interface ratio r_i and bulk ratio r_b are derived. First an expression for the interface intensity I_{int} of a signal emerging from an interface between the bulk with the element B and the overlying material L is formulated. In the bilayer system (see fig.5.1), that is used in here, the overlayer has a thickness t and does not contain the bulk element B. The real interface is atomically flat (see section 6.3 amd 6.4), but the interaction region (how far a polarization or a charging is causing a signal change in the shake-up) might be rather diffuse. The effects resulting in a change of the shake-up behavior and the range of an interface region are discussed in chapter 8. A interface thickness δ is defined as the thickness of the region in which the shake-up intensity is different from the shake-up intensity of the bulk material .

The intensity $I(d)$ of the emitted electrons traveling through a material the distance d_t is given by the Lambert-Beer law:

$$I(d_t) = I_0 \cdot e^{-d_t/\lambda} \tag{A.1}$$

where I_0 is the intensity of a pure element at the place of origin and λ is the IMFP (see sect. 3.8.1). Since the signal from a depth x under the angle of emission Θ travels the distance $d = \frac{x}{\cos\Theta}$, this signal is given by:

$$I(x) = I_0 \cdot e^{-x/(\lambda\cos\Theta)} \tag{A.2}$$

The measured intensity signal I_m can be expressed as:

$$\begin{aligned} I_m &= \int_0^\infty I(x) && \text{(A.3)} \\ &= \int_0^t I_L(x)\mathrm{d}x + \int_t^{t+\delta} I_{int}(x)\mathrm{d}x + \int_{t+\delta}^\infty I_{bulk}(x)\mathrm{d}x && \text{(A.4)} \end{aligned}$$

The shake-up process only happens in the TiN sublayer hence the signals of the overlying material are not adding any intensity to the shake-up intensity. In a more general approach a measured sublayer intensity I_m is defined, that only contains intensities from the sublayer B. Since the overlying material L does not contain the element B therefore no intensity arises from the overlayer. This means the first term in equation A.3 is zero and insertion of equation A.2 in equation A.3 leads to:

$$\begin{aligned}
I_m &= \int_t^{t+\delta} I_{0,\mathrm{int}} e^{-x/(\lambda\cos\Theta)}\,\mathrm{d}x + \int_{t+\delta}^{\infty} I_{0,\mathrm{bulk}} e^{-x/(\lambda\cos\Theta)}\,\mathrm{d}x && \text{(A.5)}\\
&= I_{0,\mathrm{int}} \left[-\lambda\cos\Theta\, e^{-x/(\lambda\cos\Theta)}\right]_t^{t+\delta} + I_{0,\mathrm{bulk}} \left[-\lambda\cos\Theta\, e^{-x/(\lambda\cos\Theta)}\right]_{t+\delta}^{\infty} && \text{(A.6)}\\
&= \lambda\cos\Theta \left(I_{0,\mathrm{int}} \left[e^{-x/(\lambda\cos\Theta)}\right]_{t+\delta}^{t} + I_{0,\mathrm{bulk}} \left[e^{-x/(\lambda\cos\Theta)}\right]_{\infty}^{t+\delta} \right) && \text{(A.7)}\\
&= \lambda\cos\Theta \left(I_{0,\mathrm{int}} \left[e^{-t/(\lambda\cos\Theta)} - e^{-(t+\delta)/(\lambda\cos\Theta)}\right] + I_{0,\mathrm{bulk}} \left[e^{-(t+\delta)/(\lambda\cos\Theta)}\right]\right) && \text{(A.8)}\\
&= \lambda\cos\Theta\, e^{-t/(\lambda\cos\Theta)} \left(I_{0,\mathrm{int}} \left(1 - e^{-\delta/(\lambda\cos\Theta)}\right) + I_{0,\mathrm{bulk}} e^{-\delta/(\lambda\cos\Theta)}\right) && \text{(A.9)}
\end{aligned}$$

If we replace

$$\begin{aligned}
c &= \lambda\cos\Theta\, e^{-t/(\lambda\cos\Theta)} && \text{(A.10)}\\
f &= 1-g && \text{(A.11)}\\
g &= e^{-\delta/(\lambda\cos\Theta)}, && \text{(A.12)}
\end{aligned}$$

then the measured intensity $\mathrm{I_m}$ of the sublayer B can be written as:

$$I_m = c\cdot\left(I_{int}\cdot f + I_{bulk}\cdot g\right) \tag{A.13}$$

Note that only the function c depends on the thickness of the overlayer.

As described in section 5.3 only the intensity ratios are of interest in this work. Therefore we define R_m as the ratio of the measured area intensity S_m of the shake-up and the measured intensity M_m of the main photoelectron line.

The measured ratio R_m can be calculated by using equation A.13:

$$R_m = \frac{S_m}{M_m} = \frac{S_{int}\cdot f + S_{bulk}\cdot g}{M_{int}\cdot f + M_{bulk}\cdot g} \tag{A.14}$$

and the measured ratio R_m becomes independent on the overlayer thickness t. Since we are interested on the intensity change in the shake-up at the interface, hence we define an interface ratio r_i of the shake-up intensity S_{int} and the intensity of the main PE line M_{int} as:

$$r_i = \frac{S_{int}}{M_{int}} \tag{A.15}$$

and in the same way a bulk ratio r_b is defined

$$r_b = \frac{S_{bulk}}{M_{bulk}} \tag{A.16}$$

The indices i and b are indicating that the signal emerges from the interface and bulk volume respectively.

A detected electron has either undergone a shake-up process or not, the sum of both shaken and not shaken electrons is constant. It is assumed that the scattering ratio of core orbitals of an atom (e.g. Ti 2p) and therefore the sensitivity factors s_c are not changing significantly neither between shake-up and main line nor if different electron densities surround the atom. Therefore the overall amount of emitted electrons between the bulk and the interface can be considered as equal and constant[i], i.e.:

$$M_{int} + S_{int} = M_{bulk} + S_{bulk} = k \tag{A.17}$$

With the above equation A.17 we can write $M_{int} = k - S_{int}$. Replacing S_{int} according to equation A.15 gives $S_{int} = r_i M_{int}$. Therefore we can write:

$$\begin{aligned} M_{int} &= k - S_{int} = k - r_i M_{int} && \text{(A.18)} \\ &\Leftrightarrow M_{int} + r_i M_{int} = k && \text{(A.19)} \\ &\Leftrightarrow M_{int} = k\frac{1}{1 + r_i} && \text{(A.20)} \end{aligned}$$

In a similar way we can write:

$$S_{int} = k\frac{r_i}{1 + r_i} \tag{A.21}$$

The same accounts for the bulk values of the shake-up intensity S_{bulk} and the main intensity M_{bulk}. If the last two equations are merged in equation A.14, then the constant k cancels and we obtain:

$$R_m = \frac{\frac{r_i}{1+r_i} f + \frac{r_b}{1+r_b} g}{\frac{1}{1+r_i} f + \frac{1}{1+r_b} g} \tag{A.22}$$

The author would like to point out the difference between the mathematical derived ratio R_m and the experimental obtained interface ratio r_i. The *fit function* for ratio R_m is independent from the overlayer thickness t since the overlayer does not contain titanium. This is integrated in equation A.13 where the Ti 2p signal from the overlayer has not been included. The *experimental results* for the interface ratio r_i show a clear thickness dependence (sect. 8.6.3).

The interface ratio r_i is obtained by rearranging equation A.22 and results in

$$r_i = \frac{g r_b - R_m - f r_b R_m}{g R_m - r_b - f} \tag{A.23}$$

---

[i] Less electrons will be emitted from deeper lying atoms, but this is already taken into account in equation A.2. Here the intensities are calculated as they appear at the origin of emission, i.e. before any scattering with neighboring atoms.

B Tail determination of TiN

In this appendix the tail shape of Ti 2p$_{3/2}$ and Ti 2p$_{1/2}$ is approximated by using the line shape of pure titanium. The line shape for Ti has been empirically found to be a function of a Gauss-Lorentzian product (GL) and an exponential decaying tail (T). The tail of the peak describes the inelastic scattering of the emitted PE, that undergoes an interaction with the electrons in the conduction band of the metal. The area A_{Ti} of the titanium peak is calculated by the function $GL(x, E_0, w, m) \cdot T(x, E_0, w, k)$ describing the intensity as a function of the kinetic energy of the PE.

$$A_{Ti} = \int_{-\infty}^{\infty} GL(x, E_0, w, m) \cdot T(x, E_0, w, k) \tag{B.1}$$

where G is a Gaussian function, L is a Lorentzian function, E_0 is the *kinetic* energy of the peak position, w is the FWHM, m is a factor describing the amount of mixing of Gaussian and Lorentzian parts, k is an asymmetry parameter and T is an exponential decaying tail function described by [320]:

$$\begin{aligned} T(x, E_0, w, k) = exp(-k\frac{x - E_0}{w}) \quad &; \quad x \leq E_0 && \text{(B.2)} \\ 1 \quad &; \quad else && \text{(B.3)} \end{aligned}$$

we can reformulate this:

$$\begin{aligned} A_{Ti} &= \int_{-\infty}^{\infty} GL(x, E_0, w, m) \cdot T(x, E_0, k) && \text{(B.4)} \\ &= \int_{-\infty}^{E_0} GL(x, E_0, w, m) \cdot T(x, E_0, k) + \int_{E_0}^{\infty} GL(x, E_0, w, m) && \text{(B.5)} \\ &= \int_{-\infty}^{E_0} GL(x, E_0, w, m) \cdot \int_{-\infty}^{E_0} T(x, E_0, k) + \int_{E_0}^{\infty} GL(x, E_0, w, m) && \text{(B.6)} \\ &= A_{Ti,elast} \cdot \int_{-\infty}^{E_0} T(x, E_0, k) + A_{Ti,elast} && \text{(B.7)} \\ &= A_{Ti,elast} \cdot (1 + T_{Ti,tail}) && \text{(B.8)} \end{aligned}$$

where the symmetry of the GL-function around E_0 has been used to replace $A_{Ti,elast} = \int_{-\infty}^{E_0} GL(x, E_0, w, m) = \int_{E_0}^{\infty} GL(x, E_0, w, m)$ and a tail form factor has been introduced $T_{Ti,tail} = \int_{-\infty}^{E_0} T(x, E_0, k)$.

$T_{Ti,tail}$ can be further simplyfied by:

$$\begin{aligned} T_{Ti} &= \int_{E_0}^{\infty} T(x, E_0, k_{Ti}) && \text{(B.9)} \\ &= \int_{E_0}^{\infty} \exp\left(-k_{Ti}\left(\frac{x-E_0}{w}\right)\right) \mathrm{d}x && \text{(B.10)} \\ &= \left[-\frac{w}{k_{Ti}} \exp\left(-k_{Ti}\left(\frac{x-E_0}{w}\right)\right)\right]_{E_0}^{\infty} = \frac{w}{k_{Ti}} && \text{(B.11)} \end{aligned}$$

Hence the area of the Ti-peak is described by:

$$A_{Ti} = A_{Ti,elast} \cdot (1 + \frac{w}{k_{Ti}}) \tag{B.12}$$

In Ti four valence electrons are in the valence band, but only one is present in TiN. Only valence electrons can contribute to the tail, therefore it is approximated that the TiN tail is only a fourth of the Ti tail:

$$T_{TiN} \overset{!}{=} \frac{1}{4} T_{Ti} \tag{B.13}$$

This means:

$$4k_{Ti} = k_{TiN} \tag{B.14}$$

C Additional XPS spectra

C.1 Detailed spectra of different overlayers

C.2 Ti 2p spectra of Si_3N_4 overlayer on TiN

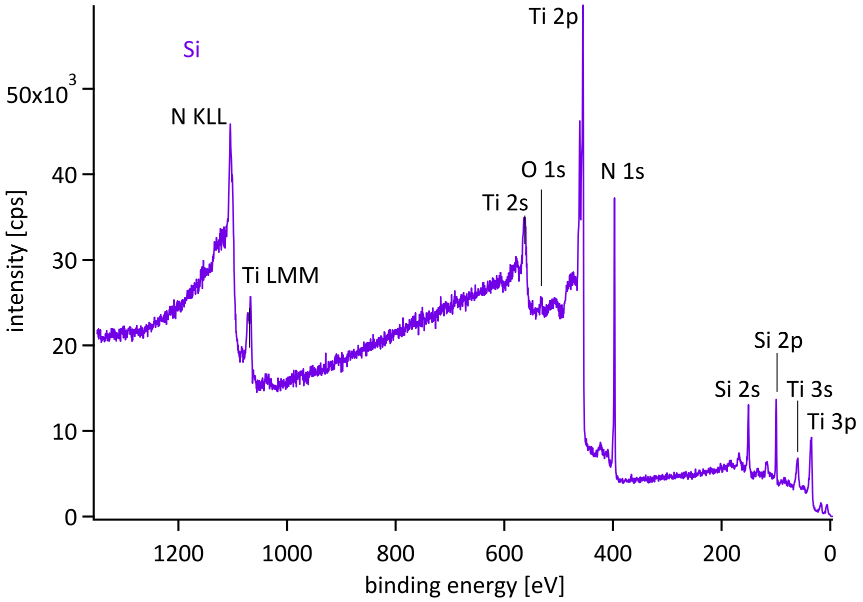

Figure C.1: Survey spectrum of a TiN/Si bilayer systems recorded at AOE = 45°, shown are 4.2 nm of Si deposited at 800 °C on sc-TiN(001). No bias is used during the deposition.

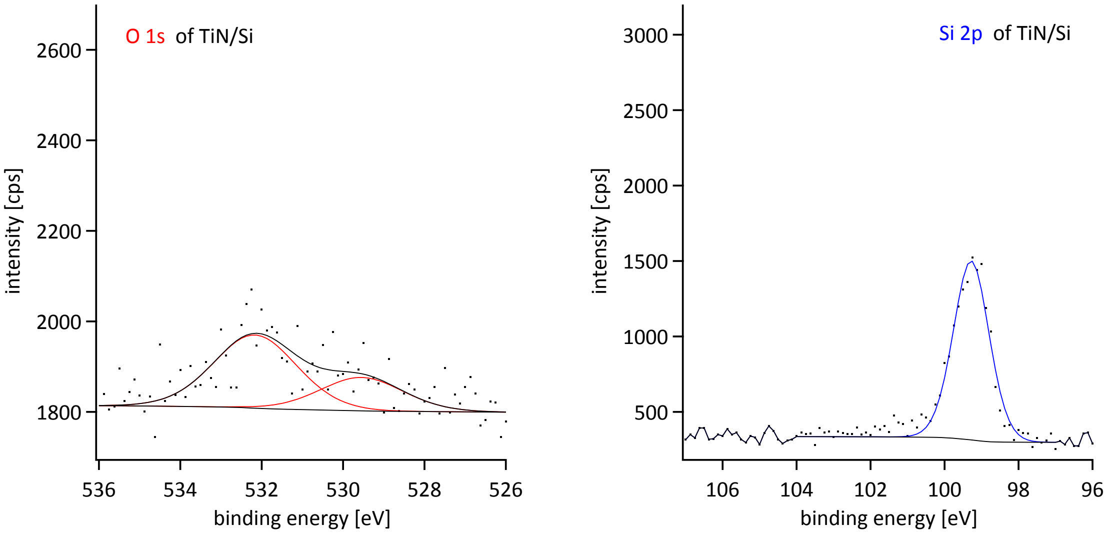

Figure C.2: Detailed O 1s (left) and Si 2p (right) spectrum of a TiN/Si bilayer recorded at AOE = 44°. In both cases a Shirley background subtraction is used. Axis are scaled in order to be comparable to other spectra.

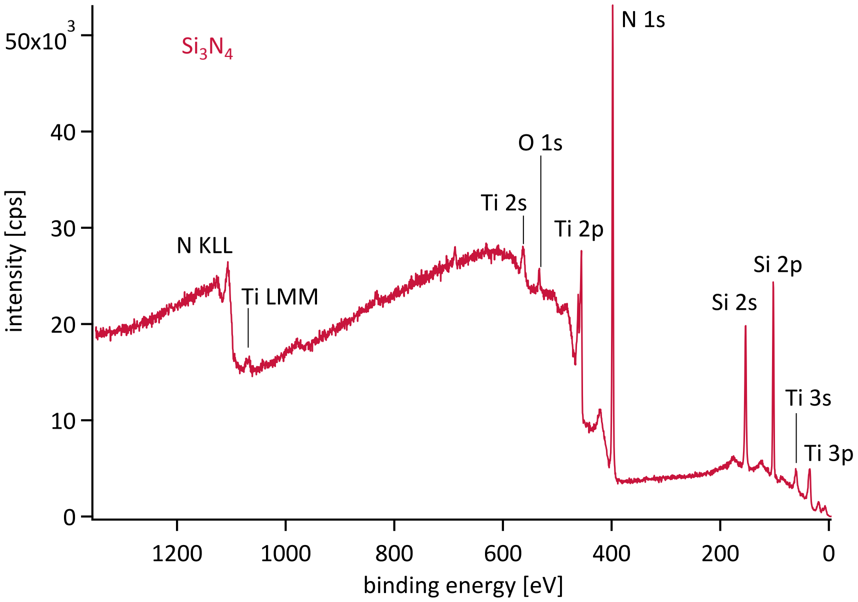

Figure C.3: Survey spectrum of a TiN/Si_3N_4 bilayer systems recorded at AOE = 45°, shown are 1.4 nm of Si_3N_4 deposited at 800 °C on sc-TiN(001). No bias is used during the deposition.

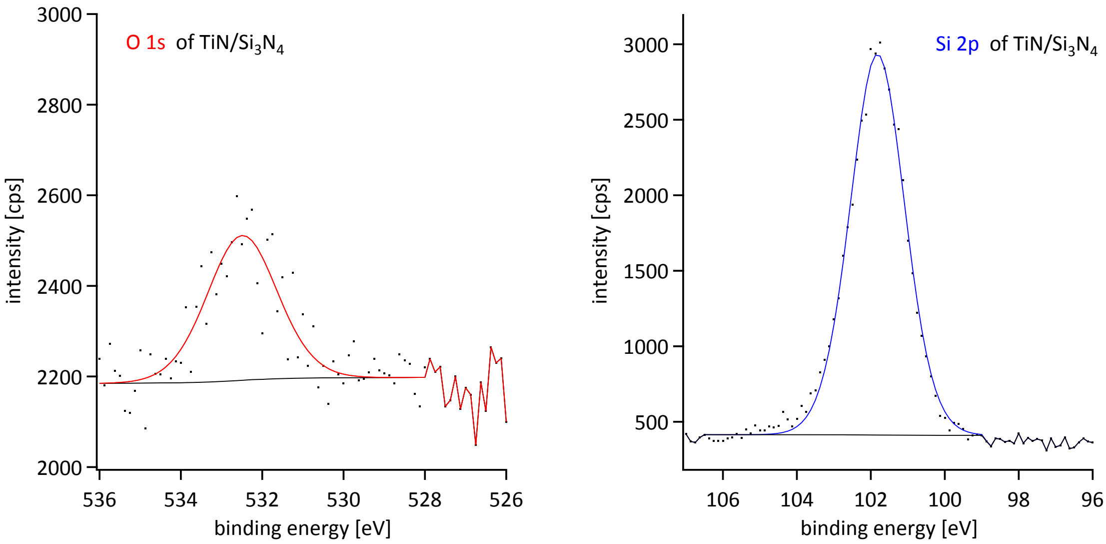

Figure C.4: Detailed O 1s (left) and Si 2p (right) spectrum of a TiN/Si_3N_4 bilayer recorded at AOE = 44°. In both cases a Shirley background subtraction is used. Axis are scaled in order to be comparable to other spectra.

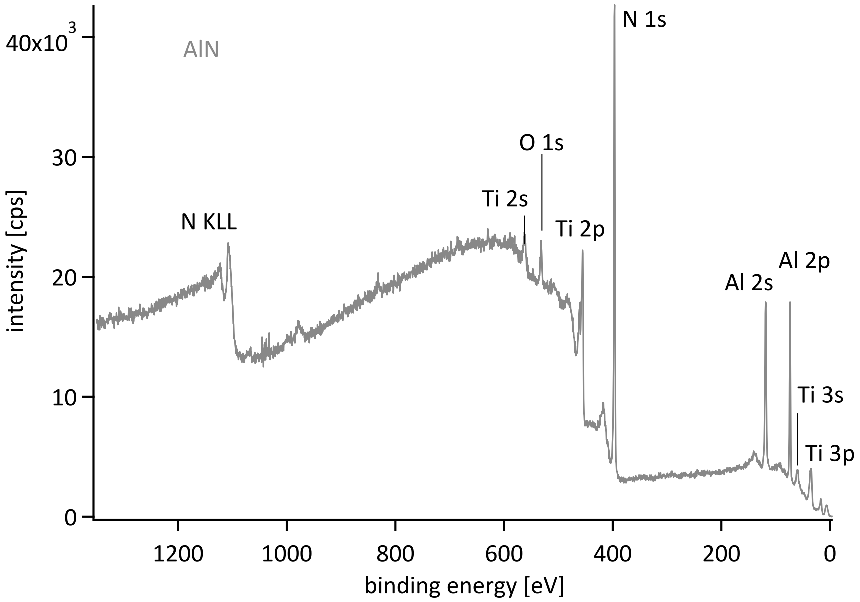

Figure C.5: Survey spectrum of a TiN/AlN bilayer systems recorded at AOE = 45°, shown are 1.5 nm of AlN deposited at 800 °C on sc-TiN(001). No bias is used during the deposition.

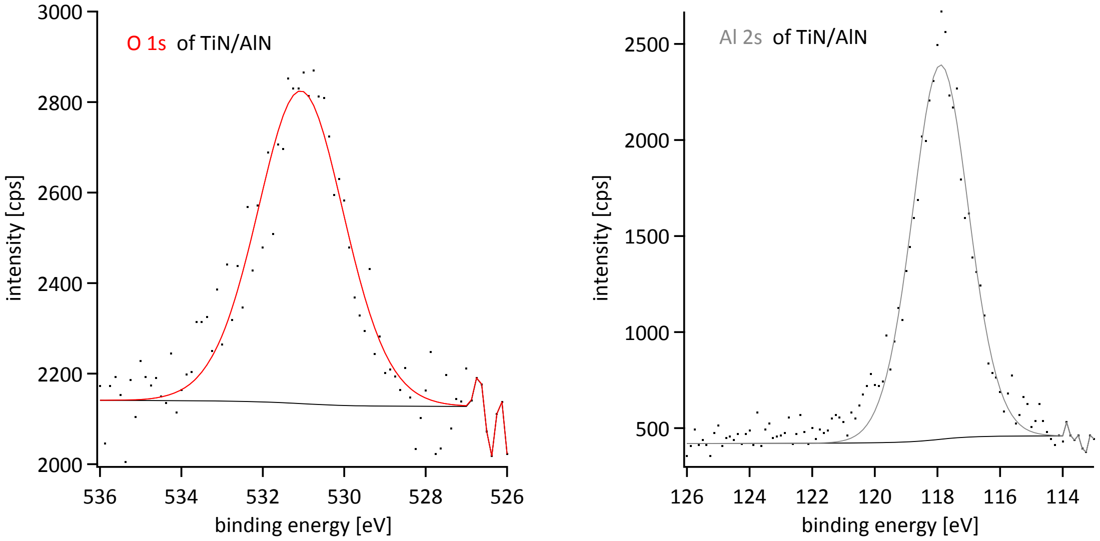

Figure C.6: Detailed O 1s (left) and Al 2s (right) spectrum of a TiN/AlN bilayer recorded at AOE = 44°. In both cases a Shirley background subtraction is used. Axis are scaled in order to be comparable to other spectra.

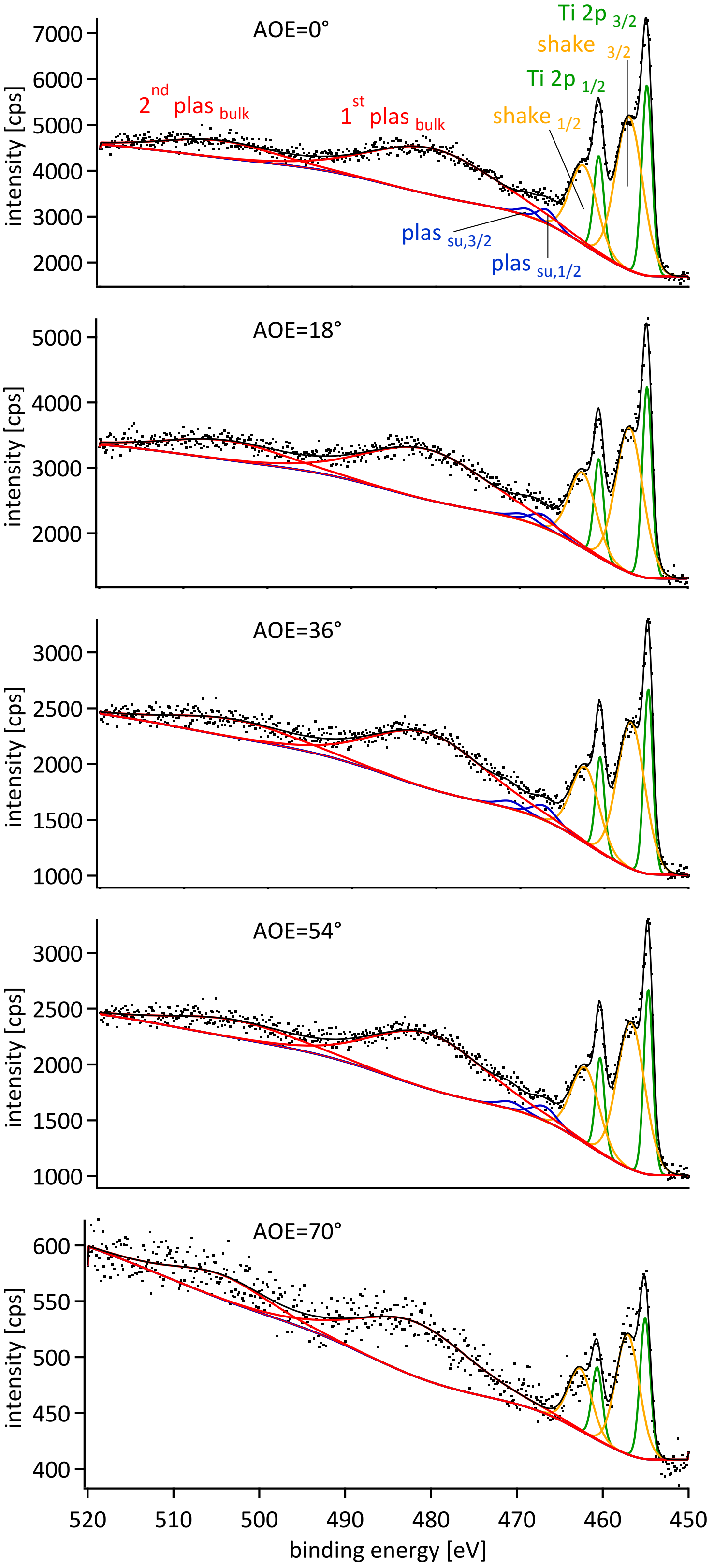

Figure C.7: Ti 2p spectra for TiN covered with a 1.7 nm overlayer of Si_3N_4. All main and shake-up peaks are fitted with a GL(20) line shape, all others with a GL(30) (sect. 7.4). The AOE increases from top to bottom. Note the y-axis scale is adjusted for each spectrum.

D Gold AR-XPS

In section 7.1 a shift in the binding energy is observed in dependence of the AOE. A gold reference sample has been measured under the same conditions as all other samples analyzed in this work (sect. 5.1). The work function has been calibrated so that E_B (Au $4f_{7/2}$)=83.95 eV. The binding energy of Au $4f_{7/2}$ shows no dependence from the AOE (see fig.D.1). The standard deviation over all AOE from 0° to 70° is ±0.03 eV.

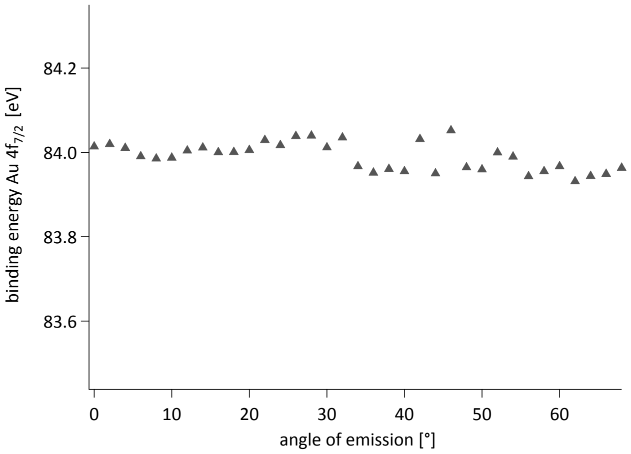

Figure D.1: The binding energy of Au $4f_{7/2}$ is independent from the AOE. For a better comparison the axis dimension of the binding energy axis has been chosen to be equivalent to the one of fig.7.2.

E Hardness estimations

The values used for the hardness calculations are shown in table E.2. The β-Si_3N_4 hardness approximations are based on experimental data obtained by Vila et al. [155], their hardness $H_{\beta-Si_3N_4}$ varies between 9 GPa and 23.4 GPa and depends on the nitrogen flow during the deposition. The big deviations result in an lower and upper guess of the hardness. For the unstable c-Si_3N_4 phase only limited experimental data is available [455]. The shear modulus for this c-Si_3N_4 phase has been indirectly inferred and is controversial [456]. Therefore *ab initio* calculated shear modulus are used in order to approximate the c-Si_3N_4 hardness.

In the case of α-Si_3N_4 and β-Si_3N_4 $\perp$ the misfit between Si_3N_4 and TiN are to large hence no epitaxial growth occurs and no coherency stress can develop to participate in an hardness increase. For $\beta-Si_3N_4$ $\parallel$the reported lattice constant of Ivashchenko et al. [195] are used.

In the cases of β-Si_3N_4 and TiN the shear modulus G has been calculated using the Young's modulus E and the Poisson's ratio ν.

$$G = \frac{E}{2(1+\nu)} \tag{E.1}$$

with a Poisson's ratio for α-, β- and c- Si_3N_4 of $\nu = 0.25$ and for TiN $\nu = 0.2$. The author is aware that ν should be different for $\nu_\perp$ and $\nu_\parallel$ depending whether the deformation occurs perpendicular or parallel to the surface, but no data is available on the non isotropic Si_3N_4 structures. Nevertheless the Poisson's ratio is not expected to deviate much from the 0.25 and hence is sufficient for the approximation used in here.

Please note: According to Koehler [132] the material with the lower shear modulus G_A controls the hardness, i.e. that $H_K = H_k + H_A$ with $G_A < G_B$ [86, 134]. The reason why the lower shear modulus is used is that the dislocation moves in a multilayer system in the layer with the lower shear stress (or line energy W [132, 457]). In the case of uni-elemental nanocomposites it has been shown by Schiøtz et al. [111] that for grain sizes of the order of 5 nm the main part of the plastic deformation is occurring at the grain boundaries and only a minor part by dislocation activity in the grains. It is further argued that the nanocomposites have no dislocations at the grain-matrix interface, while in the grain junctions dislocations are present (see fig. 2.4). Hence in the case of TiN/Si_3N_4 the dislocation activity takes only place in the Si_3N_4 interlayer/grain junctions and equation (2.6) writes as $\tau_K = \tau_k + \tau_{Si_3N_4}$. (If it would be assumed that the dislocation moves through the TiN grain, then $H_{tot}(c - Si_3N_4, low) = 34.83$ GPa and $H_{tot}(c - Si_3N_4, up) = 42.19$ GPa would be obtained.) Additionally it is pointed out, that the reported shear modulus vary over a wide range [156, 453, 458] and even a shear modulus of 148 GPa is reported [455]. This would mean that there is no Koehler stress since $G_{c-Si_3N_4} - G_{TiN} = 0$ (compare to eq.2.5).

parameter	α-Si$_3$N$_4$ $\parallel$	α-Si$_3$N$_4$ $\perp$	β-Si$_3$N$_4$ $\parallel$	β-Si$_3$N$_4$ $\perp$	c-Si$_3$N$_4$ (low)	c-Si$_3$N$_4$ (up)	TiN
Hardness H [GPa]	37.9 [459]	50.8 [459]	36.3 [459]	20.0 [459]	30 [453]	47 [156]	20.2 [188]
Young's modulus E [GPa]	145 (*)[460]	145 (*) [460]	540 [461]	280 [461]	-	-	356 [131]
Shear modulus G [GPa]	-	-	216(**)	112(**)	340 [453]	349 [156]	148 (**)
d (***) [Å]	7.77 [462]	5.63 [462]	4.67 [195]	2.93 [195]	4.13 [131]	4.13 [131]	4.26 [table 6.1]

Table E.1: Shown are all parameters which are used for the hardness approximation (sect. 9.2). (*)no direction specified (**) The shear modulus has been calculated using eq. E.1, see text. (***) for $\parallel$ the lattice constant is d_a and for $\perp$ d_c.

	α-Si$_3$N$_4$ $\parallel$	α-Si$_3$N$_4$ $\perp$	β-Si$_3$N$_4$ $\parallel$	β-Si$_3$N$_4$ $\perp$	c-Si$_3$N$_4$ (low)	c-Si$_3$N$_4$ (up)
H_K (*) [GPa]	38.0	50.9	21.9	39.7	35.6	57.2
H_{coh} [GPa]	-	-	24.9	-	7.8	10.6
H_t [GPa]	1.3	1.3	1.3	1.3	1.3	1.3
H_{tot} [GPa]	39.3	52.2	48.0	41.0	44.6	69.0

Table E.2: Results obtained from the hardness estimations, listed are the participating components: Koehler hardness H_K, coherency hardness H_{coh} and the thermal hardness H_t (sect. 9.2). In equation 2.5 the angle between the interface and the slip plane Θ is set to $\sin\Theta_s = 0.5$ according to Xu et al. [129]. For the thermal stress ΔT is 480 K, since in deposition temperatures of up to $\approx 500\,^\circ$C are often used [115, 442]. The thermally induced stress is compared to other effects small and using a different ΔT results only in slightly different stresses.(*) H_K has in all cases being calculated using $H_K = H_k + H_{Si_3N_4}$, for details see text.

Dominik A. Jaeger

Curriculum Vitae

Oberwiesenstrasse 73f
8050 Zürich, Switzerland
☎ *+41-77-462-2735*
✉ *jad125@empa.ch*

Personal Details

date of birth	18.03.1979
nationality	German

Education

since 2008	**PhD-student**, *ETH domain*, Lausanne, Dübendorf and Zürich, Switzerland. Doctoral School in the Laboratory of Physics of Complex Matter at EPFL, Lausanne Practical Work in the Laboratory of Nanoscale Materials Science at Empa, Dübendorf Teaching and Studying at the ETH, Zürich
01/2008	**diploma in physics**, *Albert-Ludwigs-University*, Freiburg, Germany.
07/1998	**graduated at German Secondary School with 'Abitur'**, *Albertus-Magnus-Gymnasium*, St.Ingbert, Germany.

Diploma Thesis

titel	*Characterisation and Simulation of Electrospun Non-Wovens*
supervisor	Prof. Dr. Michael Moseler, Dr. Raimund Jaeger
institute	Fraunhofer-Institute for Mechanics of Materials, Freiburg, Germany
description	The mechanical properties of single nanofibers and non-wovens with different distributions of fiber orientations were tested. An analytical model and computer simulations based on a molecular dynamic code were developed to describe the mechanical behavior of the non-wovens.

International Experience

08/2004 – 04/2005	**research internship**, *Departement of Biomaterials and Biomechanics*, Universitat Politécnica de Catalunya, Barcelona, Spain, Experimental investigations on the mechanical properties of polymer-bioglass-composites.
03/1999 – 09/2000	**civil service**, *Jewish Family & Children's Services*, Pittsburg, USA. after-school-program, working with the elderly, responsible for the management of a local food pantry

Practical Experience

01/2008 – 05/2008	**scientist**, *Fraunhofer-Institute for Mechanics of Materials (IWM)*, Freiburg, Germany, Laboratory of Biomedical Materials and Implants.
05/2003 – 12/2007	**student research assitant**, *Fraunhofer-Institute for Mechanics of Materials (IWM)*, Freiburg, Germany. experimental work, computer modeling, mentoring
09/2000 – 10/2004	**technical supervisor/assitant**, *Tournado (cultural event management company)*, Freiburg, Germany.
1998 – 2000	**assistant**, *VOIT*, St.Ingbert, Germany. production and assembly, quality management
1997	**assistant**, *FESTO*, St.Ingbert, Germany. production, tool setter at CNC milling machines
1994-1998	**assistant**, *Firma Klein*, St.Ingbert, Germany. production and assembly

Teaching activities

2008 – 2011	**Praktikum III, experiment P6; XRD pole figures**, *ETHZ D-MATL*.
1996 – 2008	**private tutor for maths and physics**.

Further Experiences

1994 – 2008	**volunteering in a christian youth group (KJG)**, Germany. volunteering in children and youth programs, organising local and nationwide activities, member of management teams, instructor for group leaders

Grants and Awards

2011	**Graduate Student Award**, *European Material Research Society (EMRS)*, Spring meeting, Nice, France.
2008	**Nominated for the Mechanical Material Award**, *Plansee-Mitsubishi-Group*.
2007	**Travel Grant**, *German Society for Biomaterials (DGBM)*.
1998	**Medal for the Outstanding Commitment towards the Welfare of the School Community**, *Albertus-Magnus-Gymnasium*.

Languages

German	native speaker
English	fluent in spoken and written language
Spanish	very good knowledge
French	good knowledge
Polish	level A1

Computer Skills

systems	Linux, Windows
programming	C/C++, html, VisualBasic, $\LaTeX$
modeling	finite element modeling (FEM), molecular dynamics (MD)

Publications

Dominik Jaeger, Jan Schischka, Jörg Bagdahn, and Raimund Jaeger. Tensile testing of individual ultrathin electrospun poly(L-lactic acid) fibers. *J. Appl. Polym. Sci.*, 114(6):3774–3779, 2009.

Dominik Jaeger, Jörg Patscheider, and Max Döbeli. Composition determination of thin nitride films. *Annual Report 2010, Laboratory of Ion Beam Physics*, page 95, 2011.

Franziska Conrad, Matthias Bauer, Denis Sheptyakov, Stephen Weyeneth, Dominik Jaeger, Kathrin Hametner, Pierre-Emmanuel Car, Jörg Patscheider, Detlef Günther, and Greta R. Patzke. New spinel oxide catalysts for visible-light-driven water oxidation. *RSC Adv.*, 2(7):3076–3082, March 2012.

Carl-Frederik Wyen, Dominik Jaeger, and Konrad Wegener. Influence of cutting edge radius on surface integrity and burr formation in milling titanium. *IJAMT*, 2012. accepted.

Raimund Jaeger, Michael Deissenbeck, Dominik Jaeger, and Uwe Soltész. Abrieb von dentalersatzwerkstoffen durch prophylaxepasten. *Die Quintessenz*, 56(Nr.1):61–65, 2005.

Hobbies

sports	cycling, sailing, climbing, snowboarding, kitesurfing, snowkiting
others	traveling, home improvement

Lausanne, 4. September 2012